

*TARGETING TRIPLE-NEGATIVE BREAST
CANCERS: DISCOVERY OF NOVEL LEAD
COMPOUNDS AND THEIR BIOLOGICAL
CHARACTERIZATION*



MARTIN-LUTHER-UNIVERSITÄT



HALLE-WITTENBERG

Morgan, Ibrahim

Leibniz Institute of Plant Biochemistry | Martin Luther University Halle-Wittenberg

Targeting Triple-Negative Breast Cancers: Discovery of Novel Lead Compounds and Their Biological Characterization.

Dissertation

Zur Erlangung des

Doktorgrades der Naturwissenschaften (Dr. rer. nat.)

der

Naturwissenschaftlichen Fakultät I

Biowissenschaften

der Martin-Luther-Universität

Halle-Wittenberg

vorgelegt

von Herr M.Sc. Ibrahim Ibrahim Mohamed Morgan

Halle (Saale), 2024

The work described in this dissertation has been developed at the Leibniz Institute of Plant Biochemistry (IPB).

Supervisor and thesis editor: Prof. Dr. Ludger A. Wessjohann

Co-supervisor: Dr. Robert Rennert

1st Reviewer: Prof. Dr. Markus Pietzsch (MLU-Halle)

2nd Reviewer: Prof. Dr. Ludger A. Wessjohann (IPB-Halle)

Date of Public Defense: March 11th, 2025

Declaration

“I declare that I have completed this dissertation without the unauthorized help of a second party and only with the assistance acknowledged therein. I have appropriately acknowledged and referenced all text passages that are derived from or based on the content of published or unpublished work of other authors.”

Ibrahim Ibrahim Mohamed Morgan

No part of this book can be reproduced without the permission of the author.

Acknowledgment

I want to acknowledge the support of my family, whose encouragement and understanding have been a constant source of strength. Special thanks to Prof. Dr. Ibrahim Morgan, Prof. Dr. Sahar Sedkey and Passant Morgan for their support during challenging times, which has been a constant source of strength.

I would like to express my sincere gratitude to Dr. Robert Rennert and Prof. Dr. Ludger Wessjohann for their unwavering support, guidance, and mentorship throughout the course of my Ph.D. research. I extend my heartfelt gratitude to Prof. Dr. Markus Pietzsch for graciously accepting the role of academic supervisor for this research.

I extend my appreciation to the Leibniz Institute of Plant Biochemistry for providing financial support for my research, without which this work would not have been possible. I am also grateful to my collaborators for their contribution, which is highlighted in the acknowledgment section following each chapter.

I would like to express my appreciation to my lab mates, whose friendship and collaborative spirit enriched the research environment. Special thanks to Martina Lerbs and Mohamed Saoud for their support, discussions, and shared dedication to our collective academic pursuits. Their contributions have added depth and diversity to the research process, making it a truly collaborative and rewarding experience.

I am indebted to the staff at Martin Luther University for their assistance with administrative tasks for the Ph.D. work.

Lastly, I express my heartfelt thanks to all those who have been a part of this academic journey, directly or indirectly. Your support has been invaluable.

Abstract

Triple-negative breast cancer is one of the most challenging cancers. It is characterized by its aggressive growth and the limitation of the satisfying treatment options. The utilization of the conventional treatment options of breast cancer for targeting TNBCs is mostly found ineffective due to the lack of receptors targeted in most therapies including epidermal growth factor receptor 2 (ERBB2, HER2), estrogen and progesterone receptors. In this context, the exploration of novel, innovative alternatives that could specifically target TNBCs is crucial. Therefore, this dissertation started to search the compound library of the Leibniz Institute of Plant Biochemistry to identify novel molecules that might be specifically suitable for the treatment of TNBCs. By employing various techniques, several compounds with distinct anticancer activity were identified. Moreover, the study did not aim only for the identification of novel anticancer agents but also to improve targeted therapies, offering new hope for effective and tailored interventions against TNBC. Chapter 1 introduces that topic.

Based on our high interest in selective compounds active against TNBCs, our investigation aimed initially at the exploration of novel poly(ADP-ribose) polymerase inhibitors (PARPi). The rationale behind the exploration of this family of compounds is their crucial role in DNA repair mechanisms, especially with defective homologous recombination. TNBCs often exhibit deficiencies in DNA repair pathways, making them susceptible to the synthetic lethality induced by PARP inhibition. Therefore, the study described in Chapter 2 aimed to establish several techniques combining computational, biochemical, and cell-based assays to identify and evaluate PARPi to seek for promising candidates from the Leibniz Institute of Plant Biochemistry's compound library with the potential to be developed as drugs for targeted therapies. Several novel molecules with PARP-1 inhibitory properties were identified in this study. Notably, a compound (2-(methylthio)quinazolin-4(3*H*)-one) stood out, exhibiting a five-fold higher activity compared to phthalazin-1(2*H*)-one (the core structure of the well-established PARPi reference compound, olaparib). The investigation also introduced various methodologies to assess cell permeability for PARPi. Though, the newly discovered compound had only limited cell permeability. This observation, however, aligns with the initial characteristics of phthalazin-1(2*H*)-one, which was later optimized to yield olaparib, the lead compound of the PARPi family.

During the assessment of PARPi, I empirically discovered several molecules lacking PARPi activity but, nevertheless, with notable anticancer properties. The first identified family of compounds with anticancer activity is the azaglycophymines. As described in Chapter 3, several compounds belonging to this family were found to be highly toxic to breast cancer, however, they exhibited a lack of selectivity towards TNBCs. The cytotoxicity of the family was extensively studied against various breast cancer types. Surprisingly, the most active compound, 2-((4-nitrophenyl)amino)quinazolin-4(3*H*)-one, induced cell death by different mechanisms depending on the breast cancer cell type treated. This difference could be helpful for the development of targeted therapy. Moreover, the compound's effect against an orthotopic *in vivo* model of 4T1 mouse breast cancer cells in BALB/c mice was investigated and confirmed a substantial tumor growth inhibition by that compound, highlighting the intriguing anticancer effect of that azaglycophymines.

The most remarkable discovery identified within the IPB library was 4-oxo-*N*,1-diphenyl-1,4-dihydropyridazine-3-carboxamide (selectAHRyl A). As explained in detail in Chapter 4, the compound was found to specifically target TNBC by an intriguing molecular mechanism. The study shows the utilization of various techniques to identify the mechanism of selectivity of the compound. The compound was found to act as a prodrug which activates the AHR pathway leading to the induction of CYP1A1 expression. The overexpression of CYP1A1 leads to the metabolism of the prodrug to its active form which was found absent in the healthy breast cancer cell lines.

The significance of this research lies in the identification of new promising R&D candidates for selective TNBC targeting within the compound collection of the Leibniz Institute of Plant Biochemistry. Mainly, by taking benefit from that compound library. Additionally, to contribute to the ongoing efforts to broaden the spectrum of available therapies and address the unmet clinical needs in

TNBC treatment. Further investigations are necessary to clarify the molecular mechanisms underlying the observed effects and to drive the development of these compounds towards clinical applications.

Keywords: Cancer, Breast cancer, TNBC, Drug discovery, Targeted therapy, PARP, AHR, Selectivity, Glycophymines, EGFR, CYP1A1

Zusammenfassung

Dreifach negativer Brustkrebs (TNBC) ist eine der am schwierigsten zu behandelnden Krebsarten. Denn TNBCs sind charakterisiert durch sein aggressives Wachstum und die geringe Menge der zufriedenstellenden Behandlungsmöglichkeiten. Konventionelle Behandlungsmöglichkeiten für Brustkrebs sind für die Bekämpfung von TNBC meist unwirksam, da die erforderlichen Zielrezeptoren, wie der epidermale Wachstumsfaktorrezeptor 2 (ERBB2, HER2) sowie Estrogen- und Progesteronrezeptoren, fehlen. In diesem Zusammenhang ist die Erforschung neuartiger, innovativer Alternativen, die spezifisch auf TNBC abzielen könnten, von entscheidender Bedeutung. Ziel dieser Dissertation war es daher, die Substanzbibliothek des Leibniz-Instituts für Pflanzenbiochemie (IPB) systematisch zu untersuchen, um neuartige Moleküle zu identifizieren, die speziell für die Behandlung von TNBCs geeignet sein könnten. Durch den Einsatz verschiedener chemoinformatischer, biochemischer, molekularbiologischer und zellbasierter Techniken konnten mehrere Substanzen mit vielversprechender krebshemmender Wirkung identifiziert werden. Darüber hinaus zielte die Studie nicht nur auf die Identifizierung neuartiger Substanzen mit anti-karzinogenen Eigenschaften ab, sondern auch auf die Verbesserung gezielter Therapien, die neue Hoffnung auf wirksame und persönlich zugeschnittene Maßnahmen gegen TNBCs geben. Kapitel 1 führt in dieses Thema ein.

Aufgrund unseres großen Interesses an selektiv gegen TNBCs aktiven Substanzen, zielte unsere Untersuchung zunächst auf die Erforschung neuartiger Poly(ADP-Ribose)-Polymerase-Inhibitoren (PARPi) ab. Der Grund für die Erforschung dieser Wirkstofffamilie ist ihr Potential zur Modulation der DNA-Reparaturmechanismen der Tumorzellen, insbesondere bei defekter homologer Rekombination. TNBCs weisen häufig Defizite in den DNA-Reparaturwegen auf, was sie anfällig für die durch PARP-Inhibition induzierte, sogenannte synthetische Letalität macht. Daher zielte die in Kapitel 2 beschriebene Studie darauf ab, verschiedene Techniken zu etablieren, die computergestützte, biochemische und zellbasierte Assays zur Identifizierung und Bewertung von PARPi kombinieren, um in der IPB-Substanzbibliothek nach vielversprechenden Kandidaten zu suchen, die das Potenzial haben, als Arzneimittel für zielgerichtete TNBC-Therapien entwickelt zu werden. Dabei stach vor allem die Substanz 2-(methylthio)quinazolin-4(3*H*)-on hervor, die im Vergleich zu Phthalazin-1(2*H*)-on (der Kernstruktur der etablierten PARPi-Referenzsubstanz Olaparib) eine fünffach höhere Aktivität aufwies. Im Rahmen der Untersuchungen wurden auch verschiedene Methoden zur Bewertung der Zellpermeabilität von PARPi angewandt. Die neu entdeckte Substanz war jedoch nur begrenzt zellmembrangängig. Diese Beobachtung stimmt jedoch mit den anfänglichen Eigenschaften von Phthalazin-1(2*H*)-on überein, das später optimiert wurde, um den inzwischen etablierten Wirkstoff Olaparib, die Leitsubstanz der PARPi-Familie, zu erhalten.

Während der Untersuchung von PARPi wurden zudem empirisch mehrere Moleküle entdeckt, die zwar keine PARPi-Aktivität aufweisen, aber dennoch bemerkenswerte anti-proliferative Aktivitäten gegen Krebszellen Eigenschaften aufweisen. Die erste identifizierte Substanzfamilie mit krebshemmender Wirkung sind die Azaglycophymines. Wie in Kapitel 3 beschrieben, erwiesen sich mehrere zu dieser Familie gehörende Substanzen als sehr potent gegen Brustkrebszellen, wiesen jedoch eine mangelnde Selektivität für TNBCs auf. Die Zytotoxizität dieser Substanzen wurde eingehend an verschiedenen Brustkrebs-Zelllinien untersucht. Überraschenderweise löste die aktivste Verbindung, 2-((4-nitrophenyl)amino)quinazolin-4(3*H*)-on, den Zelltod je nach behandeltem Brustkrebstyp durch unterschiedliche Mechanismen aus. Diese Unterschiede könnten für die Entwicklung einer gezielten Therapie hilfreich sein. Darüber hinaus wurde die Wirkung der Verbindung gegen ein orthotopes *in vivo* Modell von 4T1-Maus-Brustkrebszellen in BALB/c-Mäusen untersucht und eine erhebliche Hemmung des Tumorwachstums durch diese Substanz bestätigt, was die interessante krebshemmende Wirkung dieses Azaglycophymines unterstreicht.

Die bemerkenswerteste Entdeckung, die im Zuge dieser Arbeit in der IPB-Bibliothek gemacht wurde, war die Substanz 4-oxo-*N*,1-diphenyl-1,4-dihydropyridazin-3-carboxamid. Wie in Kapitel 4 ausführlich erläutert, wurde festgestellt, dass die Substanz durch einen bedeutsamen molekularen Mechanismus spezifisch gegen TNBCs wirkt. Die Studie zeigt den Einsatz verschiedener Techniken, um den Selektivitätsmechanismus der Verbindung zu aufzuklären. Es wurde festgestellt, dass die Verbindung als Prodrug wirkt, welche den AHR-Signalweg aktiviert, was zur Induktion der CYP1A1-

Expression führt. Die Überexpression von CYP1A1 führt zur Metabolisierung des Prodrugs in seine wirksame Form, die hingegen in gesunden Brustkrebszelllinien nicht detektiert werden konnte.

Die Bedeutung dieser Forschung liegt in der Identifizierung neuer vielversprechender F&E-Kandidaten für ein selektives TNBC-Targeting basierend auf der Substanzbibliothek des Leibniz-Instituts für Pflanzenbiochemie. Darüber hinaus soll ein Beitrag zu den laufenden Bemühungen geleistet werden, das Spektrum der verfügbaren Therapien zu erweitern und den drängenden klinischen Bedarf an wirksameren und nebenwirkungsärmeren TNBC-Behandlungsoptionen zu decken. Weitere Untersuchungen sind notwendig, um die molekularen Mechanismen zu klären, die den beobachteten Wirkungen zugrunde liegen, und um die Entwicklung dieser Substanzen in Richtung klinischer Anwendungen voranzutreiben.

Stichwörter: Krebs, Brustkrebs, TNBC, Wirkstoffentdeckung, gezielte Therapie, PARP, AHR, Selektivität, Glycophymines, EGFR, CYP1A1

Table of Contents

CHAPTER 1 : THE FOUNDATIONS OF CANCER AND ITS TREATMENT	1
1. CELL TURNOVER	1
1.1. Cell cycle	1
1.2. Programmed cell death	2
2. DNA HOMEOSTASIS	4
3. CANCER	5
3.1. Definition and history	5
3.2. Cancer treatment options	6
3.3. Chemotherapy classes	7
3.4. Targeted therapy	9
3.5. Classification and cancer types	10
3.6. Cancer statistics	10
3.7. Triple-negative breast cancer (TNBC)	10
4. COMPOUND LIBRARIES	11
5. LIBRARY SCREENING AND HITS CHARACTERIZATION	12
5.1. Phenotypic drug discovery approach	12
5.2. Rational drug discovery approach	13
6. AIM OF THE STUDY	14
6.1. Background	14
6.2. Methodology	14
CHAPTER 2 : IDENTIFICATION AND CHARACTERIZATION OF NOVEL INHIBITORS OF HUMAN POLY(ADP-RIBOSE) POLYMERASE-1	16
1. INTRODUCTION	17
2. MATERIALS AND METHODS	18
2.1. Chemicals and cell lines	18
2.2. <i>In silico</i> PARP-PARPi docking	19
2.3. hPARP-1 enzymatic assay	20
2.4. Differential gene expression	20
2.5. <i>In vitro</i> cell viability assay	20
2.6. <i>In vitro</i> synergistic cell viability assay	21
2.7. Fluorescence microscopy	21
3. RESULTS	21
3.1. <i>In silico</i> pre-selection of potential PARPi	21
3.2. Discovery of eight novel PARP inhibitors	21
3.3. mRNA expression levels of <i>hPARP-1</i> and <i>SLFN-11</i>	22
3.4. <i>In vitro</i> cytotoxicity of compound 57	23
3.5. Compound 57 did not exhibit synergistic effect in combination with TMZ	24
3.6. Compound 57 did not reach the nucleus-located hPARP-1 enzyme	24
4. DISCUSSION	25
5. CONCLUSION	29
CHAPTER 3 : THE IMPACT OF 9-AZAGLYCOPHYMINE DERIVATIVES ON THE PROLIFERATION OF VARIOUS BREAST CANCER CELL LINES <i>IN VITRO</i> AND <i>IN VIVO</i>	30
1. INTRODUCTION	31
2. MATERIALS AND METHODS	32
2.1. Cell lines and chemicals	32
2.2. Cell culture	32
2.3. Cell viability assays	33
2.4. Flow cytometric analyses	33
2.5. <i>In vivo</i> study	34
2.6. Histopathology	34
3. RESULTS	34
3.1. Discovery of novel 5 anticancer compounds with compound 19 as the most active compound	34
3.2. Compound 19 induced cell death in different breast cancer cell lines through different mechanisms	35
3.3. Compound 19 hinders breast tumor growth in mice	36
3.4. Histopathological observations indicate high safety margin of compound 19	37
4. DISCUSSION	38
5. CONCLUSIONS	40

CHAPTER 4 : DISCOVERY OF A HIGHLY SELECTIVE MOLECULE AGAINST TRIPLE-NEGATIVE BREAST CANCER AND CHARACTERIZATION OF ITS MODE OF ACTION 41

1.	INTRODUCTION	42
2.	MATERIALS AND METHODS.....	42
2.1.	Chemicals, reagents and kits	42
2.2.	Cell lines and cell culture	43
2.3.	Cell viability.....	43
2.4.	Flow cytometry analyses.....	44
2.5.	Proteome analyses.....	45
2.6.	Transcriptome analyses	46
2.7.	<i>In silico</i> AHR docking	46
2.8.	RT-qPCR analyses	46
2.9.	Immunofluorescence imaging	47
2.10.	Reporter gene assays.....	47
2.11.	Metabolism induction of selectAHRyl A using liver microsomes.....	47
2.12.	Synthesis of mono-hydroxylated derivatives of selectAHRyl A and identification of the enzymatically produced derivatives.....	48
2.13.	Statistical analysis statement.....	48
3.	RESULTS	49
3.1.	SelectAHRyl A causes cytotoxicity with highest selectivity for MDA-MB-468 TNBC cells	49
3.2.	SelectAHRyl A induces caspases-independent apoptotic cell death.....	49
3.3.	SelectAHRyl A induces upregulation of several proteins including heat shock protein 70	50
3.4.	Activation of the AHR pathway plays an essential role for the cell line selectivity of selectAHRyl A	51
3.5.	CYP1A1 and CYP1B1 are strongly upregulated in MDA-MB-468 upon treatment with selectAHRyl A	53
3.6.	<i>In silico</i> study indicates interaction between selectAHRyl A and AHR receptor	54
3.7.	AHR and CYP1A1 antagonists counteract the cytotoxic effect of selectAHRyl A	54
3.8.	SelectAHRyl A induces the translocation of AHR protein from cytosol into the nucleus	55
3.9.	SelectAHRyl A activates the AHR pathway and xenobiotic resistance elements.....	56
3.10.	SelectAHRyl A becomes mono- and di-hydroxylated by CYP1A1 upon agonistic AHR pathway activation.....	56
3.11.	1-(2-Hydroxyphenyl)-4-oxo-N-phenyl-1,4-dihydropyridazine-3-carboxamide (selectAHRyl B) is one of the active forms of selectAHRyl A	58
4.	DISCUSSION	58
5.	CONCLUSION	61
	GENERAL REMARKS	63
	REFERENCES.....	64
	SUPPLEMENTARY INFORMATION	72
	Chapter 2 : Identification and characterization of novel inhibitors of human poly(ADP-ribose) polymerase-1	72
	Chapter 3 : The impact of 9-azaglycophymine derivatives on the proliferation of various breast cancer cell lines in vitro and in vivo	78
	Chapter 4 : Discovery of a highly selective molecule against triple-negative breast cancer and characterization of its mode of action	87

Abbreviations

2D	Two-dimensional	L	Length (tumor dimension)
3D	Three-dimensional	LC-MS	Liquid chromatography-mass spectrometry
53BP1	p53 binding protein 1	LDEV	Large DNA-containing enveloped virus
ACN	Acetonitrile	MgCl₂	Magnesium chloride
ADME	Absorption, distribution, metabolism, and excretion	MOE	Molecular operating environment
AHR	Aryl hydrocarbon receptor	MOWSE	Molecular weight search
AHRR	Aryl hydrocarbon receptor repressor	mRNA	Messenger RNA
ALDH3A1	Aldehyde dehydrogenase 3 family member A1	MutH	Mismatch repair endonuclease
AnnV/PI	Annexin V/propidium iodide	MutL	Mismatch repair protein
ANXA2	Annexin 2	MutS	Mismatch recognition protein
AO	Acridine orange	NAD⁺	Nicotinamide adenine dinucleotide
AP site	Apurinic/aprimidinic site	NADH	Nicotinamide adenine dinucleotide
ART	ADP-ribose transferase	NADPH	Nicotinamide adenine dinucleotide phosphate
ATCC	American type culture collection	NADPH	Nicotinamide adenine dinucleotide phosphate
ATP	Adenosine triphosphate	NAP-6	(Z)-2-(2-aminophenyl)-1H-benzo[de]isoquinoline-1,3(2H)-dione
BC	Breast cancer	NER	Nucleotide excision repair
BER	Base excision repair	NF-κB	nuclear factor κ-light-chain-enhancer of activated B cells
BRCA	Breast cancer gene	NO	Nitric oxide
BRCT	BRCA1 C Terminus	NOX	NADPH oxidase
BSA	Bovine serum albumin	NSCLC	Non-small cell lung cancer
CAT	Catalytic domain	O₂	Oxygen
CD20	Cluster of differentiation 20	OLP	Olaparib
CD95L	Fas ligand	P/S	Penicillin-streptomycin
CDCl₃	Deuterated chloroform	p53	Tumor protein P53
CDK	Cyclin-dependent kinase	PARP	Poly(ADP-ribose) polymerase
CDK2	Cyclin-dependent kinase 2	PARPi	PARP inhibitor
CDK4	Cyclin-dependent kinase 4	PARPi-FL	Fluorescent PARP inhibitor
CDK6	Cyclin-dependent kinase 6	PBS	Phosphate-buffered saline
CDKI	Cyclin-dependent kinase inhibitor	PCA	Principal component analysis
CFSE	Carboxyfluorescein diacetate succinimidyl ester	PCD	Programmed cell death
Cip/Kip	CDK interacting protein/kinase inhibitory protein	PD-L1	Programmed death-ligand 1
CV	Crystal violet	PFA	Paraformaldehyde

CYP	Cytochrome P	PLS3	Plastin 3
CYP1A1	Cytochrome P 1A1	POL II	RNA polymerase II
CYP1B1	Cytochrome P 1B1	PR	Progesterone receptor
CYP51A1	Cytochrome P 51A1	qPCR	Quantitative polymerase chain reaction
DAF-FM	4-Amino-5-methylamino-2',7'-difluorofluorescein	RAB6A	Ras-related protein Rab-6A
DAPI	4',6-Diamidino-2-phenylindole	RAB6B	Ras-related protein Rab-6B
DDR	DNA damage response	RBC	Red blood cell
DHF	Dihydrofolate	RNA	Ribonucleic acid
DHFR	Dihydrofolate reductase	ROS	Reactive oxygen species
DMSO	Dimethyl sulfoxide	RT	Room temperature
DNA	Deoxyribonucleic acid	RT-qPCR	Reverse transcription quantitative polymerase chain reaction
DSB	Double strand break	S phase	Synthesis phase
EAP	Extrinsic apoptotic pathway	SAR	Structure activity relationship
EDTA	Ethylenediaminetetraacetic acid	SD	Standard deviation
EGFR	Epidermal growth factor receptor	SDS-PAGE	Sodium dodecyl sulfate polyacrylamide gel electrophoresis
ER	Estrogen receptor	SEPT11	Septin 11
ErbB-2	Human epidermal growth factor receptor 2	SEM	Standard error of the mean
FCS	Fetal calf serum	SLFN	Schlafen
FICZ	6-Formylindolo(3,2-b)carbazole	SSB	Single strand break
FPKM	Fragments per kilobase of transcript per million fragments mapped	TC-NER	Transcription-coupled nucleotide excision repair
G1 phase	Gap 1 phase	TCDD	2,3,7,8-tetrachlorodibenzo-p-dioxin
G2 phase	Gap 2 phase	TMZ	Temozolomide
GAPDH	Glyceraldehyde-3-phosphate dehydrogenase	TNBC	Triple-negative breast cancer
GART	Glycinamide ribonucleotide transformylase	TNFα	Tumor necrosis factor alpha
GG-NER	Global genome nucleotide excision repair	TOF-MS	Time-of-flight mass spectrometry
GO	Gene ontology	UHPLC-ESI-MS	Ultra-high-performance liquid chromatography-electrospray ionization-mass spectrometry
HD	Helical domain	UV	Ultraviolet
HER2	Human epidermal growth factor receptor 2	V	Volume (tumor dimension)
hPARP-1	Human poly(ADP-ribose) polymerase 1	v/v	Volume/volume
HR	Hormonal receptor	VEGFR	Vascular endothelial growth factor receptor
HSPA1A/1B	Heat shock protein A1A/1B	W	Width (tumor dimension)
i.p.	Intra peritoneal	w/v	Weight/volume

IAP	Intrinsic apoptotic pathway	WBC	White blood cells
IC₅₀	Half-maximal inhibitory concentration	XRCC-1	X-ray repair cross-complementing protein 1
ICZ	Indolo[3,2-b]carbazole	XRE	Xenobiotic response element
INK4	Inhibitor of CDK4	Zn	Zinc

Table of figures

Fig.1 An illustrated overview of the cell cycle phases G1, S, G2, and M. Each phase plays a crucial role in maintaining genomic integrity, regulating cell growth, and organizing a precise cell division.	1
Fig.2 The mitosis subphases, called prophase, metaphase, anaphase, and telophase, splitting a cell into two daughter cells, ensuring the replication of the genetic material. The figure was created by using BioRender.com.....	2
Fig.3 Different stages of apoptotic cell death. The figure was created by using BioRender.com.	3
Fig.4 An illustration of the different types of DNA damages. The figure was created by using BioRender.com.	4
Fig.5 Cancer treatment options. The figure was created by using BioRender.com.....	7
Fig.6 Structures of a , olaparib (OLP); b , niraparib and c , rucaparib.	18
Fig.7 The structure of the ART subdomain of hPARP-1 (PDB code: 3GJW) and the essential features of an established hPARP-1 inhibitor molecule (olaparib, grey). Cyan represents the position of the hydrogen bond acceptor, green represents the position of the aromatic ring and magenta represents the position of the hydrogen bond donor. Red-colored amino acids represent those that interact directly with the hPARPi and the orange-colored amino acids represent the blocked H-Y-E triad.....	19
Fig.8 Fast screening of the inhibitory impact of the selected compounds on hPARP-1 catalytic activity using the hPARP-1 enzyme assay. a , Compounds were tested at two different concentrations (1 and 10 μ M) to determine the most active hits. OLP (compound 70) was used at a concentration of 100 nM as a positive control. b , Dose-response curves to determine the IC ₅₀ values of the most active compounds.....	22
Fig.9 Structures and IC ₅₀ values of the most active novel hPARPi compounds as determined by using the hPARP-1 enzyme assays.	22
Fig.10 mRNA expression levels of a , <i>hPARP-1</i> and b , <i>SLFN-11</i> as determined in the breast cell lines under investigation by using RT-qPCR. The expression levels were calculated following the $\Delta\Delta$ Ct methodology in relation to the expression of the housekeeping gene <i>hGAPDH</i> and were normalized for illustration to the corresponding expression levels in 184B5 cells. (***p-value < 0.001).	23
Fig.11 Cell viability dose-response curves of the breast cell lines under investigation upon 72 h treatment with a , compound 57 ; b , OLP and c , TMZ. Cell viability was determined by using CV assay.	23
Fig.12 Dose-response curves of several breast cell lines. The cell lines were treated with several concentrations of TMZ combined with IC ₁₀ of a , compound 57 and b , OLP for 72 h. Cell viability was determined using CV assay.	24
Fig.13 BT-474 cells treated for 72 h with a , complete medium (non-treated reference); b , 100 μ M of compound 57 and c , 1.56 μ M of OLP, followed by hPARP-1 staining with 250 nM of PARPi-FL for 20 min. The images were captured by using the GFP channel of an EVOS™ FL Auto Imaging System and were processed and color-inverted by using FIJI software. Scale bar: 100 μ m.	24
Fig.14 The concept of the hPARP-1 enzyme assay: The assay consists of a hPARP enzyme reaction and a cycling reaction. In the hPARP reaction, the hPARP enzyme is activated in the presence of activated, i.e., strand breaks containing DNA and uses the NAD ⁺ substrate to add poly(ADP-ribose) tails as posttranslational modification to itself and other protein targets. In the second step, the cycling reaction allows a catalytically amplified fluorescent read-out of the remaining NAD ⁺ substrate that was not used up by hPARP. NAD ⁺ is transformed to NADH+H ⁺ , which is used to reduce resazurin to resorufin (excitation/emission: 540/595) which measured fluorescence indirectly indicates the activity of the hPARP enzyme. The scheme was created by BioRender.com.	26
Fig.15 Structure-activity relationship (SAR) considerations regarding compound 57 as the most active hPARPi identified.	27
Fig.16 Structure-activity relationship (SAR) considerations regarding compound 54	28
Fig.17 structures of compound 57 , quinazolin-4(3H)-one and phthalazin-1(2H)-one (the OLP core structure).	29
Fig.18 a , Quinazoline and b , quinazolinone core structures; c , gefitinib; d , erlotinib; e , vandetanib; f , raltitrexed; g , albaconazole; h , febrifugine and i , glycyphymine.	31
Fig.19 Dose-response curves of the viability of MCF-7, MDA-MB-468, BT-474, HCC1937 and 4T1 cells after 72 h treatment with the most active compounds. Cell viability was measured by using the CV assay.....	35
Fig.20 Bar graphs representing the biological impacts of compound 19 applied at IC ₅₀ for 72 h to several breast cancer cell lines on a , the induction of apoptosis and b , the cell cycle status distribution in G ⁰ /G1, S and G2/M phases. Bars represent the mean values \pm standard deviation calculated based on three independent measurements. * p < 0.05 compared to the untreated control cells.....	36
Fig.21 Impact of compound 19 on the 4T1 (mouse breast cancer cell line) tumor progression in a BALB/c mouse orthotopic model using two different doses, 5 and 20 mg/kg, applied once daily via i.p. route. Compound 19 was applied on days 6-10, 13-17 and day 20, whereby day 0 was the inoculation day. The mice were dissected on day 21, and the tumor volumes were measured using a caliper. . # p < 0.1 compared to the untreated control group.	36
Fig.22 Histopathological assessment. BALB/c mice were inoculated with 4T1 cells at day 0, eight animals per group were treated with vehicle, 5 mg/kg or 20 mg/kg. The dissection and the organ isolation were performed on day 21. a , Tumor tissues with necrotic areas (black stars) (H/E stain, 40 \times). b , Kidney tissues with intratubular protein casts (black arrowheads) and lymphocytes in interstitial space (black arrows) (H/E stain, 200 \times). c , Liver tissues with intrasinusoidal extramedullary hematopoiesis (black arrows) (H/E stain, 200 \times). d , Extramedullary hematopoiesis with megakaryocytes (black arrows) and hematopoietic cells (black arrowheads) in the red pulp of spleen (white pulp is labeled with black cross) (H/E stain, 200 \times).	37
Fig.23 Structures of compound 15 (2-(phenylamino)quinazolin-4-one, 9-azaglycyphymine) and the anti-proliferative compounds 19 , 22 , 24 , 46 , 47 , 48 and 49 . The complete set of compounds 1 – 49 is to be found in Table S6.	38
Fig.24 Illustrative chart summarizing the influence of compound 19 on various investigated breast cancer cell lines and outlining the mode of cell death induced by the respective compounds in these cells. The figure was created by using BioRender.com.	40

Fig.25 Compound' structures and cytotoxicity. a , Chemical structure of selectAHRyl A (4-oxo- <i>N</i> ,1-diphenyl-1,4-dihydropyridazine-3-carboxamide) and selectAHRyl B (1-(2-hydroxyphenyl)-4-oxo- <i>N</i> -phenyl-1,4-dihydropyridazine-3-carboxamide). b , Dose-response curves of the viability of breast cell lines treated with selectAHRyl A for 72 h and c , of MDA-MB-468 3D spheroids treated for either 72 or 120 h. The data are presented as the means of at least two independent biological replicates \pm SEM.	49
Fig.26: Impact of selectAHRyl A on common cell death-related pathways. Bar graphs illustrate the effects of selectAHRyl A at IC ₅₀ on MDA-MB-468 cells upon treatment for 72 h on a , induction of apoptosis quantified by using the AnnV/PI kit; b , cell cycle arrest upon treatment determined by using DAPI stain; c , induction of autophagic processes measured by using AO stain and d , induction of pan-caspases' activation, NO and ROS production, and the impact on cell proliferation using ApoStat, DAF-FM, DHR and CFSE stains, respectively. Data were normalized to the corresponding read-outs of the untreated control.	50
Fig.27 Impact of selectAHRyl A on cellular protein expression. a , STRING functional protein association network depicting proteins from MD-MB-468 cells with altered expression levels upon treatment with selectAHRyl A (indicated by a black arrowhead). The network was generated by using string-db.org. b , Biological processes and c , molecular functions affected in MDA-MB-468 upon selectAHRyl A treatment, as predicted by performing a GO data enrichment analysis using the analysis software tool of the PANTHER Classification System (pantherdb.org).	51
Fig.28 Impact of selectAHRyl A on genes' expression. a , Scheme of the aryl hydrocarbon receptor (AHR) pathway, genes with altered mRNA expression levels (adjusted p-value < 0.05) in MDA-MB-468 cells upon treatment with selectAHRyl A at 100 μ M for 6 h are color-coded. Upregulated genes are marked in red, while downregulated genes are marked in blue. b , Effect of selectAHRyl A on the mRNA expression levels of selected AHR pathway-associated genes in MDA-MB-468, SK-BR-3 and 184B5. The cells were treated for 0, 2, 6, 24 and 48 h with selectAHRyl A at cell line specific IC ₅₀ in case of MDA-MB-468 and SK-BR-3 and 100 μ M in case of 184B5.	53
Fig.29 Confirmation of AHR pathway modulation by selectAHRyl A. Dose-response curves of the viability of MDA-MB-468, SK-BR-3 and 184B5 cells upon 72 h treatment with a , a dilution series of selectAHRyl A alone; b , a selectAHRyl A dilution series in combination with 12.5 μ M of CH-223191, an AHR inhibitor; c , a selectAHRyl A dilution series in combination with 12.5 μ M of bergamottin, a CYP1A1 inhibitor and d , a dilution series of selectAHRyl B alone. The cell viability was determined by using CV assay. e , The impact of a selectAHRyl A treatment at IC ₅₀ for 30 and 60 min on the cellular distribution of AHR protein between nucleus and cytosol in MDA-MB-468 cells. f , Impact of selectAHRyl A on the activation of AHR protein in HepG2-AHR-Luciferase reporter cells upon 48 h treatment with a serial compound dilution.	55
Fig.30 Metabolization of selectAHRyl A as catalyzed by CYP1A1 enzyme-containing liver microsomes. a , Representative chromatogram of oxidation products of selectAHRyl A analyzed with UHPLC-HRMS. The shown chromatogram overlay summarizes the appearance of selectAHRyl A and four detectable metabolic products in the presence (magenta) and the absence (blue) of CYP1A1 enzyme. A CYP1A1-containing sample without selectAHRyl A was inspected as reference sample (red). b , Proposed positive ion mass spectral fragmentation of metabolites M1 and M2 ($[M+H]^+$ <i>m/z</i> 308), M3 and M4 ($[M+H]^+$ <i>m/z</i> 324) and selectAHRyl A ($[M+H]^+$ <i>m/z</i> 292) as generated by incubation with CYP1A1. c , Representative HPLC chromatograms of the oxidation products of selectAHRyl A as generated by using CYP1A1-containing liver microsomes (blue) overlaid with those of the synthesized hydroxylated derivatives of selectAHRyl A, as analyzed by using a HPLC-diode array detector. The shown chromatogram overlay summarizes the appearance of selectAHRyl A and its metabolic products in the presence and the absence of CYP1A1 enzyme. d , Dose-response curves of the viability of MDA-MB-468 cells treated with mono-hydroxylated derivatives (structures shown in Fig.30c) of selectAHRyl A for 72 h. The cell viability was determined by CV assay.	57
Fig.31 Putative mode of action of selectAHRyl A. The scheme summarizes the theory of the selectivity mode of action of selectAHRyl A. Upon the treatment of MDA-MB-468 cells with selectAHRyl A, it binds to the active site of AHR protein bound in the inactive AHR complex in the cytosol. The receptor binding leads to the translocation of the protein complex from the cytosol to the nucleus and the release of AHR protein from the complex. Afterwards, AHR binds to the nuclear protein ARNT forming a transcription factor complex which induces the expression of a group of genes known as xenobiotic resistance elements (XRE). Afterwards, selectAHRyl A is released from the AHR/ARNT complex and becomes subject of an oxidative modification catalyzed by one of the XRE-coded proteins, most likely the P450 enzyme CYP1A1, yielding selectAHRyl B (the hydroxylation product of selectAHRyl A). SelectAHRyl B induces caspase-independent apoptosis, ultimately leading to cancer cell death. The scheme was created by using BioRender. ²⁶⁴	60
Fig.S1 Cell viability dose-response curves of the breast cell lines under investigation upon 72 h treatment with a , compound 57 ; b , OLP, and c , TMZ. Cell viability was determined by using crystal violet (CV) assay.	76
Fig.S2 Dose-dependent curves of several breast cell lines. The cell lines were treated with several concentrations of TMZ combined with IC ₁₀ of a , compound 57 and b , OLP for 72 h and the viability was determined using CV assay.	77
Fig.S3 The structure of the ART subdomain of hPARP-1 (PDB code: 3GJW) interacting with the newly identified hPARP inhibitor (compound 57 , green).	77
Fig.S4 MCF-7 and MDA-MB-468 cells' viability after 72 h treatment with the selected compounds and indicated concentrations. Cell viability was determined by using CV assay.	81
Fig.S5 BT-474 and HCC1937 cells' viability after 72 h treatment with the selected compounds and indicated concentrations. Cell viability was determined by using CV assay.	81
Fig.S6 Representative dot plots for the impact of compound 19 applied at IC ₅₀ for 72 h on the induction of apoptosis, measured by using AnnV/PI double staining against a , MCF-7; b , MDA-MB-468; c , BT-474; d , HCC1937 and e , 4T1 cells. For the AnnV stain, the fluorescence intensity was analyzed using excitation at 488 \pm 20 nm and emission at 530 \pm 30 nm (plotted at x-axis). For the PI dye, the fluorescence intensity was analyzed by using excitation and emission at 561 \pm 20 and 610 \pm 20 nm (plotted at y-axis), respectively. The lower left, lower right and the upper right quadrants represent live cells, early and late apoptotic cells, respectively.	82
Fig.S7 Representative dot plots for the impact of compound 19 applied at IC ₅₀ for 72 h on the induction of autophagy, measured by performing acridine orange assay: a , MCF-7; b , MDA-MB-468; c , BT-474; d , HCC1937 and e , 4T1 cells. The green fluorescence intensity was analyzed by using excitation at 488 \pm 20 nm and emission at 530 \pm 30 nm (plotted at x-axis). For the AO dye, the	

fluorescence intensity was analyzed by using excitation and emission at 488 ± 20 and 695 ± 40 nm (plotted at y-axis), respectively.	82
Fig.S8 Representative histograms for the impact of compound 19 applied at IC_{50} for 72 h on the induction of ROS production, determined with DHR assay by a , MCF-7; b , MDA-MB-468; c , BT-474; d , HCC1937 and e , 4T1 cells. For the DHR stain, the fluorescence intensity was analyzed by using excitation at 488 ± 20 nm and emission at 530 ± 30 nm (plotted at x-axis).	83
Fig.S9 Representative histograms for the impact of compound 19 applied at IC_{50} for 72 h on NO production, measured by using DAF-FM dye: a , MCF-7; b , MDA-MB-468; c , BT-474; d , HCC1937 and e , 4T1. For the DAF-FM stain, the fluorescence intensity was analyzed by using excitation at 488 ± 20 nm and emission at 530 ± 30 nm (plotted at x-axis).	83
Fig.S10 Representative histograms for the impact of compound 19 applied at IC_{50} for 72 h on the inhibition of cells proliferation, in which cells were stained by using CFSE reagent, and then treated with the lead compound: a , MCF-7; b , MDA-MB-468; c , BT-474; d , HCC1937 and e , 4T1 cells. For CFSE stain, the fluorescence intensity was analyzed by using excitation at 488 ± 20 nm and emission at 530 ± 30 nm (plotted at x-axis).	83
Fig.S11 Representative histograms for the impact of compound 19 applied at IC_{50} for 72 h on the induction of pan-caspases induction, measured by using the ApoStat staining kit: a , MCF-7; b , MDA-MB-468; c , BT-474; d , HCC1937 and e , 4T1 cells. For the ApoStat stain, the fluorescence intensity was analyzed by using excitation at 488 ± 20 nm and emission at 530 ± 30 nm (plotted at x-axis). ..	84
Fig.S12 Representative histograms for the impact of compound 19 applied at IC_{50} for 72 h on the cell cycle status distribution in G0/G1, S and G2/M phases, measured by using the DAPI stain: a , MCF-7; b , MDA-MB-468; c , BT-474; d , HCC1937 and e , 4T1 cells. For DAPI stain, the fluorescence intensity was analyzed by using excitation at 375 ± 20 nm and emission at 450 ± 20 nm (plotted at x-axis).	84
Fig.S13 Bar graphs representing the impact of compound 19 applied at IC_{50} for 72 h to breast cancer cell lines, on a , the induction of ROS production; b , the induction of NO production; c , the inhibition of cell proliferation; d , the induction of pan-caspases production. Data were normalized to the corresponding value in the untreated sample. Bars represent the mean values \pm standard deviation calculated based on three independent measurements. *, **, *** and **** p < 0.05, 0.01, 0.001, 0.0001 compared to the untreated control cells.	85
Fig.S14 Body weights of BALB/c mice upon treatment with compound 19 using doses of 5 and 20 mg/kg. The body weight was measured for all mice on day 0, 6, 13, 15 and 18 and are represented as a mean value.	85
Fig.S15: Dose-response curves of the viability of various cell lines treated with selectAHRyl A for 72 h. The cell viability was determined by using resazurin assay in case of leukemia cell lines, in all other cases CV assay was used. The data are presented as the means of 2-3 independent biological replicates each with technical quadruplicates \pm SEM.	87
Fig.S16 Representative histograms and dot plots for the impact of selectAHRyl A at IC_{50} for 72 h against MDA-MB-468 cell line on a , induction of apoptosis; b , activation of autophagy; c , cells distribution in different cell cycle phases; d , NO production; e , the induction of ROS production; f , cell proliferation and g , activation of pan-caspases. For CFSE, DHR, DAF-FM, AnnV, and ApoStat stains the fluorescence was analyzed using excitation 488 ± 20 nm and emission of 530 ± 30 nm (showed on the x-axis). For DAPI channel, the fluorescence was analyzed using excitation of 375 ± 20 nm and emission of 450 ± 20 nm (presented on x-axis). For AO and PI dyes, the fluorescence was analyzed using excitation and emission of $488 \pm 20/695 \pm 40$ or $561 \pm 20/610 \pm 20$ nm, respectively, (presented on the y-axis).	87
Fig.S17 a , Heat map and b , PCA charts comparing the gene expression profiles, i.e. mRNA expression levels, of MDA-MB-468 (top), SK-BR-3 (mid) and 184B5 (bottom) treated for 6 h at 100 μ M of selectAHRyl A. Untreated samples of each cell line were included representing 0 h treatment. Data were collected from three biological replicates. c , Volcano plots representing the effects of selectAHRyl A against MDA-MB-468 (top), SK-BR-3 (mid) and 184B5 (bottom).	88
Fig.S18 Proteins that are differentially expressed in MDA-MB-468 cells upon selectAHRyl A treatment at a , IC_{20} and b , IC_{50} . c , Fused gel image of MDA-MB-468 treated with both concentrations for 6, 24 and 48 h, indicated names represent the most differentially expressed proteins upon treatment.	89
Fig.S19 Images representative for the immunofluorescence analysis of AHR in MDA-MB-468 cells treated with selectAHRyl A using IC_{50} for a , 0 min; b , 30 min and c , 60 min. The cells were stained with an AHR recombinant rabbit monoclonal antibody at a dilution of 1:200, and then incubated with a goat anti-rabbit IgG (H+L) Secondary Antibody, Alexa Fluor Plus 488-conjugated at a dilution of 1:1000 for 60 minutes at RT in the dark (green). Nuclei (blue) were stained with DAPI. Images were taken by a LSM900 at 63 \times magnification, scale bars = 10 μ m. d , Dose-response curves of the viability of breast cancer cell lines treated with FICZ for 72 h. The cell viability was determined by CV assay.	90
Fig.S20 a , 3D and b , 2D images representing the predicted interaction between selectAHRyl A and the structure of the binding pocket of AHR, the latter was predicted by using AlphaFold. The ligand-receptor docking was carried out and the images were generated by using the MOE software.	91

Table of tables

Table 1 Summary of the calculated IC ₅₀ values (given in mM) of TMZ, TMZ combined with 100 μM of compound 57 , and TMZ combined with 1.56 μM of OLP tested against the breast cell lines. Cells were treated for 72 h and assayed by using the CV assay.	24
Table 2 IC ₅₀ values (μM) of the most active compounds as determined for the cell lines under investigation.....	35
Table 3 Cell line-dependent biological impacts of compound 19 treatment at IC ₅₀ for 72 h. ↑ - induction; ↓ - inhibition; ↔ - no effect. The bar graphs used to determine these data are illustrated in Fig.S13.....	36
Table S1 List of the compounds identified as potential hPARP-1 inhibitors by the <i>in silico</i> hPARP-1 docking and screening study.	72
Table S2 Summary of the calculated IC ₅₀ values (given in mM) of TMZ, TMZ combined with 100 μM of compound 57 , and TMZ combined with 1.56 μM of OLP as tested against the breast cell lines. Cells were treated for 72 h and cell viability was determined by using the CV assay.	76
Table S3 Sequences of the qPCR primers used in the gene expression study.	77
Table S4 Binding energy of the most relative compounds' interaction with the ART domain of hPARP-1 calculated by using MOE software.	77
Table S5 The different expression levels of ER, PR, HER2/neu and BRCA-1 in the four investigated human breast cancer cell lines.....	78
Table S6 List of tested compounds 1 – 49	78
Table S7 Analysis of several biochemical markers in the urine obtained from three mice treated with compound 19 representing the control, 5 mg/kg and 20 mg/kg groups. Samples were obtained on day 6 and 20, representing the first and the last day of treatment, respectively. The urine analysis was performed by using Multistix urine test stripes. “-“: marker was not detectable in the respective urine sample; “+“: marker was detected.	86
Table S8 Differentially expressed proteins in MDA-MB-468 upon treatment with selectAHRyl A at IC ₂₀ and IC ₅₀ for 6, 24 and 48 h.....	91
Table S9 Genes showing altered expression upon treatment of MDA-MB-468 cells with selectAHRyl A at 100 μM for 6 h.....	92
Table S10 Genes showing altered expression upon treatment of SK-BR-3 cells with selectAHRyl A at 100 μM for 6 h.	95
Table S11 Genes showing altered expression upon treatment of 184B5 cells with selectAHRyl A at 100 μM for 6 h.	97
Table S12 Primers used for the qPCR analysis. The primers were designed using Primer-Blast from NCBI.	98
Table S13 Chromatographic conditions used for UHPLC separation of the samples.....	98
Table S14 Mass analyzer settings applied for MS/MS experiments. Psig - pound-force per square inch.	98
Table S15 Key ions in positive ion ESI-MS/MS spectra of selectAHRyl A and its metabolites M1-M4. Fragments are labelled like in Fig.30b.	99

Chapter 1 : The foundations of cancer and its treatment

1. Cell turnover

The primary aim of the study is to discover and develop novel anticancer agents hidden in the compound collection of the Leibniz Institute of Plant Biochemistry. To effectively target cancer, it is essential to thoroughly understand the factors governing cell turnover and the underlying causes that may contribute to the onset of malignancies. A state of equilibrium is always established to prevent uncontrolled division and the growth of the cells. This balance is maintained by the regulation of cell size and cell proliferation. The cell size homeostasis was proven to be dependent on the cell cycle length and the growth rate,¹ while cell proliferation homeostasis is maintained due to the balance between cell cycle and cell death.² In the subsequent sections these processes will be addressed in more detail to provide crucial insights into how disturbing the equilibrium of cell division and death can lead to uncontrolled cellular growth and the potential development of cancerous conditions.

1.1. Cell cycle

The cell cycle consists of four distinct phases, which regulate cellular growth and division. The first three phases are called collectively the interphase. During the interphase, cells perform their designated function and prepare themselves for the mitotic phase (M phase), the fourth and final stage of the cell cycle.³ The first phase in the cell cycle is known as the first gap phase (G₁). During the G₁ phase, the cells start to grow physically and synthesize essential building blocks including proteins, nucleotides, and RNA. The G₁ phase is followed by the synthesis phase (S). During the S phase the cells duplicate their chromosomes forming sister chromatids and the centrosome which is a microtubule-organizing structure. The third phase is called the second gap phase (G₂) and is characterized by continuous physical growth and the production of additional proteins, organelles and increase in the volume of the cytoplasm, which are essential to facilitate mitosis.⁴⁻⁶ This organized sequence of events highlights the complex nature of the cell cycle, where each phase plays a crucial role to ensure a proper cell growth and division.

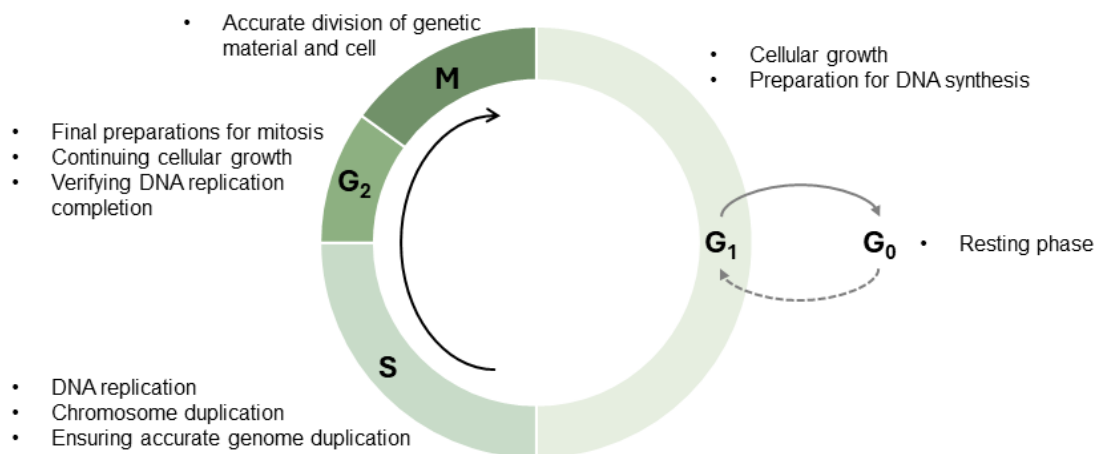


Fig.1 An illustrated overview of the cell cycle phases G₁, S, G₂, and M. Each phase plays a crucial role in maintaining genomic integrity, regulating cell growth, and organizing a precise cell division.

Mitosis is the division of a mother cell into two daughter cells. The mitotic phase comprises four sub-phases.⁷ The first phase is known as the prophase. During which the chromatin is condensed, the surrounding nuclear membrane starts to break down and the nucleolus disappears. Microtubular spindles are formed by the two centromeres and the centromeres start to move toward opposite sides of the cell. The microtubular spindles attach to the kinetochores of the chromosomes.⁸⁻¹⁰ In the next mitosis sub-phase, the metaphase, the chromosomes are aligned at the center of the cell.¹¹ Afterwards, during the so-called anaphase, the sister chromatids are separated and pulled towards the two opposite sides of

the cells by the effect of the microtubular spindles.¹² Finally, during the telophase, the separated chromosomes start to decondense, microtubular spindles disappear and new nuclear membranes are formed surrounding the separated chromosomes sets of each of both daughter cells.¹³⁻¹⁵ During the anaphase and telophase, the cell starts to contract in the middle. By the end of the telophase, the cell center is completely contracted and afterwards, it splits into two daughter cells in a process known as cytokinesis which initiates once again the cell cycle.¹⁶

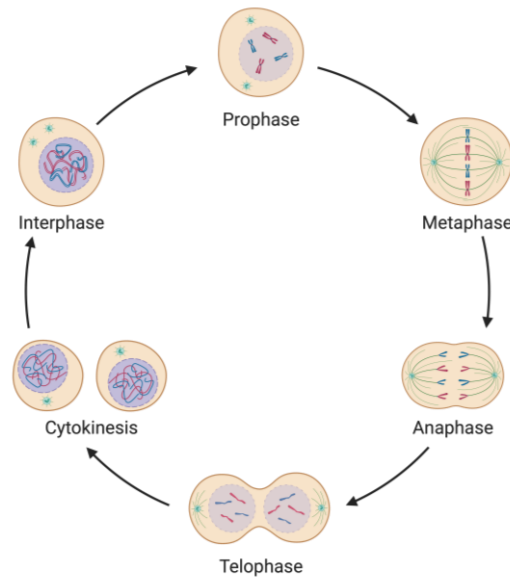


Fig.2 The mitosis subphases, called prophase, metaphase, anaphase, and telophase, splitting a cell into two daughter cells, ensuring the replication of the genetic material. The figure was created by using BioRender.com.

The progression of the cell cycle is controlled by specific checkpoints. Each checkpoint aims to ensure identical genetic material to be inherited by the daughter cells.¹⁷ The first two checkpoints are known as the G1 and G2 checkpoints which protect against error occurrence in the genetic DNA and the proper cell size for cell division.^{18,19} The third checkpoint is known as the M checkpoint ensuring that the sister chromatids are locked correctly to the microtubular spindles by the kinetochores.²⁰ Moreover, several molecules regulate the cell cycle process. The most important two protein families that orchestrate these phases are the cyclins and the cyclin-dependent kinases (CDK). These two families cooperate to organize the flow of the cycle through the formation of complexes which allow the transition from one phase to another and passing the checkpoints.²¹ Interrupting the cell cycle seeks to address the root issue. Otherwise, the cell may commit to programmed cell death (e.g., apoptosis) to prevent the amplification and proliferation of errors, potentially preventing the development of more serious issues like malignancies. The distribution of cells across various phases of the cell cycle could serve as a means to assess the effects of treatment agents against cancer. For example, DNA damaging agents may cause cells to become trapped at specific checkpoints, stopping cell cycle progression. Further elaboration on the utilization of this approach is presented in Chapter 3 and Chapter 4, where the effects of compounds on cell cycle progression were investigated.

1.2. Programmed cell death

Throughout the life cycle of cells, there are instances when these cells undergo programmed cell death (PCD), a process crucial for various functions such as tissue development, differentiation, and maintenance of cellular equilibrium. Additionally, PCD acts as a defense mechanism, guarding the DNA through recognizing mutations and preventing their replication and progression to daughter cells. These mutations have the potential to give rise to various disorders, including cancer. Additionally, PCD plays a significant role in the immune response, effectively removing any cells affected by viral or bacterial infections.

Several different types of PCD were discovered during the previous decades, such as autophagy, necroptosis, paraptosis, parthanatos, etc.^{22–25} The most frequent form of PCD is named apoptosis, in which the cell debris is recycled to be further utilized. The initiation of apoptosis can be either due to an intracellular stimulus known as the intrinsic apoptotic pathway (IAP) or due to an extracellular stimulus known as the extrinsic apoptotic pathway (EAP).²⁶ Several factors can induce cellular stress conditions which can either be pathological, such as heat, UV radiation, hypoxia, smoking, etc., or can be therapeutically induced as intended in the case of chemotherapy and radiotherapy which activate the IAP. The mitochondria are considered the key organelles of this pathway in which the stress condition will cause the activation of a tightly regulated cascade of apoptosis-inducing proteins located in the mitochondrial membrane. As an ultimate result, the mitochondria will release cytochrome C in the cytoplasm leading to the activation of caspase-9. Caspase-9 activates the downstream effector caspases (3, 6, 7) which lead to cell apoptosis.^{27,28} On the contrary, the EAP originates from an extracellular signal that activates so-called death receptors by various molecules such as CD95L and TNF α . The activated death receptors lead to signal transduction inside the cell and the activation of caspase-8, followed by downstream caspases, e.g. caspase-3, leading again to cell apoptosis.²⁹

By activating apoptosis, the cell starts to shrink and the nucleus disintegrates releasing the genetic material in the cytoplasm.³⁰ The cell membrane forms protrusions known as blebs,³¹ the organelles, genetic materials, and the cytoplasm are densely packed in the plasma membrane forming apoptotic bodies.³² The apoptotic bodies are then recognized and digested by various cells, e.g. macrophages.²⁶ Apoptosis is a fundamental process in cancer treatment, and its induction by anticancer drugs serves as a key mechanism for eliminating cancer cells. Evaluating apoptosis induction is essential in drug development and plays a vital role in assessing the efficacy of potential anticancer agents which is illustrated in the study of the novel identified anticancer compounds in Chapter 3 and Chapter 4.

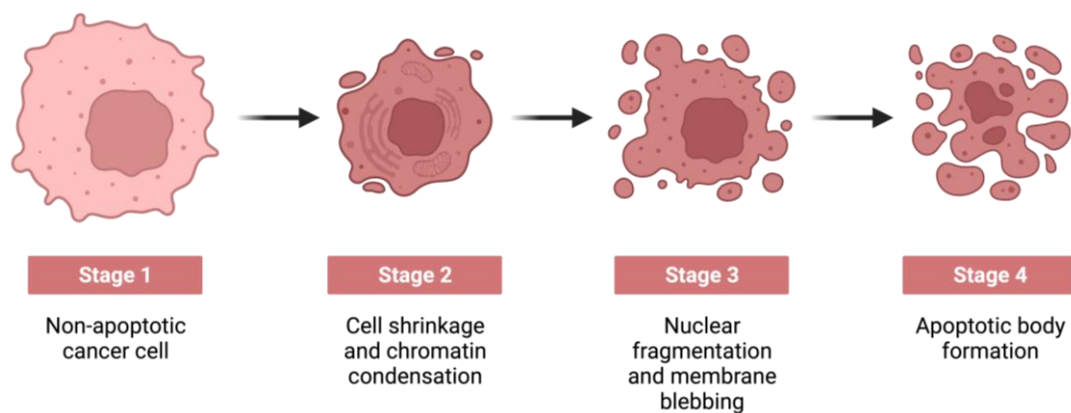


Fig.3 Different stages of apoptotic cell death. The figure was created by using BioRender.com.

The crosstalk between the cell cycle and PCD is essential for preventing malfunctions and mutations. Several conditions, such as DNA damage or stress factors, activate a family of molecules known as cyclin-dependent kinase inhibitors (CDKI).³³ CDKIs are classified based on their target molecule. The first class is known as INK4 and the second class is Cip/Kip. The activation of the INK4 inhibits cyclin-D/CDK4 and cyclin-D/CDK6 complexes leading to cell arrest at the G1 checkpoint. Whereas the activation of the Cip/Kip class leads to the unspecific inhibition of most CDKs. In the case of an activation of both classes, the higher affinity of INK4 to CDK4 and CDK6 results in the binding of Cip/Kip molecules to cyclin-E/CDK2 and cyclin-A/CDK2 complexes.³⁴ The resulting inhibition of these complexes arrests the cells in the G2 checkpoint. The cell cycle arrest allows the cell to treat the problematic condition. For example, an arrest due to DNA damage allows the cell to activate the DNA repair machinery. In those cases where a successful DNA repair or the elimination of the damaging stress condition is not possible, the cell starts the PCD program to avoid the manifestation of mutations.³⁵

2. DNA homeostasis

The most crucial criterion in the cell cycle is the integrity of the DNA. The absence of DNA errors before cell cycle commitment, the success of DNA replication during the S phase and finally, the correctness of the distribution of the genetic material between the daughter cells, all are controlled by a complex machinery in the cell. However, several errors can arise during the cell's life cycle. This can occur by exogenous factors such as UV radiation "direct effect on DNA" or can be initiated by indirect effect on DNA through smoking, pollution and obesity,³⁶ it can also be caused by endogenous factors such as oxidative stress caused by reactive oxygen and nitrogen species, or alkylating agents.³⁷ Human cells experience thousands of DNA damages per day, such as base deamination, abasic sites (AP site), oxidative damage, methylation, etc.³⁸ These alterations are ideally detected and repaired by the DNA damage response (DDR) pathways.³⁹ Single base damages induced, for instance, by oxidative stress or deamination, are repaired by the base excision repair (BER). In which the false base is removed by the enzyme DNA glycosylase. A strand break is introduced by DNA lyase at the 5'-terminal of the AP site. Afterwards, RNA polymerase II (POL II) adds the correct base, and the break is sealed by DNA ligase. Or POL II adds the correct base and continues to form a completely new strand replacing the old one in the long patch repair.⁴⁰ Contrarily, more bulky damages are repaired by nucleotide excision repair (NER). NER has two different initiation mechanisms. The global genomic NER (GG-NER) is based on a complex named XPC-Rad23B. This complex scans the DNA helix for any distortions in the structure which reflects the correctness of base pairing.^{41,42} The second mechanism is known as transcription-coupled NER (TC-NER). In which, RNA polymerase carries the function of the XPC-Rad23B during transcription and detects the DNA distortions.⁴³ The detection of any distortion leads to the activation of the DNA repair machinery, removal of the DNA strand containing the error and its replacement by a newly formed error-free strand. Finally, during the replication process, an error can arise in the newly formed strand. These types of errors are corrected by a specific mechanism known as DNA mismatch repair (MMR). The mispairing is recognized and repaired by a family of proteins known as Mut proteins. MutS protein recognizes mismatches causing the formation of MutS homodimer. The detection of mismatches by MutS directs MutL to form a homodimer which binds to the MutS dimer and activates MutH. The MutH searches the surrounding DNA strand for hemimethylated GATC site. Since the new strand is not yet methylated, the MutH can differentiate between the parent and the newly formed strand. The MutH introduces a nick in the newly formed strand as it possesses an endonuclease activity. The nick acts as a starting point for the repair and the formation of a new strand replacing the error-containing one. The nicked strand is removed by the action of helicase II and an exonuclease enzyme. Finally, a new error-free strand is synthesized by POL III, and ligated by DNA ligase.^{44,45}

Another type of damage that can occur to the DNA, is the formation of strand breaks. Those breaks vary into two different classes depending on whether the double strand or only one single strand is broken. Single-strand breaks (SSB) cause the collapse of DNA and transcription stalling. These kinds of damage are recognized by the PARP enzyme which activates the DNA repair machinery in order to close the break.⁴⁶ Chapter 2 elucidates the mechanism by which PARP resolves SSBs. The second type is the double-strand break (DSB), which is more severe as it can lead to DNA mutation and the formation of cancerous cells. DSB can be repaired by two key mechanisms, either by non-homologous end joining which is orchestrated by the 53BP1 enzyme⁴⁷ or by homologous recombination which is initiated by the MRN protein.⁴⁸

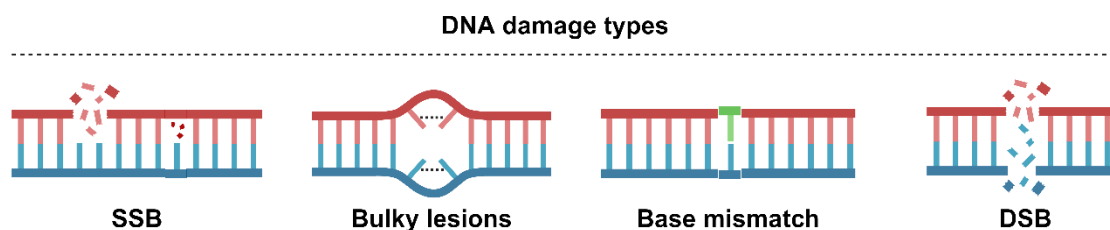


Fig.4 An illustration of the different types of DNA damages. The figure was created by using BioRender.com.

Although each DNA repair mechanism has been discussed above as a concrete distinct mechanism, they are tightly connected and function as a unit. However, some DNA damage can even escape the tight DDR, these damages can lead to the manifestation of a mutation. The consequences of such a mutation depends strongly on the affected region of the DNA. The mutation can be either neutral and without any consequences if it affects a silent region or an intron region, or it can be even beneficial when improving the function of specific proteins and participating in an evolutionary process.⁴⁹ Nevertheless, it can also be harmful with drastic consequences, for instance, if it affects a growth controlling gene which may lead to cancer development.⁵⁰

3. Cancer

3.1. Definition and history

The development of cancer is the result of complex interactions between several factors, including genetic mutations, environmental triggers and perturbations.⁵¹ The failure of regulatory mechanisms of the cell cycle or of the DNA damage response mechanisms can lead to uncontrolled cell division and the accumulation of DNA damages, which may induce the development of tumors.^{52,53}

Tumors can be classified into two main categories based on their characteristics: benign or malignant tumors.⁵⁴ Benign tumors are non-cancerous tissue abnormalities. These tumors are characterized by their slow growth rates. Moreover, they do not spread to surrounding tissues or distant parts of the body. The benign tumors usually have well-defined borders and are often encapsulated within a fibrous capsule. This type of tumor lacks life-threatening danger. However, benign tumors can still cause complications by exerting pressure on nearby organs or tissues based on their location. Examples of benign tumors include adenomas, lipomas, and uterine fibroids.⁵⁵ In contrast, malignant tumors are also known as cancerous tumors. This type of tumor is characterized by its invasive growth characteristics and the potency to spread to other parts of the body in a process called metastasis. These tumors exhibit uncontrolled cell growth and can infiltrate surrounding tissues, compromising the normal function of organs and systems. Malignant tumors pose a significant threat to health and require prompt and complicated treatment.⁵⁶

Cancer is recognized as one of mankind's most devastating diseases. Several proofs illustrate that the battle of humankind against cancer started thousands of years ago. References were found in ancient manuscripts and early medical texts describing cancer disease as a life-threatening and often incurable disease. For instance, evidence was found documented in papyrus writings of the ancient Egypt dating back to 3000 BC.⁵⁷ Moreover, several references were documented in the early Roman and Greek civilizations describing cancer-like diseases and several efforts to explain their origin and possible treatments. Nevertheless, the major advancements in the understanding of cancer pathology and its biological basics have just been made during the centuries of the modern era. It started in the 19th century with the cell theory, which postulates that all living organisms are composed of cells, what was proposed by Matthias Schleiden and Theodor Schwann in 1838. This fundamental concept laid the groundwork for further research on the cellular origins of cancer.⁵⁸ The milestone in the understanding of cell functionality helped Rudolf Virchow in 1858 to establish the idea that cancer arises from normal cells that have become abnormal, a concept that became the foundation of modern oncology.⁵⁹ In the 20th century, major milestones were established in the treatment of cancer and the understanding of the cancer inducing factors. Several efforts were made by Yamagiwa and Ichikawa in 1915 to understand the inducing factors for cancer development and the link to environmental factors. Finally, they were able to identify the meaning of carcinogens and shed light on their connection to cancer development.⁶⁰ Meanwhile, the pioneering work of Marie and Pierre Curie on radioactivity established the role of radiation as an external factor triggering cancer but also for diagnostics and treatment of cancer.⁶¹ In addition, in the 20th century, cancer staging was established by the American surgeon Zubrod revolutionizing cancer diagnosis and treatment.⁶² The second half of the 20th century brought also groundbreaking discoveries in genetics and molecular biology. These newly developed sciences supported the clarification and understanding of the genetic basis of cancer. Hence, several genes were identified which either act as tumor suppressors or oncogenes, including the landmark discovery of the

p53 gene. This illuminated the complicated molecular mechanisms driving cancer initiation and progression.⁶³

Simultaneously, several advancements were accomplished in diagnostic imaging technology, including computer tomography and magnetic resonance imaging, significantly improving cancer detection and hence, the understanding of cancer.^{64,65} During the 21st century, cancer research witnessed remarkable acceleration because of the completion of the Human Genome Project in 2003. It provided a comprehensive map of the human genome, revolutionizing the understanding of genetic variations and their implications for cancer susceptibility and treatment response.⁶⁶ Moreover, the advances in the omics fields allow the further study of the interplay between genes, proteins and metabolites supporting the characterization, understanding and fighting of cancer. The field experienced tremendous progress in the explanation of cancer, which however, till today is considered one of the most challenging diseases requiring further clarification. The collaborative efforts of researchers, healthcare professionals, and policymakers continue to drive innovations and advancements for the fight against cancer, with the ultimate goal of reducing its burden.

3.2. Cancer treatment options

Parallel to the discoveries in the pathology of cancer in the 20th century, huge efforts were made in the cancer treatment field. Several treatment options, such as surgery, radiotherapy and chemotherapy,^{67,68} have been optimized to improve therapy and prognosis. These remedies are used as standalone or combined therapy depending on the type and the stage of the targeted cancer. The oldest methodology for cancer treatment is surgery which involves the removal of the malignant tumor and parts of the surrounding tissue if indicated. Still, surgery is considered the most effective treatment option for solid tumors that are localized and have not spread to other parts of the body.⁶⁹ However, this technique solely lacks effectiveness in the treatment of metastatic tumors and non-localized cancers such as leukemia. For these types, surgery is either replaced or combined with radiotherapy and/or chemotherapy.⁷⁰

Radiotherapy is the utilization of high-energy particles or waves as X-rays or protons to induce cancer cells' death. The radiation is either applied by a radiation-omitting machine or by internally applied radioactive material.⁷¹ The emitted radiation induces damaging of the DNA of the cancerous cells hindering its growth and proliferation.⁷² However, radiotherapy induces a high incidence of side effects due to the exposure and collateral damaging of the surrounding healthy cells. Nevertheless, modern techniques have improved the precision and efficacy of radiation therapy while minimizing damage to healthy tissues.

The third traditional remedy option and the pillar of cancer treatment is chemotherapy. It is considered as a systemic treatment targeting the rapidly dividing cancer cells but also rapidly growing normal cells.⁷³ This nonspecific cytotoxic effect leads to the development of devastating side effects such as hair loss, nausea, and a weakened immune system. Traditional classes of chemotherapeutic agents have been developed over the years to effectively disrupt the growth and spread of cancer cells.⁷⁴ Each class of chemotherapeutic drugs operates distinctly, targeting various stages of the cell cycle or specific cellular processes. Some of the major traditional classes of chemotherapy are alkylating agents, antimetabolites, anthracyclines, and topoisomerase inhibitors.

Finally, the fourth type of remedy is targeted treatment. This type of remedy is considered to be the most advanced as it addresses specific characteristics of cancer, which help in overcoming the side effects of the other types of therapy. Since this topic is regarded as the main focus of the dissertation, it will be discussed in detail in section 3.4.

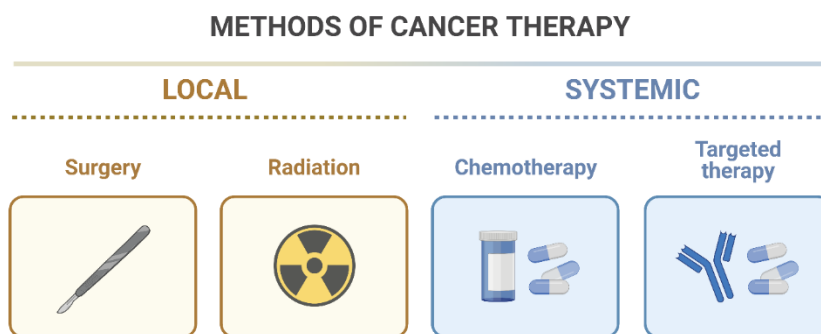


Fig.5 Cancer treatment options. The figure was created by using BioRender.com.

3.3. Chemotherapy classes

3.3.1. DNA alkylating agents

The first class of chemotherapeutics that had been discovered was the DNA alkylating medications, specifically mechlorethamine (Mustargen, a nitrogen mustard compound), synthesized by the American pharmacologist Alfred Gilman and the physician Louis Goodman in 1940s, marking the beginning of the chemotherapy era.⁶⁸ DNA alkylating agents function by adding an alkyl group to the seventh nitrogen atom of guanine bases of the DNA. These agents induce single-strand breaks or covalent cross-linkages between neighbored guanine groups in the double DNA strands, avoiding their separation for transcription and replication, and therefore interfering with protein synthesis and cell division.⁷⁵ That impacts cell growth and proliferation regardless of the cell cycle phase. Mechlorethamine belongs to the nitrogen mustards subclass, characterized by the presence of the chloroethylamine $(ClC_2H_4)_2NR$ functional group. Later, several other molecules such as cyclophosphamide and ifosfamide were discovered, still being used today for chemotherapy to treat leukemia, lymphomas, and solid tumors, including ovarian and breast cancer. However, nitrogen mustard compounds induce severe side effects such as aplastic anemia due to bone marrow suppression, hair loss, and infertility resulting from the inhibition of the gametogenesis process. Moreover, these compounds were found to be carcinogenic, and prolonged use could lead to leukemia and other malignancies.

Busulfan represents another subclass of alkylating agents, exhibiting greater selectivity against the bone marrow. Consequently, it is primarily used against leukemia and before bone marrow transplantation as myeloablative conditioning to eliminate both healthy and malignant cells from the bone marrow. Despite this selectivity, busulfan treatment is associated with various side effects related to bone marrow suppression, including depletion of platelets, red blood cells (RBCs), and white blood cells (WBCs). Additionally, it increases the risk of pulmonary fibrosis and hyperpigmentation.⁷⁶

Another subclass of DNA alkylating agents are nitrosoureas including carmustine and lomustine. This subclass is characterized by their high lipophilicity and hence they are mainly used to treat brain cancer including glioma. However, also nitrosoureas induce severe neurotoxic side effects such as seizures, ataxia and convulsions.⁷⁷

While the aforementioned examples serve to illustrate the progress in refining alkylating agents for enhanced selectivity and reduced side effects, it is important to note that several other potent agents have been discovered. These include crucial agents such as the platin family, chlorambucil and melphalan, which stand among the cornerstone therapies in modern clinical oncology.

3.3.2. Antimetabolite agents

This class of compounds interferes with the synthesis of nucleic acids and other vital cellular components by mimicking the structure of natural metabolites that are required for DNA and RNA synthesis. This effect is caused by either the direct inhibition of DNA and/or RNA synthesis or disruption of the nucleotide metabolism causing apoptotic cell death. Antimetabolite agents function by acting on the cells during the S-phase of the cell cycle. Several types of antimetabolites were discovered

and used for different cancer indications including folate antagonists, purine, pyrimidine, adenosine analogs or thymidylate synthase inhibitors.⁷⁸

One of the prominent compounds belonging to the antifolate subclass is methotrexate. This compound exhibits a higher affinity to the enzyme dihydrofolate reductase (DHFR) compared to its native substrate, DHF. Normally, DHFR is responsible for converting dihydrofolate (DHF) into tetrahydrofolate, an essential educt of the *de-novo* syntheses of purines, thymidylate, and certain amino acids. Methotrexate's interaction with DHFR leads to its irreversible inhibition, disrupting downstream processes crucial for cell replication. Consequently, it is used in the treatment of leukemia, lymphomas, and certain small solid tumors.⁷⁹

The second subclass of antimetabolite agents is known as nucleotide analogs. Several medications belonging to this family of compounds are available for the treatment of leukemia, such as azathioprine and 5-fluorouracil (5-FU) which are purine and pyrimidine analogs, respectively. The azathioprine exists in a prodrug form which is activated by thiopurine S-transferase yielding the active drug form 6-mercaptopurine. 6-mercaptopurine induces cell death via two mechanisms, either by being integrated into the replicated DNA as a purine analog what will lead to an increase in DNA damage and inhibition of further replication by DNA polymerase or through the inhibition of the two essential enzymes phosphoribosyl pyrophosphate synthetase and adenosine monophosphate deaminase causing a depletion of inosinic acid, which inhibits the synthesis of the purine bases, adenine and guanine, and hence ultimately the DNA replication process. Another compound belonging to this class is 5-fluorouracil which acts as pyrimidine analog. The compound also exists in an inactive, prodrug form and is activated upon administration yielding fluorodeoxyuridylate. This active drug form impacts cell growth by being incorporated in the DNA or RNA as pyrimidine nucleotide leading to the inhibition of DNA synthesis and replication. It can also form a complex with tetrahydrofolate, a molecule that binds and activates the enzyme thymidylate synthetase, responsible for the synthesis of thymidine.⁷⁸

While the antimetabolite class has demonstrated particular effectiveness against blood-related cancers such as leukemia, its use is compromised by significant drawbacks associated with its impact on the bone marrow. This can cause several side effects, including megaloblastic anemia, pancytopenia, and immunosuppression, consequently increasing the risk of infection.

3.3.3. Anthracyclines

This family of compounds is characterized by the presence of a defined core structure consisting of an aglycone ring coupled with an amino sugar. The first two members of this family, daunorubicin and doxorubicin, were discovered in the early 1960s when isolated from *Streptomyces* species. Several other molecules were discovered later, such as idarubicin and epirubicin. These molecules are used for the treatment of various cancer types – including breast, lymphoma, melanoma, and uterine cancers – and are exerting their anticancer effects by different modes of action.⁸⁰ First, the aglycone moiety of the anthracyclines intercalates with the adjacent DNA base pairs leading to a deformation of the DNA. Second, the molecules bind to the topoisomerase II-DNA complex leading to its stabilization, increasing the formation of the double strand breaks. Moreover, anthracyclines exert an anticancer effect via the induction of oxidative stress, since the enzymatic reduction of the anthraquinone ring yielding a semiquinone free radical, inducing toxicity to tumor cells. However, they also impact healthy cells, especially cardiac cells, leading to cardiotoxicity as the most common and dangerous side effect of anthracyclines. Furthermore, several cancers, including solid tumors and hematological cancers, meanwhile show resistance against these drugs. The resistance is mostly attributed to the expression of p-glycoprotein which acts as a transmembrane efflux pump.⁸¹

3.3.4. Topoisomerase inhibitors

The topoisomerase inhibitor class exerts its anticancer effect by inhibiting the topoisomerase enzyme family. These enzymes play a crucial role in the homeostasis of the DNA, including DNA replication, transcription and chromosome segregation and recombination. Topoisomerases are responsible for relaxing the supercoiled DNA and changing its topology. This exposes different parts of the DNA to the functional proteins that are essential for DNA processing. The topoisomerases family can induce this effect by the introduction of either single or double strand breaks which are specific for

topoisomerase type I or type II, respectively.⁸² Topoisomerase inhibitors function by binding to and stabilizing the topoisomerase-DNA complex causing the failure of the re-ligation function of the topoisomerase and, hence, DNA damage.⁸³ The first discovered topoisomerase inhibitor was camptothecin that was isolated from *Camptotheca acuminata* and characterized in 1966. Afterwards, several other topoisomerase inhibitors were discovered such as etoposide, amsacrine, etc.⁸⁴

3.4. Targeted therapy

Targeted therapy represents a novel treatment option resembling traditional chemotherapeutic agents, where they both aim to destroy cancer cells. Nevertheless, it differs in its mechanism of action. Chemotherapeutics primarily target rapidly dividing cells, diseased but also healthy cells. In contrast, targeted therapies specifically focus on malignant cells or at least specific cell types through addressing various explicitly cancer-associated molecules and mechanisms or cell type specific ones, respectively. These diverse targeting strategies are aimed to facilitate improved selectivity, thereby reducing the incidence of side effects. Within this category, the molecules used can be small molecules, RNA/DNA, peptides or proteins including antibodies.⁸⁵

As an example of targeted therapy, monoclonal antibodies which are designed to target cancer-specific antigens, that are highly regulated in specific cancer types. Trastuzumab, for instance, targets the human epidermal growth factor receptor 2 (ERBB2, HER2), which is highly expressed in HER2⁺ breast carcinoma. This high abundance of the antigen and its high specificity allow the monoclonal antibody to effectively target these cancer types.⁸⁶ Another therapeutic antibody is rituximab, which targets the cluster of differentiation molecule CD20. CD20 is found to be overexpressed in certain cancer types, such as non-Hodgkin lymphoma and chronic lymphocytic leukemia, thus enabling precise targeting by rituximab.⁸⁷

Small molecules also can be used as targeted therapy by addressing specific molecules or pathways that are specifically upregulated in cancer cells. For example, the high expression of epidermal growth factor receptor (EGFR), which characterizes some cancer types, such as non-small cell lung (NSCLC), prostate and triple-negative breast carcinomas (TNBC), could be targeted using the small molecule drug erlotinib. Erlotinib acts by reversibly binding to the ATP binding site of the EGFR preventing the interaction of EGFR molecules and the formation of homodimers which is essential for its receptor tyrosine kinase activity.⁸⁸ Poly(ADP-ribose)polymerase inhibitors (PARPi) represent another class of small molecules which have been developed for targeted cancer therapy. These inhibitors are suitable to specifically target cancer cells with defective DNA repair mechanisms, such as those found in TNBC. This targeted PARPi effect leads to synthetic lethality, causing further damage to cancer cells while sparing normal cells that have intact DNA repair mechanisms.⁴⁶ The high potential of this compound class in cancer treatment, in conjunction with its low risk of side effects, motivated us to focus the primary objective of the thesis on identifying novel PARPi, as described in Chapter 2.

Targeted therapies show a significant impact on cancer treatment, as they improve the prognosis and reduce the accompanied side effects. These advantages are due to their higher specificity compared to traditional chemotherapeutics. Additionally, a combination of both a targeted and a traditional chemotherapy could be also applied in order to benefit from the best of both worlds, the high toxicity of the traditional chemotherapy and the selectivity of the targeted ones. Such a concept has been realized, for instance, in peptide- and antibody-drug conjugates (PDC and ADC, respectively).^{89,90} Ado-trastuzumab emtansine is an antibody-drug conjugate that combines the previously mentioned HER2-targeting antibody, trastuzumab, combined with the highly cytotoxic molecule emtansine, also named DM1. The conjugation of DM1 allows the delivery of the highly cytotoxic agent specifically to the cancer cells by trastuzumab-mediated targeting of their highly expressed HER2 receptors.^{91,92} Hence, targeted therapies offer more personalized and less toxic approaches to treat cancers, minimizing damaging effects on healthy cells and reducing the severity of side effects often associated with traditional chemotherapies. As research continues to unveil new molecular targets and pathways, the potential for targeted therapies to revolutionize and further improve cancer treatment remains promising. This encouraged us to conduct an in-depth study of a newly identified small molecule demonstrating a novel mechanism of selectivity against triple-negative breast cancer (TNBC), as

detailed in Chapter 4. The mechanism of action of that novel molecule could be a new way to target cancer cells utilizing the cells' own metabolism machinery to activate a prodrug to its active metabolite. Which improves the cancer selectivity of the treatment and reduces side effects.

3.5. Classification and cancer types

Cancer classification covers a diverse range of malignancies, distinguished by the affected cell type or the site of origin within the body. Cancer can be classified as carcinoma, sarcoma, leukemia, lymphoma, blastoma and others. Each classification characterizes cancer in specific types of cells. Carcinoma are malignancies affecting epithelial cells. Subclassifications are adenocarcinoma, basal cell carcinoma and squamous cell carcinoma. Sarcoma signifies the cancer occurrence in connective tissues, including either bone sarcomas or soft tissue sarcomas. Leukemia and lymphoma cover the occurrence of malignancies in white blood cells (WBCs) or lymph nodes, respectively. While blastoma are cancers of embryonic tissues. Cancer also could be classified based on the affected organs, for example, prostate, breast, and lung cancers. Each type can be further classified based on specific features, such as gene mutations, upregulated or downregulated pathways, etc.⁹³

The understanding of the classification of cancers based on their location is vital for precise diagnosis and effective treatment strategies. Cancers that arise in distinct organs or tissues may exhibit different growth patterns, responses to treatment, and prognoses, necessitating tailored therapeutic approaches. For instance, cancers originating in vital organs such as the brain or lungs may require specialized treatments due to the challenges posed by their location and the potential impact on essential functions. In contrast, cancers originating in the musculoskeletal system may demand a unique approach that considers the complex interplay between the tumor and the surrounding supportive tissues. Additionally, the specific molecular characteristics of different cancer types, based on their location, can provide critical insights into their behavior and potential vulnerabilities, facilitating the development of targeted therapies and personalized treatment plans. For instance, breast cancer classification relies on identifying expressed receptors such as hormonal, HER2, or TNBC. This categorization serves as a crucial guide for determining the most effective therapy.

3.6. Cancer statistics

Cancer stands as one of the most difficult and critical health challenges worldwide as it ranks either as the first or second leading cause of death of humans before reaching their age of 70 years in 112 countries. The latest global study counted approximately 19.3 million new cancer cases and around 10 million cancer-caused deaths in 2020. Notably, breast, lung, prostate, colon and stomach cancers consistently maintain their prominence among the most prevalent cancer types on a global scale.⁹⁴

Gender-specific differences add a further layer of complexity to this health crisis. For males, lung cancer takes the lead worldwide with an incidence of 39 new cases per 100,000, closely followed by prostate cancer with 37.5 new cases per 100,000. In contrast, breast cancer is the predominant cancer in females, with an incidence rate of 55.9 cases per 100,000. The alarming frequency of breast cancer, nearly 1.5 times higher than the next prevalent tumor type, highlights the urgency of directing resources toward enhancing its prognosis.⁹⁴ In particular, the TNBC subtype of breast cancer stands out due to its aggressive nature and the challenges associated with its treatment.

3.7. Triple-negative breast cancer (TNBC)

Breast cancer (BC), a heterogeneous disease with various subtypes, is a significant global health threat especially for women. Among the diverse forms of breast cancer, triple-negative breast cancers (TNBCs), are known to have unique challenges in terms of diagnosis, treatment and research. Statistical studies indicate that TNBCs counts for 15 - 20% of all breast cancer cases.⁹⁵ Within this subset, younger women, particularly those under the age of 35, show a higher incidence.⁹⁶ This subtype is characterized by the absence of the three key receptors which are commonly found in other breast cancer subtypes, namely the estrogen (ER), progesterone (PR) and epidermal growth factor 2 (ERBB2, HER2) receptors. However, the lack of these receptors causes the difficulty to therapeutically target the TNBCs and, hence, makes them far more challenging to treat compared to the other breast cancer types where advanced hormonal and HER2-targeting therapies can be used. That renders the TNBCs a formidable

and clinically very challenging cancer entity. The absence of the aforementioned receptors does not lead only to the difficulty of treatment but also contributes to the development of aggressive clinical behavior of the tumor, which means rapid progression of the disease accompanied by the deterioration of the patient's health. Therefore, TNBCs show the worst survival rates compared to other breast cancer subtypes (4-year survival rates: 77% for TNBC, 93% for HR⁺ and HER2⁺ subtypes).⁹⁷ Moreover, several studies indicate that TNBCs have a higher risk of early recurrence and metastasis, making timely and effective intervention crucial for the patient's outcome.

The treatment of TNBCs is more challenging compared to that of the other subtypes. Still, targeted and chemotherapies are considered to be the cornerstones for its treatment to eradicate any remaining leftover cancer cells after the initial cancer removal by surgery. Yet, the treatment strategies require a tailored and multidimensional approach. For instance, one of the predisposing factors for TNBC development is a BRCA1 mutation affecting the cellular DNA repair.⁹⁸ In TNBCs characterized by that mutation, the tumor can be targeted by using PARP inhibitors, such as olaparib. These drugs utilize the cancer cells' impaired ability to repair DNA damages, leading to cell death.⁹⁹ Some TNBCs also show strong overexpression of the PD-L1 (CD274) gene, and could be therefore targeted by using immune checkpoint inhibitors such as atezolizumab.¹⁰⁰ These previously mentioned points highlight that the majority of the available treatment options are considered to be tailored therapy. These therapies depend on the presence or absence of specific characteristics that could be targeted in the TNBCs cases. However, they could not be used for all TNBCs. This emphasizes the importance of further research dedicated to identifying novel molecules for TNBC treatment or targeting new traits within TNBC tumors to enhance their prognostic outcomes. That served as the main motivation behind this thesis, prompting the decision to explore the compound library of Leibniz Institute of Plant Biochemistry in search of new drug compounds specifically active against TNBCs.

4. Compound libraries

Large compound libraries represent a milestone in modern drug discovery and scientific research, serving as reservoirs of multiple chemical entities with the potential to act on multiple biological targets. These libraries consist of systematically organized collections of small molecules, peptides or other elements, representing a wide range of structural and physicochemical properties. The use of compound libraries has revolutionized the field of drug development, allowing researchers to explore a vast chemical space and accelerate the identification of novel therapeutic candidates.¹⁰¹ The sheer diversity within compound libraries allows researchers to probe various biological pathways, study disease mechanisms, and identify potential drug candidates with specific activities. These libraries often hold thousands to millions of compounds, providing an extensive repertoire for high-throughput screening and target validation. The synthesis and curation of compound libraries have become indispensable in the pursuit of new drug discovery, offering a systematic approach to explore the chemical space and discover compounds with desirable pharmacological profiles.¹⁰² In this context, the effective utilization of compound libraries relies on advanced screening technologies, computational methods, and interdisciplinary collaborations. High-throughput screening platforms, coupled with robotics and automation, allow researchers to rapidly test large numbers of compounds against specific biological targets. Computational approaches, such as virtual screening and structure-based drug design, enhance the efficiency of library screening by predicting the potential binding sites, affinities and activities of compounds before experimental validation.¹⁰³

Compound libraries may encompass a variety of compounds sourced from natural, semi-synthetic, or synthetic origins. These categories have demonstrated significant worth in the continuous quest for innovative cancer therapies. Numerous studies have affirmed the importance of these diverse classes, underscoring the essence of examining libraries characterized by the broad spectrum of compound origins. Several natural products contributed to transforming the development of anticancer agents. The most prominent proof of natural products' contribution to anticancer agents are the vinca alkaloids, namely vincristine and vinblastine, derived from the Madagascar periwinkle plant.¹⁰⁴ Similarly, paclitaxel, a cornerstone in chemotherapy, originates from the Pacific yew tree.¹⁰⁵ These examples indicate that nature can be used as the fundamental platform for the discovery of anticancer agents. However, several limitations could be faced during the use of natural products. Hence, natural

products could be modified to yield semi- or fully-synthetic analogs to overcome the limitation of their supply, optimize their pharmacological properties, bioavailability and stability, reduce side effects and overcome resistances. For instance, the semi-synthetic modification of the natural product paclitaxel yielded in docetaxel. This process not only overcame supply challenges but also exhibited an enhanced clinical efficacy. Therefore, the semi-synthetic modification of natural products acts ideally as a fine-tuning of the natural products to improve their effect.¹⁰⁶

In contrast to natural products, which have long served as valuable sources of anticancer agents, synthetic compounds are designed and engineered in laboratories. The synthetic compounds are fine-crafted based on specific targets either affecting a specific pathway or protein. This allows the development of highly precise products with optimized efficacy, selectivity and pharmacokinetic properties. Amongst these advancements, the development of imatinib is considered one of the most outstanding achievements in the realm of targeted cancer therapy. Imatinib acts as a tyrosine kinase inhibitor targeting the cancer-associated protein kinase BCR-ABL, which is produced by a specific gene fusion mutation known as the Philadelphia chromosome.¹⁰⁷ This mutation leads to the development of chronic myeloid leukemia. This discovery allowed the development of highly selective compounds targeting tumor cells characterized by that mutation. Imatinib's success exemplifies the power of synthetic compounds in precisely addressing the molecular underpinnings of cancer, marking a milestone in personalized and targeted cancer treatment.

The Leibniz Institute of Plant Biochemistry possesses one of Germany's most extensive libraries of natural products, derivatives and extracts. Comprising approximately 30,000 entities, encompassing small molecules and peptides. The collection is derived from a spectrum of origins – natural, semisynthetic, or entirely synthetic. Among these entities, approximately 25,000 are distinct compounds. Furthermore, the library features an additional 5,000 diverse extracts sourced from various plants, fungi, bacteria and marine organisms. This repository is a treasure trove, potentially harboring invaluable compounds with anticancer properties. Therefore, the whole research project was targeted to develop and apply methodologies to identify promising anticancer compounds throughout that IPB library.

5. Library screening and hits characterization

With vast compound libraries containing numerous entities, an efficient methodology is crucial for studying and identifying potential hits. To achieve this, a high-throughput approach must be employed to navigate through these libraries. In the quest for discovering anticancer agents within such collections, two distinct techniques are well established: the phenotypic and the rational drug discovery approaches.

5.1. Phenotypic drug discovery approach

This approach focuses on identifying compounds that demonstrate beneficial therapeutic effects (growth inhibition for anticancer agents). Once these hits are identified, deeper mechanistic studies can be conducted to elucidate their modes of action. This approach offers the advantage of potentially identifying a wider range of compounds with anticancer activity. However, it also presents challenges such as the complexity and costliness of elucidating the precise molecular mechanisms underlying the hits.^{108,109} An example of successful drug discovery based on the phenotypic approach is the characterization of trametinib, which was found to exhibit an antiproliferative effect. Subsequently, the molecular target was identified as a MEK inhibitor. Trametinib is now utilized in the treatment of melanoma and glioma.¹¹⁰

The primary step in this methodology involves identifying hits with inhibitory effects against cancer. To achieve this, cell viability assays are employed. Cell viability assays are essential tools in cellular biology, where they provide researchers with critical insights into the health, functionality, and responses of cells under varying experimental conditions. The utilization of cell viability assays can be used as a powerful tool for the characterization of compounds with intriguing anticancer activity. A comprehensive understanding of cell viability assays is essential for the proper selection of the suitable assay, considering the underlying mechanisms, types of cells and the compound under investigation.

One of the intriguing cell viability assays is the crystal violet assay (CV assay) which is considered to be a cell adherence-based assay. This staining method relies on the characteristic attachment of adherent cells to a surface during incubation. In the presence of a cytotoxic, cell death-inducing agent, adherent cells lose their attachment ability and can be easily washed off. Crystal violet is a triarylmethane dye that binds to ribose type molecules such as DNA in nuclei, which allows the staining of the remaining adherent cells. This staining serves as a method to quantify the viable cell population indirectly. Crystal violet staining is cost-effective, easy to measure (with absorbance at 570 nm), and applicable to a wide range of adherent cells. However, it is not suitable for suspension or low-adhesion cells. Furthermore, false positives may occur if the investigated compounds impact the cells' adhesion ability, emphasizing the importance of confirming positive hits by using alternative methodologies.¹¹¹ Another types of available cell viability assays are metabolism-, membrane integrity- and DNA staining-based assays. Understanding the diverse mechanisms and characteristics of these cell viability assays empowers researchers to make informed decisions in selecting the most appropriate method for their specific experimental needs. While each assay offers unique advantages, it is essential to consider potential limitations to ensure accurate and reliable assessments of the investigation of the cellular viability.¹¹² For this study, CV assay was selected to determine cell viability which was a judicious choice given the highly adherent nature of the cell lines studied.

After identifying hits, they need to be validated. The next challenge lies in understanding their mode of action. To tackle this, a combination of targeted and untargeted studies can be employed. Untargeted experiments, such as omics analyses, offer insights into how hits affect the transcriptome, proteome, or metabolome of the cell. Employing robust bioinformatics tools, researchers can illuminate pathways impacted by the hits, allowing for a detailed exploration to pinpoint their exact molecular targets. Targeted techniques encompass a range of experiments, for instance, flow cytometry-based, immune-based, kinase, gene expression and enzymatic assays. These methodologies enable researchers to confirm the impact of compounds on various cellular processes. Additionally, they aid in identifying the primary target of the compound. This comprehensive approach was extensively utilized in the thesis, where Chapter 3 and Chapter 4 serve as a prime example of the phenotypic drug discovery approach in action.

5.2. Rational drug discovery approach

In contrast to (initially) random screening, this approach is based on the hypothesis that targeting specific known biological elements, particularly proteins, will induce therapeutic effects (growth inhibition for anticancer agents). The initial step involves the identification of the target protein, followed by the optimization of protein cloning, production, and purification. Subsequently, the purified protein is utilized to establish an enzymatic assay for determining the active molecules.¹¹³ Computer-aided drug design can improve the search or design process. Where initial screening of promising hits is conducted through sophisticated *in silico* studies, based on the existing knowledge of essential interactions between the predetermined molecular target and known ligands. Selected hits then undergo primary enzymatic assays to confirm true positives. Confirmed hits are further evaluated for growth-inhibitory effects using cell viability assays. The advantage of this method lies in the predefined molecular target, dodging the challenges of target identification. However, it is common for compounds exhibiting inhibitory effects against the target to lack activity in cell assays, often due to physicochemical properties such as low permeability through cell membranes or instability in cellular environments. Nevertheless, these challenges can be addressed through extensive application of structure-activity relationship knowledge and compound derivatization techniques. A successful example of the rational approach is the discovery of imatinib. After establishing the connection between the BCR-ABL1 mutation and CML incidence, high-throughput screening of chemical libraries was performed to identify hits that could inhibit the activity of the mutated kinase. Initially, 2-phenylaminopyrimidine was identified as a lead compound and a BCR-ABL inhibitor. Subsequently, the compound was further modified by introducing methyl and benzamide groups to enhance its protein binding properties.¹¹⁴ Therefore, this approach was also utilized in this dissertation for the identification of novel anticancer agents where Chapter 2 of the thesis provides a concise and illustrative demonstration of its implementation.

6. Aim of the study

6.1. Background

Triple-negative breast cancer (TNBC) represents a particularly aggressive form of breast cancer, characterized by the absence of estrogen receptors (ER), progesterone receptors (PR), and human epidermal growth factor receptors 2 (ERBB2, HER2). Accordingly, all advanced hormone-based and receptor-targeting treatments do not address TNBCs properly. Therefore, satisfying targeted therapies for these tumors are still lacking. Consequently, there is an urgent need to explore innovative therapeutic strategies in order to improve the treatment of TNBC patients.

The primary aim of this study was specifically focusing on the discovery and development of PARPi. PARP enzymes play a crucial role in DNA repair. Hence, the inhibition of these enzymes has shown promise in selectively targeting cancer cells, particularly those with deficiencies in other DNA repair mechanisms including specific TNBC types. These types are ideal candidates for a PARPi therapy. This was proven in several recent preclinical studies, which demonstrated the efficacy of PARPi in TNBC models, highlighting their potential as a targeted therapeutic approach. Traditional chemotherapy, while effective to some extent, often results in severe side effects and fails to address the specific molecular characteristics of TNBC. By focusing on PARPi, this study aims to bridge this gap by providing a more precise and tailored approach to TNBC treatment. The successful discovery and development of novel PARPi for TNBC could significantly enhance treatment options for patients. Furthermore, the PARPi, which were proven to improve the prognosis of TNBCs, have additionally shown promise in other cancer types, such as ovarian and prostate cancers. By improving response rates and minimizing toxicity, PARPi has the potential to enhance the quality of life for TNBC patients, providing them with a more effective and tolerable treatment option.

However, the study did not conclude with uncovering new PARPi. It also aimed to pinpoint novel compounds within the selected compound library capable of demonstrating anti-cancer properties through innovative targeting mechanisms. This effort aimed to help create customized treatments for TNBCs.

6.2. Methodology

In my quest to address the urgent need for effective treatments of TNBC, the thesis work was dedicated to the identification of novel PARPi by *in silico* and *in vitro* screening of the compound library of the Leibniz Institute of Plant Biochemistry since previous projects in the department generated many plant PARPi, we expected promising molecules. My approach started with unveiling the essential chemical motif responsible for the activity of clinically approved PARP inhibitors – the benzamide motif. A scan of the compound library led to the identification of 178 compounds bearing the benzamide motif, forming the basis of our investigation.

The research process is detailed in Chapter 2. This chapter serves as a comprehensive guide, illustrating the methodologies employed to unveil and evaluate the PARP inhibiting activity of the pre-selected compounds. By conducting a systematic and multi-faceted approach, I aspire to pinpoint different methodologies with the potential to support TNBC treatment, offering a pathway toward targeted and personalized therapeutic interventions.

In the preliminary stages of our investigation, the selected 178 compounds were evaluated using CV assay. This initial screening revealed the presence of two distinct compound classes, both demonstrating noteworthy cytotoxicity. Particularly intriguing was the discovery of the azaglycophymines family, which exhibited a striking antiproliferative effect against various breast cancer types. The respective chapter (Chapter 3) describes a comprehensive examination of this compound family. Involving a detailed characterization, shedding light on the mechanisms underlying their potent antiproliferative properties. By employing a range of experimental techniques, I aim to unravel the molecular effects that render this compound family promising, providing an understanding of its potential therapeutic effect.

Finally, while screening the IPB compound library, one compound emerged as a standout candidate, displaying remarkable selectivity against triple-negative breast cancers (TNBCs) independently of PARP impact. This discovery deserved dedicated attention, leading to an independent study detailed in Chapter 4. Herein, I employ a synergistic approach, comprising multiomics analyses, computational modeling, cell-based, biochemical and molecular studies. This comprehensive strategy aimed to elucidate the compound's mode of selectivity, uncovering valuable insights into its promising potential as a targeted therapeutic agent for TNBCs.

In summary, our study unfolds in a planned sequence – from an initial target-driven compound library screening to the in-depth exploration of the azaglycophymine compounds family, PARP inhibitors and finally to the independent study of a potent compound with outstanding TNBC selectivity. This systematic approach reflects our commitment to understand the complexities of breast cancer and, more specifically, TNBC, with the ultimate goal of advancing targeted and effective therapeutic interventions.

Author Contributions: The individual authors' contributions to the presented work are as follows: conceptualization: Ludger A. Wessjohann and Robert Rennert; writing – original draft preparation: Ibrahim Morgan; review and editing: Robert Rennert, Ludger A. Wessjohann; supervision: Robert Rennert, Ludger A. Wessjohann (main); project administration: Ludger A. Wessjohann; funding acquisition: Ludger A. Wessjohann.

Chapter 2 : Identification and characterization of novel inhibitors of human poly(ADP-ribose) polymerase-1

Abstract: Poly(ADP-ribose) polymerases (PARP) are a family of enzymes that were proven to play an essential role in the initiation and activation of DNA repair processes in case of DNA single-strand breaks. The inhibition of PARP enzymes might be a promising option for the treatment of several challenging types of cancers, including triple-negative breast cancer (TNBC) and non-small cell lung carcinoma (NSCLC). The presented study aimed to utilize several techniques to search and screen the compound collection of the Leibniz Institute of Plant Biochemistry in order to identify novel hPARP-1 inhibitors. First, an *in silico* pharmacophore docking study was conducted in order to virtually screen for compounds with potentially inhibitory effects. To *in vitro* test these compounds, a cell-free enzyme assay was developed, optimized and utilized to select hPARP-1 inhibitors, yielding compound **57** as the most active compound of the studied library. Furthermore, several experiments are described that were performed in order to investigate the cellular and nuclear path and effects of the hPARP-1 inhibitor **57** and a potential synergistic effect with the DNA-damaging agent temozolomide.

1. Introduction

Based on the Global Cancer Statistics 2020, around 19.2 million cancer patients were newly diagnosed, of which approximately 2.3 million were females with breast cancer. Breast cancer is considered the most frequently occurring cancer type in females with an incidence of 24.5% of all newly diagnosed patients, followed by colorectal and lung cancer with incidence rates of 9.4% and 8.4%, respectively, excluding non-basal cell carcinoma.⁹⁴ Breast cancers can be classified into different types based on the receptors expressed by the cancer cells, which are either hormone receptor-positive cancer cells (expressing progesterone and/or estrogen receptors), HER2/neu-positives (expressing erbB-2 receptors) or triple-negative breast cancer cells (TNBC; lacking the aforementioned receptors).¹¹⁵ The disease's prognosis as well as the selection of the optimal therapy are highly dependent on the type of breast cancer. Estrogen receptor-positive breast cancers can be treated, for instance, with either estrogen receptor modulators such as tamoxifen or aromatase inhibitors such as anastrozole.^{116,117} The HER2/neu-positive breast cancer type can be treated with monoclonal antibodies like trastuzumab or more advanced HER2-targeting antibody-drug conjugates.^{91,118} However, the most challenging breast cancer type is TNBC which accounts for 15-20% of the newly diagnosed breast tumors.¹¹⁹ Due to the lack of the aforementioned standard breast cancer associated receptors, the targeted treatment of TNBCs demands alternative molecular targets. Amongst those, the poly(ADP-ribose) polymerase enzyme can play a vital role in the treatment of TNBC tumors, but also as a prognostic marker.¹²⁰

Poly(ADP-ribose) polymerases (hPARP) are a family of proteins consisting of 17 members in *homo sapiens* sharing a conserved catalytic domain. This family is characterized by the ability to add either a single (mono) or several (poly) ADP-ribose molecule(s) to target proteins, a posttranslational modification (PTM) that plays a significant role in the regulation of the modified proteins' function and activity.¹²¹ In that sense, hPARP-1 is considered to be responsible for 80-90% of PARylations taking place in human cells.¹²² The enzyme consists of six domains, namely the Zn1, Zn2, Zn3, BRCT, WGR and CAT domain. The catalytic domain (CAT) consists of two subdomains known as helical subdomain (HD) and an ADP-ribose transferase (ART) subdomain.¹²³ Upon the occurrence of DNA strand breaks, the zinc finger domains (Zn1, Zn2) recognize and bind the DNA leading to further interaction of the Zn3 and WGR domain with the damaged DNA.¹²⁴ These interactions activate the hPARP-1 enzyme caused by a conformational change of the HD increasing the ART domain's exposure to NAD⁺ molecules.¹²⁵ Bound NAD⁺ binds to the ART domain through a His-Tyr-Glu (H-Y-E) triad by H-bonding and ring stacking which then acts as a donor for an ADP-ribose unit to initiate PARylation at an acidic amino acid moiety of the acceptor protein. Followed by the elongation or branching of the PAR chain through the formation of 2',1''-O-glycosidic ribose-ribose or 2'',1'''-glycosidic bonds, respectively.¹²⁶ In the context of DNA repair, the PARylation of hPARP-1 triggers the protein-protein interaction between the BRCA1 C-terminal (BRCT) domains of hPARP-1 and XRCC1.¹²⁷ Subsequently, the XRCC1 protein acts as a scaffold for DNA ligase III- α and DNA polymerase- β which repair the DNA through either base or nucleotide excision repair mechanisms based on the type of the DNA damage.¹²⁸

hPARP was classified as an essential protein that could be chemotherapeutically targeted for the treatment of several cancer types, including more difficult-to-treat cancers such as TNBC or non-small cell lung carcinoma.^{129,130} As aforementioned, hPARP's main function is to assist the DNA damage repair. Hence, upon the exposure of tumor cells to DNA-damaging factors such as therapeutic radiation or chemotherapeutics like temozolomide (TMZ), the inhibition of hPARP can cause the failure of DNA repair and therefore tumor cell death.^{131,132} However, that promising effect was mainly noticed in cancer types that have a mutation in the Breast cancer gene (BRCA). That protein family is responsible for DNA repair through homologous recombination,¹³³ and in healthy cells a tumor suppressor mechanism. However, it acts as an additional escape and resistance mechanism upon DNA-targeting chemotherapy in BRCA-positive tumor cells.¹³⁴ Conversely, a synergistic interaction of hPARP inhibition and BRCA deficiency of tumor cells can permit selectivity targeting of cancer cells while avoiding healthy cells according to a concept known as synthetic lethality.¹³⁵ Additionally, a new family of proteins named Schlafen (SLFN) was acknowledged for being crucial for hPARP activity, especially SLFN-11, and was found to be a predictive biomarker for hPARP inhibitor-sensitive cancer types.^{136,137} SLFN-11 plays an essential function in DNA repair as well. It is a helicase protein that is

recruited to the stressed replication fork leading to replication blockage and finally cell death. In other words, cancer cells that are characterized by high SLFN-11 expression are predicted to be more sensitive to hPARP inhibitors.¹³⁸

hPARP inhibitors (hPARPi) are compounds that occupy the ART subdomain of the hPARP enzyme through interaction with Tyr907, Ser904 and Gly863 preventing the binding of NAD⁺ by blocking its interaction with the H-Y-E triad, which leads to the failure of the PARylation process and, finally, the DNA repair.¹³⁹ Moreover, it traps the hPARP enzyme to the damaged DNA preventing it from detecting any further damaged DNA loci.¹⁴⁰ Due to these promising effects, several hPARPi were developed – including olaparib (OLP), rucaparib and niraparib (Fig.6) – and already approved for clinical usage, either as a standalone medication or as an adjuvant for DNA damaging chemotherapeutics like TMZ.^{141,142} In homologous recombination-deficient cancer, a correlation of 88.9% was found between the effectiveness of olaparib as a monotherapy and the deficiency of homologous recombination.⁹⁹ Which means that hPARPi clearly can help to improve the treatment and prognosis of cancer patients, and therefore are still a very promising inhibitor class concerning oncological purposes.

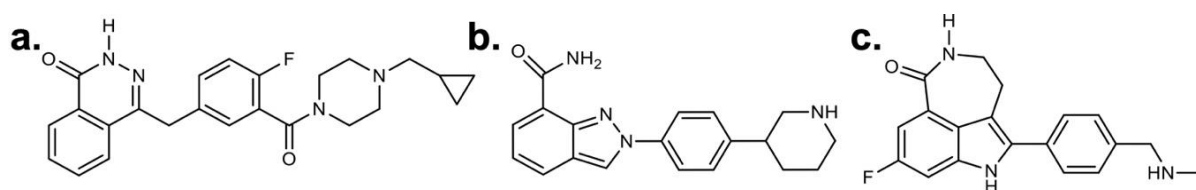


Fig.6 Structures of **a**, olaparib (OLP); **b**, niraparib and **c**, rucaparib.

Consequently, it was the goal of the presented study to seek novel hPARP-1 inhibitors by initially using a cell-free, enzyme-based screening assay. An *in silico* docking study was performed to preselect potential hPARPi out of the compound library of the Leibniz Institute of Plant Biochemistry (IPB) comprising more than 30,000 natural products from plants and fungi and (semi)synthetic derivatives. Preselected potential inhibitor molecules were screened at two concentrations (1 and 10 μ M) by using the developed hPARP-1 enzyme assay to identify true hPARP inhibitors. Active compounds were characterized in more detail to evaluate their IC₅₀ values of enzyme inhibition. Subsequently, the most active inhibitor candidates were selected to be further tested in cell-based assays using different breast cell lines – namely 184B5, MDA-MB-468, MCF-7, HCC1937 and BT474 – to determine its antiproliferative effect in breast cancer cells and its synergistic effect with a DNA damaging drug (TMZ) in comparison with OLP.

2. Materials and methods

2.1. Chemicals and cell lines

Deoxyribonucleic acid sodium salt from calf thymus, MgCl₂, NAD⁺, resazurin, alcohol dehydrogenase, diaphorase and crystal violet were purchased from Sigma-Aldrich (St. Louis, Missouri, United States). High glucose DMEM with glutamine, 0.05% trypsin-EDTA, FCS, RPMI1640, PBS, glutamine and penicillin/streptomycin were bought from Capricorn Scientific (Ebsdorfergrund, Germany), the Endopan 3 kit was from PAN-Biotech (Aidenbach, Germany). TRIS, agarose and paraformaldehyde were supplied by Carl Roth (Karlsruhe, Germany). Recombinant hPARP-1 and PARPi-FL were purchased from Bio-Techne (Minneapolis, Minnesota, United States), DMSO from Duchefa Biochemie (Haarlem, The Netherlands), olaparib from Hycultec GmbH (Beutelsbach, Germany) and temozolomide from MedChemExpress (Monmouth Junction, New Jersey, United States). The qPCR primers were synthesized and supplied by Eurofins Genomics (Ebersberg, Germany). The RNA miniprep kit was purchased from Zymo Research (Freiburg, Germany), qPCR GreenMaster from Jena Bioscience (Jena, Germany) and RevertAid RT Reverse Transcription Kit from Thermo Fisher Scientific (Waltham, Massachusetts, United States).

Several breast cell lines representing the diverse types of breast cancer were investigated in the study. HCC1937 and MDA-MB-468 represent triple-negative breast cancer (TNBC), MCF-7 as a

hormone receptor-positive cell line, and BT474 as HER2/neu-positive cell line.¹⁴³ Moreover, the 184B5 cell line is chemically transformed, originates from normal mammary tissue representing healthy breast cells.¹⁴⁴ All cell lines were obtained from the cell line stock of the Leibniz Institute of Plant Biochemistry and originally purchased from DSMZ (Braunschweig, Germany) and ATCC (Manassas, VA, USA). 184B5 was cultured using the Endopan 3 kit, while MDA-MB-468 was cultured in high glucose DMEM supplemented with 10% (v/v) heat-inactivated FCS. BT474, HCC1937 and MCF-7 were cultured in RPMI1640 medium supplemented with 10% (v/v) heat-inactivated FCS, 1% (v/v) L-glutamine and 1% (v/v) penicillin/streptomycin. Cells were grown in their media in a humidified atmosphere with 5% CO₂ at 37°C. The confluence was monitored daily using light microscopy. Whenever the confluency reached 90%, cells were detached using 0.05% trypsin-EDTA and diluted as indicated by the American Type Culture Collection (ATCC) guidelines. The cell density used for seeding depended on the surface area of the plates used. For 96 well plates and 6 well plates, 6×10^3 cells/well and 1.5×10^5 cells/well, respectively, were used.

2.2. *In silico* PARP-PARPi docking

To screen the compound collection of the Leibniz Institute of Plant Biochemistry (IPB) and to preselect potential hPARP-1 inhibitors, an *in silico* docking study was performed. The chemoinformatic investigation was conducted by using the molecular modeling software package MOE (Molecular Operating Environment; Chemical Computing Group, Montreal, Canada). The X-ray structure of the hPARP-1 enzyme was obtained from the protein databank (PDB code: 3GJW).¹⁴⁵ The protein structure was initially prepared for the docking process by adding the missing hydrogens using the 3D protonation feature of MOE. Afterward, a pharmacophore was designed based on interactions with the ART domain that were found to be essential for the inhibitory effect of established hPARP-1 inhibitors, namely olaparib and rucaparib. Three interactions with the enzyme's ART domain were found crucial for the binding of the hPARP-1 inhibitors, namely the hydrophobic interaction between an aromatic ring of the inhibitor (green, Fig.7) and tyrosines at position 907 and 896, the presence of a hydrogen bond acceptor (cyan, Fig.7) to form a H-bond with serine at position 904, and a hydrogen bond donor (magenta, Fig.7) which forms a H-bond with the glycine residue at position 863. These interactions were found to block the ART subdomain and prevent the interaction of the NAD⁺ with its binding H-Y-E triad. Five poses were generated for each compound. Subsequently, the created pharmacophore was used to dock the compounds of IPB's (semi)natural products library and the binding energies were calculated by using MOE software for each compound pose and used to rank the compounds regarding to their proposed potential to inhibit hPARP-1 enzyme.

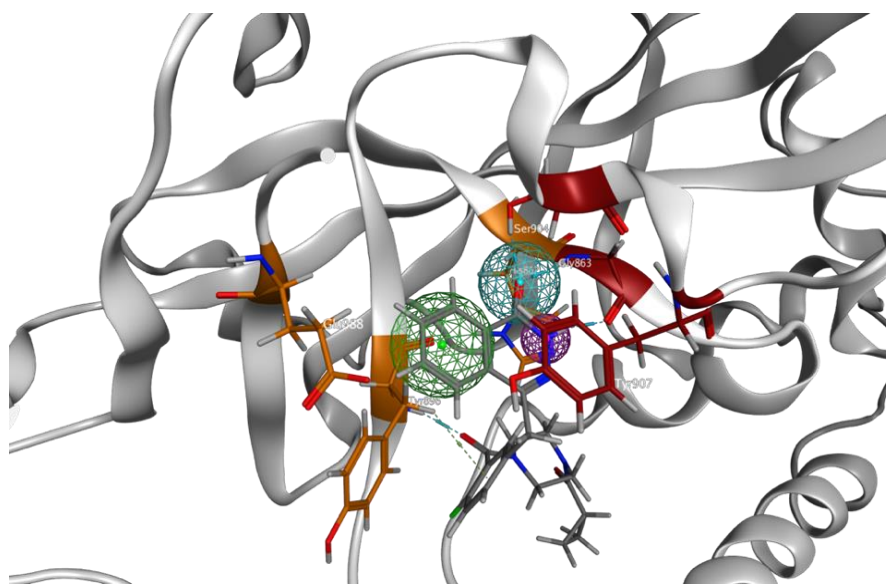


Fig.7 The structure of the ART subdomain of hPARP-1 (PDB code: 3GJW) and the essential features of an established hPARP-1 inhibitor molecule (olaparib, grey). Cyan represents the position of the hydrogen bond acceptor, green represents the position of the aromatic ring and magenta represents the position of the hydrogen bond donor. Red-colored amino acids represent those that interact directly with the hPARPi and the orange-colored amino acids represent the blocked H-Y-E triad.

2.3. hPARP-1 enzymatic assay

The putative PARP inhibitors, which were preselected in the *in silico* study, were subsequently evaluated by using an optimized biochemical hPARP-1 enzyme assay. The experiment was performed in black half area 96-well plates. For the PARP reaction, 12.5 μL of PARP reaction solution were added. The solution was composed of 0.5 μg deoxyribonucleic acid (DNA) sodium salt from calf thymus, 2 U of recombinant hPARP-1 and 1 μL of the compound of interest in PARP reaction buffer (50 mM TRIS and 2 mM MgCl_2 in ddH_2O , $\text{pH} = 8$).¹⁴⁶ These test compounds' working solutions were prepared from 20 mM DMSO stock solutions and diluted using PARP reaction buffer to reach 25 \times of the required final concentration to be tested. As a positive control, 1 μL of 2.5 μM OLP was used (final concentration: 100 nM), and as a negative control, 1 μL of the PARP reaction buffer instead of the test item's working solution. Afterwards, 12.5 μL of NAD^+ solution were added to all wells to reach a final NAD^+ concentration of 50 nM, and to start the enzyme reaction.

Besides PARP reaction wells, NAD^+ calibration wells were included to measure the linearity of the detection of NAD^+ concentrations. In each well, 12.5 μL of NAD^+ calibration solution were added. The solution was composed of 0.5 μg deoxyribonucleic acid sodium salt from calf thymus in PARP reaction buffer, followed by 12.5 μL of decreasing concentrations of NAD^+ solution in calibration wells (final concentrations: 50, 40, 30, 20, 10, 0 nM).

Subsequently, the assay plate including both the PARP reaction and NAD^+ calibration wells was gently shaken, and incubated at 25 $^\circ\text{C}$ in the dark for 90 min. After incubation, 25 μL of detection solution were added to each well. The detection solution was composed of 50 μM resazurin, 2.1% (v/v) ethanol, 2 U alcohol dehydrogenase and 0.2 U diaphorase in PARP reaction buffer.¹⁴⁷ The assay plate was again gently shaken and incubated at 25 $^\circ\text{C}$ in the dark for 40 min. Finally, after reductive conversion of resazurin to resorufin, fluorescence was measured using excitation/emission wavelength of 545/595 nm by using a SpectraMax iD5 plate reader (Molecular Devices, San Jose, CA, USA). The obtained data were expressed as mean values normalized by using the positive control as 100% inhibition and negative control as 0% inhibition.

Following the aforementioned protocol, the compounds that were determined by the *in silico* study as putative hPARP-1 inhibitors were tested at two different concentrations (1 and 10 μM). Those that were found to induce a significant reduction in hPARP-1 activity were further tested at five more concentrations (50, 10, 5, 1, 0.1 μM) to determine their IC_{50} values against hPARP-1 activity. The IC_{50} s were calculated by using GraphPad Prism software and a non-linear four-parametric regression function.

2.4. Differential gene expression

The gene expression levels of *hPARP-1* and *SLFN-11*, a predictive biomarker for hPARP sensitivity of cancer cells, [22,23] in the breast cell lines under investigation were measured by using RT-qPCR. For that purpose, RNA was isolated from 5×10^6 cells of each cell line using an RNA miniprep kit. Afterward, the integrity and concentration of the isolated RNA were determined by using 1% (w/v) agarose gel and a SpectraMax iD5 with SpectraDropTM Micro-Volume kit. 500 ng of isolated RNA were utilized to produce a first-strand cDNA by using a RevertAid RT Reverse Transcription kit. Finally, 12.5 ng of the synthesized cDNA were used as a template for the RT-qPCR reaction. The qPCR primers were designed using the open-source Primer Design Tool from NCBI (Table S3). qPCR GreenMaster mix was used as a reporter for the amplicon amplification which was performed by using a CFX96TM Real-Time PCR Detection System (Bio-Rad, Hercules, CA, USA). Finally, the data were analyzed according to the $\Delta\Delta\text{Ct}$ methodology and normalized to the expression of the housekeeping gene glyceraldehyde 3-phosphate dehydrogenase (*GAPDH*).¹⁴⁸ RNA isolation, cDNA synthesis and the qPCR were performed as indicated by the manufacturers' guidelines of the used kits.¹⁴⁹

2.5. *In vitro* cell viability assay

The impact of the putative PARP-1 inhibitors on the breast (cancer) cells' viability was determined by using the crystal violet (CV) assay, an assay which quantifies the number of adherent cells and hence indirectly indicates the number of viable cells since cell adherence is a characteristic of

these types of cell lines as long as they are viable and upon death, cells lose the adherence ability.¹¹¹ Cells were seeded in 96-well cell culture plates and were allowed to adhere for 24 h in a humidified atmosphere with 5% CO₂ at 37°C. Afterward, cells were treated at several concentrations with the test items for 72 h. Complete medium and 125 μM of digitonin in medium, a strongly cytotoxic saponin, were used as negative and positive control, respectively.¹⁵⁰ After the finalized treatment, the treatment solutions were discarded and the cells were washed once with PBS. Subsequently, the cells were fixed by incubation in 4% (v/v) paraformaldehyde in PBS for 15 min at room temperature (RT). The fixing solution was discarded and the cells were allowed to dry at RT for 15 min. The cells were stained with 0.1% (w/v) crystal violet in PBS for 15 min at RT, afterward washed with ddH₂O and dried overnight at RT. Finally, the stain was dissolved using 33% (v/v) acetic acid and the CV absorbance at 570 nm and the reference wavelength of 670 nm were measured by using a SpectraMax iD5 plate reader.¹⁵¹ The obtained absorbance data were normalized based on the negative and positive controls representing 100% and 0% cell viability, respectively. IC₅₀ values were calculated by using a four-parametric nonlinear regression analysis in GraphPad Prism software.¹⁵²

2.6. *In vitro* synergistic cell viability assay

In order to determine whether the most promising compound **57** could act synergistically in conjunction with an established anti-cancer drug, it was tested in combination with temozolomide (TMZ). For that purpose, cells were seeded in 96-well plates and incubated in a humidified atmosphere with 5% CO₂ for 24 h at 37°C. Afterward, the medium was discarded and cells were treated for 72 h with 100 μM of compound **57** or 1.56 μM of olaparib (OLP), combined with several concentrations of TMZ in 100 μL of the medium. Finally, cell viability was determined by using the CV assay, and IC₅₀ values were calculated as mentioned above.¹⁵³

2.7. Fluorescence microscopy

For the determination of the interaction of the proposed PARPi and the PARP binding pocket, a fluorescent microscopic inspection was performed. Using a green fluorescent stain named PARPi-FL, that is characterized by the ability to occupy specifically the binding pocket of the PARP enzyme. Moreover, it could be replaced by PARPi molecules hence the loss of the fluorescent signal. Thus, cells were seeded in 6-well plates and incubated in a humidified atmosphere with 5% CO₂ for 24 h at 37°C. After incubation, cells were treated at 100 μM of either compound **57** or 1.56 μM of OLP for 72 h under standard growth conditions. Subsequently, the treatment solutions were discarded and the cells were washed with PBS. Afterward, the cells were stained by using 250 nM of PARPi-FL in PBS for 20 min. Finally, cells were imaged by using the GFP channel of an EVOS™ FL Auto Imaging System (Thermo Fisher Scientific, Massachusetts, USA).^{154,155}

3. Results

3.1. *In silico* pre-selection of potential PARPi

By applying the hPARP-ligand *in silico* docking approach based on the established PARPi pharmacophore (Fig.7), a subset of IPB's natural and natural-like products library was virtually screened and compounds were ranked according to the calculated binding energies of their interaction with hPARP-1. In consequence, 49 compounds, which showed the lowest binding energies were selected to be studied in wet lab assays. Further 20 compounds – comprising a benzamide group, i.e. a known hallmark of hPARP-1 inhibitors – were additionally included in the study.¹⁵⁶ In sum, 69 compounds (Table S1) were pre-selected and tested next for their *in vitro* hPARP-1 inhibitory potency.

3.2. Discovery of eight novel PARP inhibitors

The 69 pre-selected compounds (Table S1) were assayed for their enzyme inhibition potency by using the established hPARP-1 enzyme assay. Initially, each compound was tested at two concentrations (1 and 10 μM). As summarized in Fig.8a, the compounds **18**, **21**, **22**, **45**, **54**, **56**, **57** and **58** were found to induce more than 50% inhibition of hPARP-1 when using a concentration of 10 μM. Hence, these compounds were selected and tested (Fig.8b) at a wider range of concentrations (0, 0.1, 1, 5, 10 and 50 μM), and their IC₅₀ values were calculated as shown together with their chemical structures in Fig.9. The approved PARPi drug olaparib (OLP) was tested as a reference. As a result, compound

57 was identified as the most active hPARPi from the tested compounds, with a calculated IC_{50} value of $\approx 2.3 \mu\text{M}$. Therefore, compound **57** was selected to be characterized in more detail by further investigations.

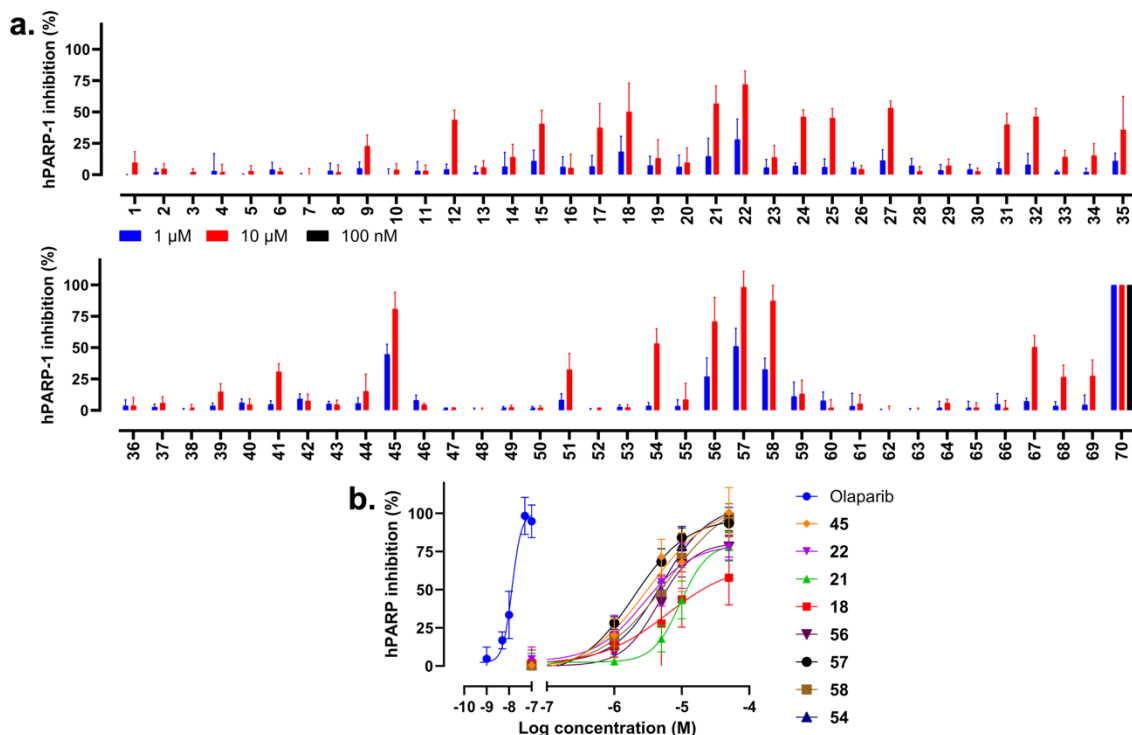


Fig.8 Fast screening of the inhibitory impact of the selected compounds on hPARP-1 catalytic activity using the hPARP-1 enzyme assay. **a**, Compounds were tested at two different concentrations (1 and 10 μM) to determine the most active hits. OLP (compound **70**) was used at a concentration of 100 nM as a positive control. **b**, Dose-response curves to determine the IC_{50} values of the most active compounds.

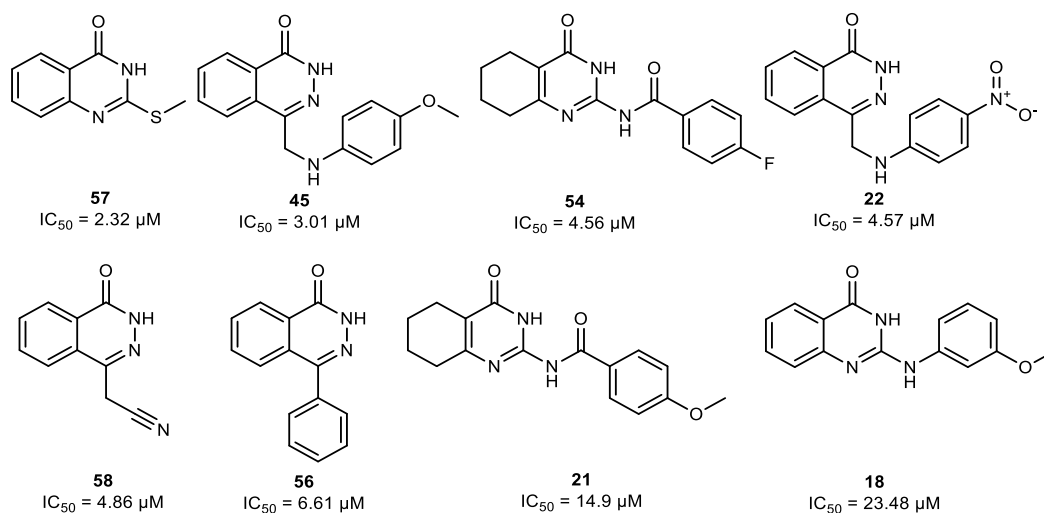


Fig.9 Structures and IC_{50} values of the most active novel hPARPi compounds as determined by using the hPARP-1 enzyme assays.

3.3. mRNA expression levels of *hPARP-1* and *SLFN-11*

The mRNA expression levels of *hPARP-1* and *SLFN-11* in the breast (cancer) cell lines were measured by using RT-qPCR. In contrast to the other cell lines, 184B5 is not a breast cancer cell line, but a healthy chemically transformed epithelial breast cell line. BT-474 cells showed the highest

hPARP-1 expression compared to the other cell lines (Fig.10a). However, the expression level of *SLFN-11* was found to be significantly higher in MDA-MB-468 compared to the other cell lines as shown in Fig.10b.

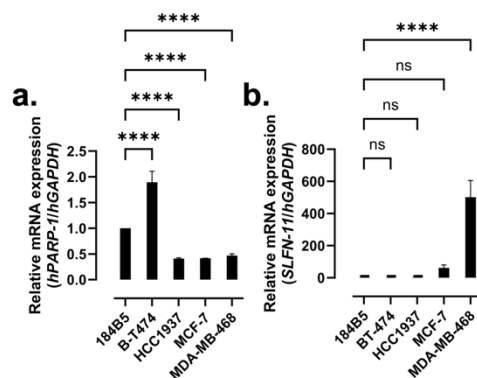


Fig.10 mRNA expression levels of **a**, *hPARP-1* and **b**, *SLFN-11* as determined in the breast cell lines under investigation by using RT-qPCR. The expression levels were calculated following the $\Delta\Delta C_t$ methodology in relation to the expression of the housekeeping gene *hGAPDH* and were normalized for illustration to the corresponding expression levels in 184B5 cells. (****p-value < 0.001).

3.4. *In vitro* cytotoxicity of compound 57

Compound **57**, as well as olaparib (OLP) and temozolomide (TMZ) as reference compounds, were tested *in vitro* for their cytotoxic activity against the selected breast (cancer) cell lines by conducting crystal violet (CV) cytotoxicity assays. Each of the compounds was tested in a suitable concentration range individually adjusted based on its expected activity, as illustrated in Fig.11 and Fig.S1. The dose-response data were analyzed by using the GraphPad Prism software, and IC_{50} and IC_{10} values were calculated, if possible based on the data, by using four parametric non-linear regression analyses. The calculated IC_{10} values of compound **57** in BT-474 cells (100 μ M) and of OLP in MDA-MB-468 cells (1.56 μ M) as illustrated in Fig.S1 were used in the synergistic cytotoxicity assay. The IC_{50} values of TMZ were calculated as well and are illustrated in Table 1 and Table S2.

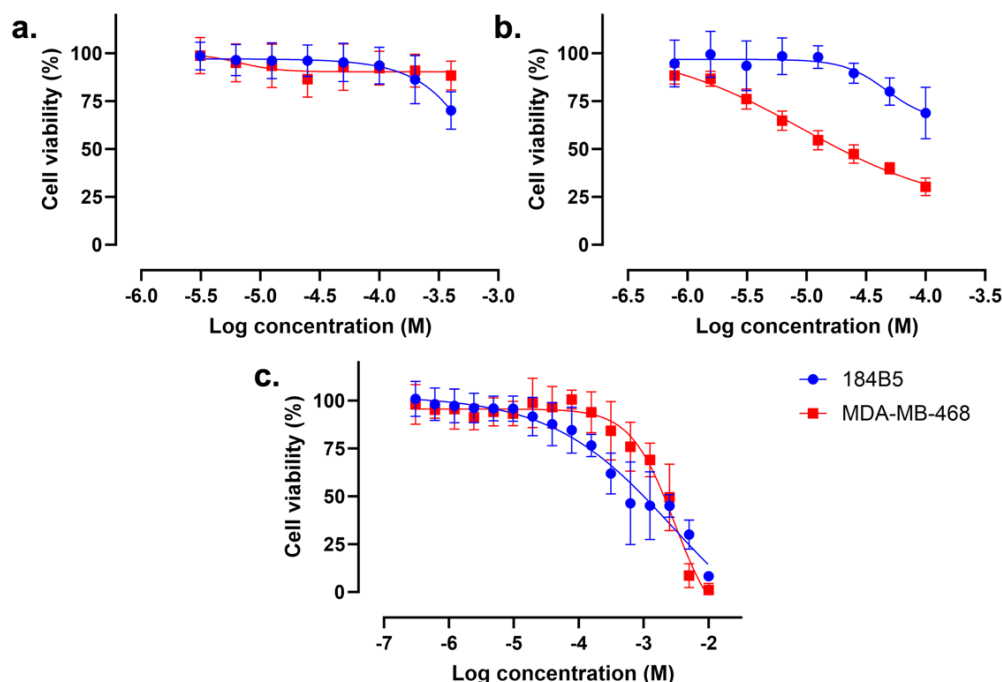


Fig.11 Cell viability dose-response curves of the breast cell lines under investigation upon 72 h treatment with **a**, compound **57**; **b**, OLP and **c**, TMZ. Cell viability was determined by using CV assay.

3.5. Compound 57 did not exhibit synergistic effect in combination with TMZ

IC₁₀ concentrations of OLP and compound 57, were used as co-treatments with several concentrations of TMZ to explore the possibility of a synergistic enhancement of the cytotoxicity of TMZ. However, as shown in Table 1 and Table S2, OLP improved the IC₅₀ of TMZ against MDA-MB-468 by \approx 21-fold, while compound 57 did not induce a synergistic improvement of the TMZ activity (Fig.12 and Fig.S2).

Table 1 Summary of the calculated IC₅₀ values (given in mM) of TMZ, TMZ combined with 100 μ M of compound 57, and TMZ combined with 1.56 μ M of OLP tested against the breast cell lines. Cells were treated for 72 h and assayed by using the CV assay.

Treatment	184B5	MDA-MB-468
TMZ	0.98 ± 0.82	2.06 ± 0.79
TMZ + compound 57	0.32 ± 0.07	2.77 ± 0.25
TMZ + OLP	4.95 ± 3.90	0.13 ± 0.04

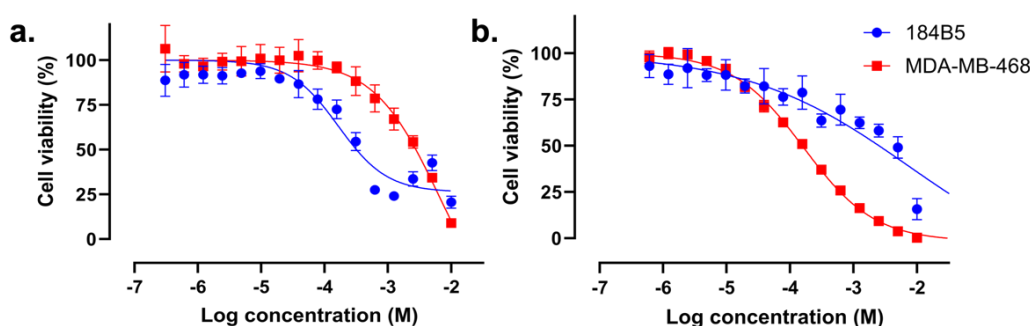


Fig.12 Dose-response curves of several breast cell lines. The cell lines were treated with several concentrations of TMZ combined with IC₁₀ of **a**, compound 57 and **b**, OLP for 72 h. Cell viability was determined using CV assay.

3.6. Compound 57 did not reach the nucleus-located hPARP-1 enzyme

Based on the mRNA expression levels of *hPARP-1*, BT-474 showed the highest expression level. Consequently, the BT-474 cell line was chosen for the fluorescence microscopy investigations on a supposed spatial colocalization of compound 57 and hPARP-1. The investigation was conducted by using the green fluorescent PARP ligand PARPi-FL, which occupies the ART domain of the hPARP-1 enzyme and it was proven to be competitively displaced using active PARP inhibitors. Accordingly, PARPi-FL occupied the enzyme pocket of hPARP-1 in the cells' nuclei and produced green nuclei-located fluorescence as illustrated in Fig.13a. However, compound 57 failed to reach the nucleus of BT-474 cells (Fig.13b). On the contrary, OLP was able to reach the hPARP-1 enzymes in the nuclei competing and replacing PARPi-FL from binding to the enzyme and, hence, reducing the nuclear PARPi-FL fluorescence, as shown in Fig.13c.

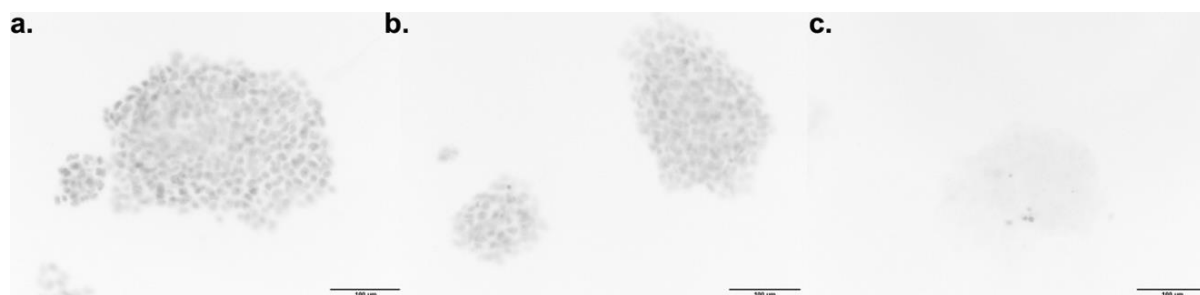


Fig.13 BT-474 cells treated for 72 h with **a**, complete medium (non-treated reference); **b**, 100 μ M of compound 57 and **c**, 1.56 μ M of OLP, followed by hPARP-1 staining with 250 nM of PARPi-FL for 20 min. The images were captured by using the GFP channel of an EVOSTM FL Auto Imaging System and were processed and color-inverted by using FIJI software. Scale bar: 100 μ m.

4. Discussion

By conducting a pharmacophore-based *in silico* screening of the Leibniz Institute of Plant Biochemistry's natural and natural-like compound library, 69 compounds were defined as potential hPARP inhibitors (hPARPi). Thus, an hPARP-1 enzyme assay was developed to prove these pre-selected compounds for actual hPARP inhibition. The hPARP-1 assay was based on the fact that the hPARP-1 enzyme requires NAD^+ as a cofactor and a supply of ADP-ribose units. Upon activation of hPARP-1 in the presence of activated DNA, i.e., DNA containing strand breaks, the enzyme starts consuming NAD^+ . However, the inhibition of hPARP-1 leads to the inhibition of the NAD^+ consumption which can be quantified using a cycling reaction (Fig.14). The cycling reaction utilizes the unconsumed NAD^+ to reduce resazurin to its fluorescent derivative resorufin through the activity of alcohol dehydrogenase. Moreover, it amplifies the fluorescent resorufin signal, as a measure of the NAD^+ remained after the hPARP-1 reaction, due to the redundant cyclic catalysis of the combination of diaphorase and alcohol dehydrogenase. In brief, the amount of the remaining NAD^+ is directly proportional to the inhibition of the hPARP-1 enzyme using a hPARPi. Initially, the linearity of the cycling reaction that detects the remaining NAD^+ concentration available in the reaction mixture was confirmed. Several concentrations of NAD^+ were measured and the obtained absolute fluorescent values were analyzed in a calibration curve. Afterwards, several concentrations of hPARP-1 were tested to determine which enzyme concentration was suitable to induce around 80% consumption of 50 nM of NAD^+ , which was found to be 2 U of hPARP-1. However, the optimal hPARP-1 concentration to be used should be determined for each enzyme batch individually due to its high dependency on each batch and its enzymatic activity.

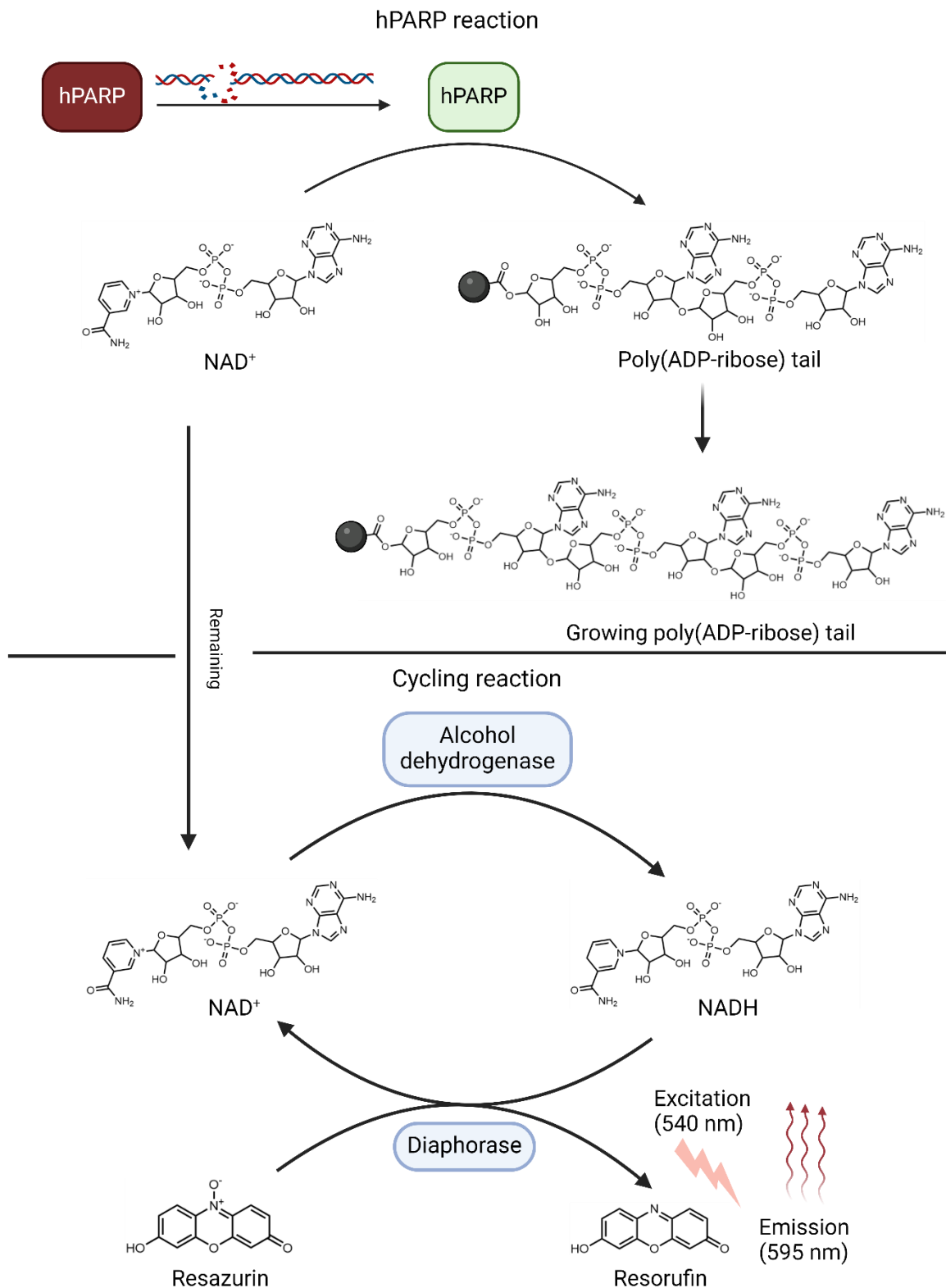


Fig.14 The concept of the hPARP-1 enzyme assay: The assay consists of a hPARP enzyme reaction and a cycling reaction. In the hPARP reaction, the hPARP enzyme is activated in the presence of activated, i.e., strand breaks containing DNA and uses the NAD^+ substrate to add poly(ADP-ribose) tails as posttranslational modification to itself and other protein targets. In the second step, the cycling reaction allows a catalytically amplified fluorescent read-out of the remaining NAD^+ substrate that was not used up by hPARP. NAD^+ is transformed to $\text{NADH}+\text{H}^+$, which is used to reduce resazurin to resorufin (excitation/emission: 540/595) which measured fluorescence indirectly indicates the activity of the hPARP enzyme. The scheme was created by BioRender.com.

Initially, as experimental proof of assay, the aforementioned hPARP-1 enzyme assay protocol was used to determine the IC_{50} value of the reference PARPi OLP. A value of 13 nM was in good agreement with the 5 nM IC_{50} value previously published in the literature for OLP against hPARP-1.¹⁵⁷ Consequently, the enzyme assay was used to screen our pre-selected compounds for hPARP-1 inhibition. Compounds **18**, **21**, **22**, **45**, **54**, **56**, **57**, and **58** (shown in Fig.9) inhibited hPARP-1 and were further tested to determine their IC_{50} values, which ranged from 2.3 to 23.5 μ M.

Compound **57** (2-(methylthio)quinazolin-4(3*H*)-one) was found to be the most active hPARPi with an IC_{50} of 2.3 μ M against hPARP-1. Accordingly, the binding of compound **57** to the ART subdomain of hPARP-1 was studied by *in silico* molecular modelling and it was found to follow the interactions that were found essential for the activity of hPARPi as shown in Fig.S3 which are the hydrophobic interaction with Tyr907 and H-bonding with Ser904 and Gly863. Concerning the structure-activity relationship (SAR), several features were identified to be essential for its activity as a hPARPi. By comparing compound **57** with the compounds **62** and **63**, it was noticed that any substitution at the nitrogen position 3 (Fig.15; red part of the structures) led to a complete abolishment of the activity as an hPARP-1 inhibitor. The rationale behind that observation is that the replaced hydrogen ion seems to be essential for the formation of a H-bond with the oxygen group of the glycine at position 863 of hPARP-1 as described in the literature.¹⁵⁸ Moreover, the modifications at meta and/or para positions in the compounds **64**, **65** and **66** (Fig.15; blue parts of the structures) lead to a dramatic decrease in activity as it disturbs the crucial hydrophobic interaction that has to be formed with the tyrosine residue of the ART subdomain.¹³⁹ A modification at the thiomethyl group, as realized in compounds **67**, **68** and **69** (Fig.15; green part of the structures), does not lead to complete loss of the compounds' activity, however it causes a reduction of the PARPi activity by at least 4-fold. Remarkably, compound **57** (IC_{50} = 2.3 μ M) has shown 2.5-fold higher activity inhibiting hPARP-1 compared to quinazolin-4(3*H*)-one shown in Fig.17 (IC_{50} = 5.8 μ M), lacking the thiomethyl group.¹⁵⁹

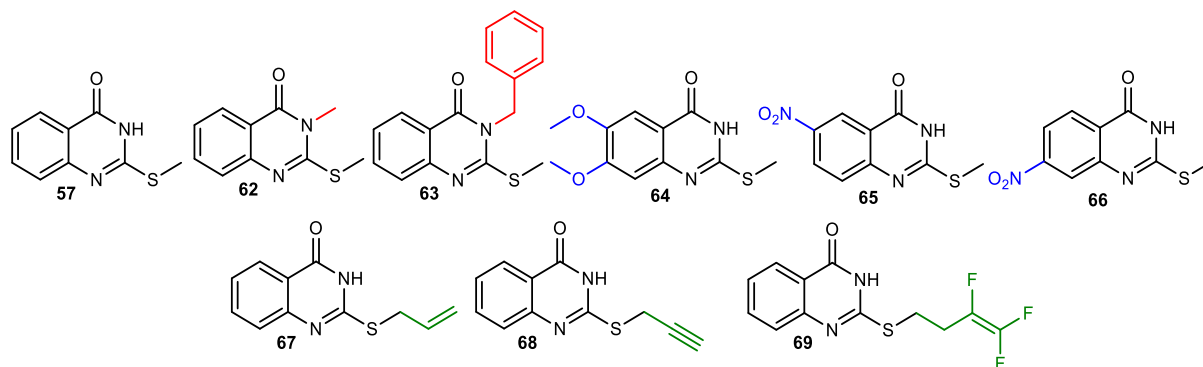


Fig.15 Structure-activity relationship (SAR) considerations regarding compound **57** as the most active hPARPi identified.

Besides the compound **57** scaffold, another new core structure (4-methyl-*N*-(4-oxo-3,4,5,6,7,8-hexahydroquinazolin-2-yl)benzamide) was identified permitting hPARP inhibitory activity. Based on the available compounds, several modifications were identified that heavily affect its activity. The most active compound sharing that core structure was compound **54** (IC_{50} = 4.56 μ M) with a fluoride group at the para position of the phenyl group. However, the replacement of the fluoride group by either methoxy, methyl or chloride group, as realized in compounds **21**, **32** and **34** (Fig.16; red part of the structures) causes a decline in the compounds' PARPi activity by at least 3-fold. The high activity of this family of compounds could be related to the presence of an additional benzamide group attached to the core structure of the aforementioned compound **57** family in which the aromatic group may form a π - π interaction with Tyr896 similar to that formed by the benzyl group in the case of OLP as shown in Fig.7.¹⁶⁰

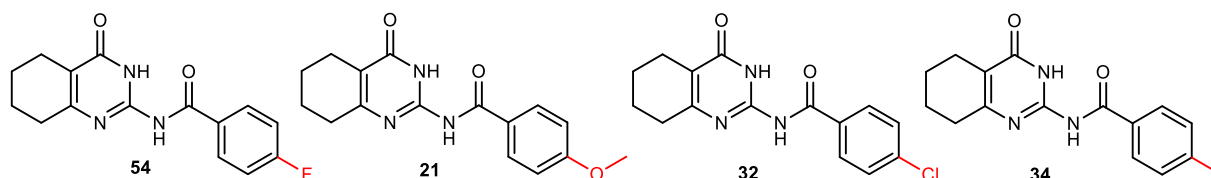


Fig.16 Structure-activity relationship (SAR) considerations regarding compound **54**.

According to several previous studies, the cancer cells' susceptibility to hPARP inhibition should be inversely proportional to their BRCA gene expression.^{161,162} Nevertheless, during the last years, various studies highlighted a new, more important cornerstone for the prediction of hPARPi susceptibility which was the expression of the *SLFN-11* gene.^{137,163,164} Hence, the expression levels of the *SLFN-11* in the breast (cancer) cell lines under investigation was tested first by using RT-qPCR, along with those of *hPARP-1* itself. The highest *SLFN-11* expression level was found in MDA-MB-468 triple-negative breast cancer cells, which was more than 10-fold higher compared to MCF-7 hormone receptors-positive breast cancer cells and at least 300-fold higher compared to the other breast (cancer) cell lines. Based on the *SLFN-11* expression results in conjunction with the given *hPARP-1* expression, it was expected to observe the highest impact of the PARPi reference drug OLP as well as the newly discovered PARPi compounds, in particular of compound **57**, against MDA-MB-468 cells. And as expected, OLP improved the cytotoxicity of TMZ towards MDA-MB-468 by approximately 21-fold. In which TMZ induces the formation of single-strand breaks, and OLP inhibits the repair of the DNA leading to cell death and enhanced cellular toxicity. Additionally, OLP as a monotherapy also showed selectivity against MDA-MB-468. However, such an effect was not observed with compound **57**. One possible explanation for that result could be the too weak cellular and/or nuclear permeability for compound **57**, and therefore the failure to reach the hPARP-1 enzymes in the nuclei.¹⁶⁵ Hence, to investigate compound **57**'s capacity to penetrate the cellular membranes, fluorescence microscopy was performed. For that purpose, BT-474 cells, showing the highest expression of *hPARP-1* (see Fig.10), were stained with PARPi-FL. That green fluorescent PARP ligand was developed as an imaging tool for binding at the NAD⁺ binding pocket of PARP enzymes. Consequently, PARPi-FL can be used to screen for hPARP inhibitors competitively displacing the ligand from its binding to the hPARP-1 enzyme. By comparing the images shown in Fig.13, OLP showed high affinity binding to the hPARP-1 enzymes, located in the cells' nuclei, leading to complete PARPi-FL displacement, and dissolution of its fluorescent signal. On the contrary, compound **57** did not impact the fluorescent appearance of the stain, indicating a lack of hPARP-1 enzyme binding in the cell's nucleus. This could be an indication of its poor nuclear and/or cellular penetration. Nonetheless, compound **57** was determined with a 5-fold higher PARPi activity compared to the core structure of OLP, phthalazin-1(2*H*)-one, (IC₅₀ = 12 μM) as illustrated in Fig.17.¹⁶⁶ Which indicates that the scaffold could be used for the advancement of PARPi development.

The first steps in a hit-to-lead strategy for the determination of novel hPARP-1 inhibitors have been taken in this study. Starting with a target validation as shown by the confirmation of the impact of the clinically proven hPARP inhibitor (OLP) against the hPARP-1 enzyme and PARP inhibitor sensitive cell lines. The second step was the development of an assay that is easy, robust, cheap and up scalable to perform a high throughput screening for hPARP-1 inhibitors. It was applied to determine several hit compounds which indicates the first accomplishment to lead generation step. These compounds can be further improved through lead optimization as previously performed with phthalazin-1(2*H*)-one leading to the development of OLP. Initially, for phthalazin-1(2*H*)-one also just relatively weak PARP inhibitor activity in cell-based assays was reported. However, due to its promising hPARP enzyme inhibition, step-by-step molecule modifications and optimizations towards the very potent PARPi OLP were implemented. The structural modification by the introduction of a benzyl group at position 4 led to the remarkable improvement of the compound's IC₅₀ from 12 μM to 550 nM and led to an also cellularly active hPARP inhibitor.¹⁶⁷ By introducing a fluoride group at the para position of the benzyl group, a further improvement of the permeability and potency was noted. Further introduction of the piperazine group at the meta position of the benzyl group improved the solubility of the compound.^{168,169} These illustrated OLP modifications might be used for further lead

optimization of the newly discovered scaffold **57** too, which could unveil novel molecules with even higher activity compared to OLP, as indicated by the lower IC_{50} of compound **57** compared to phthalazine-1(2*H*)-one, the OLP core structure, as shown in Fig.17. Those optimized derivatives could then be applied in cancer treatment as potential adjuvants in combination with a DNA damaging agents, especially against those tumors characterized by overexpression of SLFN-11 as they are more sensitive to DNA damage as previously proven by several studies and also shown in this study by the potentiation of the cytotoxic effect of temozolomide (TMZ) towards the highly SLFN-11 expressing cell line MDA-MB-468 by using the a bioavailable hPARP-1 inhibitor olaparib (OLP).



Fig.17 structures of compound **57**, quinazolin-4(3*H*)-one and phthalazin-1(2*H*)-one (the OLP core structure).

5. Conclusion

This study aimed to implement a cost-effective screening methodology to discover hPARP inhibitors. Therefore, a cell-free hPARP-1 enzyme assay was established, optimized and utilized to screen for hPARP-1 inhibitors in the natural and natural-like compound library of the Leibniz Institute of Plant Biochemistry. Out of 69 *in silico* pre-selected compounds, six molecules were detected to inhibit the hPARP-1 enzyme at exceptionally low micromolar concentrations. The most active candidate was compound **57** with an IC_{50} of 2.3 μM . However, the compound failed to have cellular impact seemingly due to its weak nuclear membrane penetration. Interestingly, the lead molecule, i.e., compound **57**, showed 5-fold higher PARPi activity than the olaparib (OLP) core structure (phthalazin-1(2*H*)-one) itself. Therefore, further chemical substitution and optimization based on compound **57** as a core structure could lead to a novel PARP inhibitor class with PARPi activities and drug likeliness in the range or beyond OLP and other already approved PARP inhibitors. Moreover, besides compound **57**, a second new and promising core structure was unveiled. Even though compound **54** showed lower activity compared to compound **57**, its PARPi activity was still 2-fold higher compared to the OLP core structure. Furthermore, a first structure-activity relationship (SAR) was devised and several features were highlighted that affect the interaction of the PARPi molecules with the hPARP-1 enzyme consequently determining their inhibitory potency. These findings will help to improve the development and optimization of novel hPARP inhibitors.

Author Contributions: The individual authors' contributions to the presented work are as follows: conceptualization: Ludger A. Wessjohann and Robert Rennert; methodology: Ibrahim Morgan, Robert Rennert, Ludger A. Wessjohann; compound synthesis: Robert Berger; resources: Ludger A. Wessjohann; data curation: Ibrahim Morgan; writing – original draft preparation: Ibrahim Morgan; review and editing: Robert Rennert, Ludger A. Wessjohann; supervision: Robert Rennert, Ludger A. Wessjohann (main); project administration: Ludger A. Wessjohann; *in silico* study: Ahmed Hassanin, Daniela Eisenschmidt-Boenn, Mehdi Davari; funding acquisition: Ludger A. Wessjohann.

Chapter 3 : The impact of 9-azaglycophymine derivatives on the proliferation of various breast cancer cell lines *in vitro* and *in vivo*

Abstract: Quinazolinones, particularly 9-azaglycophymines, and closely related derivatives and precursors were tested *in vitro* against various breast cancer cell lines representing the major types of breast tumors. Among the 49 compounds tested, compound **19** demonstrated the most significant anti-proliferative effects, with IC₅₀ values of around 4 μM. Extensive cell-based investigations revealed that compound **19** induced caspase-dependent apoptosis in HCC1937 (human TNBC), BT-474 (human HER2+/HR+), and 4T1 (mouse TNBC) cells. In contrast, in MDA-MB-468 (human TNBC) and MCF-7 (human HR+) cells, the cell death was induced via a non-apoptotic pathway. The *in vivo* efficacy of compound **19** was validated using a syngeneic orthotopic 4T1 model in BALB/c mice, resulting in significant reduction of 4T1 breast tumor growth upon intraperitoneal (i.p.) application of doses of 5 or 20 mg/kg. These findings highlight the potential of compound **19** as a promising scaffold for the development of new therapeutic agents for various types of breast cancer.

1. Introduction

The precise regulation of cellular growth is a tightly controlled process. Conversely, dysregulations may lead to uncontrolled and abnormal proliferation of cells developing a benign or malignant tumor.¹⁷⁰ Amongst the malignant tumor diseases, breast cancer is one of the most often diagnosed types worldwide. In 2018, around 2.3 million cases were counted, outpacing for the first time the number of new lung cancer cases. Breast cancer now accounts for 11.7% of all reported tumors in women and men.¹⁷¹ Whereby, in women, breast cancers represented 24.5% of all newly diagnosed cancer cases in 2020.⁹⁴ One of the criteria for the selection of the treatment regimen for breast cancers is the type of receptors overexpressed by the tumor cells. Estrogen receptors (ER) are expressed by around 80% of all breast cancer cells, 65% of these cells overexpress additionally the progesterone receptor (PR). These so-called hormone receptor (HR) positive breast cancers can be treated, for instance, by estrogen receptor modulators, such as tamoxifen,¹⁷² or aromatase inhibitors like anastrozole.^{173,174} The human epidermal growth factor receptor 2 (EGFR2 or HER2/neu) is overexpressed by around 20% of all breast cancer cells. Compared to HR-positive breast cancers, these tumors are in most cases more aggressive and less responsive to conventional chemotherapeutic treatments. However, they can be treated by applying monoclonal antibodies targeting HER2/neu receptors, such as trastuzumab (HerceptinTM) or the corresponding antibody-drug conjugates (e.g. trastuzumab emtansine, KadcylaTM).^{86,175} Other breast cancers neither overexpress HRs nor HER2/neu. These types of breast cancer are named triple-negative breast cancers (TNBC). Treatment strategies that can be applied in these cases are, for instance, poly(ADP-ribose) polymerase (PARP) inhibitors, such as olaparib, or programmed death-ligand 1 (PD-L1) blockers like atezolizumab.^{176,177} However, the treatment of TNBCs is still very challenging. With four-year survival rates of just 77% in the case of TNBCs, the prognosis is worse than for HR- and HER2/neu-positive breast cancers (93%).¹⁷⁸

Quinazoline and quinazolinone (illustrated in Fig.18a and b, respectively) derivatives, are core structures attributed to several pharmaceutical effects. Derivatives thereof have been described to be beneficial as anti-inflammatory drugs by inhibiting NF- κ B transcription and TNF- α production.¹⁷⁹ Moreover, such compounds have been described to have anti-fungal activities, e.g. albaconazole (Fig.18g), by inhibiting the cytochrome P450-dependent lanosterol 14 α -demethylase (CYP51A1) leading to an inhibition of ergosterol synthesis.¹⁸⁰ Furthermore, several quinazolinone derivatives, e.g. febrifugine (Fig.18h) isolated from *Dichroa febrifuga*, have been investigated for their anti-malarial effects against *Plasmodium falciparum* and *Plasmodium vivax*.¹⁸¹

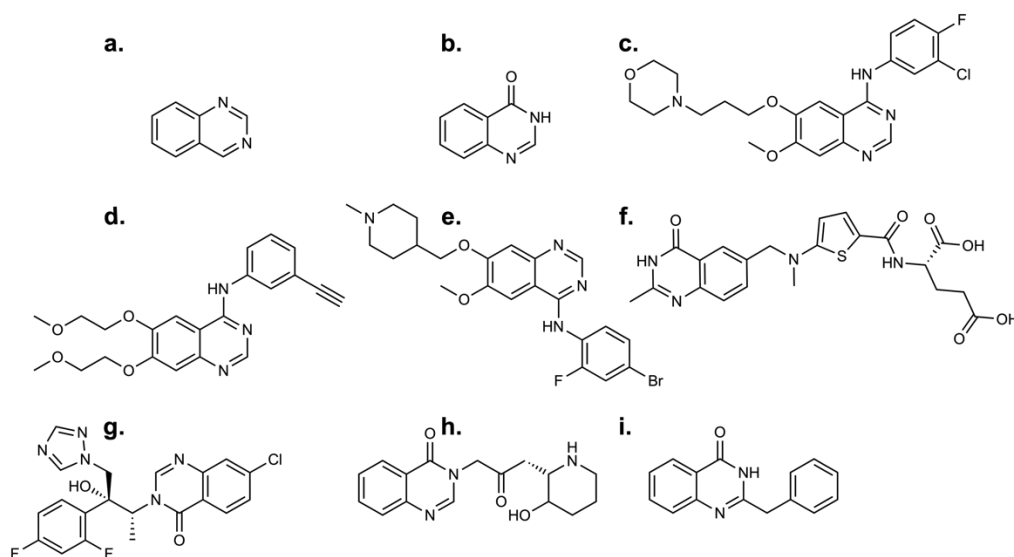


Fig.18 a, Quinazoline and b, quinazolinone core structures; c, gefitinib; d, erlotinib; e, vandetanib; f, raltitrexed; g, albaconazole; h, febrifugine and I, glycophymine.

Other derivatives have been proven to possess anticancer activities and are used as chemotherapeutic agents. Gefitinib and erlotinib (Fig.18c,d) are quinazoline derivatives that act as inhibitors of epidermal growth factor receptors (EGFRs). They are clinically approved to treat EGFR overexpressing cancers, such as non-small cell lung cancer.^{88,182} Vandetanib (Fig.18e), another quinazoline derivative, is used as a chemotherapeutic agent based on its antagonistic effect against the vascular endothelial growth factor receptor (VEGFR) for the treatment of advanced and metastatic thyroid cancer.¹⁸³ Another quinazolinone derivative, raltitrexed (Fig.18f), has a chemical resemblance to folic acid. This similarity causes an anti-metabolite effect and therefore, an inhibition of the thymidylate synthase and DNA repair. Hence, raltitrexed is used in the treatment of advanced colorectal cancers.¹⁸⁴ Furthermore, these derivatives were found to possess significant potency to inhibit protein kinases which control crucial pathways regulating cell division and thus cancer progression.¹⁸⁵

Glycophymine (2-benzyl-4(1*H*)-quinazolinone, illustrated in Fig.18i) was originally isolated from *Glycosmis arborea* (Rutaceae, the citrus plant family) and later other species.¹⁸⁶ Several glycophymine derivatives were proven to act as cytotoxins. For instance, 2-(3,4,5-trimethoxybenzoyl)quinazolin-4(3*H*)-one was reported with an IC₅₀ of 1.22 ± 0.12 μM against the HepG2 cell line.¹⁸⁷ The goal of this study was to investigate the potential activities of 2-(phenylamino)quinazolinone (9-azaglycophymine) derivatives, available from previous synthetic works from the compound library of the Leibniz Institute of Plant Biochemistry, against various breast cancer cell lines representing the different overexpression patterns of the breast cancer-related receptor classes. The most active derivative was found to be 2-((4-nitrophenyl)amino)quinazolin-4(3*H*)-one (compound **19**). Therefore, it was studied in more detail to determine its biological impact on cell cycle regulation, cellular proliferation, autophagy and apoptosis induction, NO production and the formation of ROS (reactive oxygen species). Moreover, the *in vivo* antitumor effect of compound **19** was proven by using a syngeneic mouse TNBC model induced by orthotopic implantation of 4T1 cells in BALB/c mice.

2. Materials and Methods

2.1. Cell lines and chemicals

The breast cancer cells used in this study were the human cell lines MCF-7, BT-474, HCC1937, MDA-MB-468, and the mouse cell line 4T1. All cell culture reagents, i.e., RPMI1640, fetal calf serum (FCS), penicillin/streptomycin (P/S), Dulbecco's phosphate-buffered saline (PBS), glutamine and 0.05% trypsin-EDTA, were purchased from Capricorn Scientific (Ebsdorfergrund, Germany).

Annexin V/propidium iodide (AnnV/PI) kit and trypan blue were obtained from Invitrogen (Waltham, Massachusetts, USA). ApoStat was supplied by R&D systems (Minneapolis, Minnesota, USA). Acridine orange (AO) and crystal violet (CV) were from Sigma Aldrich (St. Louis, Missouri, USA). Carboxyfluorescein succinimidyl ester (CFSE) and dihydrorhodamine 123 (DHR) were purchased from BD Horizon (Franklin Lakes, New Jersey, USA). 4-amino-5-methylamino-2',7'-difluorofluorescein diacetate (DAF-FM) was bought from Cayman Chemical Compounds (Ann Arbor, Michigan, USA). Dimethyl sulfoxide (DMSO) was from Duchefa Biochemie (Haarlem, The Netherlands). Acetic acid and paraformaldehyde were purchased from Carl Roth (Karlsruhe, Germany), and 4',6-diamidino-2-phenylindole (DAPI) from Roche (Basel, Switzerland).

2.2. Cell culture

For this study, four human breast cancer cell lines differing in their ER, PR, EGFR, HER2/neu and BRCA-1 (breast cancer gene 1) expression levels were investigated,¹⁷³ namely MCF-7, BT-474, HCC1937 and MDA-MB-468. The characteristic expression levels of the essential receptor genes in these human cell lines are illustrated in Table S5.¹⁸⁸⁻¹⁹⁰

The cell lines were cultured in RPMI1640 medium supplemented with 10% (v/v) heat-inactivated FCS, 1% (v/v) penicillin/streptomycin and 1% (v/v) glutamine.¹⁹¹⁻¹⁹⁵ For passaging and seeding, cells were treated as previously described.¹⁹⁶ In brief, seeding was done in low density with 6 × 10³ cells/100 μL in 96-well plates, and with 1.5 × 10⁵ cells/1 mL in 6-well plates. Prepared cell flasks

and plates were maintained in a humidified atmosphere with 5% CO₂ at 37°C (standard culture conditions).

2.3. Cell viability assays

For initial testing of the cytotoxic effect of the available glycyphymine compounds (Table S6), cells were treated with each compound at three concentrations: 1, 10 and 50 µM. Cells were seeded in 96-well plates and allowed to adhere overnight. Then they were treated for 72 h under standard culture conditions. Those compounds that showed a cytotoxic effect when applying ≤10 µM concentration and caused a reduction of the cell viability by at least 50% were selected for the determination of their IC₅₀ value. For IC₅₀ determination, the compounds were tested at seven concentrations (0.78, 1.56, 3.13, 6.25, 12.5, 25 and 50 µM). Subsequently, the cell viability was determined by using the crystal violet (CV) assay. Moreover, the selected compounds were tested against the mouse breast cancer cell line 4T1 (TNBC) as well.

For CV assays, after 72 h treatment, the treatment medium was discarded from the 96-well plates, and the cells were washed using 50 µL of PBS. Cells were fixed by adding 50 µL of 4% (v/v) paraformaldehyde (PFA) in PBS for 15 min at room temperature (RT). Afterward, PFA was discarded, and the plates were dried for 15 min at RT. 50 µL of CV working solution (0.1% w/v CV in PBS) were added to the wells, followed by 15 min incubation at RT. Subsequently, the CV solution was discarded, and the plates were washed using aqua-bidistilled water (ddH₂O) to remove any remaining CV solution. The plates were dried overnight at RT, and then 50 µL of 33% (v/v) acetic acid in ddH₂O were added to each well. Finally, the absorbance was measured at 570 nm by using a SpectraMax M5 plate reader (Molecular Devices, California, USA) and at 670 nm as the background wavelength.¹¹¹ The results were normalized to a negative control representing viable cells (untreated cells) and a positive control representing dead cells (cells treated with 125 µM of digitonin).¹⁵²

2.4. Flow cytometric analyses

2.4.1. Cell cycle, apoptosis, pan-caspase activation and autophagy analyses

Cells were seeded in 6-well plates and incubated for 24 h under standard culture conditions. Afterward, the cells were treated with compound **19** at IC₅₀ for 72 h under standard culture conditions.

For cell cycle analyses, cell fixation was performed with 70% (v/v) ethanol for 24 h at 4°C. The cell suspension was centrifuged for 3 min at 800 rpm, and the cell pellet was stained using the DAPI staining solution (1 µg/mL of DAPI, 1% (v/v) TritonTM X-100 in PBS) for 10 min at RT.

For apoptosis analyses, the cell suspension was centrifuged for 3 min at 800 rpm, and the cell pellet was stained by using 100 µL of AnnV/PI working solution (5 µL of AnnV, 2 µL of PI in 100 µL of PBS) for 15 min at RT and protected from light. The staining was terminated by the addition of 900 µL of annexin binding buffer.

For the analyses of pan-caspase activation, the cell suspension was centrifuged for 3 min at 800 rpm, and the cell pellet was stained with 100 µL of ApoStat working solution (1 µl of ApoStat and 5% (v/v) FCS in 100 µl of PBS). Cells were incubated for 30 min under standard culture conditions. The cell suspension was centrifuged for 3 min at 800 rpm, and the cell pellet was washed with 1 mL of fresh PBS.

For the analyses of autophagy induction, the cell suspension was centrifuged for 3 min at 800 rpm, and the cell pellet was stained with 1 mL of AO working solution (1 µg/mL of AO in growth medium). Cells were incubated for 15 min under standard culture conditions. The cell suspension was centrifuged for 3 min at 800 rpm, and the cell pellet was washed with 1 mL of fresh PBS.

Finally, all samples were analyzed using flow cytometry (FACSAria III, BD Biosciences, New Jersey, USA).

2.4.2. Cell division analyses

The cells were stained with CFSE (1 μM) in PBS containing 0.1% (v/v) FCS for 10 min. Afterwards, the cells were washed with PBS and then seeded with growth medium in 6-well plates. The plates were incubated for 24 h under standard culture conditions. After incubation, cells were treated with compound **19** at IC_{50} and incubated for 72 h under standard culture conditions. Subsequently, the cells were detached using 0.5 mL of 0.05% (v/v) Trypsin-EDTA for 3 min at 37°C. Then trypsin was deactivated by the addition of FCS-containing growth medium. The cell suspensions were collected, centrifuged for 3 min at 800 rpm, and the cell pellets were resuspended in fresh PBS. Finally, the samples were analyzed by using flow cytometry.¹⁹⁷

2.4.3. Investigation of ROS and NO production

For ROS production analyses, the procedure was performed exactly as described above for the cell division experiments, except that the CFSE staining solution was replaced by DHR staining solution resulting in 1 μM of DHR in PBS containing 0.1% (v/v) FCS.^{198,199}

For NO production detection, cells were seeded in 6-well plates, allowed to adhere for 24 h under standard culture conditions, then treated with compound **19** at IC_{50} , and incubated for 72 h under standard culture conditions. Afterward, the medium was discarded and the cells were stained with DAF-FM (5 μM) in RPMI1640 with 10% (v/v) FCS for 1 h at 37°C. The stain was completed by additional incubation for 15 min with a serum-free medium. The cells were then detached, re-suspended in PBS and analyzed by flow cytometry.

2.5. *In vivo* study

Compound **19** was selected to be tested against a syngeneic breast cancer model induced by orthotopic inoculation of 4T1 mouse breast cancer cells (TNBC) into BALB/c mice. 5×10^4 of 4T1 cells in 50 μL of PBS were inoculated in the fourth right mammary fat pad of female mice at day 0. Three groups were included in the study, each comprising eight animals; the control group was treated with 400 μL of vehicle solution, the low dose compound **19** group with 5 mg/kg in 400 μL of vehicle, and the high dose group with 20 mg/mL in 400 μL of vehicle. The vehicle was 4% (v/v) DMSO in PBS, and the administration route was intraperitoneal (i.p.). The animals were treated daily on days 6-10 (starting from the day when tumors became palpable), 13-17 and day 20. Animals were visually examined regularly, and urine samples were collected on the first and last day of treatment and analyzed by Multistix urine test stripes (Siemens Healthineers, Erlangen, Germany). At day 21, the mice were sacrificed with cervical dislocation, the tumor diameters were measured using a caliper, and the volume was calculated as $V = L * W^2 * 0.52$,²⁰⁰ where L is the longest and W shortest diameter.

2.6. Histopathology

Tissue samples of the tumors, kidneys, livers and spleens were fixed in 4% (v/v) formalin. After fixation, tissues were embedded in paraffin blocks, and 4 μm thick sections were obtained, mounted on glass slides, stained with Hematoxylin Eosin, and analyzed by using an Olympus BX43 microscope (Olympus, Tokyo, Japan). All slides were scanned with a Leica Biosystems Aperio AT2 with 400 \times magnification (n = 3 per group). Virtual slides generated from Leica Aperio AT2 were additionally analyzed with Aperio ImageScope (v12.4.3.5008) and with FIJI-ImageJ software.

3. Results

3.1. Discovery of novel 5 anticancer compounds with compound **19** as the most active compound

The fast screening was performed to determine the antiproliferative activity of 49 compounds (Table S6) against MCF-7, MDA-MB-468, BT-474 and HCC1937 breast cancer cells. The cell viabilities detected after 72 h of treatment are illustrated in Fig.S4 and Fig.S5. The compounds **19**, **22**, **24**, **46** and **47** significantly reduced cell proliferation of all four cell lines. These compounds were selected for further studies, testing them at a wider range of concentrations to determine their IC_{50} values (as a mean), using a four-parameter logistic function. Moreover, the most active compounds were also tested against the aggressive triple-negative 4T1 mouse breast cancer cell line, aimed for the selection

of the most relevant substances for further syngeneic *in vivo* mouse studies. The obtained cell viability dose-response curves are shown in Fig.19, the accordingly calculated IC₅₀ values are summarized in Table 2.

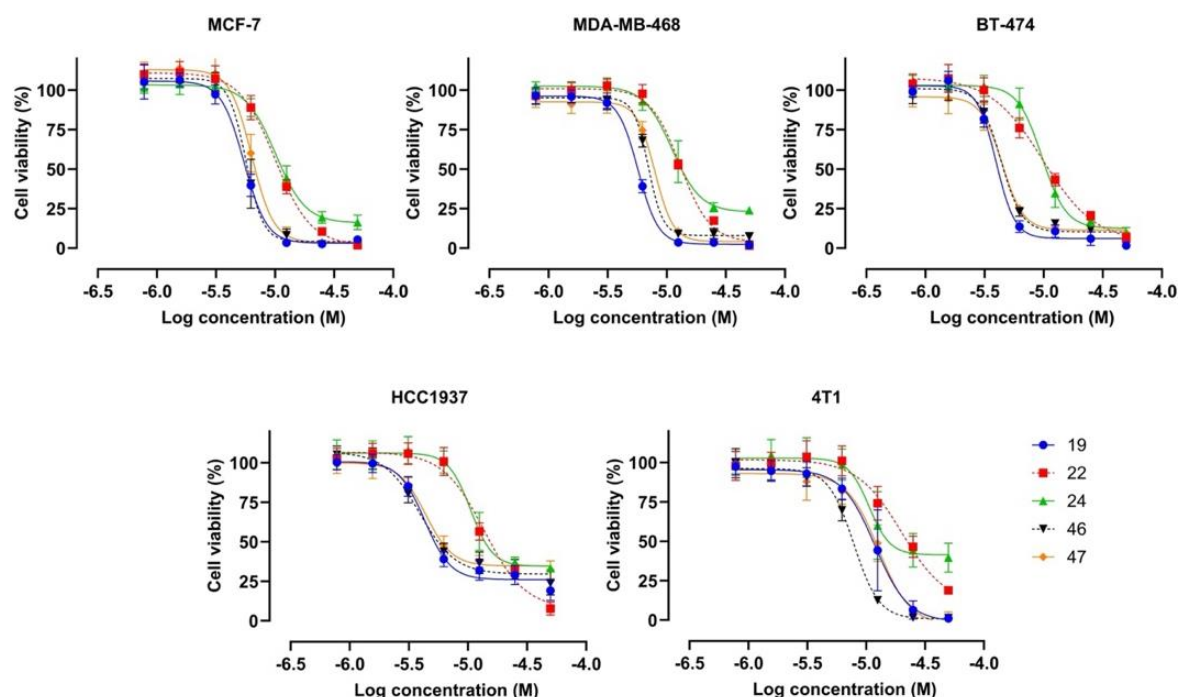


Fig.19 Dose-response curves of the viability of MCF-7, MDA-MB-468, BT-474, HCC1937 and 4T1 cells after 72 h treatment with the most active compounds. Cell viability was measured by using the CV assay.

Table 2 IC₅₀ values (μM) of the most active compounds as determined for the cell lines under investigation.

Compound	MCF-7	MDA-MB-468	BT-474	HCC1937	4T1
19	5.5 ± 0.6	5.8 ± 0.3	4.0 ± 0.2	4.3 ± 0.1	12.5 ± 3.7
22	10.0 ± 0.5	13.0 ± 0.4	9.9 ± 1.5	14.8 ± 3.7	23.5 ± 7.2
24	10.3 ± 1.3	11.2 ± 1.8	9.7 ± 1.3	11.0 ± 1.9	11.3 ± 3.5
46	5.7 ± 0.6	6.9 ± 0.2	4.4 ± 0.1	3.9 ± 0.2	7.9 ± 0.6
47	6.3 ± 0.4	8.0 ± 0.3	4.5 ± 0.2	4.4 ± 0.3	12.6 ± 1.2

Compound **19** was found to be the most active test item against most of the breast cancer cell lines, with IC₅₀ values of 4 – 6 μM . Although compounds **46** and **47** showed comparable results, they were slightly less active in some cell lines. Based on these data, compound **19** was selected for further analyses using flow cytometry and *in vivo* application.

3.2. Compound 19 induced cell death in different breast cancer cell lines through different mechanisms

Flow cytometric studies pointed out that compound **19** varies in its modes of action in different cell lines. In BT-474, HCC1937 and 4T1, it induced inhibition of proliferation and an activation of pan-caspases leading to apoptosis (percentage of apoptotic cells increased upon treatment with **19** when compared to control cells as follows: in treated BT-474 51% vs. 20% in control cells, in HCC1937 47% vs. 19%, and 4T1 69% vs. 31%, as illustrated in Fig.20a). The presence of acidic vesicles including autolysosomes, which is an indicator of autophagy activation,^{201,202} was not changed by the treatment. Interestingly, enhanced NO production in BT-474, HCC1937, 4T1 and MCF-7 was well synchronized with ROS downregulation and pan-caspase activation, except in caspase-3 deficient MCF-7 cells. This might be caused by the inhibition of membrane enzymes which produce superoxide anion by NO, further enabling pan-caspase activation and successful induction of apoptosis.²⁰³ In this context, MCF-7 cells could not respond to the treatment by induction of the caspase-3 initiated intrinsic apoptosis program, despite excessive production of NO. Interestingly, in MDA-MB-468, the confirmed cytotoxic

effect of compound **19** seemingly is not mediated by any of the investigated processes. The functional impacts of compound **19** on the cell lines are summarized in Table 3. The underlying histograms, dot plots and bar graphs are shown in the Supplementary Information Fig.S6-Fig.S13.

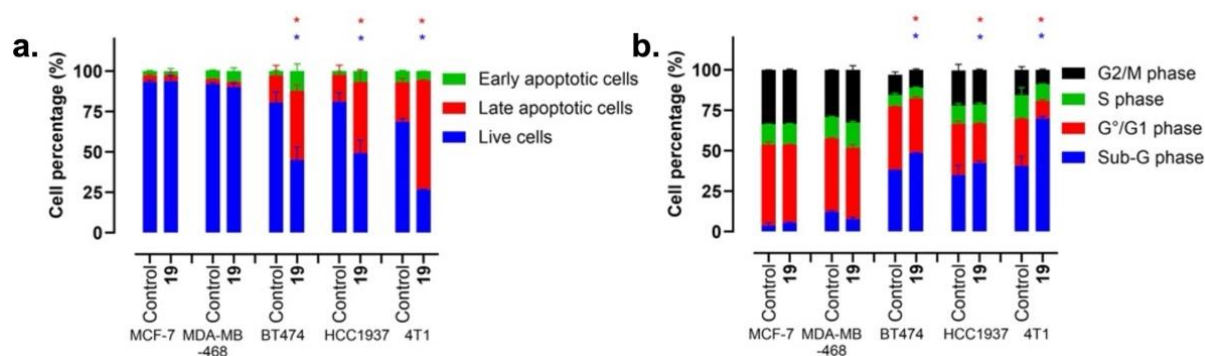


Fig.20 Bar graphs representing the biological impacts of compound **19** applied at IC₅₀ for 72 h to several breast cancer cell lines on **a**, the induction of apoptosis and **b**, the cell cycle status distribution in G⁰/G1, S and G2/M phases. Bars represent the mean values ± standard deviation calculated based on three independent measurements. * p < 0.05 compared to the untreated control cells.

Table 3 Cell line-dependent biological impacts of compound **19** treatment at IC₅₀ for 72 h. ↑ - induction; ↓ - inhibition; ↔ - no effect. The bar graphs used to determine these data are illustrated in Fig.S13.

Cell response	MCF-7	MDA-MB-468	BT-474	HCC1937	4T1
ROS	↔	↔	↓	↓	↔
NO	↑	↔	↑	↑	↑
Autophagy	↔	↔	↔	↔	↔
Proliferation	↔	↔	↓	↓	↓
Pan-caspases	↔	↔	↑	↑	↑

3.3. Compound **19** hinders breast tumor growth in mice

The i.p. treatment with 5 mg/kg of compound **19**, decreased the median tumor volume from 205 mm³ (control group) to 143 mm³ (5 mg/kg treated group) as illustrated in Fig.21. Using a higher dose of 20 mg/kg, no further improvement of the tumor suppression was observed. The systemic toxicity of the treatment was monitored regularly by observing the animals' body mass (Fig.S14), behavioral changes, fur color and loss, and food intake (data not shown). However, no significant abnormalities of these health parameters were observed during the whole study, indicating the absence of acute systemic toxicity caused by compound **19**. In addition, biochemical markers measured in urine samples indicated compound **19** lacks systemic toxicity for both doses tested (Table S7).

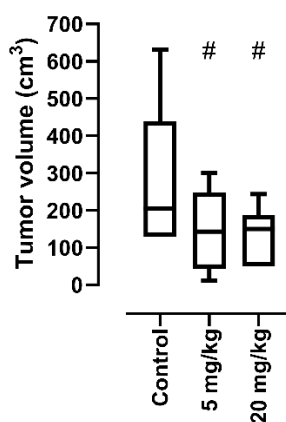


Fig.21 Impact of compound **19** on the 4T1 (mouse breast cancer cell line) tumor progression in a BALB/c mouse orthotopic model using two different doses, 5 and 20 mg/kg, applied once daily via i.p. route. Compound **19** was applied on days 6-10, 13-17 and day 20, whereby day 0 was the inoculation day. The mice were dissected on day 21, and the tumor volumes were measured using a caliper. # p < 0.1 compared to the untreated control group.

3.4. Histopathological observations indicate high safety margin of compound 19

Along with the aforementioned efficacy study, tissue samples of the 4T1 breast tumors, kidneys, livers and spleens were taken from all mice and analyzed histopathologically (Fig.22). Necrotic sections were present in all tumor tissue samples including the samples of the control group, except one sample treated with 20 mg/kg of compound 19. In that specific animal, the tumor volume was the lowest in the group and stayed without a necrotic core. The extent of necrosis was variable, ranging from the absence of necrosis to around 85% of tumor tissue being necrotic in the cross-section. However, in comparison to the control group, a higher extent of necrosis was found in treated animals. Kidneys from the control group showed no changes. Furthermore, some additional parameters were observed to be slightly changed in both dosing groups. Those changes were represented by the presence of tubular protein casts, foci of periglomerular fibroblastic proliferation, and paucicellular interstitial medullary lymphocytic infiltrates. Extramedullary hematopoiesis was present in all samples of liver and spleen tissues, independent of vehicle or compound treatment, as it is described in the same tumor model by Tao et al. 2008,²⁰⁴ postulating that the induction of hematopoiesis in the liver and spleen was induced rather by the tumor cells themselves, than by the treatment. Hematopoietic cells in the liver were present in small groups within liver sinusoids. The spleen's red pulp was occupied by hematopoietic cells, with easily visible megakaryocytes. In conclusion, histopathological inspections showed that compound 19 treatments did not cause significant morphological changes in the kidney, spleen and liver tissue when compared to the control group, indicating the absence of substantial acute tissue toxicity.

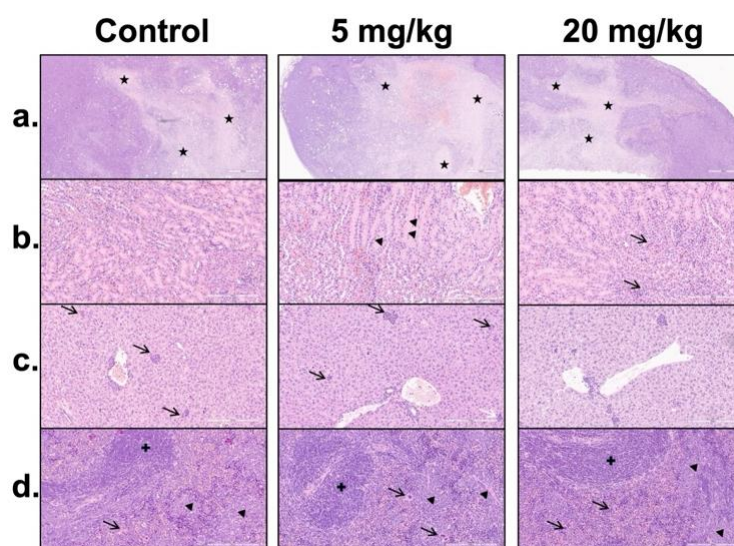


Fig.22 Histopathological assessment. BALB/c mice were inoculated with 4T1 cells at day 0, eight animals per group were treated with vehicle, 5 mg/kg or 20 mg/kg. The dissection and the organ isolation were performed on day 21. **a.** Tumor tissues with necrotic areas (black stars) (H/E stain, 40 \times). **b.** Kidney tissues with intratubular protein casts (black arrowheads) and lymphocytes in interstitial space (black arrows) (H/E stain, 200 \times). **c.** Liver tissues with intrasinusoidal extramedullary hematopoiesis (black arrows) (H/E stain, 200 \times). **d.** Extramedullary hematopoiesis with megakaryocytes (black arrows) and hematopoietic cells (black arrowheads) in the red pulp of spleen (white pulp is labeled with black cross) (H/E stain, 200 \times).

4. Discussion

In this study, the biological effects of several derivatives of 2-(phenylamino)quinazolin-4-one (Fig.23, parent compound **15**) on various breast cancer cell lines were extensively studied. Out of initially 49 screened compounds, five hits (**19**, **22**, **24**, **46** and **47**) caused $\geq 50\%$ reduction of cell viability after 72 h of treatment, recognizing them as bioactive compounds based on the National Cancer Institute guidelines,²⁰⁵ as they possess IC_{50} values $< 30 \mu\text{g/mL}$. All these compounds contain nitro- or amino-substituents at the aromatic benzene rings, however, the nitro compounds are the more active ones with similar IC_{50} values in their group, interestingly, independent of the positioning of the nitro group. Compound **19** was slightly more active against most of the breast cancer cell lines under investigation, especially against BT-474 with an IC_{50} of $4 \mu\text{M}$.

Several structural features have been noticed to contribute to the cytotoxicity of quinazolinones. The core structure without any modifications did not show any cytotoxic effect against the breast cancer cell lines up to $50 \mu\text{M}$ (compound **15**, Fig.S4, Fig.S5). However, substituents at the core structure (compounds **19**, **22**, **24**, **46** and **47**), drastically increased its cytotoxicity. The impact of the nitro group (compounds **46** and **47**) becomes obvious when compared with the respective amino group derivatives (compounds **48** and **49**), which completely lack cytotoxic activity. This is of importance since aromatic nitro groups ("nitroarenes") are considered metabolically unstable, being prone to be reduced in their various stages down to amino groups.^{206,207} However, in medicinal chemistry they also constitute an isostere and substitute for carboxylate in hydrogen bridging, but with the difference of being strongly electron-withdrawing to the aromatic core. Also, aromatic amines play a dual role, being indispensable moieties in some drugs while being suspicious of causing cancer in other compounds (hair dye aniline derivatives, for instance), depending on the compound structure and application context.^{208–210}

Contrarily, the exact position of the nitro group seems to have insignificant effect on the molecule's anti-proliferative activity. This might be seen as an indication that its physicochemical (electron-withdrawing) properties are most relevant, while a function as a hydrogen bridge acceptor would be expected to require explicit regioselectivity. Importantly, compound **22**, lacking a nitro group, is cytotoxic as well, albeit 2-fold less than compound **19** (Fig.23). This can be discussed as another indication is that the electron-withdrawing effect on the core 2-(phenylamino)quinazolin-4-one is crucial for cytotoxic efficacy, not the nitro group as such. However, compound **24**, decoupled from the core, shows a similar effect as **22**.

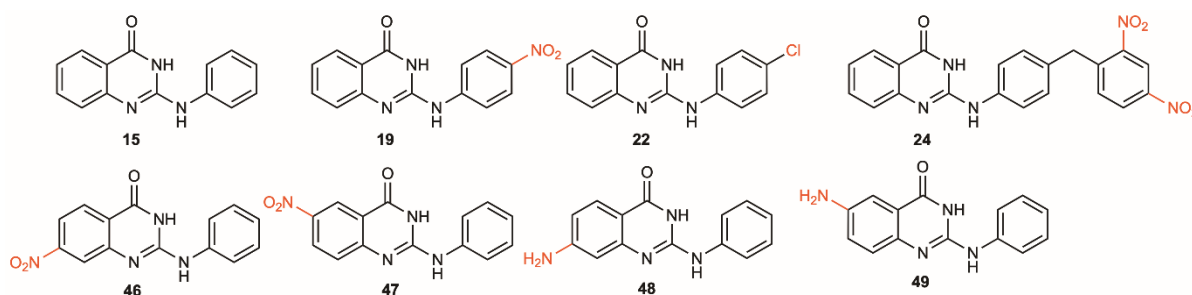


Fig.23 Structures of compound **15** (2-(phenylamino)quinazolin-4-one, 9-azaglycophymine) and the anti-proliferative compounds **19**, **22**, **24**, **46**, **47**, **48** and **49**. The complete set of compounds **1** – **49** is to be found in Table S6.

Compound **19** showed the strongest anti-proliferative and cytotoxic activity. It caused a cell viability reduction in BT-474 cells by 50% after 72 h treatment at a concentration of $4.0 \mu\text{M}$. Hence, **19** was selected for more detailed studies to determine its mode of action. Indeed, compound **19** triggered various cell-specific responses. In BT-474, HCC1937 and 4T1 cells it caused caspase-dependent apoptosis (Fig.20, Fig.S6).²¹¹ This process culminates in the cleavage of chromosomal DNA into oligonucleosomal fragments which explains the accumulation of the hypodiploid cells in the sub-G1 phase in the cell cycle assay (Fig.20, Fig.S12).²¹² It is indicative that in all three cell lines mentioned above, enhanced production of NO was orchestrated with diminished ROS generation. One of the

possible explanations for this is the fact that in the membrane of these cells, NADPH oxidase (NOX) complexes can actively produce moderate quantities of superoxide anions and provoke tumor progression. NO generated in response to the treatment inhibits their activity, preventing superoxide anion release, thus liberating caspase-3 from O₂-mediated suppression, resulting in the completion of the apoptotic process. Consequently, ROS accumulation was disrupted, leading to a ROS-deficient environment that is not stimulative for tumor cell metabolism and proliferation.²⁰³ Contrarily, in the case of MCF-7 and MDA-MB-468, caspase-dependent apoptosis had to be excluded as a potential cause for the observed cell death since compound **19** did neither activate pan-caspases nor apoptotic cell death in these cell lines. Since it was previously described that caspase-3 deficient MCF-7 cells²¹³ usually undergo necroptosis,²⁴ this special cell death process could be an explanation for compound **19**'s effect on this cell line. Contrarily to the other investigated breast cancer cell lines, MDA-MB-468 is characterized by a tremendous expression of EGFR.^{214,215} As the use of gefitinib was described to induce cancer cell death by activation of caspases-independent pathways in EGFR-expressing cells,²¹⁶ one can thus hypothesize that the structurally similar compound **19** might act similarly, however this requires further testing to prove that the compound acts through the modulation EGFR activity.

The 4T1 cell line is an established animal model for stage IV human triple-negative breast cancer derived from BALB/c mice, known for its high invasiveness and tumorigenicity.²¹⁷ 4T1 cells are challenging as they can metastasize to various locations such as bone, liver, or lung. Since compound **19** had an *in vitro* IC₅₀ of 12.6 μM (Fig.19, Table 2), it was tested *in vivo* with two different doses of 5 and 20 mg/kg against the syngeneic and orthotopic 4T1 cell line-based BALB/c mouse model. At the lower concentration, compound **19** provoked a 30% reduction in the tumor volume (Fig.21) compared to the control group. Interestingly, the higher dosage of 20 mg/kg did not further increase the compound's effectiveness indicating that the effective therapeutic dose has been reached already with 5 mg/kg, or secondary factors, like bioavailability or ADME effects limited the *in vivo* effect of the higher dosage. Histopathological analysis revealed massive necrosis within the tumor mass after treatment. The observed effect was associated with a reduced tumor volume, indicated by its positive involvement in therapy-induced tissue damage. The role of necrosis in tumor progression and its role in response to therapy is highly controversial.²¹⁸ Many authors have shown that the presence of central necrosis is a poor prognostic marker in numerous tumor types.²¹⁹ However, numerous contradictory data are available, about the meaning of the presence of necrotic areas in breast tumor tissue mainly due to its heterogeneity. They range from a strong correlation between the presence of necrosis and tumor grade, aggressiveness, and unfavorable outcomes, indicating that even centrally necrotizing breast cancer should be classified as a new type, to those showing that there was no association between necrosis and tumor progression and prognosis.^{220,221} In addition, several studies have revealed necrosis as an important pathological predictive factor for therapy response.²²² Given that cancer cells develop numerous mechanisms to avoid the induction of cell death in the first instance of apoptosis, there has been great interest in recent years for agents able to initiate regulated forms of necrosis. In general, spontaneous vs. drug-induced necrotic changes often have the opposite effect on tumor progression and disease outcome.²¹⁸ In this context, the relevance of our finding of increased tumor necrosis after treatment remains unclear and should be a matter of future investigations.

Apart from the obvious antitumor effect, no systemic toxicity of the treatment was observed based on the biochemical, behavioral, and external appearance of the animals. Furthermore, minor histopathological changes, dominantly in the kidney, from the histopathologist's view were rather related to the tumors' influence and not to compound **19**'s treatment, which did not significantly damage the non-tumor tissues. However, the absence of apparent morphological changes visible by microscopy must be correlated with the functional status of the liver and kidneys to exclude ultrastructural changes that are not microscopically visible, e.g., by conducting urine sample tests. Taken together, the new experimental therapeutic 4'-nitro-9-aza-glycophymine (**19**) shows promising *in vitro* and *in vivo* efficacy against both hormone receptor- (MCF-7) and HER2/neu-positive (BT-474) cell lines but also to hormone-independent, more aggressive triple-negative breast cancer types (MDA-MB-468, HCC1937 and 4T1). Other derivatives with electron-withdrawing substituents, ideally such not being metabolically labile like the nitro group, e.g., fluorides, might result in even better azaglycophymine derivatives to be tested in the future.

5. Conclusions

The main goal of the described work was to investigate the anticancer activities of 9-azaglycophymine derivatives against various breast cancer cell lines with different genetic backgrounds, namely MCF-7, MDA-MB-468, BT-474 and HCC1937, as well as the mouse 4T1 cell line. 49 compounds were initially screened for their cytotoxicity, whereof the compounds **19**, **22**, **24**, **46** and **47** were active below 10 μM concentration. The IC_{50} values of these hit compounds were subsequently determined ranging from 3.9 to 14 μM . Whereby, compound **19** permitted the highest anti-proliferative effects against most of the investigated human breast cancer cell lines with a most active IC_{50} of 4 μM against HER2/neu-positive BT-474 cells. **19** induced caspase-dependent apoptosis in BT-474, 4T1 and HCC1937 cells. Contrarily, the compound caused its cytotoxic effect in MCF-7 and MDA-MB-468 cells without engagement of any of the investigated cell death processes, indicating that cell line-specific characteristics seem to define different mode of actions for compound **19**'s action. An *in vivo* i.p. dosage of only 5 mg/kg significantly reduced the 4T1 breast tumor growth in BALB/c mice. Moreover, a further increase of the compound's dosage (20 mg/kg) did not show additional improvement in the antitumor effect, indicating that the therapeutically effective dose was already reached with 5 mg/kg (or below). The impact of the pattern of the side chains attached to the 9-azaglycophymine core on the biological activity, i.e., a rudimentary structure-activity relationship, was studied and several structural features were found to be essential for activity. Neither the absence of substitution nor the presence of electron-donating substitution resulted in cytotoxic derivatives within the scope of this study. However, the introduction of an electron-withdrawing chloro or especially nitro group renders the 9-azaglycophymine derivatives cytotoxic, interestingly without clear relevance to the positioning of the nitro group. Compound **19**, harboring it at the para ($4'$ -) position of the phenyl group, showed the lowest IC_{50} value. Based on the positive results, further structural optimizations of 9-azaglycophymine derivatives, ideally avoiding the potential deficits that aromatic nitro compounds can (but not necessarily) have *in vivo*, deserve further evaluation. As a conclusion, the study highlights that azaglycophymines, in light of these results, a very promising scaffold for advanced drug R&D in future studies.

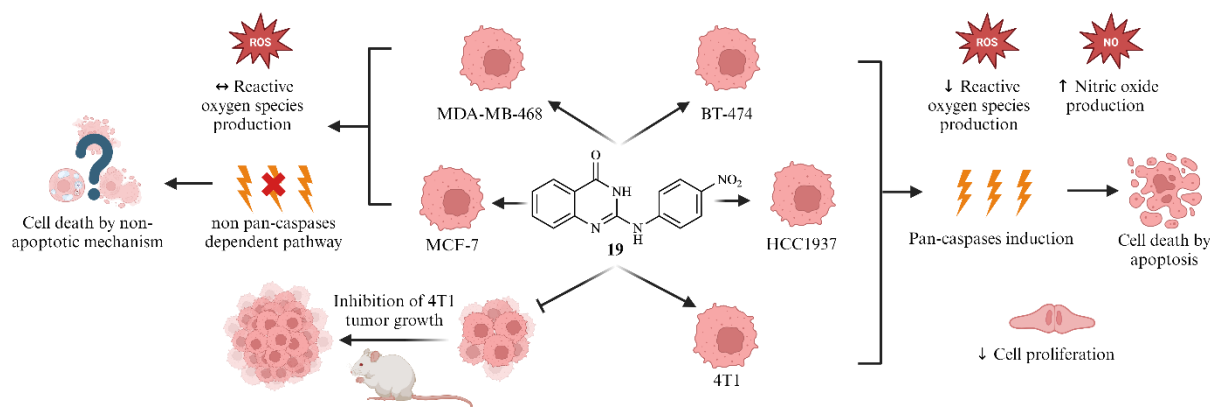


Fig.24 Illustrative chart summarizing the influence of compound **19** on various investigated breast cancer cell lines and outlining the mode of cell death induced by the respective compounds in these cells. The figure was created by using BioRender.com.

Author Contributions: The individual authors' contributions to the presented work are as follows: conceptualization: Ludger A. Wessjohann and Robert Rennert; methodology: Ibrahim Morgan, Robert Rennert, Ludger A. Wessjohann, Danijela Maksimović-Ivanić, Sanja Mijatović, Goran N. Kaluđerović; compound synthesis: Robert Berger; *in vivo* assay: Ibrahim Morgan, Sanja Jelača. Histopathology: Duško Dunderović; software: Ibrahim Morgan; resources: Ludger A. Wessjohann; data curation: Ibrahim Morgan; writing – original draft preparation: Ibrahim Morgan; review and editing: Robert Rennert, Ludger A. Wessjohann, Goran N. Kaluđerović; supervision: Robert Rennert, Danijela Maksimović-Ivanić, Sanja Mijatović, Ludger A. Wessjohann (main); project administration: Ludger A. Wessjohann; funding acquisition: Ludger A. Wessjohann, Sanja Mijatović, Danijela Maksimović-Ivanić. A manuscript submission is in progress.

Chapter 4 : Discovery of a highly selective molecule against triple-negative breast cancer and characterization of its mode of action

Abstract: From the compound collection of the Leibniz Institute of Plant Biochemistry, a compound emerged that is highly selective against the triple-negative cell line MDA-MB-468 with an $IC_{50} = 0.22 \mu M$. Consequently, this compound, 4-oxo-*N*,1-diphenyl-1,4-dihydropyridazine-3-carboxamide (named selectAHRyl A), was tested in more detail against numerous human cancer and non-cancer cell lines. The compound did not impact the cells' viability and proliferation of most tested cell lines, including healthy breast cell lines, even at high micromolar concentrations. To determine the mode of selectivity of selectAHRyl A, several methodologies were utilized, e.g., transcriptome and proteome analyses of different cell lines upon treatment. The results showed that the compound's selectivity was based on its agonistic effect on the AHR pathway acting as a cellular gatekeeper mechanism, which was confirmed by using synergistic assays, immunofluorescent microscopy, transcriptomics and RT-qPCR.

1. Introduction

According to the International Agency for Research on Cancer, cancer was recognized as the leading cause of death worldwide in 2020, attributing to around 10 million cancer-related deaths, and 19.3 million newly diagnosed cancer cases.⁹⁴ The most frequent cancer type in female patients is breast cancer contributing 11.7% of all newly diagnosed female cancers. Breast cancers are classified into different tumor types, either based on their location or based on the type of receptor proteins expressed by the cancer cells. These classifications strongly influence the treatment regimen and its prognoses. Based on the expression of several surface receptors, tumors can be classified either into hormone receptors-positive (HR⁺), HER2/neu-positive (HER⁺) or triple-negative (TNBC) breast cancers.²²³ The most aggressive type of breast cancers are the so-called triple-negative breast cancers (TNBC). Such tumors lack the high expression level of both HR and HER2/neu receptors, making it very challenging to specifically target these cancer cells. This results in the lowest 4-year survival rates (77%) compared to the other breast cancer types.⁹⁵ Therefore, nowadays several new strategies are being extensively studied to unveil new treatment options especially for the TNBC type, for instance, poly(ADP-ribose) polymerase inhibitors, such as olaparib, or programmed death-ligand 1 (PD-L1) blockers like atezolizumab. However, the therapeutic performance of those options is still not satisfying, that is why there is still a great need and research interest in novel and better therapy options for TNBCs.^{176,177}

One of the novel and emerging therapies for targeting several types of cancer, specifically TNBC, is AHR (aryl hydrocarbon receptor) modulators. These are compounds that impact the activity of AHR protein that plays an essential role in the cellular response against environmental pollutants. The AHR activates the transcription of several genes involved in elimination of toxic agents including halogenated aromatic hydrocarbons, polyaromatic compounds, flavonoids, indoles and dioxin like compounds.²²⁴ However, this pathway was also found to modulate the activity of synthetic compounds by their chemical modification. This modulation could either promote an activation of procarcinogens as in the case of benzo[a]pyrene and 2-amino-1-methyl-6-phenylimidazo[4,5-b]pyridine or prodrugs like eupatorine and diindolylmethane.^{225,226} These prodrugs were found to be selectively activated in TNBC, specifically MDA-MB-468 cell line with high selectivity margin due to their low effect against non-malignant cell lines such as MCF10A. This data indicates the potential of this class of compounds owing to their potency and selectivity against cancer cells.

The department of Bioorganic Chemistry of the Leibniz Institute of Plant Biochemistry is dedicated to and specialized in extraction, purification as well as analytical and biological characterization of natural products (NP) from plants and fungi. Accordingly, a wide-ranging compound library, consisting of approximately around 30,000 samples, primarily NPs and (semi)synthetic NP derivatives as well as natural extracts, is available for bioactivity screenings.²²⁷ The study started by screening this compound library for promising novel substances exhibiting anti-proliferative and cytotoxic effects against human breast cancer cell lines. During the screening process, selectAHRyl A was identified with an outstanding selectivity against the TNBC cell line MDA-MB-468. Therefore, a study was initiated to understand and clarify the cellular mechanism explaining this selectivity. For that purpose, different types of breast cell lines as well as non-tumorigenic healthy cell lines were analyzed.

2. Materials and methods

2.1. Chemicals, reagents and kits

DMEM high glucose (4.5 g/L), McCoy's 5a Medium Modified, MEM with Earle's Salts, RPMI1640, L-glutamine (200 mM), penicillin (10⁷ Units/L)/streptomycin (10 g/L), 0.05% trypsin-EDTA, Phosphate Buffered Saline (PBS) and fetal calf serum (FCS) were purchased from Capricorn Scientific GmbH (Ebsdorfergrund, Germany), while Endopan 3 medium kit was from PAN-Biotech (Aidenbach, Germany). Zeocin, Quanti-Luc-Gold and HepG2-AhR-Lucia reporter cells were purchased from Invivogen (Toulouse, France). Digitonin was supplied by Riedel De Haën (Seelze, Germany) and dimethyl sulfoxide (DMSO) from Duchefa Biochemie (Haarlem, The Netherlands). Liver microsomes containing CYP1A1, crystal violet (CV), resazurin, acridine orange (AO), triton X-100, tween-20, glucose-6-phosphate, β -nicotinamide adenine dinucleotide phosphate disodium salt (NADP⁺), and glycine were bought from Sigma-Aldrich (St. Louis, MO, USA). Matrigel Growth

Factor-reduced Basement Membrane Matrix (Phenol Red-free, LDEV-free) was obtained from Corning (Corning, NY, USA). Paraformaldehyde (PFA), agarose, bovine serum albumin (BSA) and acetic acid were supplied by Carl Roth (Karlsruhe, Germany). LC-MS grade ethanol and dipotassium hydrogen phosphate trihydrate were from Merck (Darmstadt, Germany). While potassium dihydrogen phosphate and LC-MS grade formic acid (FA) was bought from Fluka Chemie (Buchs, Switzerland). 4,6-diamidino-2-phenylindole (DAPI) and glucose-6-phosphate dehydrogenase were purchased from Roche (Basel, Switzerland), annexin V/propidium iodide (AnnV/PI), prolong diamond antifade, RevertAid RT Reverse transcription kit, goat anti-rabbit IgG (H+L) highly cross-adsorbed secondary antibody, and Alexa Fluor™ Plus 488 were purchased from Thermo Fisher Scientific (Waltham, MA, USA). AhR (D5S6H) rabbit mAb was bought from Cell Signaling Technology (Danvers, MA, USA). FICZ, CH-223191 and bergamottin were purchased from Hycultec (Beutelsbach, Germany). Carboxyfluorescein succinimidyl ester (CFSE) and dihydrorhodamine 123 (DHR) were from BD Horizon (Franklin Lakes, NJ, USA). 4-amino-5-methylamino-2',7'-difluorofluorescein diacetate (DAF-FM) was bought from Cayman Chemical (Ann Arbor, MI, USA), and ApoStat was supplied by R&D Systems (Minneapolis, MN, USA). Serva lightning scidye was from Serva Electrophoresis GmbH (Heidelberg, Germany) and Coomassie brilliant blue G-250 was bought from AppliChem GmbH (Darmstadt, Germany). LC-MS grade ethyl acetate, acetonitrile (ACN) and methanol were obtained from Honeywell (Charlotte, NC, USA). The RNA miniprep kit was acquired from Zymo Research (Irvine, CA, USA), and GreenMaster from Jena Bioscience (Jena, Germany). SPE columns (CHROMABOND C18 ec, 45 µm, 1 mL/100 mg) were obtained from Macherey-Nagel (Düren, Germany). All primers were acquired from Eurofins Genomics (Ebersberg, Germany).

2.2. Cell lines and cell culture

SelectAHRyl A was tested against several types of human cell lines including breast cancer cell lines (MCF-7, T-47D, MDA-MB-468, BT-474, MDA-MB-231, HCC1937 and SK-BR-3), colon cancer cell lines (HCT116, HT-29 and Caco-2), prostate cancer cell line (PC3), hepatocarcinoma (HepG2), cervical cancer cell line (HeLa), Ewing's sarcoma (SK-N-MC, SK-ES-1, CAD0-ES-1 and MHH-ES-1), lung adenocarcinoma (HCC827), leukemia cell lines (HEL, Kasumi-1, THP-1, K562 and MV4-11), human embryonic kidney cell line (HEK293) and non-malignant (fibrocystic) breast cell lines (184B5, MCF10A). All human cell lines used were obtained from DSMZ (Braunschweig, Germany) and ATCC (Manassas, VA, USA). Cell culture and other lab plastics were purchased from TPP (Trasadingen, Switzerland), Greiner Bio-One (Frickenhäusen, Germany), Sarstedt (Nürnbrecht, Germany) and Corning (Corning, NY, USA). MDA-MB-468 and SK-BR-3 cells were grown in DMEM supplemented with 4.5 g/L of glucose and 10% (v/v) heat-inactivated FCS. SK-N-MC was cultivated using MEM with Earle's Salts supplemented with 10% (v/v) heat-inactivated FCS and 1% (v/v) penicillin/streptomycin. 184B5 and MCF10A were grown in Endopan 3 medium kit as indicated by the manufacturer's guidelines. The HCT116 cell line was cultivated in McCoy's 5a Medium Modified supplemented with 10% (v/v) heat-inactivated FCS. All other cell lines were grown in RPMI 1640 supplemented with 1% (v/v) glutamine, 1% (v/v) penicillin/streptomycin and 10% (v/v) heat-inactivated FCS. HepG2-AHR-Lucia reporter cells were cultured in complete RPMI 1640 culture medium additionally supplemented with 100 µg/mL zeocin; for experiments, the same medium without antibiotics was used. The cell lines were cultivated in a humidified atmosphere at 37°C and 5% CO₂ (standard growth conditions).

2.3. Cell viability

For 2D cultures, cells were seeded in 96-well plates using different cell densities which is based on the growth properties of the distinct cell lines. For leukemia cell lines, 2×10^4 cells/100 µL were seeded in each well. For the other cell lines, 6×10^3 /100 µL were seeded in each well.²²⁸ The cells were incubated for 24 h under standard growth conditions. Afterwards, 100 µL of 2× desired concentration were added to each well to reach the desired 1× test concentration, and cells were treated for 72 h under standard growth conditions. After incubation, cell viability was determined using CV in case of adherent cells and resazurin assay for suspension cells. Moreover, the mentioned protocol was also followed to determine the cytotoxicity of the hydroxylated derivatives of selectAHRyl A.

Synergistic assays were performed with three different breast cell lines: MDA-MB-468, SK-BR-3 and 184B5. CH-223191 (AHR inhibitor) and bergamottin (CYP inhibitor) as reference compounds were used. Where selectAHRyl A was tested at various concentrations against the selected cell lines for 72 hours, in combination with each reference compound in separate experiments, each at 12 μ M. Cell viability was then determined using a CV assay.

The effect of selectAHRyl A against MDA-MB-468 3D spheroids was studied as well. For that purpose, MDA-MB-468 cells were seeded in a density of 5×10^3 cells/80 μ L/well in spheroid medium (DMEM supplemented with 4.5 g/L of glucose, 10% v/v heat-inactivated FCS and 3% v/v matrigel) using ultra-low adhesion 96-well plates. Afterwards, plates were centrifuged for 10 min and incubated under standard growth conditions. After incubation for 48 h, 80 μ L of $2 \times$ desired concentration were added to each well to reach the desired $1 \times$ test concentration, and cells were treated for 72 or 120 h under standard growth conditions. Finally, the cell viability was determined by using the resazurin assay.²²⁹

Besides the read-out of the MDA-MB-468 spheroid assays, the resazurin assay was also used for all leukemia suspension cell lines. For leukemia cell lines, 50 μ L, and for MDA-MB-468 spheroids, 40 μ L of $5 \times$ resazurin working solution were added to each well to reach a final concentration of 50 μ M. The cells were incubated for 2 h, and fluorescence from the conversion of resazurin to resorufin by viable cells ($exc/em = 545/595$ nm) was measured using a SpectraMax iD5 plate reader (Molecular Devices, San Jose, CA, USA).²³⁰

For all other adherent cell lines, the viability determination was performed by using the CV assay. For that purpose, the incubation medium was discarded and cells were washed once with PBS. Afterwards, the cells were fixed using 50 μ L/well of 4% PFA (w/v) in PBS for 15 min. Then the solution was discarded and the plates were dried at RT for 15 min followed by staining with 50 μ L/well of CV working solution (0.1% CV w/v in PBS) for 15 min. The staining solution was discarded, plates were washed with ddH₂O and dried overnight at RT. Finally, 50 μ L/well of 33% (v/v) acetic acid were used to solubilize the stain, and the absorbance of the plates was measured at wavelengths of 570 nm and 670 nm for the determination of the background by using a SpectraMax iD5 plate reader.²³¹

Finally, the cell viability was calculated and normalized. Where the read-outs of untreated cells were considered to represent 100% viability and those of cells treated with 125 μ M of the cytotoxic saponin digitonin as 0% viability.

2.4. Flow cytometry analyses

2.4.1. Cell cycle, apoptosis, autophagy and pan-caspases induction analyses

MDA-MB-468 cells were seeded in 6-well plates with a density of 1.5×10^5 /1 mL and allowed to adhere for 24 h under standard growth conditions. Afterwards, the cells were treated with 1 mL of selectAHRyl A at its IC₅₀ for 72 h and incubated under standard growth conditions (37°C and 5% CO₂). Upon completion of the treatment period, the incubation medium was collected from the wells, cells were detached using 0.05% trypsin-EDTA and combined with the previously collected medium. The cell suspension was centrifuged (3 min, 800 rpm, RT), the supernatant was discarded and the cells were washed using 300 μ L of PBS.

For the cell cycle analyses, cells were fixed by adding 700 μ L of ice-cold 96% ethanol and incubating for at least 24 h at 4°C. Subsequently, the cells were centrifuged (3 min, 800 rpm, RT), the supernatant was discarded, and the cells were stained with 1 mL of DAPI staining solution (1 μ g/mL of DAPI in PBS) for 10 min at RT.^{152,232}

Apoptosis assays were performed as indicated by the manufacturer's guidelines. Briefly, the cell suspension was centrifuged (3 min, 800 rpm, RT). The supernatant was discarded, and the cells were washed twice using PBS. Afterwards, the cells were stained by resuspending in 100 μ L of AnnV/PI working solution (5 μ L of AnnV and 2 μ L of PI in 100 μ L of PBS) for 15 min at RT. The staining process was deactivated by the addition of 900 μ L of annexin binding buffer.²³³

For autophagy induction assays, the cell suspension was centrifuged (3 min, 800 rpm, RT), then the cells were washed once with PBS, and stained in 1 mL of AO working solution (1 $\mu\text{g}/\text{mL}$ of AO in complete medium) for 15 min at 37°C and 5% CO_2 . After staining, the cell suspension was centrifuged (3 min, 800 rpm, RT), cells were washed once with and finally resuspended in PBS.²³⁴

For examinations regarding the induction of pan-caspases' activation, the cell suspension was centrifuged (3 min, 800 rpm, RT), the supernatant was discarded, and the cells were washed once with PBS. Then, the cells were stained in 100 μL of ApoStat working solution (1 μL of ApoStat, 5% FCS in 100 μL of PBS) for 30 min at 37°C and 5% CO_2 . After deactivation of the stain by adding 900 μL of PBS, cells were centrifuged (3 min, 800 rpm, RT), and the supernatant was replaced by fresh PBS.

2.4.2. Cell division and ROS/RNS production analyses

The cells were stained for 10 minutes with 1 mL of either 1 μM of CFSE or DHR in PBS containing 0.1% (v/v) heat-inactivated FCS for cell division analysis or ROS/RNS production analysis, respectively. Afterwards, the cells were washed with PBS then resuspended in complete medium. Subsequently, the cells were seeded with a density of $1.5 \times 10^5/1$ mL in a 6-well plate and incubated for 24 h under standard growth conditions. These cells were treated with 1 mL of selectAHRyl A at its IC_{50} and incubated for 72 h under standard growth conditions. Finally, the cells were detached by using 0.05% trypsin-EDTA, centrifuged (3 min, 800 rpm, RT), the supernatant was discarded and the cells were washed once with and resuspended in 1 mL of PBS.^{151,235}

2.4.3. Analyses of nitric oxide production

To assay NO production, cells were seeded in 6-well plates with a density of $1.5 \times 10^5/1$ mL and allowed to adhere for 24 h under standard growth conditions. Afterwards, the cells were treated with 1 mL of selectAHRyl A at its IC_{50} and incubated for 72 h under standard growth conditions. Subsequently, the incubation medium was discarded, and the cells were washed once using PBS. The cells were stained by 1 mL of 5 μM DAF-FM in RPMI 1640 with 10% (v/v) heat-inactivated FCS and incubated for 1 h under standard growth conditions. Afterwards, the cells were incubated in 1 mL of serum free medium for 15 min to deactivate the stain. Finally, the stained cells were detached by using 0.05% trypsin-EDTA, centrifuged, the supernatant was discarded, and the cells were washed once and resuspended in PBS.

For flow cytometric read-out, all the aforementioned samples (section 2.4) were analyzed by using a FACSAria III device (BD Biosciences, Franklin Lakes, NJ, USA).²³⁶

2.5. Proteome analyses

MDA-MB-468 cells were seeded in T175 flasks and treated at either IC_{20} or IC_{50} for different time intervals (6, 24 and 48 h). As a negative control untreated cells representing 0 h were included. After completion of the treatment, the cells' proteins were isolated and labeled as recommended by the manufacturer's guideline for the usage of the SERVA Lightning SciDye Set. Briefly, 25 μg of the isolated proteins were labeled using 200 pmol of either Sci3 or Sci5 dye. 30 μg of internal protein standard consisting of a mixture of proteins pooled from all samples were labeled using 200 pmol of Sci2 dye. The proteins were separated in the 1st dimension by isoelectric focusing by using Immobiline DryStrips pH 3–10 NL (GE Healthcare, Chicago, IL, USA), and afterwards in the 2nd dimension SDS-PAGE separation was performed as previously described.¹⁴⁹ After protein separation, the gels were washed with ddH_2O and fixed by incubation in fixing solution (10% v/v acetic acid and 40% v/v methanol in ddH_2O) for 45 min, followed by another washing step with ddH_2O . Finally, the gels were scanned by using a Fujifilm FLA-5100 laser scanner (FUJIFILM Europe GmbH, Ratingen, Germany). The gel images were processed using the Delta2D software (Decodon GmbH, Greifswald, Germany). Those proteins with expression levels altered upon treatment by more than 1.5 fold were marked as hits for identification.¹⁴⁹

For that purpose, a preparative gel was prepared similarly to the analytical gel, however, the preparative gel was loaded with 500 μg of the protein mixture and gel staining was done with Coomassie blue stain as previously mentioned.²³⁷ The visible spots of the proteins marked for identification were picked by using GelPal Genetix and were placed on 96-well elution plates. Afterwards, the isolated

spots were processed automatically by using a DigestPro device (Intavis, Cologne, Germany), i.e., the isolated spots were destained, in-gel digested, purified using ZipTips (C18, Merck Millipore) and transferred to a MALDI target plate (MTP-384 ground steel, Bruker Daltonics Inc., Bremen, Germany). An ultrafleXtremeTM mass spectrometer (Bruker Daltonics Inc., Billerica, MA, USA) was used for the analyses of the data obtained from TOF-MS measurements in which Bruker's peptide calibration standard II (Bruker Daltonics Inc., Billerica, MA, USA) was used for the calibration of the obtained spectra. The masses of the examined peptides were compared to theoretical values obtained from the Matrix/Mascot database (Bruker Daltonics Inc., Billerica, MA, USA) using the Biotoools 3.2 software (Bruker Daltonics Inc., Billerica, MA, USA). Finally, the Molecular Weight Search (MOWSE) score was calculated by the software for each protein. A MOWSE score higher than 56 represented a successful identification.²³⁸

2.6. Transcriptome analyses

10⁶ cells of either MDA-MB-468, SK-BR-3 or 184B5 cell lines were seeded in T-25 flasks and allowed to adhere for 24 h under standard growth conditions. Afterwards, the cells were treated at 100 μ M of selectAHRyl A for 6 h under same conditions. Untreated cells were included as negative control. Subsequently, RNA extraction was performed by using the quick-RNA miniprep kit (Zymo Research, Freiburg i. Br., Germany). The integrity of the isolated RNA was confirmed by using a Bioanalyzer device (Agilent, Santa Clara, CA, USA). The preparation of the RNA library and transcriptome sequencing was conducted by Novogene Co., LTD (Beijing, China). Statistical analysis and pathway enrichment were performed using R Statistical Software (version: 2022.7.1.554; R Core Team 2021). Several R packages were used for the analysis, including RCy3, rWikipathways, RColorBrewer, tidy, clusterProfiler, DOSE, AnnotationDbi, DEseq2, dplyr, gplots and ggplot2. mRNA expression data from Novogene were obtained as FPKM values that, initially, were transformed to log₂ values. Using the log₂ values, PCA plots were drawn for each cell line. Moreover, the data were used to draw a hierarchical heat map for all samples. Further, the data were filtered using an adjusted p-value. Genes with transcription levels affected by the treatment compared to the control sample and an adjusted p-value below 0.05 were considered to have altered transcriptional expression. These genes were then used for further analyses and WikiPathways enrichment using the Cytoscape software.

2.7. *In silico* AHR docking

The interaction between AHR and selectAHRyl A was studied in more detail by conducting an *in silico* study. The AHR protein structure was predicted using AlphaFold DB prediction software based on the sequence of AHR obtained from NCBI (reference sequence: NP_001612.1).^{239,240} Subsequently, the molecular modelling software package MOE (Molecular Operating Environment; Chemical Computing Group, Montreal, Canada) was used to investigate the AHR-selectAHRyl A binding. For the modelling, the predicted protein structure was used. Initially, the protein structure was prepared for the docking experiment through the addition of the missing hydrogen atoms using the 3D protonation feature from MOE. Afterwards, the binding site was determined using the site finder option from MOE. The optimal binding site was selected based on previously performed docking studies for AHR binding molecules, such as FICZ, ICZ, etc... The amino acids which were found essential for the interaction are Thr289, His291, Phe295, Phe324, Ile325, Cys333, Phe351, Leu354 and Ser365.²⁴¹ The compound was tested in five different poses and the binding energy was calculated by MOE software for each pose. The pose with the lowest energy was selected for the study. The aforementioned procedure was repeated in order to calculate the binding energy of FICZ (AHR ligand).

2.8. RT-qPCR analyses

MDA-MB-468, SK-BR-3 and 184B5 cell lines were treated with selectAHRyl A at IC₅₀ (100 μ M in case of 184B5 where no IC₅₀ was detectable) for different time intervals (2, 6, 24 and 48 h) and a negative control of untreated cells representing 0 h treatment was included. The RNA was isolated by using the quick-RNA miniprep kit (Zymo Research, Freiburg i. Br., Germany), the integrity and the concentration of the isolated RNA were determined by using agarose gel (0.5% w/v) electrophoresis and the SpectraDropTM of a SpectraMax iD5 (Molecular Devices, San Jose, CA, USA), respectively. 0.5 μ g of isolated RNA were used to synthesize the first cDNA strand by using RevertAid RT Reverse

Transcription Kit and oligo dT primers (Thermo Fisher Scientific, Waltham, MA, USA). Afterwards, qPCR analyses were performed. For that purpose, NCBI's Primer-Blast was used to design target-specific qPCR primers (Table S12) that were synthesized by and purchased from Eurofins Genomics (Ebersberg, Germany). GreenMaster mix (Jena Bioscience, Jena, Germany) was used to conduct the qPCR analyses that were carried out by using a CFX96™ Real-Time PCR Detection System (BioRad, Hercules, CA, USA). The qPCR data were analyzed by using the $\Delta\Delta C_t$ methodology with glyceraldehyde 3-phosphate dehydrogenase (GAPDH) as referencing housekeeping gene. RNA isolation, cDNA synthesis and qPCR were performed as indicated by the manufacturer's guidelines.²⁴²

2.9. Immunofluorescence imaging

MDA-MB-468 cells were seeded in 8-well chamber slides with a density of 5×10^4 cells/well and allowed to adhere for 24 h under standard growth conditions. Afterwards, cells were treated with selectAHRyl A at IC_{50} for 30 or 60 min. Untreated cells were included to represent the no treatment condition (0 h). Upon completion of the treatment period, the cells were washed once with PBS and fixed by addition of 4% (w/v) PFA in PBS solution and incubation for 10 min at RT, followed by washing intensively with ice-cold PBS. Next, cell permeabilization was achieved by applying PBS containing 0.1% (v/v) triton X-100 for 10 min, followed by intensive washing using ice-cold PBS. Then, the cells were treated for blocking with 1% (w/v) BSA and 22.52 mg/mL glycine in PBST (PBS + 0.1% v/v Tween 20) for 30 min at RT. Afterwards, the blocking solution was discarded, and the cells were incubated overnight with diluted AHR antibody (1:200) in 1% (w/v) BSA in PBST at 4°C. Subsequently, the cells were washed intensively with ice-cold PBS, followed by the incubation with the secondary antibody (1:1000) in 1% (w/v) BSA in PBST for 1 h at RT in the dark.^{243,244} Intensive washing was repeated, and cells were mounted by applying ProLong® Diamond Antifade Mountant for 24 h at RT.²⁴⁵ Finally, cells were imaged by using a LSM900 confocal laser scanning microscope (Zeiss, Oberkochen, Germany) using the Alexa fluor 488 and DAPI channels. Fiji software (NIH, Bethesda, MD, USA) was used for data analysis. The DAPI channel was used to determine the location of the nuclei, whereas the mean Alexa fluor 488 fluorescence intensity in the cytosol and nuclei representing the expression and localization of the AHR protein was measured. The sum of AHR protein in the nuclei and the cytosol was considered as 100%, and the distribution of AHR between nuclei and cytosol was calculated as a percentage.²⁴⁶

2.10. Reporter gene assays

HepG2-AHR-Lucia reporter cells were detached from plates using 0.05% trypsin/EDTA in PBS, counted and seeded in white, flat-bottom 96-well plates (Brand GmbH, Wertheim, Germany) with 2×10^5 cells/well. Cells were settled overnight in the incubator. Afterwards, cells were stimulated with 20 μ L of complete RPMI1640 culture medium without antibiotics containing selectAHRyl A at several concentrations up to 25 μ M. Compound-free and 0.2 μ M of FICZ in complete RPMI1640 culture medium without antibiotics were included as negative and positive controls, respectively. After adding the test items, the plate was agitated for 10 seconds and then incubated for 48 h under standard growth conditions in the cell incubator. For endpoint signal detection, 20 μ L of cell supernatant were transferred into a white 96-well plate, and 50 μ L of Quanti-Luc-Gold reagent were added, followed by 10 seconds agitation. Afterwards, luciferase-catalyzed luminescence signals were measured immediately in a wavelength range of 480/80 nm by using a ClarioStarPlus reader (BMG Labtech, Ortenberg, Germany).

2.11. Metabolism induction of selectAHRyl A using liver microsomes

A cell-free enzymatic assay was conducted to verify the possibility of a CYP1A1-catalyzed metabolism of selectAHRyl A. For the analysis, a reaction mixture was prepared consisting of 50 μ L of selectAHRyl A solution (100 μ M in 100 mM phosphate buffer, pH 7.4) and 50 μ L of liver microsomes containing CYP1A1 (1 pmol/ μ L). Additionally, a NADPH reaction solution containing 1 mM glucose-6-phosphate, 0.4 U/mL glucose-6-phosphate dehydrogenase, and 0.5 mM NADP⁺ in phosphate buffer (100 mM in ddH₂O, pH = 7.4) was prepared. All solutions were pre-warmed to 37°C. To initiate the enzymatic reaction, 50 μ L of the NADPH reaction solution were added to the CYP1A1 reaction mixture, which was then incubated for 30 min at 37°C. The reaction was terminated by adding 150 μ L of ethyl acetate, and the sample was centrifuged for 10 min at 12,000 rpm and 4°C. The ethyl

acetate phase was transferred to a fresh tube, and the prior extraction step with ethyl acetate was repeated to ensure the complete removal of the enzyme and salts. The resulting samples were then dried using a high stream of N₂ gas. Two control samples, compound- and enzyme-free reaction mixtures, were prepared in parallel. After drying, the samples were resuspended in acetonitrile and analyzed by using high-resolution LC-MS.^{247,248}

The high-resolution UHPLC-ESI-MS analysis employed an ACQUITY UPLC I-Class system (Waters, Eschborn, Germany) coupled online to a tandem quadrupole-time-of-flight mass spectrometer TripleTOF 6600 (AB Sciex, Darmstadt, Germany) equipped with a DuoSpray™ ion source, and operated in positive ion mode. Chromatographic separation of the samples was performed by using a Waters Acquity UPLC BEH C18 column (50 × 2.1 mm, 1.7 μm particle size; Waters, Eschborn, Germany), with eluents A and B containing 0.1% formic acid (v/v) in water and 0.1% (v/v) formic acid in acetonitrile, respectively. The column was thermostated to 50°C, and the samples were kept at 8°C throughout the analysis. The flow rate was set to 0.3 mL/min, and the separation gradient was applied as follows: 5% of eluent B in A for 1 min, followed by a gradient from 5% of B to 95% of B over 9 min, an isocratic step at 95% of B for 3 min, and then back to 5% of B over 1 min, followed by re-equilibration at 3% of B for 5 min. Injection was performed in partial loop mode with an injection volume of 2 μL. Conditions and settings used are summarized in Table S13 and Table S14. Data were acquired in a m/z range of 50 – 1000, for ions with m/z 308, 324 and 292 a series of targeted MS/MS experiments was performed with collision energies of 15, 20, 25, 35, 45 and 55 V. The instruments were operated under the control of the Analyst TF 1.7.1 software, whereas PeakView™ version 2.2 (both AB Sciex, Darmstadt, Germany) was used for LC-MS data processing.

2.12. Synthesis of mono-hydroxylated derivatives of selectAHRyl A and identification of the enzymatically produced derivatives

To identify the cytotoxically active form of selectAHRyl A, several of its mono-hydroxylated derivatives were synthesized. The syntheses and the structure confirmations were performed by Dr. Tuvshinjargal Budragchaa and Julius Steidele. The retention times of the synthetically obtained mono-hydroxylated derivatives were determined by using analytical RP18 HPLC and the derivatives with the same retention time as those gained from the liver microsomes enzymatic assay were chosen for further analyses in order to determine their cytotoxicity and selectivity. These compounds were tested against the selected breast cell lines (MDA-MB-468, SK-BR-3 and 184B5) to determine their IC₅₀ values.

The analytical RP18 HPLC analysis was performed using an Agilent 1260/1290 system (Agilent Life Sciences, Santa Clara, CA, USA) equipped with the following components: a quaternary pump (G1311A), an autosampler (G1329B), a thermostated column compartment (G1316A), a fluorescence detector (G1321A), and a diode array detector VL+ (G1315C) set at a wavelength of 280 nm. Separation was achieved using a Nucleodur 100-5 C18ec column (150 mm × 4.6 mm, 5 μm pore size, 110 Å, Macherey-Nagel, Düren, Germany). The flow rate was maintained at 0.8 mL/min, and the separation gradient was as follows: an initial gradient of 5% solvent B (0.1% (v/v) formic acid in acetonitrile) in solvent A (0.1% (v/v) formic acid in water), increased to 100% B over 15 minutes, followed by an isocratic hold at 100% B for 5 minutes, and then returned to 5% B over 1 minute. The entire system was operated using Agilent ChemStation software (Rev. C.01.05).

2.13. Statistical analysis statement

The data in this study are expressed as mean values with standard error of the mean (SEM), calculated from a minimum of three independent biological replicates, unless otherwise specified in the figure captions. Significance levels are denoted as follows: *, **, ***, and **** indicate p-values of less than 0.05, 0.01, 0.001, and 0.0001, respectively, when compared to the untreated control group. Statistical analysis was conducted by applying ordinary two-way analysis of variance (ANOVA) followed by Sidak's multiple comparisons test, utilizing GraphPad Prism software (San Diego, CA, USA).

3. Results

3.1. SelectAHRyl A causes cytotoxicity with highest selectivity for MDA-MB-468 TNBC cells

As a result of the *in vitro* cell viability assays, selectAHRyl A (Fig.25a) showed cytotoxicity of varying degrees against a broader panel of human cell lines, as illustrated in Fig.25b and Fig.S15. The compound was found to be most active against the triple-negative breast cancer (TNBC) cell line MDA-MB-468 with an absolute IC_{50} value of 0.22 μ M. Moreover, the compound caused a substantial cytotoxic effect against the cancer cell lines MCF-7, SK-BR-3 (both breast, HR⁺ and TNBC, respectively) and HepG2 (liver) as well (IC_{50} = 21.28, 5.22 and 5.53 μ M, respectively). Interestingly, the compound showed a significantly lower effect against all the other human cell lines, notably, also the non-cancerous cell lines 184B5, MCF10A (both breast, IC_{50} = 287.1 μ M and > 375 μ M, respectively) and HEK293 (embryonic kidney, IC_{50} > 375 μ M). Additionally, the compound also caused a cytotoxic and/or anti-proliferative effect in MDA-MB-468 3D spheroids after 72 h and 120 h of treatment with relative IC_{50} values of 1.02 and 0.83 μ M, respectively, as displayed in Fig.25c. The outstanding selectivity and cytotoxicity of selectAHRyl A directed us to use several targeted and untargeted methodologies including proteomics, transcriptomics and flow cytometry to investigate its biochemical mode of action.

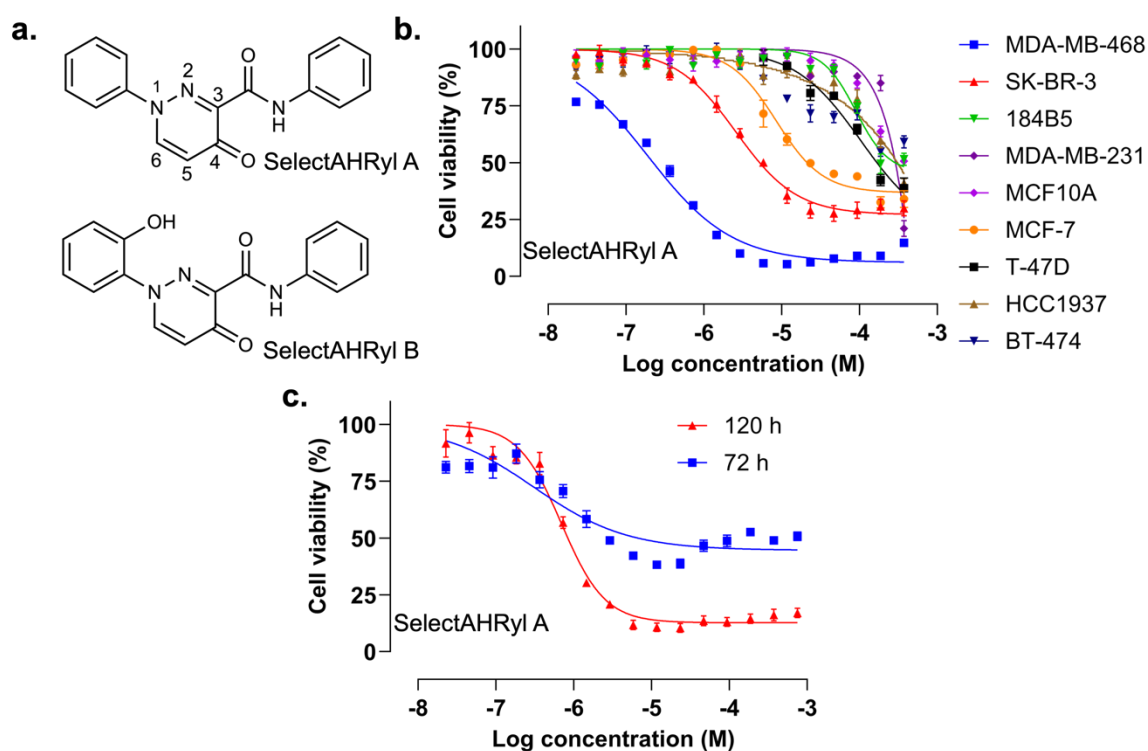


Fig.25 Compound' structures and cytotoxicity. **a**, Chemical structure of selectAHRyl A (4-oxo-*N*,1-diphenyl-1,4-dihydropyridazine-3-carboxamide) and selectAHRyl B (1-(2-hydroxyphenyl)-4-oxo-*N*-phenyl-1,4-dihydropyridazine-3-carboxamide). **b**, Dose-response curves of the viability of breast cell lines treated with selectAHRyl A for 72 h and **c**, of MDA-MB-468 3D spheroids treated for either 72 or 120 h. The data are presented as the means of at least two independent biological replicates \pm SEM.

3.2. SelectAHRyl A induces caspases-independent apoptotic cell death

The impact of selectAHRyl A on specific mechanisms in MDA-MB-468 involved in cell death was studied. The compound led to an increase of apoptotic events as illustrated in Fig.26a and Fig.S16a (control: 25.8% versus IC_{50} treatment with selectAHRyl A: 45.3%), accompanied with the accumulation of cells in the sub-G phase (control: 20.2% versus IC_{50} treatment with selectAHRyl A: 42.2%) as shown in Fig.26b and Fig.S16c. Additionally, an induction of the NO production upon treatment with selectAHRyl A was detected (Fig.26d). On the other hand, selectAHRyl A slightly decreased the

activation of pan-caspases. Furthermore, no significant impact on neither autophagy activation, cell proliferation nor ROS production was observed as illustrated in Fig.26c and Fig.26d. Corresponding histograms and dot plots of the flow cytometry raw data are summarized in Fig.S16.

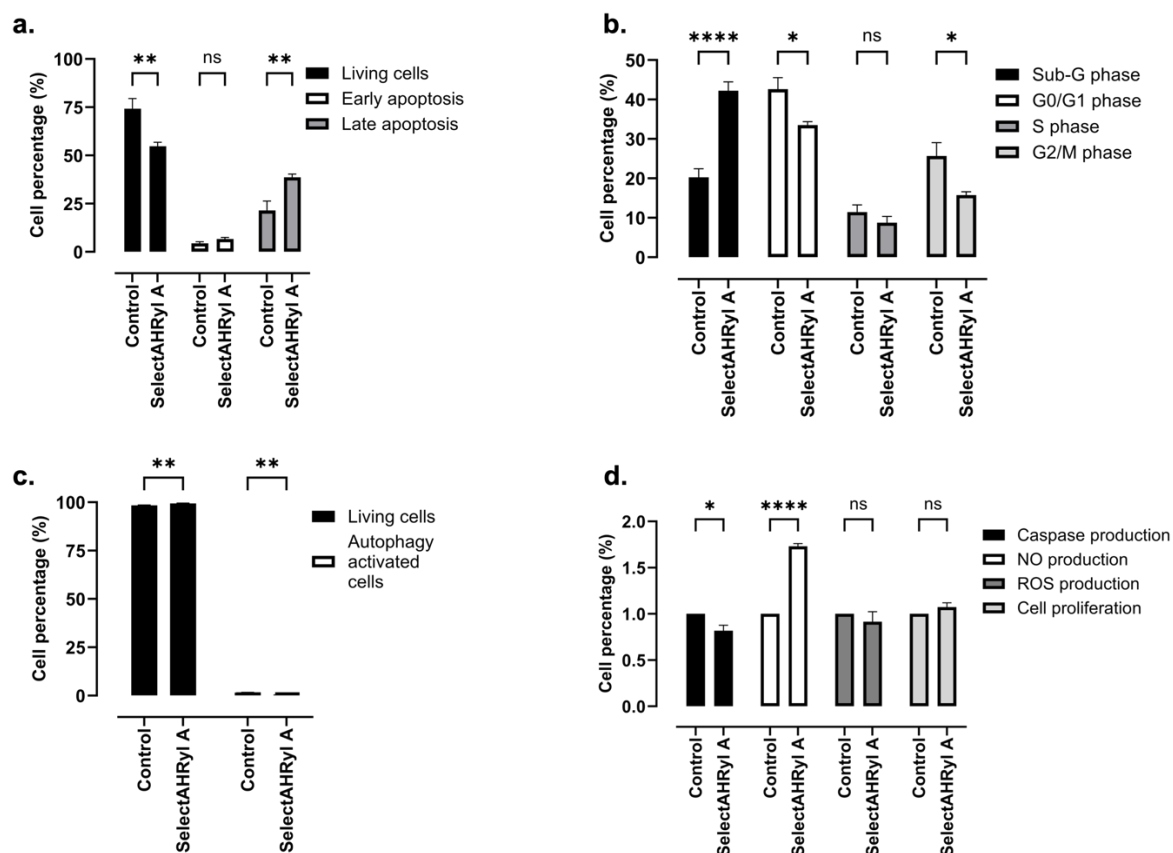


Fig.26: Impact of selectAHRyl A on common cell death-related pathways. Bar graphs illustrate the effects of selectAHRyl A at IC₅₀ on MDA-MB-468 cells upon treatment for 72 h on **a**, induction of apoptosis quantified by using the AnnV/PI kit; **b**, cell cycle arrest upon treatment determined by using DAPI stain; **c**, induction of autophagic processes measured by using AO stain and **d**, induction of pan-caspases' activation, NO and ROS production, and the impact on cell proliferation using ApoStat, DAF-FM, DHR and CFSE stains, respectively. Data were normalized to the corresponding read-outs of the untreated control.

3.3. SelectAHRyl A induces upregulation of several proteins including heat shock protein 70

Using a differential protein expression of more than 1.5-fold over untreated cells as a selection criterion, 33 proteins were found to be accordingly affected upon compound treatment. Subsequently, 14 out of these 33 proteins were identified (Table S8) by using an ultrafleXtreme™ mass spectrometer and BiTools 3.2 software. Based on a Gene Ontology (GO) enrichment analysis, selectAHRyl A mainly modulated in MDA-MB-468 the expression of proteins involved in the regulation of cellular (44%) and metabolic (22%) processes by affecting protein binding processes (48%) and catalytic activities (33%) as summarized in Fig.27b,c. Most of the proteins detected to be modulated by selectAHRyl A could be mapped in a coherent STRING functional protein association network (Fig.27a). Furthermore, as illustrated in Fig.S18, several of the proteins showed an immediate induction of expression even after just 6 h of treatment, such as PLS3, RAB6B and especially HSPA1A/1B. However, others as SEPT11 and GART were found to be highly upregulated only after longer cells' exposure (48 h) to selectAHRyl A. It is worth noting that ANXA2 and RAB6A expressions were strongly downregulated upon selectAHRyl A treatment, regardless of the incubation time.

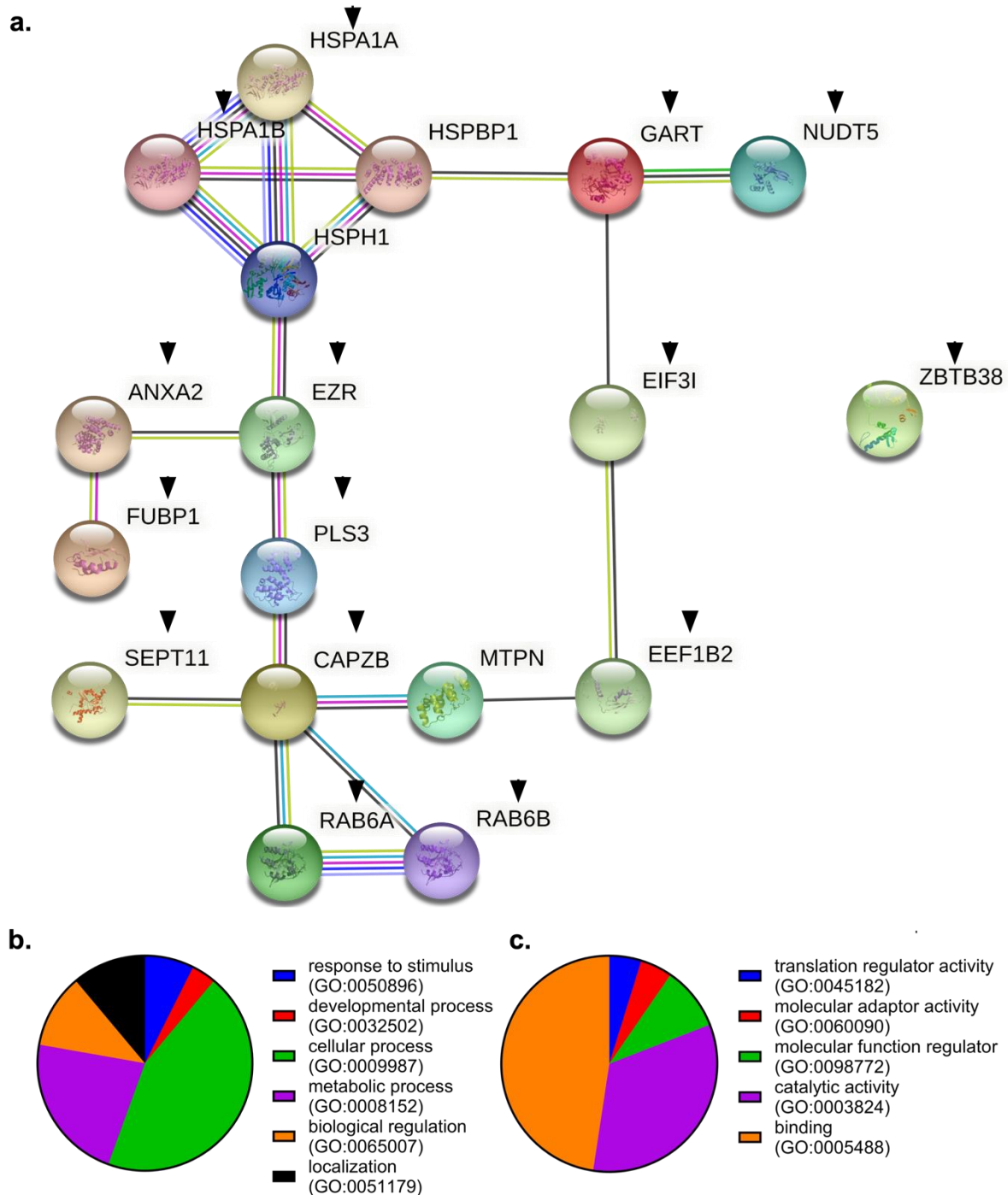
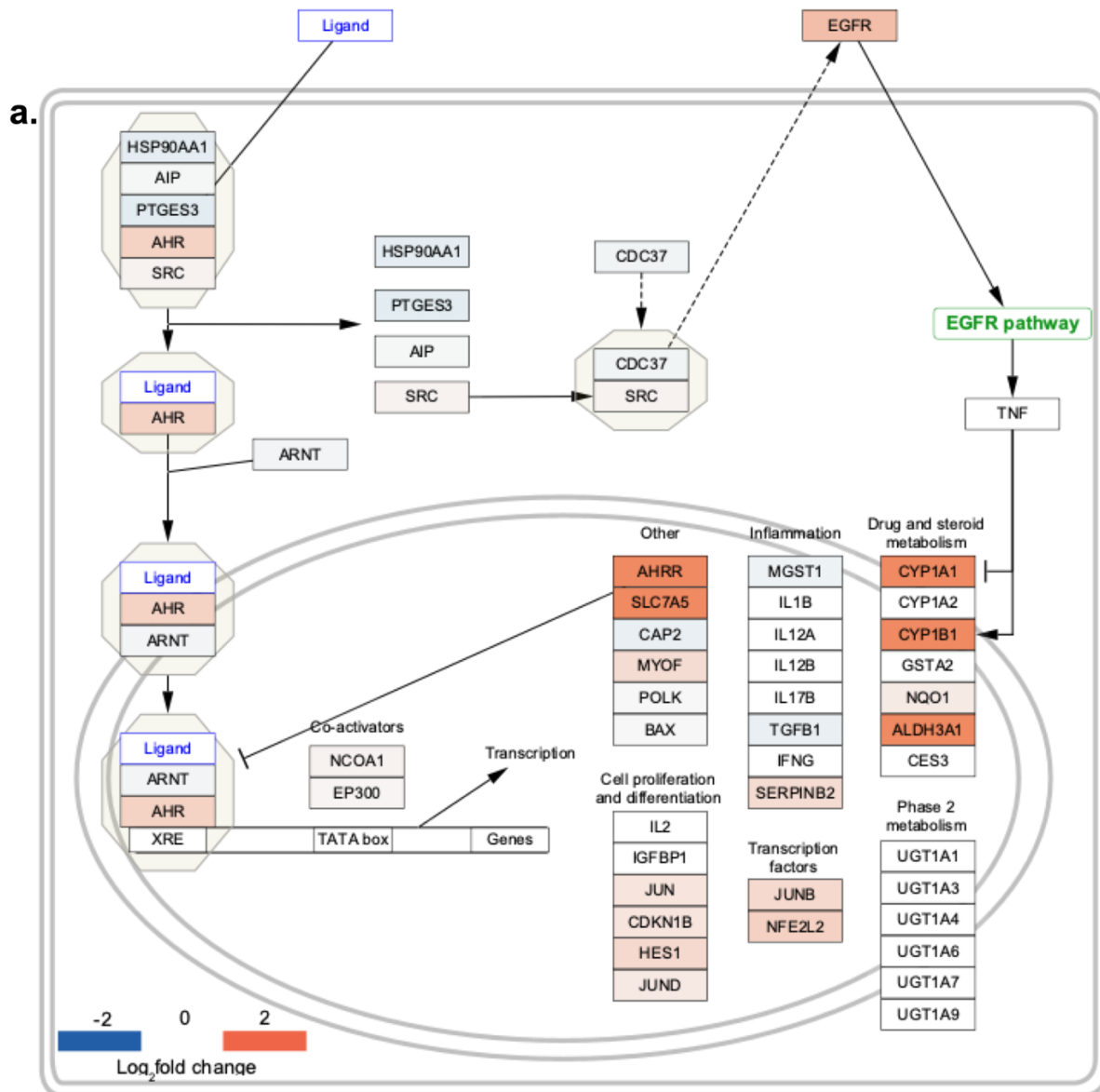


Fig.27 Impact of selectAHRyl A on cellular protein expression. **a**, STRING functional protein association network depicting proteins from MD-MB-468 cells with altered expression levels upon treatment with selectAHRyl A (indicated by a black arrowhead). The network was generated by using string-db.org. **b**, Biological processes and **c**, molecular functions affected in MDA-MB-468 upon selectAHRyl A treatment, as predicted by performing a GO data enrichment analysis using the analysis software tool of the PANTHER Classification System (pantherdb.org).

3.4. Activation of the AHR pathway plays an essential role for the cell line selectivity of selectAHRyl A

Several genes were found to be differentially expressed upon treatment with selectAHRyl A in both breast cancer cell lines MDA-MB-468 and SK-BR-3, especially *CYP1A1*, *CYP1B1*, *AHRR* and *SLC7A5*. However, no alterations of these genes' expression (mRNA) levels were detected in non-cancerous 184B5 breast cells (Fig.S17, Table S9 - Table S11). A Wiki-pathway data enrichment indicated that these affected genes cluster primarily in the aryl hydrocarbon receptor (AHR) pathway.

Furthermore, it was observed that additional affected genes, beyond those that were previously mentioned, were regulated in or by this pathway as illustrated in Fig.28a. These transcriptomics data guided us to further study whether the difference in the impact of selectAHRyl A against MDA-MB-468, SK-BR-3 and 184B5, might also be caused by its action on the AHR pathway even when using the cell line specific IC_{50} s. Hence, the effect of the selectAHRyl A treatment on the expression of *AHR*, *CYP1A1*, *CYP1B1* and *AHRR* was studied in more detail by using RT-qPCR.



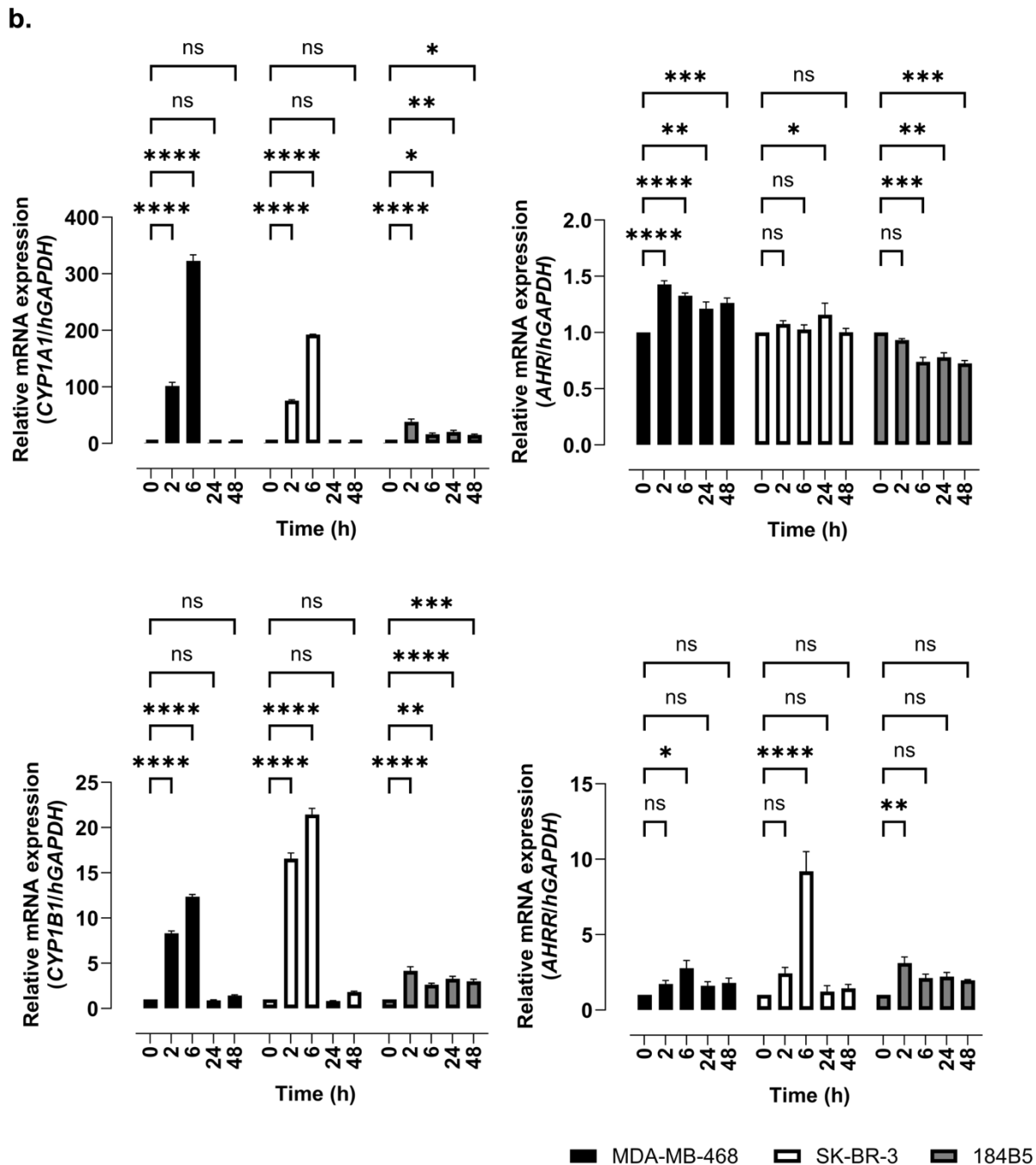


Fig.28 Impact of selectAHRyl A on genes' expression. **a.** Scheme of the aryl hydrocarbon receptor (AHR) pathway, genes with altered mRNA expression levels (adjusted p-value < 0.05) in MDA-MB-468 cells upon treatment with selectAHRyl A at 100 μ M for 6 h are color-coded. Upregulated genes are marked in red, while downregulated genes are marked in blue. **b.** Effect of selectAHRyl A on the mRNA expression levels of selected AHR pathway-associated genes in MDA-MB-468, SK-BR-3 and 184B5. The cells were treated for 0, 2, 6, 24 and 48 h with selectAHRyl A at cell line specific IC_{50} in case of MDA-MB-468 and SK-BR-3 and 100 μ M in case of 184B5.

3.5. CYP1A1 and CYP1B1 are strongly upregulated in MDA-MB-468 upon treatment with selectAHRyl A

To confirm the upregulation of the genes regulated by the AHR pathway upon treatment with selectAHRyl A as indicated by the transcriptome analysis (section 3.4), RT-qPCR was performed. Four selected genes were studied, namely *CYP1A1*, *CYP1B1*, *AHRH* and *AHR*. As shown in Fig.28b, selectAHRyl A induced substantial induction of *CYP1A1* and *CYP1B1* expression in both MDA-MB-

468 and SK-BR-3 breast cancer cells. This is in stark contrast to the non-cancerous 184B5 cells where such an effect was completely not observed.

Remarkably, a strong induction of AHRR expression after 6 h treatment was prominent in SK-BR-3 though not in MDA-MB-468 and 184B5. Furthermore, it was observed that selectAHRyl A induced a significant increase in AHR expression in MDA-MB-468 and SK-BR-3, but it led to a slight reduction of AHR expression in 184B5. These data highlight the importance of the *AHR* and *CYP1A1* expression levels and activities for the cytotoxicity of selectAHRyl A. Hence, the effect of an inhibition of the AHR and CYP1A1 proteins on the activity of the compound was examined next.

3.6. *In silico* study indicates interaction between selectAHRyl A and AHR receptor

The *in silico* study confirmed the possibility of a selectAHRyl A binding to the AHR binding pocket similar to FICZ, BNF, IR and leflunomide (Fig.S20). Compared to the typical hydrophobic AHR binders (such as TCDD, benzo[a]pyrene), these compounds are characterized by the presence of groups capable of polar interactions and hydrogen-bonding. SelectAHRyl A showed a hydrogen bond interaction with Ser365 which was also observed for the other compounds of that group.²⁴¹ Additionally, selectAHRyl A forms another hydrogen bond interaction with Cys333. This additional H-bond explains the slightly lower interaction energy observed compared to FICZ (selectAHRyl A = -6.76, FICZ = -6.46).

3.7. AHR and CYP1A1 antagonists counteract the cytotoxic effect of selectAHRyl A

To confirm the importance of the AHR pathway for the activity of selectAHRyl A, cells (MDA-MB-468, SK-BR-3 and 184B5) were treated with selectAHRyl A in combination with several AHR pathway-affecting compounds. First, cells were co-treated with a fixed concentration of the proven AHR antagonist CH-223191 (12.5 μ M) and a serial dilution of selectAHRyl A (0.02-375 μ M). The AHR antagonist led to a 10-fold reduction of selectAHRyl A activity (Fig.29b). Additionally, cells were co-treated with the serial dilution of selectAHRyl A and 12.5 μ M of the CYP1A1 inhibitor bergamottin. Interestingly, in MDA-MB-468 cells, the inhibition of CYP1A1 reduced the cytotoxic effect of selectAHRyl A by nearly 200-fold, as shown in Fig.29c. A comparable impact of AHR and CYP1A1 inhibition on the compound's effect, however to a lower extent, was also detected in SK-BR-3 cell. Noteworthy is that no comparable effect of bergamottin was observed in the non-cancerous 184B5 cell line. These results showed that the CYP1A1 and AHR proteins are crucial for the cytotoxicity of selectAHRyl A.

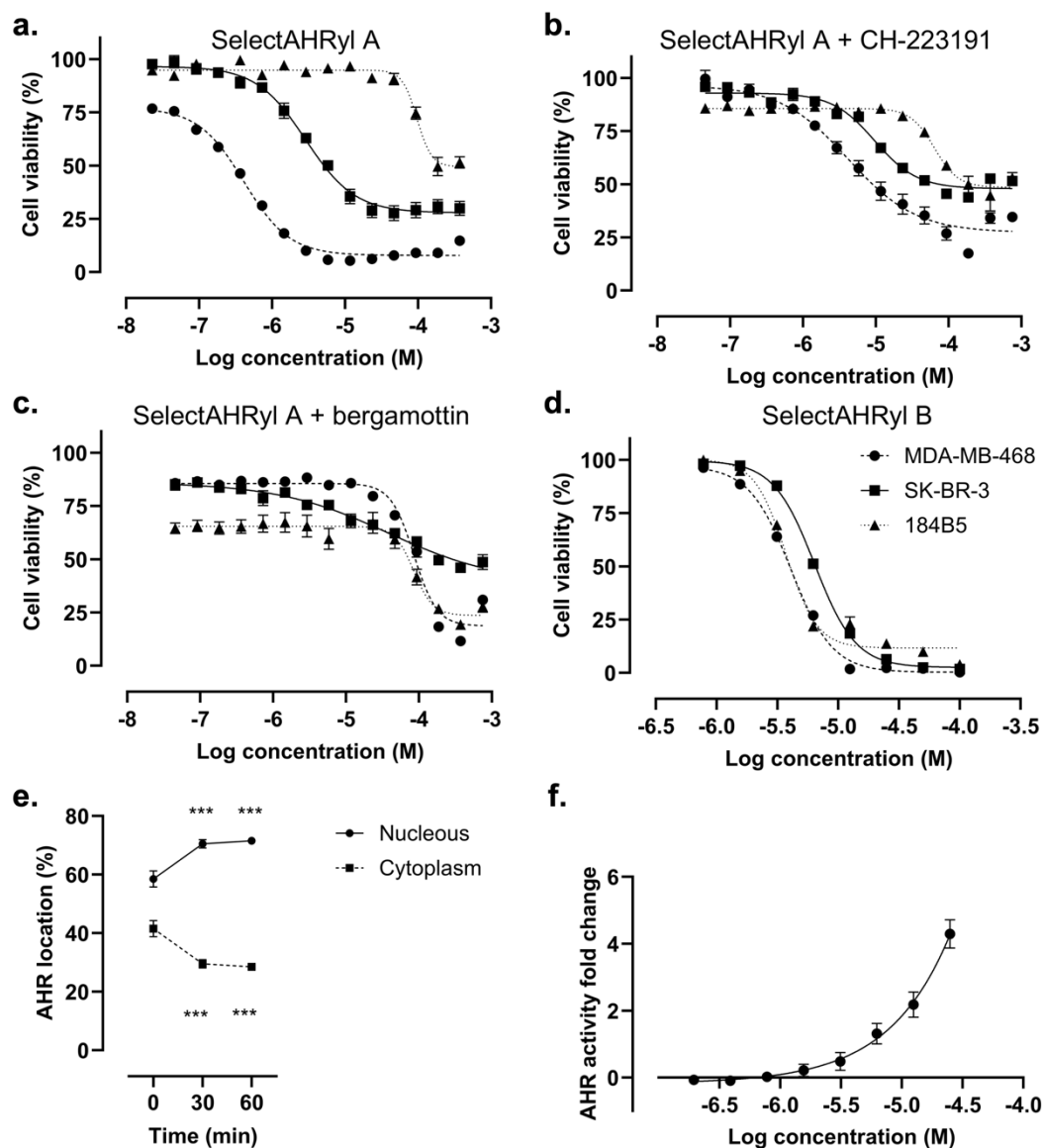


Fig.29 Confirmation of AHR pathway modulation by selectAHRyl A. Dose-response curves of the viability of MDA-MB-468, SK-BR-3 and 184B5 cells upon 72 h treatment with **a**, a dilution series of selectAHRyl A alone; **b**, a selectAHRyl A dilution series in combination with 12.5 μ M of CH-223191, an AHR inhibitor; **c**, a selectAHRyl A dilution series in combination with 12.5 μ M of bergamottin, a CYP1A1 inhibitor and **d**, a dilution series of selectAHRyl B alone. The cell viability was determined by using CV assay. **e**, The impact of a selectAHRyl A treatment at IC₅₀ for 30 and 60 min on the cellular distribution of AHR protein between nucleus and cytosol in MDA-MB-468 cells. **f**, Impact of selectAHRyl A on the activation of AHR protein in HepG2-AHR-Lucia reporter cells upon 48 h treatment with a serial compound dilution.

3.8. SelectAHRyl A induces the translocation of AHR protein from cytosol into the nucleus

The hypothesis that selectAHRyl A could directly interfere with the AHR pathway, potentially as an AHR agonist, was tested by investigating the flux of AHR protein upon treatment with selectAHRyl A using fluorescence microscopy. Agonistic AHR activation would be indicated by a delocalization of AHR protein from the cytosol into the cells' nuclei. Indeed, compared to the untreated cells, a differential distribution of AHR protein between the cells' nucleus and cytosols was detected in the cells treated with selectAHRyl A. Before treatment, the distribution of AHR protein was determined to be 59% in the nuclei and 41% in the cytosols. However, a 30 min treatment with the compound led to an increase in nuclei accumulation of AHR protein by 11%, accompanied with a reduced AHR quantity in the cytosol (nuclei: 70% and cytosols: 30%) as illustrated in Fig.29e and Fig.S19a-c.

Accordingly, the observed induction of the translocation of the AHR protein from the cytosol into the nucleus gives evidence for an agonistic activation of the AHR protein by selectAHRyl A.

3.9. SelectAHRyl A activates the AHR pathway and xenobiotic resistance elements

To further confirm the impact of selectAHRyl A on AHR protein and pathway, a reporter gene assay was performed in which a commercially available reporter gene cell line, HepG2-AHR-Luciferase cells, was treated with selectAHRyl A. The reporter cell line harbors a luciferase under control of an XRE promoter that is activated upon activation of the upstream AHR protein. Accordingly, the degree of AHR activation is directly linked to the level of luciferase protein expression and hence luminescence output. As illustrated in Fig.29f, the reporter gene assay proved activation of the AHR protein by selectAHRyl A in a dose-dependent manner, confirming that selectAHRyl A acts as an AHR activator.

3.10. SelectAHRyl A becomes mono- and di-hydroxylated by CYP1A1 upon agonistic AHR pathway activation

Since selectAHRyl A was found to agonistically activate the AHR and its downstream pathway including upregulating, CYP1A1, the next experiment was to investigate whether the compound itself might be a substrate of CYP1A1. And if so, how exactly does CYP1A1 metabolize selectAHRyl A. For this purpose, selectAHRyl A was incubated with liver microsomes containing mainly CYP1A1, leading to a depletion of the parent compound accompanied with the formation of four metabolites of selectAHRyl A, designated as M1-M4 (see Fig.30a). The metabolites were detected using RP-UHPLC-ESI-HRMS in positive ion mode.

In the full mass spectra, the parent ions $[M+H]^+$ of the mono-hydroxylated (M1, M2) and di-hydroxylated products (M3, M4) could be detected at m/z 308.1038 (calculated for $C_{17}H_{14}N_3O_3^+$ 308.1030, Table S15) and m/z 324.0989 (calculated for $C_{17}H_{14}N_3O_4^+$ 324.0979, Table S15) showing a mass difference of 16 and 32 Da in comparison to selectAHRyl A ($[M+H]^+$ at m/z 292.1088, calculated for $C_{17}H_{14}N_3O_2^+$ 292.1081, Table S15), respectively.

Additionally, MS/MS experiments were conducted to determine the substitution patterns of the metabolization products M1 – M4 based on their specific fragmentation behavior. The resulting MS/MS spectra show also mass differences of 16 or 32 Da in the observed key fragments in comparison to selectAHRyl A indicating the generation of four metabolites which were either mono- or di-hydroxylated as presented in Fig.30b. Different MS/MS collision energies (see Table S14) were applied to detect even smaller fragment ions, which are important to characterize the hydroxylation pattern.

MS/MS fragmentation of selectAHRyl A ($[M+H]^+$ at m/z 292) leads to an ion at m/z 274 ($C_{17}H_{12}N_3O^+$, Fig.30b) corresponding to an unspecific water loss. This fragment was also detected for the metabolites M1 and M2 (m/z 290) as well as M3 and M4 (m/z 306). The key fragment **I**, which led to the determination of the positioning of the hydroxy groups, results from the break of the amide bond during collision-induced dissociation. For selectAHRyl A and metabolite M2 the resulting ion was detected at m/z 199, showing no hydroxylation on positions R^1 or R^2 (Fig.30b). In contrast, ions at m/z 215 (M1, M3, M4) suggest a mono- or di-hydroxylation at the positions R^1 and/or R^2 for these metabolization products. The ion, which theoretically forms its counterpart after the amide bond cleavage, could not be detected for any of the analytes investigated. The key fragments **II** and **IV**, which result from the loss of CO (m/z 171 and 187) and C_2H_2NO (m/z 116 and 132), could be detected for all analytes. These fragments differ by 16 Da, which indicates hydroxylation at the aromatic ring of this structural element for the metabolites M1, M3 and M4. This was further confirmed by the key fragment ions at m/z 104 (**IV**) and 93.

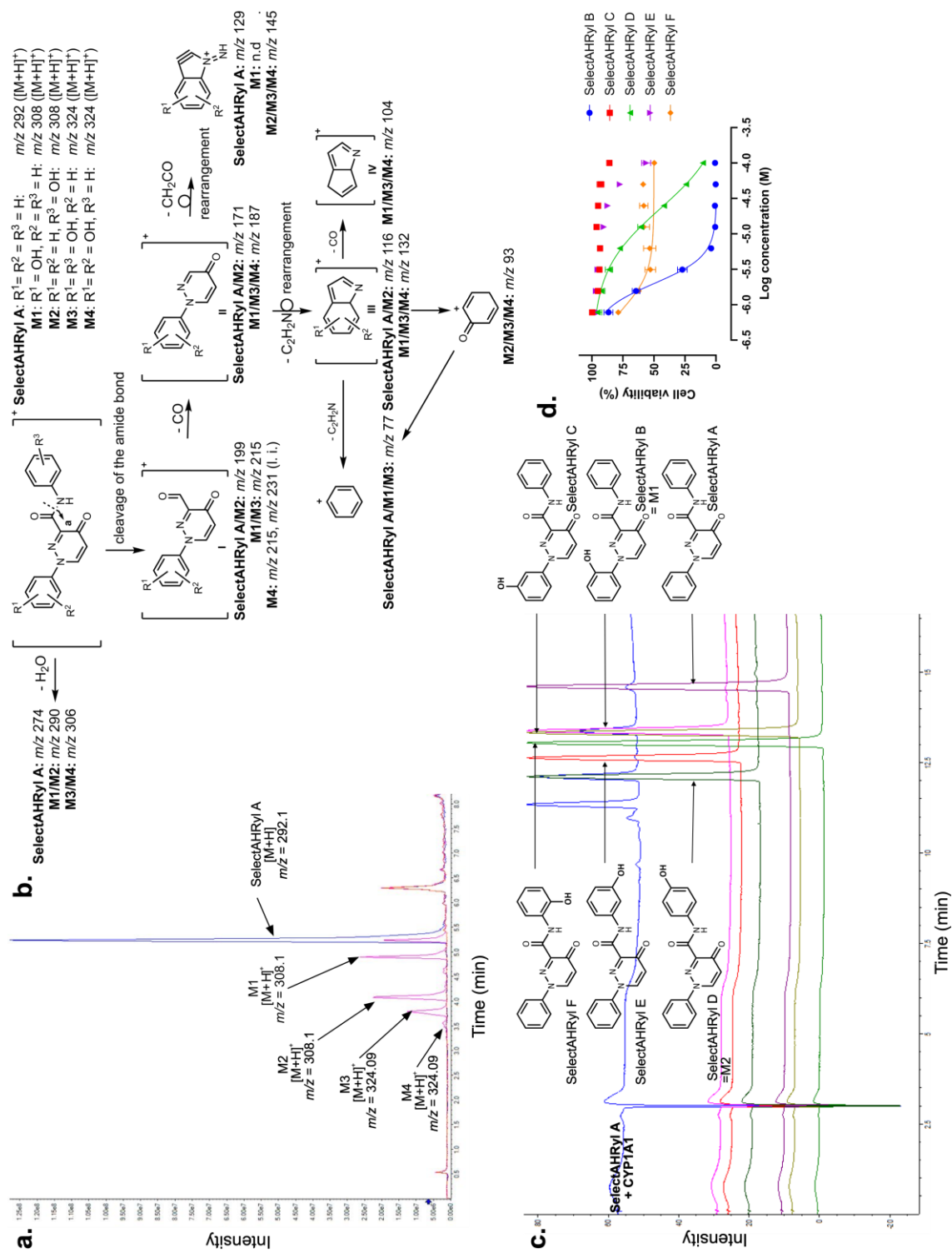


Fig.30 Metabolization of selectAHRyl A as catalyzed by CYP1A1 enzyme-containing liver microsomes. **a**, Representative chromatogram of oxidation products of selectAHRyl A analyzed with UHPLC-HRMS. The shown chromatogram overlay summarizes the appearance of selectAHRyl A and four detectable metabolic products in the presence (magenta) and the absence (blue) of CYP1A1 enzyme. A CYP1A1-containing sample without selectAHRyl A was inspected as reference sample (red). **b**, Proposed positive ion mass spectral fragmentation of metabolites M1 and M2 ($[M+H]^+$ m/z 308), M3 and M4 ($[M+H]^+$ m/z 324) and selectAHRyl A ($[M+H]^+$ m/z 292) as generated by incubation with CYP1A1. **c**, Representative HPLC chromatograms of the oxidation products of selectAHRyl A as generated by using CYP1A1-containing liver microsomes (blue) overlaid with those of the synthesized hydroxylated derivatives of selectAHRyl A, as analyzed by using a HPLC-diode array detector. The shown chromatogram overlay summarizes the appearance of selectAHRyl A and its metabolic products in the presence and the absence of CYP1A1 enzyme. **d**, Dose-response curves of the viability of MDA-MB-468 cells treated with mono-hydroxylated derivatives (structures shown in Fig.30c) of selectAHRyl A for 72 h. The cell viability was determined by CV assay.

3.11. 1-(2-Hydroxyphenyl)-4-oxo-*N*-phenyl-1,4-dihydropyridazine-3-carboxamide (selectAHRyl B) is one of the active forms of selectAHRyl A

A

The mono-hydroxylated derivatives, which were predicted upon the CYP1A1-catalyzed metabolism of selectAHRyl A, were synthesized chemically and used for the determination of the active metabolite. The retention times of the synthesized hydroxylated derivatives were compared to those obtained by the liver microsomes enzymatic reaction as illustrated in Fig.30c. These aligned derivatives were tested to determine their cytotoxicity against the MDA-MB-468 cell line (Fig.30d). The derivative with an ortho-hydroxy group at the 1-phenyl motif (selectAHRyl B) retained a cytotoxic activity and aligned with the most prominent compound produced by the enzymatic reaction (M1 peak). As illustrated in Fig.30d, this derivative was the only compound to induce cytotoxicity towards the MDA-MB-468 cell line, additionally it showed complete abolishment in the selectivity also affecting 184B5 cell line now as shown in Fig.29d.

4. Discussion

In the course of an anti-cancer *in vitro* screening of the compound collection of the Leibniz Institute of Plant Biochemistry (IPB, Halle, Germany) against a human breast cancer cell line panel, the compound 4-oxo-*N*,1-diphenyl-1,4-dihydropyridazine-3-carboxamide (named selectAHRyl A), stood out with extraordinary cytotoxicity and exceptional selectivity against the triple-negative breast cancer (TNBC) cell line, MDA-MB-468, with an absolute IC₅₀ of 0.22 μM and, with a good activity against SK-BR-3 with an IC₅₀ of 5.22 μM. Most importantly, the compound's impact was remarkably lower against all other breast cell lines including two non-cancerous breast cell lines, namely MCF10A and 184B5 (Fig.25b).^{249,250} As a better simulation of the compound's anti-proliferative and cytotoxic effect on a solid tumor, the compound was further tested against 3D spheroids developed from MDA-MB-468 cells and was found to cause a strong cytotoxic effect with an IC₅₀ of 0.84 μM even in those more advanced 3D cancer cell structures. Due to the outstanding selectivity of the compound in that preliminary breast cells panel, it was further tested against a higher number of diverse types of cancer cell lines, comprising human colorectal, blood, sarcoma, lung, prostate, liver and stomach cancer cell lines. The compound showed a rather weak cytotoxic effect on all other cell lines tested as shown in Fig.S15, Except for the human liver HepG2 cancer cells (IC₅₀ = 5.53 μM). Hence, the compound was investigated in more detail to shed light on its selective mode of action. Initially, flow cytometric analyses were performed, indicating that the compound induces apoptotic cell death, however, seemingly without inducing caspases-dependent pathways (see Fig.26). As a result of the induced caspase-independent apoptosis, the DNA of the treated cells should become fragmented, and the cells accumulate in the sub-G phase, what was, indeed, noticed in the cell cycle analysis. Furthermore, the compound induced a remarkable increase of the nitric oxide level, which could be either a reason for the induction of apoptosis or an adaptive reaction of the compound-stressed cells.²⁵¹

In order to better understand the mode of action of selectAHRyl A, its impact on the transcriptome of MDA-MB-468 (high sensitivity), SK-BR-3 (medium sensitivity), and 184B5 (low sensitivity) cells was studied. Based on the results of a comparative transcriptomics analysis and subsequent data enrichment by using WikiPathways, it was recognized that the AHR pathway was highly modulated in case of the MDA-MB-468 and SK-BR-3 breast cancer cell lines, however, not affected in the non-cancerous human breast cell line 184B5. Especially, *CYP1A1* and *CYP1B1* were detected to be highly upregulated which was independently confirmed by using RT-qPCR. These results raised the hypothesis that the selectivity of the compound could be mediated by the AHR pathway by acting as an AHR activator.²⁵² The proteomics 2D electrophoresis analysis of MDA-MB-468 cells treated with selectAHRyl A confirmed an increase of the heat shock proteins HSPA1A and HSPA1B expression. Interestingly, as previously published, a strong correlation has been proven between an upregulation of heat shock protein 70 and the activation of the AHR pathway.²⁵³

The aryl hydrocarbon receptor signaling pathway is central part of a mechanism in cells to metabolize and detoxify xenobiotic chemicals.^{254,255} Under normal conditions, the AHR protein is localized in the cytosol in form of an inactive heteromeric protein complex formed together with several

other regulatory proteins.²⁵⁶ Upon the binding of a ligand, the complex moves from the cytosol into the nucleus.²⁵⁷ Hence, to initially confirm the activation of the AHR pathway upon selectAHRyl A treatment, the location of AHR protein was inspected by using immunofluorescence microscopy. Indeed, the compound caused an increased accumulation of the AHR protein in the cells' nuclei accompanied with a corresponding decrease of AHR in the cytosol (Fig.29e).²⁴¹ Moreover, by co-treatment of MDA-MB-468 with selectAHRyl A and the AHR antagonist CH-223191, the cytotoxicity of the compound was significantly inhibited, which confirmed the activation of AHR by the tested compound.²⁵⁸ After the translocation of the AHR complex into the cell nucleus, the AHR complex dissociates leading to the release of AHR protein. The AHR protein forms another complex with ARNT. The AHR/ARNT complex plays a role as a transcription factor leading to the upregulation of a class of genes known as xenobiotic responsive elements (XRE) including *CYP1A1*, *CYP1B1*, *ALDH3A1*, *AHRR*, *TIPARP* and *NQO1*. These genes were upregulated in MDA-MB-468 or SK-BR-3 after the treatment with selectAHRyl A.^{259,260} The impact of selectAHRyl A on the activation of XRE was also confirmed by using a reporter gene assay as shown in Fig.29f. The XRE genes code for a number of corresponding proteins, each of which can metabolize a specific class of compounds. Normally, these enzymes metabolize xenobiotic compounds, increasing their hydrophilicity in order to improve their detoxification. *CYP1A1* catalyzes the epoxidation and the hydroxylation of the AHR ligand improving its elimination.²²⁵ However, in rare cases, some polycyclic aromatic compounds such as 2,3,7,8-tetrachlordibenzodioxin (TCDD), the hydroxylation leads to a hydroxy or an epoxy derivative that has a tumorigenic effect.^{259,261} But these modifications can also induce the activation of a prodrug, as known for eupatorin that permits similar selectivity against the MDA-MB-468 cell line ($IC_{50} = 0.5 \mu M$) compared to several other cell lines.²²⁶ Therefore, to test if *CYP1A1* plays an essential role in selectively activating selectAHRyl A, the compound was co-administered with the *CYP1A1* inhibitor bergamottin.²⁶² Definitely, the *CYP1A1* inhibitor caused a strong decline in the cytotoxicity of the compound, proving that *CYP1A1* metabolizes selectAHRyl A yielding a derivative/derivatives that possess the ultimately observed cytotoxic effect, especially in MDA-MB-468 cells. To determine the modified products catalyzed by *CYP1A1*, the compound was incubated with liver microsomes bearing the enzyme. This expectedly leads to the depletion of the parent compound and the formation of four new metabolites which were identified as the corresponding mono- or di-hydroxylated derivatives. Based on the inhibition of selectAHRyl A activity due to its co-administration of the *CYP1A1* inhibitor bergamottin, it is not the cytotoxin itself. Instead, one or several of the hydroxylated derivatives or intermediate epoxides could be the active cytotoxic forms of the compound. Hence, several mono-hydroxylated derivatives were synthesized and their cytotoxicity and selectivity were determined. The mono-hydroxylated derivative 1-(2-hydroxyphenyl)-4-oxo-N-phenyl-1,4-dihydropyridazine-3-carboxamide was the only one to display both an outstanding cytotoxicity and a complete loss of selectivity since it also induced cytotoxicity in the healthy breast cell line (184B5). These observations indicate that *CYP1A1*, induced by agonistic AHR activation, acts as a gate keeper mechanism where it induces the *ortho*-hydroxylation of selectAHRyl A at the 1-phenyl group yielding the cytotoxic molecule that induces cell apoptosis. Nevertheless, liver microsomes also showed the induction of further hydroxylations of selectAHRyl A (Fig.30, M3 and M4), where dihydroxy-metabolites were detected as well. These metabolites could include the aforementioned *ortho*-hydroxylation combined with further hydroxylations at other positions leading to higher cytotoxicity.

Moreover, an essential element of the XREs is the protein AHRR. Encoded by *AHRR*, which in turn binds to ARNT. It competes with AHR and prevents the binding of AHR to ARNT and hence the formation of the transcription factor.²⁶³ *AHRR* expression was induced by 4-fold higher in SK-BR-3 compared to MDA-MB-468. This might explain the lower activity of selectAHRyl A in SK-BR-3 cells.

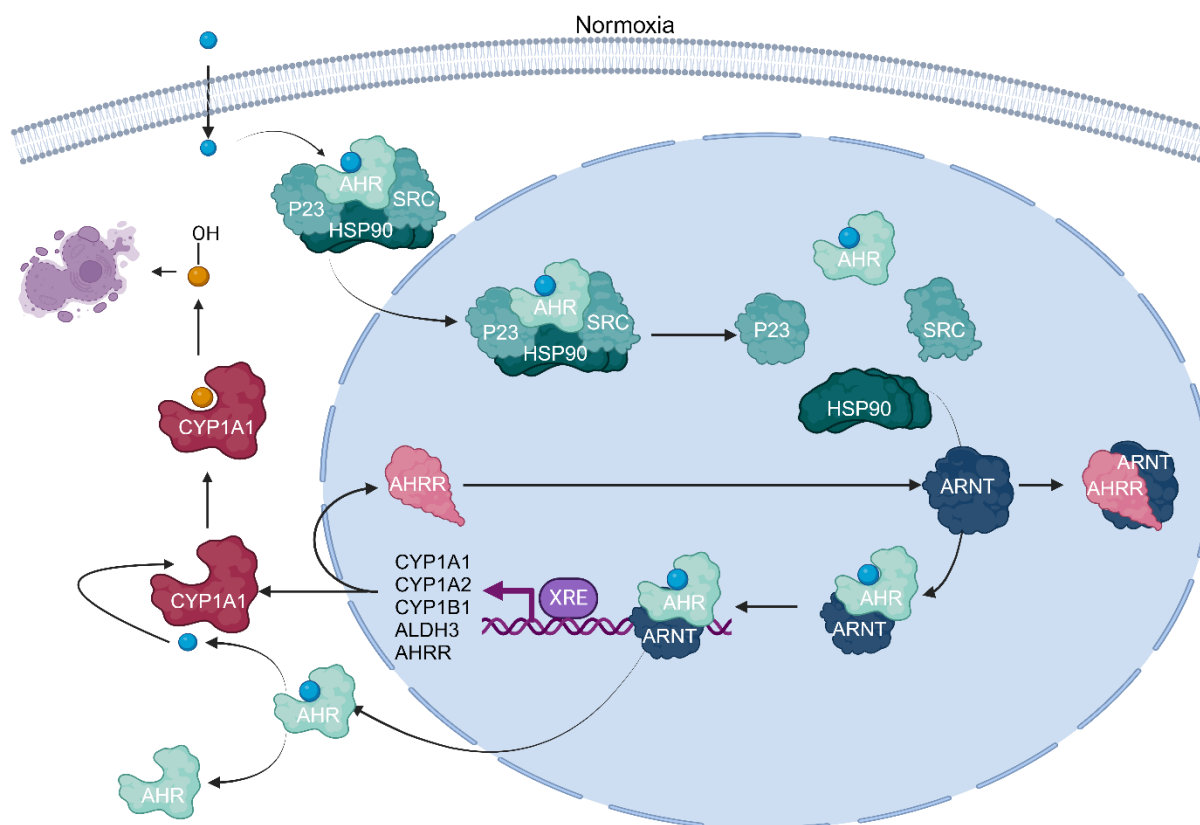


Fig.31 Putative mode of action of selectAHRyl A. The scheme summarizes the theory of the selectivity mode of action of selectAHRyl A. Upon the treatment of MDA-MB-468 cells with selectAHRyl A, it binds to the active site of AHR protein bound in the inactive AHR complex in the cytosol. The receptor binding leads to the translocation of the protein complex from the cytosol to the nucleus and the release of AHR protein from the complex. Afterwards, AHR binds to the nuclear protein ARNT forming a transcription factor complex which induces the expression of a group of genes known as xenobiotic resistance elements (XRE). Afterwards, selectAHRyl A is released from the AHR/ARNT complex and becomes subject of an oxidative modification catalyzed by one of the XRE-coded proteins, most likely the P450 enzyme CYP1A1, yielding selectAHRyl B (the hydroxylation product of selectAHRyl A). SelectAHRyl B induces caspase-independent apoptosis, ultimately leading to cancer cell death. The scheme was created by using BioRender.²⁶⁴

During the last years, AHR modulators have gained increasing attention in research because of their promising effects as immunomodulatory and anti-cancer agents.²⁶⁵ Our experiments illustrate that selectAHRyl A permits a weaker agonistic effect than that induced by the previously mentioned traditional AHR agonists like TCDD and FICZ. However, the observed agonistic effect is obviously sufficient to induce a robust activation of the downstream pathways including CYP1A1 expression and catalysis. To confirm the higher cytotoxicity of the resulting active principle of selectAHRyl A compared to those of traditional AHR agonists, a traditional AHR agonist (FICZ) was tested against MDA-MB-468, SK-BR-3 and 184B5 under the same testing conditions. The results (Fig.S19d) show that FICZ had a remarkably lower anti-proliferative, primarily cytostatic effect on MDA-MB-468 cell growth ($IC_{50} = 4.56 \mu\text{M}$) and hence, a weaker selectivity towards TNBCs compared to selectAHRyl A.

According to our hypothesis, selectAHRyl A acts as a prodrug that is activated through the self-triggered induction and activity of CYP1A1, an effector protein regulated by AHR pathway. The phenomenon was previously reported for several compounds including the natural products family of flavonoids.²⁶⁶ The most extensively studied and most active compound belonging to this family is eupatorin which, indeed, shows high resemblance to the newly reported compound regarding the mode of action. It was shown that eupatorin is metabolized by CYP1A1 as well to a hydroxylated derivative called cirsiolol that was found to induce cell death. Although selectAHRyl A follows the same mode of action as eupatorine, selectAHRyl A showed a remarkably higher selectivity toward MDA-MB-468. SelectAHRyl A induced cell death in MDA-MB-468 in comparison to non-cancerous MCF10A cells at IC_{50} values of $0.2 \mu\text{M}$ and more than $375 \mu\text{M}$, respectively (> 1875 -fold difference of cancer vs. non-

cancer). However, the comparable IC_{50} values of eupatorine have been published with 0.5 μM and 50 μM , respectively (100-fold difference). Hence, the selectivity index for selectAHRyl A is more than 18-fold higher than eupatorine.²²⁶ Another interesting molecule that follows a comparable mode of action is 6-NAP. It also demonstrated high selectivity against breast cancer cell lines, especially MDA-MB-468. As previously reported by Gilbert et al., the compound showed a 500-fold higher activity against MDA-MB-468 compared to other tumor-derived cell models, which is, nevertheless, again lower selectivity index than that for selectAHRyl A.²⁶⁷ Additionally, 6-NAP showed a slight reduction in the viability of MCF10A, which was not observed in the case of selectAHRyl A. Consequently, in comparison with previously known compounds, our newly discovered selectAHRyl A permits enhanced selectivity and specificity towards some TNBCs and to a yet much lower extent to hepatic cancer cells, which could lead to a better safety margin and reduced undesired side effects of a drug treatment. The enhanced selectivity and tolerance of selectAHRyl A in contrast to eupatorin and NAP-6 might originate from the diminished toxicity of its prodrug prior to its activation by CYP. On the other hand, the higher cytotoxicity of a selectAHRyl A treatment, compared to eupatorin and FICZ, might prove that the activated form of the novel compound selectAHRyl B is more efficient in inducing cell death compared to the active form of the other two, FICZ and eupatorin. The selectAHRyl A prodrug metabolism and activation through the AHR pathway activation and CYP induction might offer the advantage of protecting healthy cells from the cytotoxic effect of the active drug form. The functionalization of that molecule, along with understanding its activation principle, could significantly contribute to the development of novel targeted therapies, potentially offering TNBC patients greater benefit through enhanced selectivity.

Though, further comprehensive preclinical studies and safety evaluations are necessary for the confirmation including an investigation of the mode of action of the final step, determining the target of the active, cytotoxic metabolite. Furthermore, structure-activity relationships of the compound supporting a hit-to-lead optimization, and *in vivo* efficacy and safety margins of the compound and related derivatives are required.

5. Conclusion

A compound (4-oxo-*N*,1-diphenyl-1,4-dihydropyridazine-3-carboxamide) was discovered and named selectAHRyl A, showing remarkable anti-cancer activity and especially selectivity against the human TNBC cell line MDA-MB-468 ($IC_{50} = 0.2 \mu\text{M}$) which results in an 1,800-fold higher anti-cancer activity compared to its effect towards the human non-cancerous breast cell lines MCF10A and 184B5. Moreover, the compound's IC_{50} against MDA-MB-468 3D spheroids, closer to a solid tumor situation, was detected to be sub-micromolar as well (0.84 μM). Multiple methodologies were applied to shed light on the compound's mechanisms of selectivity and action. It was proven that the compound acts as an agonistic AHR activator, leading to its own enzymatic metabolism by the upregulated AHR effector P450 enzyme CYP1A1, and ultimately resulting in its transformation into a cytotoxically active derivative, however, only in specific cell lines, e.g., MDA-MB-468 and SK-BR-3. One of the active derivatives was found to be an ortho mono-hydroxylated metabolite of the parent compound, namely 1-(2-hydroxyphenyl)-4-oxo-*N*-phenyl-1,4-dihydropyridazine-3-carboxamide. These intriguing data prove that the compound might be a very promising novel agent as starting point of a hit-to-lead optimization for the treatment of TNBCs and ideally other cancer types (since the third most sensitive cell line was HepG2, a human liver cancer line). However, it requires further studies to investigate the mode of action and the target of the active metabolite, the structure-activity relationships of the compound supporting a hit-to-lead optimization, and to investigate *in vivo* efficacy and safety margins of the compound and related derivatives, which could lead to the development of a novel targeted therapy for TNBC.

Author Contributions: The individual authors' contributions to the presented work are as follows: conceptualization: Ibrahim Morgan, Ludger A. Wessjohann and Robert Rennert; methodology: Ibrahim Morgan, Robert Rennert, Ludger A. Wessjohann; synthesis design: Ludger A. Wessjohann; compound synthesis: Tuvshinjargal Budragchaa, Julius Steidele; resources: Ludger A. Wessjohann; data curation: Ibrahim Morgan; writing – original draft preparation: Ibrahim Morgan; review and editing: Robert Rennert, Ludger A. Wessjohann; supervision: Robert Rennert, Ludger A. Wessjohann (main); project

administration: Ludger A. Wessjohann; *in silico* study: Ibrahim Morgan, Reporter gene assay: Anne Großkopf, Andreas Simm. Proteomics assay: Ibrahim Morgan, Rudolf Lichtenfels, Barbara Seliger; MS assays and data curation: Ibrahim Morgan, Elana Kysil, Annegret Laub; funding acquisition: Ludger A. Wessjohann. This work yielded in a recent patent application and a manuscript submission is in progress

General remarks

In the study, I aimed to improve the treatment options available for triple-negative breast cancer (TNBC). My interest in this special cancer type as it is considered to be a challenging cancer to treat. In contrast, other types of breast cancer can be effectively managed with a high prognosis rate. Initially, the research of my thesis focused on an optimization of the treatment of TNBCs, namely the search for novel PARP inhibitors. PARPi are known for their capacity to target TNBCs, since these are characterized by specific mutations in the BRCA1 gene. This mutation leads to a higher cytotoxic sensitivity and, hence, selectivity of PARPi drugs of and towards the cancer cells through a process known as synthetic lethality. Our study outlined a systematic process, starting with an *in silico* screening of compound libraries identifying potential PARPi. This was followed by a newly established enzymatic PARP assay for the assessment and evaluation of the proposed PARPi. Furthermore, the identified PARPi was also evaluated in terms of bioavailability and cellular permeability through cell-based assays, employing a competitive PARP binding approach with fluorescence read-out. Finally, the impact of PARPi in combination with a DNA-damaging agent was also studied. This comprehensive investigation led to the discovery of a new molecule with cytotoxic activity, namely 2-(methylthio)quinazolin-4(3*H*)-one. This novel molecule exhibited significantly higher activity compared to the core structure of olaparib, emphasizing the potential of further optimizing this compound. A more advanced hit-to-lead optimization could unveil a novel drug scaffold with remarkable bioavailability and higher activity compared to olaparib (Chapter 2).

Furthermore, in the course of our investigation, I identified a novel category of compounds, the azaglycophymines, which exhibited anticancer activity against various breast cancer types, including TNBCs. The most potent compound within this group was determined to be 2-((4-nitrophenyl)amino)quinazolin-4(3*H*)-one. Our examination of the induced mode of cell death of different breast cancer types revealed that the compound triggers cell death by diverse mechanisms. In the MCF-7 and MDA-MB-468 cell lines representing TNBC and HR⁺ breast cancers, respectively, the compound prompted cell death via non-caspase-dependent, non-apoptotic pathways. Conversely, in the BT-474 and HCC1937 cell lines representing HER2⁺ and BRCA1-deficient breast cancers, respectively, the compound induced cell death by the activation of caspase-dependent apoptosis. Additionally, the compound was *in vivo* tested against 4T1 mouse breast tumors inoculated in BALB/c mice, demonstrating a reduction of tumor growth lacking observable systemic side effects. This emphasizes the highly promising impact of this compound family against various types of breast cancer (Chapter 3).

Ultimately, the most intriguing disclosure in this study was the rational identification and investigation of a molecule, 4-oxo-*N*,1-diphenyl-1,4-dihydropyridazine-3-carboxamide, finally referred to as selectAHRyl A. This compound exhibited exceptional selectivity in targeting specific cancer types, with the highest efficacy observed against TNBCs, followed by HER2⁺ breast cancer and liver cancer cells. Notably, the compound had minimal impact on various cancer types and showed especially low effects on healthy cells, such as MCF10A and 184B5, which are both normal breast cell lines. Further investigation revealed that the compound functions as both activator and prodrug. It is self-metabolized and activated through agonistic activation of the AHR and its downstream pathway, leading to the induction of CYP1A1. This enzyme, CYP1A1, activates the selectAHRyl A prodrug by catalytic hydroxylation, i.e., introducing hydroxyl groups. Additionally, rigorous metabolic and analytical assays identified several hydroxyl derivatives, including a specific one responsible for the anti-cancer effect. This explains the selective activity observed against different cell types. (Chapter 4).

In conclusion, the study has unveiled several innovative discoveries that could be promising for the development of novel drug candidates and further the advancements in targeted therapies against, especially but not exclusively, breast cancer. The findings are specifically significant for TNBCs, offering a beacon of hope for the enhancement of prognosis and, ultimately, the improvement of the patients' survival rates.

References

1. Björklund, M. Cell size homeostasis: Metabolic control of growth and cell division. *Biochimica et Biophysica Acta (BBA) - Molecular Cell Research* **1866**, 409–417 (2019).
2. King, K. L. & Cidlowski, J. A. Cell Cycle Regulation and Apoptosis. *Annual Review of Physiology* **60**, 601–617 (1998).
3. Owa, T., Yoshino, H., Yoshimatsu, K. & Nagasu, T. Cell cycle regulation in the G1 phase: a promising target for the development of new chemotherapeutic anticancer agents. *Current Medicinal Chemistry* **8**, 1487–1503 (2001).
4. Foster, D. A., Yellen, P., Xu, L. & Saqena, M. Regulation of G1 Cell Cycle Progression. *Genes & Cancer* **1**, 1124–1131 (2010).
5. Mercadante, A. A., Dimri, M. & Mohiuddin, S. S. Biochemistry, Replication and Transcription. in *StatPearls* (StatPearls Publishing, Treasure Island (FL), 2020).
6. Lodish, H. *et al. Molecular Cell Biology*. (W. H. Freeman, 2000).
7. El-Labban, A., Zisserman, A., Toyoda, Y., Bird, A. W. & Hyman, A. Temporal models for mitotic phase labelling. *Medical Image Analysis* **18**, 977–988 (2014).
8. Cooper, G. M. The Nucleus during Mitosis. *The Cell: A Molecular Approach. 2nd edition* (2000).
9. Gibcus, J. H. *et al.* A pathway for mitotic chromosome formation. *Science (New York, N.Y.)* **359**, (2018).
10. Guo, Y. & Zheng, Y. Lamins position the nuclear pores and centrosomes by modulating dynein. *Molecular Biology of the Cell* **26**, 3379–3389 (2015).
11. Klemm, A. H., Bosilj, A., Glunčić, M., Pavin, N. & Tolic, I. M. Metaphase kinetochore movements are regulated by kinesin-8 motors and microtubule dynamic instability. *Molecular Biology of the Cell* **29**, 1332–1345 (2018).
12. Malumbres, M. Keeping Order in Anaphase. *Developmental Cell* **35**, 403–404 (2015).
13. Meyer, H., Drozdowska, A. & Dobrynin, G. A role for Cdc48/p97 and Aurora B in controlling chromatin condensation during exit from mitosis. *Biochemistry and Cell Biology = Biochimie Et Biologie Cellulaire* **88**, 23–28 (2010).
14. Afonso, O., Figueiredo, A. C. & Maiato, H. Late mitotic functions of Aurora kinases. *Chromosoma* **126**, 93–103 (2017).
15. Saxton, W. M. & McIntosh, J. R. Interzone microtubule behavior in late anaphase and telophase spindles. *The Journal of Cell Biology* **105**, 875–886 (1987).
16. Canman, J. C. & Cabernard, C. Mechanics of cell division and cytokinesis. *Molecular Biology of the Cell* **29**, 685–686 (2018).
17. WENZEL, E. S. & SINGH, A. T. K. Cell-cycle Checkpoints and Aneuploidy on the Path to Cancer. *In Vivo* **32**, 1–5 (2018).
18. Hasvold, G. *et al.* Hypoxia-induced alterations of G2 checkpoint regulators. *Molecular Oncology* **10**, 764–773 (2016).
19. Chao, H. X. *et al.* Orchestration of DNA damage checkpoint dynamics across the human cell cycle. *Cell systems* **5**, 445–459.e5 (2017).
20. Matellán, L. & Monje-Casas, F. Regulation of Mitotic Exit by Cell Cycle Checkpoints: Lessons From *Saccharomyces cerevisiae*. *Genes* **11**, (2020).
21. de Gooijer, M. C. *et al.* The G2 checkpoint—a node-based molecular switch. *FEBS Open Bio* **7**, 439–455 (2017).
22. Denton, D. & Kumar, S. Autophagy-dependent cell death. *Cell Death & Differentiation* **26**, 605–616 (2019).
23. Kessel, D. Paraptosis and Photodynamic Therapy: A Progress Report. *Photochemistry and Photobiology* **96**, 1096–1100 (2020).
24. Dhuriya, Y. K. & Sharma, D. Necroptosis: a regulated inflammatory mode of cell death. *Journal of Neuroinflammation* **15**, 199 (2018).
25. Khoury, M. K., Gupta, K., Franco, S. R. & Liu, B. Necroptosis in the Pathophysiology of Disease. *The American Journal of Pathology* **190**, 272–285 (2020).
26. Elmore, S. Apoptosis: A Review of Programmed Cell Death. *Toxicologic pathology* **35**, 495–516 (2007).
27. Salvesen, G. S. & Duckett, C. S. IAP proteins: blocking the road to death's door. *Nature Reviews Molecular Cell Biology* **3**, 401–410 (2002).
28. Loreto, C. *et al.* The Role of Intrinsic Pathway in Apoptosis Activation and Progression in Peyronie's Disease. *BioMed Research International* **2014**, (2014).
29. Fulda, S. & Debatin, K.-M. Extrinsic versus intrinsic apoptosis pathways in anticancer chemotherapy. *Oncogene* **25**, 4798–4811 (2006).
30. Ijiri, K. Apoptosis (cell death) induced in mouse bowel by 1,2-dimethylhydrazine, methylazoxymethanol acetate, and gamma-rays. *Cancer Research* **49**, 6342–6346 (1989).
31. Majno, G. & Joris, I. Apoptosis, oncosis, and necrosis. An overview of cell death. *The American Journal of Pathology* **146**, 3–15 (1995).
32. Hauser, P., Wang, S. & Didenko, V. V. Apoptotic Bodies: Selective Detection in Extracellular Vesicles. in *Signal Transduction Immunohistochemistry: Methods and Protocols* (ed. Kalyuzhny, A. E.) 193–200 (Springer, New York, NY, 2017). doi:10.1007/978-1-4939-6759-9_12.
33. Yang, V. W. Chapter 8 - The Cell Cycle. in *Physiology of the Gastrointestinal Tract (Sixth Edition)* (ed. Said, H. M.) 197–219 (Academic Press, 2018). doi:10.1016/B978-0-12-809954-4.00008-6.
34. Liu, D. X. & Greene, L. A. Neuronal apoptosis at the G1/S cell cycle checkpoint. *Cell and Tissue Research* **305**, 217–228 (2001).
35. Yang, V. W. Chapter 8 - The Cell Cycle. in *Physiology of the Gastrointestinal Tract (Sixth Edition)* (ed. Said, H. M.) 197–219 (Academic Press, 2018). doi:10.1016/B978-0-12-809954-4.00008-6.
36. McDaniel, L. & Schultz, R. The role of endogenous and exogenous DNA damage and mutagenesis. *Current opinion in genetics & development* **14**, 5–10 (2004).
37. Marnett, L. J. & Plastaras, J. P. Endogenous DNA damage and mutation. *Trends in Genetics* **17**, 214–221 (2001).
38. Chakarov, S., Petkova, R., Russev, G. C. & Zhelev, N. DNA damage and mutation. Types of DNA damage. *BioDiscovery* **11**, e8957 (2014).
39. Hakem, R. DNA-damage repair; the good, the bad, and the ugly. *The EMBO Journal* **27**, 589–605 (2008).

40. Chatterjee, N. & Walker, G. C. Mechanisms of DNA damage, repair and mutagenesis. *Environmental and molecular mutagenesis* **58**, 235–263 (2017).
41. Spivak, G. Nucleotide excision repair in humans. *DNA repair* **36**, 13–18 (2015).
42. Marteiijn, J. A., Lans, H., Vermeulen, W. & Hoeijmakers, J. H. J. Understanding nucleotide excision repair and its roles in cancer and ageing. *Nature Reviews. Molecular Cell Biology* **15**, 465–481 (2014).
43. Vermeulen, W. & Foustero, M. Mammalian Transcription-Coupled Excision Repair. *Cold Spring Harbor Perspectives in Biology* **5**, (2013).
44. Li, G.-M. Mechanisms and functions of DNA mismatch repair. *Cell Research* **18**, 85–98 (2008).
45. Adams, R. L. & Lindsay, H. What is hemimethylated DNA? *FEBS letters* **320**, 243–245 (1993).
46. del Rivero, J. & Kohn, E. C. PARP Inhibitors: The Cornerstone of DNA Repair-Targeted Therapies. *Oncology (Williston Park, N.Y.)* **31**, 265–273 (2017).
47. Liu, Y. *et al.* TOPBP1Dpb11 plays a conserved role in homologous recombination DNA repair through the coordinated recruitment of 53BP1Rad9. *The Journal of Cell Biology* **216**, 623–639 (2017).
48. Marini, F., Rawal, C. C., Liberi, G. & Pellicoli, A. Regulation of DNA Double Strand Breaks Processing: Focus on Barriers. *Frontiers in Molecular Biosciences* **6**, (2019).
49. Armour, J. A. L. Human Genetics: Measuring the Raw Material of Evolution. *Current Biology* **19**, R736–R738 (2009).
50. Bertram, J. S. The molecular biology of cancer. *Molecular Aspects of Medicine* **21**, 167–223 (2000).
51. Bignold, L. P. Variation, ‘evolution’, immortality and genetic instabilities in tumour cells. *Cancer Letters* **253**, 155–169 (2007).
52. Green, B. M. & Li, J. J. Loss of rereplication control in *Saccharomyces cerevisiae* results in extensive DNA damage. *Molecular Biology of the Cell* **16**, 421–432 (2005).
53. Vafa, O. *et al.* c-Myc can induce DNA damage, increase reactive oxygen species, and mitigate p53 function: a mechanism for oncogene-induced genetic instability. *Molecular Cell* **9**, 1031–1044 (2002).
54. Kurman, R. J. & Ronnett, B. M. Ovarian intestinal-type mucinous borderline tumors: a nomenclature change is long overdue. *International Journal of Gynecological Pathology: Official Journal of the International Society of Gynecological Pathologists* **29**, 552–553; author reply 553–554 (2010).
55. Fidler, I. J. Angiogenic heterogeneity: regulation of neoplastic angiogenesis by the organ microenvironment. *Journal of the National Cancer Institute* **93**, 1040–1041 (2001).
56. Nicolson, G. L. Molecular mechanisms of cancer metastasis: tumor and host properties and the role of oncogenes and suppressor genes. *Current Opinion in Oncology* **3**, 75–92 (1991).
57. Wang, F. Cancer immunotherapy and immunonutrition. *MOJAP* **3**, 146–147 (2017).
58. Ribatti, D. An historical note on the cell theory. *Experimental Cell Research* **364**, 1–4 (2018).
59. Narod, S. A. Reflections on screening mammography and the early detection of breast cancer: A Countercurrents Series. *Current Oncology (Toronto, Ont.)* **21**, 210–214 (2014).
60. Kemp, C. J. Animal models of chemical carcinogenesis: driving breakthroughs in cancer research for 100 years. *Cold Spring Harbor protocols* **2015**, 865–874 (2015).
61. Gasinska, A. The contribution of women to radiobiology: Marie Curie and beyond. *Reports of Practical Oncology and Radiotherapy: Journal of Great Poland Cancer Center in Poznan and Polish Society of Radiation Oncology* **21**, 250–258 (2016).
62. Gordon Zubrod, C. Combining talents for the management of cancer patients. *Cancer* **36**, 623–626 (1975).
63. Levine, A. J. p53: 800 million years of evolution and 40 years of discovery. *Nature Reviews. Cancer* **20**, 471–480 (2020).
64. Hounsfield, G. N. Computerized transverse axial scanning (tomography). 1. Description of system. *The British Journal of Radiology* **46**, 1016–1022 (1973).
65. Lauterbur, P. C. Image formation by induced local interactions. Examples employing nuclear magnetic resonance. 1973. *Clinical Orthopaedics and Related Research* 3–6 (1989).
66. Lander, E. S. *et al.* Initial sequencing and analysis of the human genome. *Nature* **409**, 860–921 (2001).
67. Gamlen, H. E. X-Ray Treatment of Epithelioma of the Tongue. *Archives of The Roentgen Ray* **7**, 97–99 (1903).
68. Goodman, L. S. *et al.* Nitrogen mustard therapy. Use of methyl-bis(beta-chloroethyl)amine hydrochloride and tris(beta-chloroethyl)amine hydrochloride for Hodgkin’s disease, lymphosarcoma, leukemia and certain allied and miscellaneous disorders. *JAMA* **251**, 2255–2261 (1984).
69. Aliperti, L. A., Predina, J. D., Vachani, A. & Singhal, S. Local and systemic recurrence is the Achilles heel of cancer surgery. *Annals of Surgical Oncology* **18**, 603–607 (2011).
70. Bindal, A. K. *et al.* Surgery versus radiosurgery in the treatment of brain metastasis. *Journal of Neurosurgery* **84**, 748–754 (1996).
71. Lee, T.-F. *et al.* Technical Advancement of Radiation Therapy. *BioMed Research International* **2014**, 797412 (2014).
72. Wright, C. M., Dan, T., Dicker, A. P. & Simone, N. L. microRNAs: The Short Link between Cancer and RT-Induced DNA Damage Response. *Frontiers in Oncology* **4**, 133 (2014).
73. Taşkın-Tok, T., Gowder, S., Taşkın-Tok, T. & Gowder, S. Anticancer Drug — Friend or Foe. in *Pharmacology and Therapeutics* (IntechOpen, 2014). doi:10.5772/58552.
74. Borgeaud, M. *et al.* The Evolving Role of Immune-Checkpoint Inhibitors in Malignant Pleural Mesothelioma. *Journal of Clinical Medicine* **12**, 1757 (2023).
75. Shearman, C. W. & Loeb, L. A. On the fidelity of DNA replication. Specificity of nucleotide substitution by intercalating agents. *The Journal of Biological Chemistry* **258**, 4477–4484 (1983).
76. Kaulen, L. D. & Baehring, J. M. Treatment Options for Recurrent Primary CNS Lymphoma. *Current Treatment Options in Oncology* **23**, 1548–1565 (2022).

77. Wu, W. *et al.* Glioblastoma Multiforme (GBM): An overview of current therapies and mechanisms of resistance. *Pharmacological research* **171**, 105780 (2021).
78. Tiwari, M. Antimetabolites: Established cancer therapy. *Journal of Cancer Research and Therapeutics* **8**, 510 (2012).
79. Cronstein, B. N. The mechanism of action of methotrexate. *Rheumatic Diseases Clinics of North America* **23**, 739–755 (1997).
80. Hortobágyi, G. N. Anthracyclines in the treatment of cancer. An overview. *Drugs* **54 Suppl 4**, 1–7 (1997).
81. McGowan, J. V. *et al.* Anthracycline Chemotherapy and Cardiotoxicity. *Cardiovascular Drugs and Therapy* **31**, 63–75 (2017).
82. Ewesuedo, R. B. & Ratain, M. J. Topoisomerase I Inhibitors. *The Oncologist* **2**, 359–364 (1997).
83. Nitiss, J. L., Soans, E., Rogojina, A., Seth, A. & Mishina, M. Topoisomerase Assays. *Current Protocols in Pharmacology CHAPTER*, Unit3.3 (2012).
84. Wall, M. E. *et al.* Plant Antitumor Agents. I. The Isolation and Structure of Camptothecin, a Novel Alkaloidal Leukemia and Tumor Inhibitor from *Camptotheca acuminata*1,2. *Journal of the American Chemical Society* **88**, 3888–3890 (1966).
85. Shuel, S. L. Targeted cancer therapies. *Canadian Family Physician* **68**, 515–518 (2022).
86. McKeage, K. & Perry, C. M. Trastuzumab: a review of its use in the treatment of metastatic breast cancer overexpressing HER2. *Drugs* **62**, 209–243 (2002).
87. Salles, G. *et al.* Rituximab in B-Cell Hematologic Malignancies: A Review of 20 Years of Clinical Experience. *Advances in Therapy* **34**, 2232–2273 (2017).
88. Wang, Y., Schmid-Bindert, G. & Zhou, C. Erlotinib in the treatment of advanced non-small cell lung cancer: an update for clinicians. *Therapeutic Advances in Medical Oncology* **4**, 19–29 (2012).
89. Fu, Z., Li, S., Han, S., Shi, C. & Zhang, Y. Antibody drug conjugate: the ‘biological missile’ for targeted cancer therapy. *Signal Transduction and Targeted Therapy* **7**, 93 (2022).
90. Zhu, Y.-S., Tang, K. & Lv, J. Peptide-drug conjugate-based novel molecular drug delivery system in cancer. *Trends in Pharmacological Sciences* **42**, 857–869 (2021).
91. Cortés, J. *et al.* Trastuzumab Deruxtecan versus Trastuzumab Emtansine for Breast Cancer. *The New England Journal of Medicine* **386**, 1143–1154 (2022).
92. Barok, M., Joensuu, H. & Isola, J. Trastuzumab emtansine: mechanisms of action and drug resistance. *Breast cancer research: BCR* **16**, 209 (2014).
93. Goswami, G. miRNA: An Overview of its Role in Cancer Research and Diagnosis. *Advances in Biotechnology & Microbiology* **6**, (2017).
94. Sung, H. *et al.* Global Cancer Statistics 2020: GLOBOCAN Estimates of Incidence and Mortality Worldwide for 36 Cancers in 185 Countries. *CA: A Cancer Journal for Clinicians* **71**, 209–249 (2021).
95. Wu, Q., Siddharth, S. & Sharma, D. Triple Negative Breast Cancer: A Mountain Yet to Be Scaled Despite the Triumphs. *Cancers* **13**, 3697 (2021).
96. Loibl, S. *et al.* Abstract S3-1: Neoadjuvant Chemotherapy in the very young 35 years of age or younger. *Cancer Research* **72**, S3-1 (2012).
97. Gogia, A. *et al.* Taxane and anthracycline based neoadjuvant chemotherapy for locally advanced breast cancer: institutional experience. *Asian Pacific journal of cancer prevention: APJCP* **15**, 1989–1992 (2014).
98. Koppiker, C. B. Abstract P3-07-08: Germline mutational profiling in Indian TNBCs. *Cancer Research* **82**, P3-07–08 (2022).
99. Eikesdal, H. P. *et al.* Olaparib monotherapy as primary treatment in unselected triple negative breast cancer. *Annals of Oncology: Official Journal of the European Society for Medical Oncology* **32**, 240–249 (2021).
100. Mittendorf, E. A. *et al.* PD-L1 Expression in Triple Negative Breast Cancer. *Cancer immunology research* **2**, 361–370 (2014).
101. Gong, Z. *et al.* Compound Libraries: Recent Advances and Their Applications in Drug Discovery. *Current Drug Discovery Technologies* **14**, 216–228.
102. Gorse, D. & Lahana, R. Functional diversity of compound libraries. *Current Opinion in Chemical Biology* **4**, 287–294 (2000).
103. Fukunishi, Y. & Lintuluoto, M. Development of Chemical Compound Libraries for In Silico Drug Screening. *Current Computer-Aided Drug Design* **6**, 90–102.
104. Moudi, M., Go, R., Yien, C. Y. S. & Nazre, Mohd. Vinca Alkaloids. *International Journal of Preventive Medicine* **4**, 1231–1235 (2013).
105. Kumar, S. *et al.* Clinical trials and progress with paclitaxel in ovarian cancer. *International Journal of Women’s Health* **2**, 411–427 (2010).
106. Fitzpatrick, F. A. & Wheeler, R. The immunopharmacology of paclitaxel (Taxol), docetaxel (Taxotere), and related agents. *International Immunopharmacology* **3**, 1699–1714 (2003).
107. Moen, M. D., McKeage, K., Plosker, G. L. & Siddiqui, M. A. A. Imatinib: a review of its use in chronic myeloid leukaemia. *Drugs* **67**, 299–320 (2007).
108. Moffat, J. G., Vincent, F., Lee, J. A., Eder, J. & Prunotto, M. Opportunities and challenges in phenotypic drug discovery: an industry perspective. *Nature Reviews Drug Discovery* **16**, 531–543 (2017).
109. Swinney, D. C. & Lee, J. A. Recent advances in phenotypic drug discovery. *F1000Research* **9**, F1000 Faculty Rev-944 (2020).
110. Yoshida, T. *et al.* Identification and Characterization of a Novel Chemotype MEK Inhibitor Able to Alter the Phosphorylation State of MEK1/2. *Oncotarget* **3**, 1533–1545 (2012).
111. Feoktistova, M., Geserick, P. & Leverkus, M. Crystal Violet Assay for Determining Viability of Cultured Cells. *Cold Spring Harbor Protocols* **2016**, pdb.prot087379 (2016).
112. Adan, A., Kiraz, Y. & Baran, Y. Cell Proliferation and Cytotoxicity Assays. *Current Pharmaceutical Biotechnology* **17**, 1213–1221.
113. Ganellin, C. R., Jefferis, R. & Roberts, S. M. *Introduction to Biological and Small Molecule Drug Research and Development: Theory and Case Studies.* (Academic Press, 2013).

114. Druker, B. J. & Lydon, N. B. Lessons learned from the development of an Abl tyrosine kinase inhibitor for chronic myelogenous leukemia. *Journal of Clinical Investigation* **105**, 3–7 (2000).
115. Weigelt, B., Geyer, F. C. & Reis-Filho, J. S. Histological types of breast cancer: How special are they? *Molecular Oncology* **4**, 192–208 (2010).
116. Briest, S. & Stearns, V. Tamoxifen metabolism and its effect on endocrine treatment of breast cancer. *Clinical Advances in Hematology & Oncology: H&O* **7**, 185–192 (2009).
117. Morgan, M. M., Arendt, L. M., Alarid, E. T., Beebe, D. J. & Johnson, B. P. Mammary adipose stromal cells derived from obese women reduce sensitivity to the aromatase inhibitor anastrozole in an organotypic breast model. *The FASEB Journal* **33**, 8623–8633 (2019).
118. Baker, J. H. E. *et al.* Heterogeneous distribution of trastuzumab in HER2-positive xenografts and metastases: role of the tumor microenvironment. *Clinical & Experimental Metastasis* **35**, 691–705 (2018).
119. Tečić Vuger, A. *et al.* CHARACTERISTICS AND PROGNOSIS OF TRIPLE-NEGATIVE BREAST CANCER PATIENTS: A CROATIAN SINGLE INSTITUTION RETROSPECTIVE COHORT STUDY. *Acta Clinica Croatica* **59**, 97–108 (2020).
120. Gupta, G. K. *et al.* Perspectives on Triple-Negative Breast Cancer: Current Treatment Strategies, Unmet Needs, and Potential Targets for Future Therapies. *Cancers* **12**, 2392 (2020).
121. Lüscher, B. *et al.* ADP-Ribosylation, a Multifaceted Posttranslational Modification Involved in the Control of Cell Physiology in Health and Disease. *Chemical Reviews* **118**, 1092–1136 (2018).
122. Matta, E., Kiribayeva, A., Khassenov, B., Matkarimov, B. T. & Ishchenko, A. A. Insight into DNA substrate specificity of PARP1-catalysed DNA poly(ADP-ribosylation). *Scientific Reports* **10**, 3699 (2020).
123. van Beek, L. *et al.* PARP Power: A Structural Perspective on PARP1, PARP2, and PARP3 in DNA Damage Repair and Nucleosome Remodelling. *International Journal of Molecular Sciences* **22**, 5112 (2021).
124. Ali, A. A. E. *et al.* The zinc-finger domains of PARP1 cooperate to recognize DNA strand breaks. *Nature Structural & Molecular Biology* **19**, 685–692 (2012).
125. Alesosova, E. E. & Lavrik, O. I. Poly(ADP-ribosylation) by PARP1: reaction mechanism and regulatory proteins. *Nucleic Acids Research* **47**, 3811–3827 (2019).
126. Herceg, Z. & Wang, Z.-Q. Functions of poly (ADP-ribose) polymerase (PARP) in DNA repair, genomic integrity and cell death. *Mutation Research/Fundamental and Molecular Mechanisms of Mutagenesis* **477**, 97–110 (2001).
127. Loeffler, P. A. *et al.* Structural studies of the PARP-1 BRCT domain. *BMC Structural Biology* **11**, 37 (2011).
128. Cuneo, M. J., Gabel, S. A., Krahn, J. M., Ricker, M. A. & London, R. E. The structural basis for partitioning of the XRCC1/DNA ligase III- α BRCT-mediated dimer complexes. *Nucleic Acids Research* **39**, 7816–7827 (2011).
129. Beniey, M., Haque, T. & Hassan, S. Translating the role of PARP inhibitors in triple-negative breast cancer. *Oncoscience* **6**, 287 (2019).
130. Spigel, D. R. PARP Inhibitors in Lung Cancer. *Journal of Thoracic Oncology* **7**, S392–S393 (2012).
131. Higuchi, F. *et al.* Restoration of Temozolomide Sensitivity by PARP Inhibitors in Mismatch Repair Deficient Glioblastoma is Independent of Base Excision Repair. *Clinical Cancer Research* **26**, 1690–1699 (2020).
132. pubmeddev & al, F. A., *et.* Combination Olaparib and Temozolomide in Relapsed Small Cell Lung Cancer. - PubMed - NCBI. <https://www.ncbi.nlm.nih.gov/pubmed/31416802>.
133. Papadimitriou, M., Mountzios, G. & Papadimitriou, C. A. The role of PARP inhibition in triple-negative breast cancer: Unraveling the wide spectrum of synthetic lethality. *Cancer Treatment Reviews* **67**, 34–44 (2018).
134. Zhu, Y. *et al.* Tamoxifen-resistant breast cancer cells are resistant to DNA-damaging chemotherapy because of upregulated BARD1 and BRCA1. *Nature Communications* **9**, 1595 (2018).
135. Ashworth, A. & Lord, C. J. Synthetic lethal therapies for cancer: what's next after PARP inhibitors? *Nature Reviews Clinical Oncology* **15**, 564–576 (2018).
136. Zoppoli, G. *et al.* Putative DNA/RNA helicase Schlafen-11 (SLFN11) sensitizes cancer cells to DNA-damaging agents. *Proceedings of the National Academy of Sciences* **109**, 15030–15035 (2012).
137. Coleman, N., Zhang, B., Byers, L. A. & Yap, T. A. The role of Schlafen 11 (SLFN11) as a predictive biomarker for targeting the DNA damage response. *British Journal of Cancer* **124**, 857–859 (2021).
138. Stewart, C. A. *et al.* Dynamic variations in epithelial-to-mesenchymal transition (EMT), ATM, and SLFN11 govern response to PARP inhibitors and cisplatin in small cell lung cancer. *Oncotarget* **8**, 28575–28587 (2017).
139. Wang, R. *et al.* Molecular Mechanism of Selective Binding of NMS-P118 to PARP-1 and PARP-2: A Computational Perspective. *Frontiers in Molecular Biosciences* **7**, 50 (2020).
140. Sachdev, E., Tabatabai, R., Roy, V., Rimel, B. J. & Mita, M. M. PARP Inhibition in Cancer: An Update on Clinical Development. *Targeted Oncology* **14**, 657–679 (2019).
141. Slade, D. PARP and PARG inhibitors in cancer treatment. *Genes & Development* **34**, 360–394 (2020).
142. Farago, A. F. *et al.* Combination Olaparib and Temozolomide in Relapsed Small-Cell Lung Cancer. *Cancer Discovery* **9**, 1372–1387 (2019).
143. Dai, X., Cheng, H., Bai, Z. & Li, J. Breast Cancer Cell Line Classification and Its Relevance with Breast Tumor Subtyping. *Journal of Cancer* **8**, 3131–3141 (2017).
144. Ruberte, A. C. *et al.* Novel selenadiazole derivatives as selective antitumor and radical scavenging agents. *European Journal of Medicinal Chemistry* **157**, 14–27 (2018).
145. Berman, H. M. *et al.* The Protein Data Bank. *Nucleic Acids Research* **28**, 235–242 (2000).
146. Nottbohm, A. C., Dothager, R. S., Putt, K. S., Hoyt, M. T. & Hergenrother, P. J. A Colorimetric Substrate for Poly(ADP-Ribose) Polymerase-1, VPARP, and Tankyrase-1. *Angewandte Chemie* **119**, 2112–2115 (2007).

147. Kanamori, K. S. *et al.* Two Different Methods of Quantification of Oxidized Nicotinamide Adenine Dinucleotide (NAD⁺) and Reduced Nicotinamide Adenine Dinucleotide (NADH) Intracellular Levels: Enzymatic Coupled Cycling Assay and Ultra-performance Liquid Chromatography (UPLC)-Mass Spectrometry. *Bio-protocol* **8**, e2937 (2018).
148. Rao, X., Huang, X., Zhou, Z. & Lin, X. An improvement of the 2^{−ΔΔCT} method for quantitative real-time polymerase chain reaction data analysis. *Biostatistics, bioinformatics and biomathematics* **3**, 71–85 (2013).
149. Rahn, J. *et al.* Altered protein expression pattern in colon tissue of mice upon supplementation with distinct selenium compounds. *PROTEOMICS* **17**, 1600486 (2017).
150. Seixas, N., Ravanello, B. B., Morgan, I., Kaluderović, G. N. & Wessjohann, L. A. Chlorambucil Conjugated Ugi Dendrimers with PAMAM-NH₂ Core and Evaluation of Their Anticancer Activity. *Pharmaceutics* **11**, (2019).
151. Sultani, H. N. *et al.* Access to New Cytotoxic Triterpene and Steroidal Acid-TEMPO Conjugates by Ugi Multicomponent-Reactions. *International Journal of Molecular Sciences* **22**, 7125 (2021).
152. Morgan, I., Wessjohann, L. A. & Kaluderović, G. N. In Vitro Anticancer Screening and Preliminary Mechanistic Study of A-Ring Substituted Anthraquinone Derivatives. *Cells* **11**, 168 (2022).
153. Hwang, K. *et al.* The Combination PARP Inhibitor Olaparib With Temozolomide in an Experimental Glioblastoma Model. *In Vivo* **35**, 2015–2023 (2021).
154. Irwin, C. P. *et al.* PARPi-FL - a Fluorescent PARP1 Inhibitor for Glioblastoma Imaging. *Neoplasia (New York, N.Y.)* **16**, 432–440 (2014).
155. Salinas, B. *et al.* Radioiodinated PARP1 tracers for glioblastoma imaging. *EJNMMI Research* **5**, 46 (2015).
156. Ryu, H., Ahn, J. & Choi, H. K. Novel Benzamide Derivatives: Synthesis and Bioactivity as Potent PARP-1 Inhibitors. *Bulletin of the Korean Chemical Society* **38**, 935–943 (2017).
157. Menear, K. A. *et al.* 4-[3-(4-Cyclopropanecarbonyl)piperazine-1-carbonyl]-4-fluorobenzyl]-2H-phthalazin-1-one: A Novel Bioavailable Inhibitor of Poly(ADP-ribose) Polymerase-1. *Journal of Medicinal Chemistry* **51**, 6581–6591 (2008).
158. Maksimainen, M. M. *et al.* Analogs of TIQ-A as Inhibitors of Human Mono-ADP-Ribosylating PARPs. 2021.08.30.458193 <https://www.biorxiv.org/content/10.1101/2021.08.30.458193v1> (2021) doi:10.1101/2021.08.30.458193.
159. Kulkarni, S. S., Singh, S., Shah, J. R., Low, W.-K. & Talele, T. T. Synthesis and SAR optimization of quinazolin-4(3H)-ones as poly(ADP-ribose)polymerase-1 inhibitors. *European Journal of Medicinal Chemistry* **50**, 264–273 (2012).
160. Rudolph, J., Jung, K. & Luger, K. Inhibitors of PARP: Number crunching and structure gazing. *Proceedings of the National Academy of Sciences* **119**, e2121979119 (2022).
161. Pilić, P. G., Gay, C. M., Byers, L. A., O'Connor, M. J. & Yap, T. A. PARP Inhibitors: Extending Benefit Beyond BRCA-Mutant Cancers. *Clinical Cancer Research* **25**, 3759–3771 (2019).
162. Dziadkowiec, K. N., Gašiorowska, E., Nowak-Markwitz, E. & Jankowska, A. PARP inhibitors: review of mechanisms of action and BRCA1/2 mutation targeting. *Przegląd Menopauzalny = Menopause Review* **15**, 215–219 (2016).
163. Murai, J. *et al.* Resistance to PARP inhibitors by SLFN11 inactivation can be overcome by ATR inhibition. *Oncotarget* **7**, 76534–76550 (2016).
164. Lok, B. H. *et al.* PARP Inhibitor Activity Correlates with SLFN11 Expression and Demonstrates Synergy with Temozolomide in Small Cell Lung Cancer. *Clinical cancer research : an official journal of the American Association for Cancer Research* **23**, 523–535 (2017).
165. Krishnakumar, R. & Kraus, W. L. The PARP Side of the Nucleus: Molecular Actions, Physiological Outcomes, and Clinical Targets. *Molecular cell* **39**, 8–24 (2010).
166. Ferraris, D. Overview of PARP Inhibitor Design and Optimization. in *PARP Inhibitors for Cancer Therapy* (eds Curtin, N. J. & Sharma, R. A.) 183–203 (Springer International Publishing, Cham, 2015). doi:10.1007/978-3-319-14151-0_7.
167. Cockcroft, X. *et al.* Phthalazinones 2: Optimisation and synthesis of novel potent inhibitors of poly(ADP-ribose)polymerase. *Bioorganic & Medicinal Chemistry Letters* **16**, 1040–1044 (2006).
168. Johannes, J. W. *et al.* Discovery of AZ0108, an orally bioavailable phthalazinone PARP inhibitor that blocks centrosome clustering. *Bioorganic & Medicinal Chemistry Letters* **25**, 5743–5747 (2015).
169. Coussens, N. P. *et al.* Small-Molecule Screens: A Gateway to Cancer Therapeutic Agents with Case Studies of Food and Drug Administration-Approved Drugs. *Pharmacological Reviews* **69**, 479–496 (2017).
170. Lambert, A. W., Pattabiraman, D. R. & Weinberg, R. A. Emerging biological principles of metastasis. *Cell* **168**, 670–691 (2017).
171. Martel, C. de, Georges, D., Bray, F., Ferlay, J. & Clifford, G. M. Global burden of cancer attributable to infections in 2018: a worldwide incidence analysis. *The Lancet Global Health* **8**, e180–e190 (2020).
172. Shaguftha, null & Ahmad, I. Tamoxifen a pioneering drug: An update on the therapeutic potential of tamoxifen derivatives. *European Journal of Medicinal Chemistry* **143**, 515–531 (2018).
173. Bobach, C. *et al.* Multiple readout assay for hormonal (androgenic and antiandrogenic) and cytotoxic activity of plant and fungal extracts based on differential prostate cancer cell line behavior. *Journal of Ethnopharmacology* **155**, 721–730 (2014).
174. Foglietta, J. *et al.* Cardiotoxicity of aromatase inhibitors in breast cancer patients. *Clinical Breast Cancer* **17**, 11–17 (2017).
175. Diaby, V. *et al.* A cost-effectiveness analysis of trastuzumab-containing treatment sequences for HER-2 positive metastatic breast cancer patients in Taiwan. *Breast (Edinburgh, Scotland)* **49**, 141–148 (2020).
176. Lyons, T. G. Targeted therapies for triple-negative breast cancer. *Current Treatment Options in Oncology* **20**, 82 (2019).
177. Heimes, A.-S. & Schmidt, M. Atezolizumab for the treatment of triple-negative breast cancer. *Expert Opinion on Investigational Drugs* **28**, 1–5 (2019).
178. Hsu, J.-Y., Chang, C.-J. & Cheng, J.-S. Survival, treatment regimens and medical costs of women newly diagnosed with metastatic triple-negative breast cancer. *Scientific Reports* **12**, 729 (2022).

179. Tobe, M. *et al.* Discovery of quinazolines as a novel structural class of potent inhibitors of NF-kappa B activation. *Bioorganic & Medicinal Chemistry* **11**, 383–391 (2003).
180. Guillon, R. *et al.* Discovery of a novel broad-spectrum antifungal agent derived from albaconazole. *ACS medicinal chemistry letters* **4**, 288–292 (2013).
181. Jiang, S. *et al.* Antimalarial activities and therapeutic properties of febrifugine analogs. *Antimicrobial Agents and Chemotherapy* **49**, 1169–1176 (2005).
182. Sim, EHA, Yang, IA, Wood-Baker, R, Bowman, RV & Fong, K. Gefitinib for advanced non-small cell lung cancer. *Cochrane Database of Systematic Reviews* (2018) doi:10.1002/14651858.CD006847.pub2.
183. Yoshikawa, D. *et al.* Vandetanib (ZD6474), an inhibitor of VEGFR and EGFR signalling, as a novel molecular-targeted therapy against cholangiocarcinoma. *British Journal of Cancer* **100**, 1257–1266 (2009).
184. Blackledge, G. New developments in cancer treatment with the novel thymidylate synthase inhibitor raltitrexed ('Tomudex'). *British Journal of Cancer* **77 Suppl 2**, 29–37 (1998).
185. Shagufta, null & Ahmad, I. An insight into the therapeutic potential of quinazoline derivatives as anticancer agents. *MedChemComm* **8**, 871–885 (2017).
186. Pakrashi, S. C., Bhattacharyya, J., Johnson, L. F. & Budzikiewicz, H. Studies on indian medicinal plants—VI: Structures of glycosmicine, glycorine and glycosminine, the minor alkaloids from *Glycosmis arborea* (roxb.) DC. *Tetrahedron* **19**, 1011–1026 (1963).
187. Wang, C.-J. *et al.* Discovery of penipanoic C-inspired 2-(3,4,5-trimethoxybenzoyl)quinazolin-4(3H)-one derivatives as potential anticancer agents by inhibiting cell proliferation and inducing apoptosis in hepatocellular carcinoma cells. *European Journal of Medicinal Chemistry* **224**, 113671 (2021).
188. Subik, K. *et al.* The Expression Patterns of ER, PR, HER2, CK5/6, EGFR, Ki-67 and AR by Immunohistochemical Analysis in Breast Cancer Cell Lines. *Breast Cancer: Basic and Clinical Research* **4**, 35–41 (2010).
189. Holliday, D. L. & Speirs, V. Choosing the right cell line for breast cancer research. *Breast cancer research: BCR* **13**, 215 (2011).
190. Rae, J. M. *et al.* EGFR and EGFRvIII expression in primary breast cancer and cell lines. *Breast Cancer Research and Treatment* **87**, 87–95 (2004).
191. Veß, A. *et al.* A dual phenotype of MDA-MB-468 cancer cells reveals mutual regulation of tensin3 and adhesion plasticity. *Journal of Cell Science* **130**, 2172–2184 (2017).
192. Padró, M. *et al.* Genome-independent hypoxic repression of estrogen receptor alpha in breast cancer cells. *BMC cancer* **17**, 203 (2017).
193. Tassone, P. *et al.* BRCA1 expression modulates chemosensitivity of BRCA1-defective HCC1937 human breast cancer cells. *British Journal of Cancer* **88**, 1285–1291 (2003).
194. Zhang, Y. *et al.* Long noncoding RNA LINP1 regulates repair of DNA double-strand breaks in triple-negative breast cancer. *Nature Structural & Molecular Biology* **23**, 522–530 (2016).
195. Luberto, C. *et al.* Inhibition of tumor necrosis factor-induced cell death in MCF7 by a novel inhibitor of neutral sphingomyelinase. *The Journal of Biological Chemistry* **277**, 41128–41139 (2002).
196. Khan, M. F. *et al.* Cichorins D-F: Three new compounds from cichorium intybus and their biological effects. *Molecules (Basel, Switzerland)* **25**, E4160 (2020).
197. Kaluđerović, G. N. *et al.* Ruthenium(II) p-cymene complex bearing 2,2'-dipyridylamine targets caspase 3 deficient MCF-7 breast cancer cells without disruption of antitumor immune response. *Journal of Inorganic Biochemistry* **153**, 315–321 (2015).
198. Krajinović, T., Kaluđerović, G. N., Wessjohann, L. A., Mijatović, S. & Maksimović-Ivanić, D. Versatile antitumor potential of isoxanthohumol: Enhancement of paclitaxel activity in vivo. *Pharmacological Research* **105**, 62–73 (2016).
199. Maksimovic-Ivanic, D. *et al.* Anticancer properties of the novel nitric oxide-donating compound (S,R)-3-phenyl-4,5-dihydro-5-isoxazole acetic acid-nitric oxide in vitro and in vivo. *Molecular Cancer Therapeutics* **7**, 510–520 (2008).
200. Faustino-Rocha, A. *et al.* Estimation of rat mammary tumor volume using caliper and ultrasonography measurements. *Lab Animal* **42**, 217–224 (2013).
201. Evangelatov, A. *et al.* Epirubicin loading in poly(butyl cyanoacrylate) nanoparticles manifests via altered intracellular localization and cellular response in cervical carcinoma (HeLa) cells. *Drug Delivery* **23**, 2235–2244 (2016).
202. Murugan, S. & Amaravadi, R. K. Methods for Studying Autophagy Within the Tumor Microenvironment. *Advances in experimental medicine and biology* **899**, 145–166 (2016).
203. Pervaiz, S. & Clement, M.-V. Tumor Intracellular Redox Status and Drug Resistance-Serendipity or a Causal Relationship? *Current Pharmaceutical Design* **10**, 1969–1977 (2004).
204. Tao, K., Fang, M., Alroy, J. & Sahagian, G. G. Imagable 4T1 model for the study of late stage breast cancer. *BMC cancer* **8**, 228 (2008).
205. Hostettmann, K., Dey, P. M. & Harborne, J. B. *Methods in Plant Biochemistry Vol. 6, Vol. 6.* (Academic Press., London, 1991).
206. Rickert, D. E. Metabolism of nitroaromatic compounds. *Drug Metabolism Reviews* **18**, 23–53 (1987).
207. Kovacic, P. & Somanathan, R. Nitroaromatic compounds: Environmental toxicity, carcinogenicity, mutagenicity, therapy and mechanism. *Journal of Applied Toxicology* **34**, 810–824 (2014).
208. Ringe, D., Turesky, R. J., Skipper, P. L. & Tannenbaum, S. R. Structure of the single stable hemoglobin adduct formed by 4-aminobiphenyl in vivo. *Chemical Research in Toxicology* **1**, 22–24 (1988).
209. Sabbioni, G. Hemoglobin Adducts and Urinary Metabolites of Arylamines and Nitroarenes. *Chemical Research in Toxicology* **30**, 1733–1766 (2017).
210. Cenas, N., Prast, S., Nivinskas, H., Sarlauskas, J. & Arnér, E. S. J. Interactions of Nitroaromatic Compounds with the Mammalian Selenoprotein Thioredoxin Reductase and the Relation to Induction of Apoptosis in Human Cancer Cells*. *Journal of Biological Chemistry* **281**, 5593–5603 (2006).

211. Li, J. & Yuan, J. Caspases in apoptosis and beyond. *Oncogene* **27**, 6194–6206 (2008).
212. Zhang, J. H. & Xu, M. DNA fragmentation in apoptosis. *Cell Research* **10**, 205–211 (2000).
213. Jänicke, R. U. MCF-7 breast carcinoma cells do not express caspase-3. *Breast Cancer Research and Treatment* **117**, 219–221 (2009).
214. Prat, A. *et al.* Characterization of cell lines derived from breast cancers and normal mammary tissues for the study of the intrinsic molecular subtypes. *Breast Cancer Research and Treatment* **142**, 237–255 (2013).
215. Mueller, K. L., Yang, Z.-Q., Haddad, R., Ethier, S. P. & Boerner, J. L. EGFR/Met association regulates EGFR TKI resistance in breast cancer. *Journal of Molecular Signaling* **5**, 8 (2010).
216. Yamaguchi, H. *et al.* Caspase-independent cell death is involved in the negative effect of EGF receptor inhibitors on cisplatin in non-small cell lung cancer cells. *Clinical Cancer Research: An Official Journal of the American Association for Cancer Research* **19**, 845–854 (2013).
217. Pulaski, B. A. & Ostrand-Rosenberg, S. Mouse 4T1 breast tumor model. *Current Protocols in Immunology* **Chapter 20**, Unit 20.2 (2001).
218. Woo, Y., Lee, H.-J., Jung, Y. M. & Jung, Y.-J. Regulated Necrotic Cell Death in Alternative Tumor Therapeutic Strategies. *Cells* **9**, 2709 (2020).
219. Richards, C. H., Mohammed, Z., Qayyum, T., Horgan, P. G. & McMillan, D. C. The prognostic value of histological tumor necrosis in solid organ malignant disease: a systematic review. *Future Oncology* **7**, 1223–1235 (2011).
220. Dietzel, M. *et al.* The Necrosis Sign in Magnetic Resonance-Mammography: Diagnostic Accuracy in 1,084 Histologically Verified Breast Lesions. *The Breast Journal* **16**, 603–608 (2010).
221. Zhang, Y. *et al.* Clinicopathological study of centrally necrotizing carcinoma of the breast. *BMC Cancer* **15**, 282 (2015).
222. Pu, R. T., Schott, A. F., Sturtz, D. E., Griffith, K. A. & Kleer, C. G. Pathologic Features of Breast Cancer Associated With Complete Response to Neoadjuvant Chemotherapy: Importance of Tumor Necrosis. *The American Journal of Surgical Pathology* **29**, 354 (2005).
223. Jayasekara, H. *et al.* Mortality after breast cancer as a function of time since diagnosis by estrogen receptor status and age at diagnosis. *International journal of cancer* **145**, 3207–3217 (2019).
224. Safe, S., Lee, S.-O. & Jin, U.-H. Role of the Aryl Hydrocarbon Receptor in Carcinogenesis and Potential as a Drug Target. *Toxicological Sciences* **135**, 1–16 (2013).
225. Androutsopoulos, V. P., Tsatsakis, A. M. & Spandidos, D. A. Cytochrome P450 CYP1A1: wider roles in cancer progression and prevention. *BMC Cancer* **9**, 187 (2009).
226. Androutsopoulos, V., Arrou, R. R., Hall, J. F., Surichan, S. & Potter, G. A. Antiproliferative and cytostatic effects of the natural product eupatorin on MDA-MB-468 human breast cancer cells due to CYP1-mediated metabolism. *Breast Cancer Research : BCR* **10**, R39 (2008).
227. Hussain, H. Prof. Ludger Wessjohann: A Lifelong Career Dedicated to a Remarkable Service in “Natural Products Sciences”. *International Journal of Molecular Sciences* **23**, 5440 (2022).
228. Mladenović, M. *et al.* pH-Responsive Release of Ruthenium Metallotherapeutics from Mesoporous Silica-Based Nanocarriers. *Pharmaceutics* **13**, 460 (2021).
229. Ivascu, A. & Kubbies, M. Rapid generation of single-tumor spheroids for high-throughput cell function and toxicity analysis. *Journal of Biomolecular Screening* **11**, 922–932 (2006).
230. Lam, Y. T. H. *et al.* Rare Glutamic Acid Methyl Ester Peptaibols from *Sepedonium ampullosporum* Damon KSH 534 Exhibit Promising Antifungal and Anticancer Activity. *International Journal of Molecular Sciences* **22**, 12718 (2021).
231. Ware, I. *et al.* Bioactive Phenolic Compounds from *Peperomia obtusifolia*. *Molecules* **27**, 4363 (2022).
232. Herceg, Z. & Wang, Z. Q. Functions of poly(ADP-ribose) polymerase (PARP) in DNA repair, genomic integrity and cell death. *Mutation Research* **477**, 97–110 (2001).
233. Kaluđerović, G. N. *et al.* Ruthenium(II) p-cymene complex bearing 2,2'-dipyridylamine targets caspase 3 deficient MCF-7 breast cancer cells without disruption of antitumor immune response. *Journal of Inorganic Biochemistry* **153**, 315–321 (2015).
234. Smolko, L. *et al.* Two isostructural Co(II) flufenamato and niflumato complexes with bathocuproine: Analogues with a different cytotoxic activity. *Journal of Inorganic Biochemistry* **210**, 111160 (2020).
235. Seixas, N., Ravello, B. B., Morgan, I., Kaluđerović, G. N. & Wessjohann, L. A. Chlorambucil Conjugated Ugi Dendrimers with PAMAM-NH₂ Core and Evaluation of Their Anticancer Activity. *Pharmaceutics* **11**, E59 (2019).
236. Gao, L., Loveless, J., Shay, C. & Teng, Y. Targeting ROS-Mediated Crosstalk Between Autophagy and Apoptosis in Cancer. *Advances in Experimental Medicine and Biology* **1260**, 1–12 (2020).
237. Neuhoff, V., Stamm, R. & Eibl, H. Clear background and highly sensitive protein staining with Coomassie Blue dyes in polyacrylamide gels: A systematic analysis. *ELECTROPHORESIS* **6**, 427–448 (1985).
238. Lennicke, C. *et al.* Individual effects of different selenocompounds on the hepatic proteome and energy metabolism of mice. *Biochimica et Biophysica Acta (BBA) - General Subjects* **1861**, 3323–3334 (2017).
239. Varadi, M. *et al.* AlphaFold Protein Structure Database: massively expanding the structural coverage of protein-sequence space with high-accuracy models. *Nucleic Acids Research* **50**, D439–D444 (2022).
240. Jumper, J. *et al.* Highly accurate protein structure prediction with AlphaFold. *Nature* **596**, 583–589 (2021).
241. Bisson, W. H. *et al.* Modeling of the Aryl Hydrocarbon Receptor (AhR) Ligand Binding Domain and Its Utility in Virtual Ligand Screening to Predict New AhR Ligands. *Journal of Medicinal Chemistry* **52**, 5635–5641 (2009).
242. Lichtenfels, R. *et al.* Comparative Expression Profiling of Distinct T Cell Subsets Undergoing Oxidative Stress. *PLoS one* **7**, e41345 (2012).
243. Cichočka, M. *et al.* The Novel Role of hnRNP UL1 in Human Cell Nucleoli. *International Journal of Biological Sciences* **18**, 4809–4823 (2022).

244. Quintana, F. J. The aryl hydrocarbon receptor: a molecular pathway for the environmental control of the immune response. *Immunology* **138**, 183–189 (2013).
245. Jacobs, K. A. & Gavard, J. 3D Endothelial Cell Migration. *Methods in Molecular Biology (Clifton, N.J.)* **1749**, 51–58 (2018).
246. Meinhardt, A.-L. *et al.* The BCL-2 family member BOK promotes KRAS-driven lung cancer progression in a p53-dependent manner. *Oncogene* **41**, 1376–1382 (2022).
247. Arlt, V. M. *et al.* Metabolic activation of benzo[a]pyrene in vitro by hepatic cytochrome P450 contrasts with detoxification in vivo: experiments with hepatic cytochrome P450 reductase null mice. *Carcinogenesis* **29**, 656–665 (2008).
248. Moserová, M. *et al.* Analysis of benzo[*a*]pyrene metabolites formed by rat hepatic microsomes using high pressure liquid chromatography: optimization of the method. *Interdisciplinary Toxicology* **2**, 239–244 (2009).
249. Golubkov, V. S. *et al.* Membrane type-1 matrix metalloproteinase confers aneuploidy and tumorigenicity on mammary epithelial cells. *Cancer Research* **66**, 10460–10465 (2006).
250. Cai, G. *et al.* MicroRNA-181a suppresses norethisterone-promoted tumorigenesis of breast epithelial MCF10A cells through the PGRMC1/EGFR-PI3K/Akt/mTOR signaling pathway. *Translational Oncology* **14**, 101068 (2021).
251. Kröncke, K. D., Fehsel, K. & Kolb-Bachofen, V. Nitric oxide: cytotoxicity versus cytoprotection—how, why, when, and where? *Nitric Oxide: Biology and Chemistry* **1**, 107–120 (1997).
252. Santes-Palacios, R. *et al.* Regulation of Human Cytochrome P4501A1 (hCYP1A1): A Plausible Target for Chemoprevention? *BioMed Research International* **2016**, 5341081 (2016).
253. Moyano, P. *et al.* Aryl Hydrocarbon Receptor Activation Produces Heat Shock Protein 90 and 70 Overexpression, Prostaglandin E2/Wnt/ β -Catenin Signaling Disruption, and Cell Proliferation in MCF-7 and MDA-MB-231 Cells after 24 h and 14 Days of Chlorpyrifos Treatment. *Chemical Research in Toxicology* **34**, 2019–2023 (2021).
254. Barouki, R. Aryl Hydrocarbon Receptor. in *Encyclopedia of Cancer* (ed. Schwab, M.) 372–377 (Springer, Berlin, Heidelberg, 2017). doi:10.1007/978-3-662-46875-3_405.
255. Grishanova, A. Y. & Perepechaeva, M. L. Aryl Hydrocarbon Receptor in Oxidative Stress as a Double Agent and Its Biological and Therapeutic Significance. *International Journal of Molecular Sciences* **23**, 6719 (2022).
256. Stevens, E. A., Mezrich, J. D. & Bradfield, C. A. The aryl hydrocarbon receptor: a perspective on potential roles in the immune system. *Immunology* **127**, 299–311 (2009).
257. Shivanna, B., Chu, C. & Moorthy, B. The Aryl Hydrocarbon Receptor (AHR): A Novel Therapeutic Target for Pulmonary Diseases? *International Journal of Molecular Sciences* **23**, 1516 (2022).
258. Zhao, B., Degroot, D. E., Hayashi, A., He, G. & Denison, M. S. CH223191 is a ligand-selective antagonist of the Ah (Dioxin) receptor. *Toxicological Sciences: An Official Journal of the Society of Toxicology* **117**, 393–403 (2010).
259. Patrizi, B. & Siciliani de Cumis, M. TCDD Toxicity Mediated by Epigenetic Mechanisms. *International Journal of Molecular Sciences* **19**, E4101 (2018).
260. Grimaldi, G., Rajendra, S. & Matthews, J. The aryl hydrocarbon receptor regulates the expression of TIPARP and its cis long non-coding RNA, TIPARP-AS1. *Biochemical and Biophysical Research Communications* **495**, 2356–2362 (2018).
261. Al-Ghezi, Z. Z. *et al.* AhR Activation by TCDD (2,3,7,8-Tetrachlorodibenzo-p-dioxin) Attenuates Pertussis Toxin-Induced Inflammatory Responses by Differential Regulation of Tregs and Th17 Cells Through Specific Targeting by microRNA. *Frontiers in Microbiology* **10**, (2019).
262. Olguín-Reyes, S., Camacho-Carranza, R., Hernández-Ojeda, S., Elinos-Baez, M. & Espinosa-Aguirre, J. J. Bergamottin is a competitive inhibitor of CYP1A1 and is antimutagenic in the Ames test. *Food and Chemical Toxicology: An International Journal Published for the British Industrial Biological Research Association* **50**, 3094–3099 (2012).
263. Larigot, L., Juricek, L., Dairou, J. & Coumoul, X. AhR signaling pathways and regulatory functions. *Biochimie Open* **7**, 1–9 (2018).
264. Coelho, N. R. *et al.* Pharmacological blockage of the AHR-CYP1A1 axis: a call for in vivo evidence. *Journal of Molecular Medicine* **100**, 215–243 (2022).
265. Murray, I. A., Patterson, A. D. & Perdew, G. H. AH RECEPTOR LIGANDS IN CANCER: FRIEND AND FOE. *Nature reviews. Cancer* **14**, 801–814 (2014).
266. Zhang, S., Qin, C. & Safe, S. H. Flavonoids as aryl hydrocarbon receptor agonists/antagonists: effects of structure and cell context. *Environmental Health Perspectives* **111**, 1877–1882 (2003).
267. Gilbert, J., De Iuliis, G. N., McCluskey, A. & Sakoff, J. A. A novel naphthalimide that selectively targets breast cancer via the arylhydrocarbon receptor pathway. *Scientific Reports* **10**, 13978 (2020).

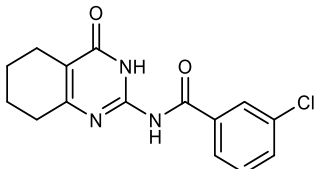
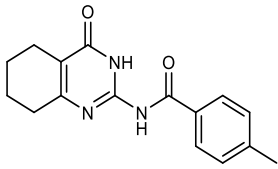
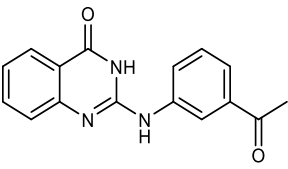
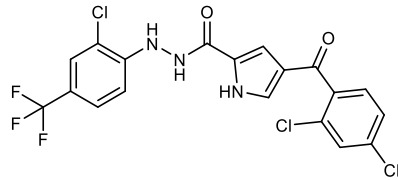
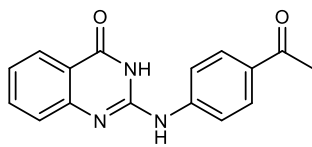
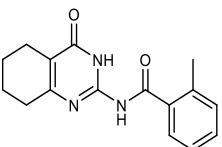
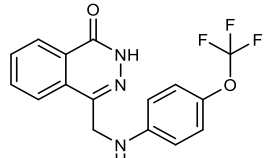
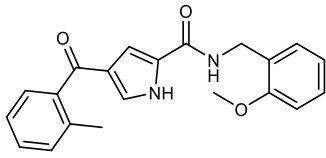
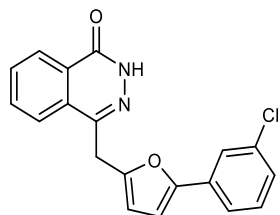
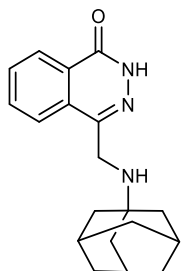
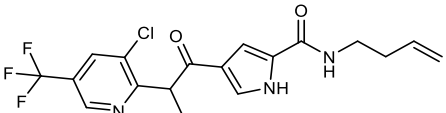
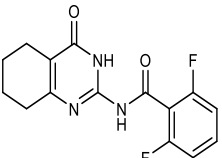
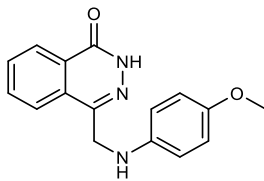
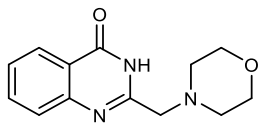
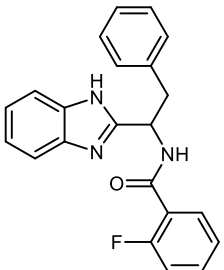
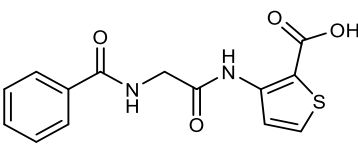
Supplementary information

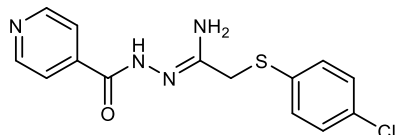
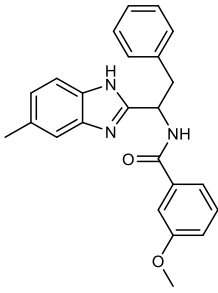
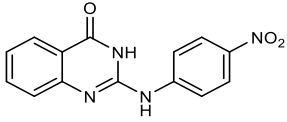
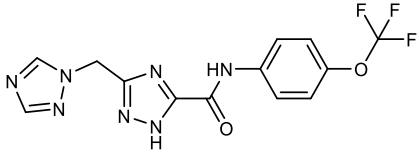
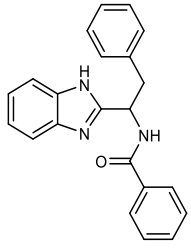
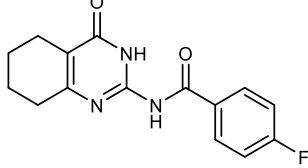
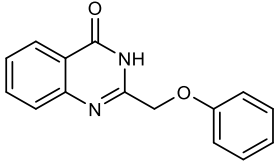
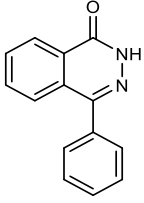
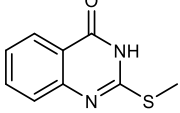
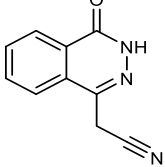
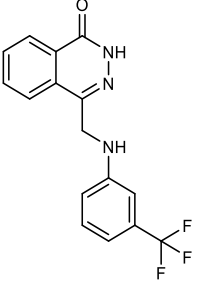
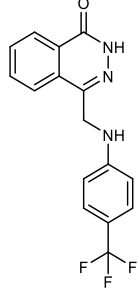
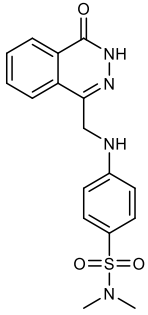
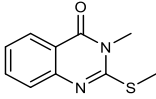
Chapter 2 : Identification and characterization of novel inhibitors of human poly(ADP-ribose) polymerase-1

Table S1 List of the compounds identified as potential hPARP-1 inhibitors by the *in silico* hPARP-1 docking and screening study.

Compound	Structure	Compound	Structure
1		2	
3		4	
5		6	
7		8	
9		10	
11		12	

13		14	
15		16	
17		18	
19		20	
21		22	
23		24	
25		26	
27		28	
29		30	
31		32	

33		34	
35		36	
37		38	
39		40	
41		42	
43		44	
45		46	
47		48	

49		50	
51		52	
53		54	
55		56	
57		58	
59		60	
61		62	

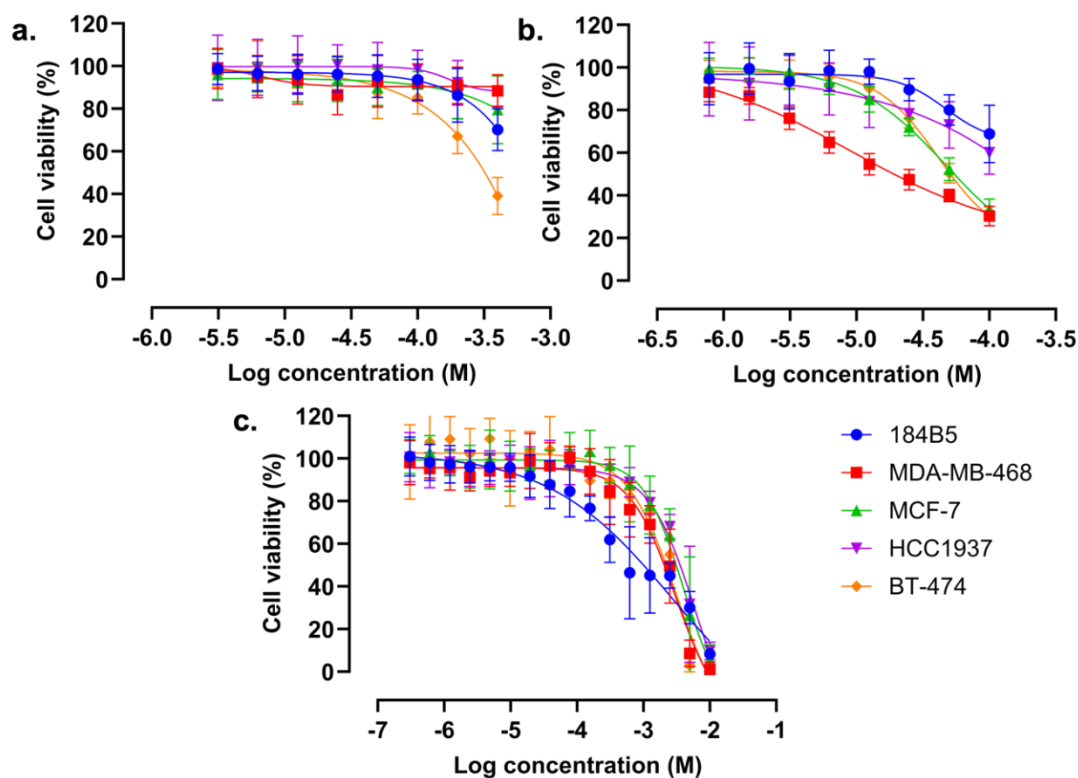
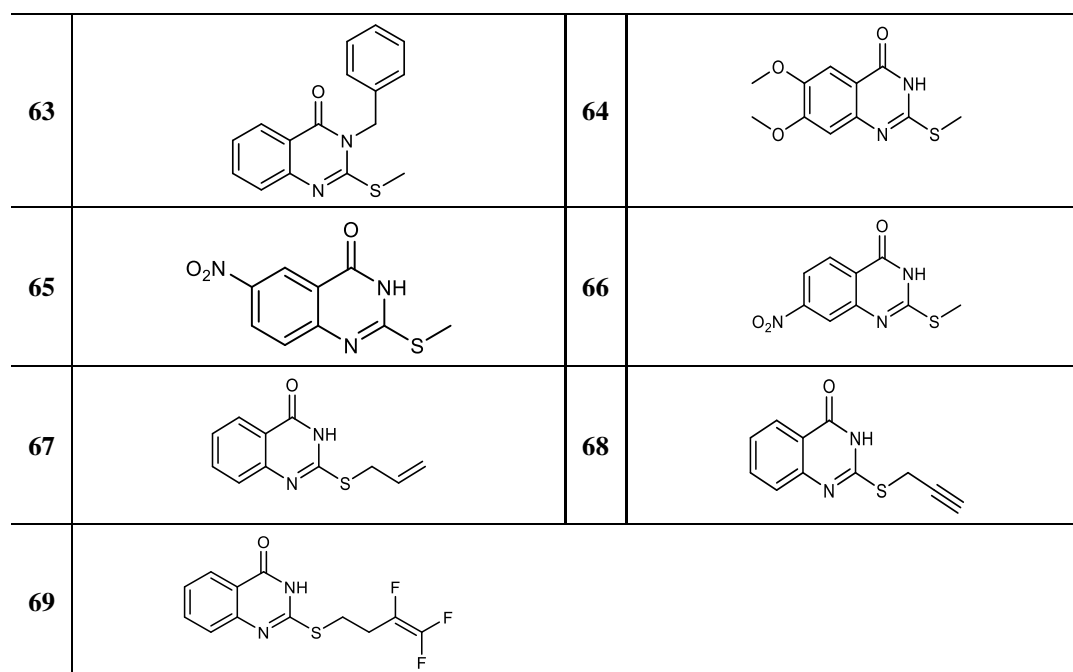


Fig.S1 Cell viability dose-response curves of the breast cell lines under investigation upon 72 h treatment with **a**, compound **57**; **b**, OLP, and **c**, TMZ. Cell viability was determined by using crystal violet (CV) assay.

Table S2 Summary of the calculated IC_{50} values (given in mM) of TMZ, TMZ combined with 100 μ M of compound **57**, and TMZ combined with 1.56 μ M of OLP as tested against the breast cell lines. Cells were treated for 72 h and cell viability was determined by using the CV assay.

Treatment	184B5	MDA-MB-468	MCF-7	HCC1937	BT-474
TMZ	0.98 ± 0.82	2.06 ± 0.79	3.44 ± 1.72	3.74 ± 1.5	2.21 ± 0.01
TMZ + compound 57	0.32 ± 0.07	2.77 ± 0.25	2.23 ± 0.74	5.66 ± 0.32	4.87 ± 6.42
TMZ + OLP	4.95 ± 3.9	0.13 ± 0.04	2.85 ± 2.08	3.66 ± 1.04	5.05 ± 0.56

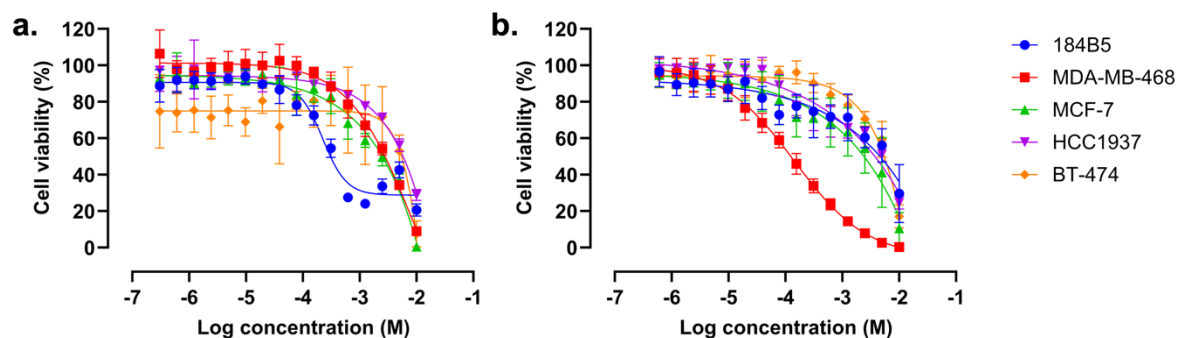


Fig.S2 Dose-dependent curves of several breast cell lines. The cell lines were treated with several concentrations of TMZ combined with IC₁₀ of **a**, compound 57 and **b**, OLP for 72 h and the viability was determined using CV assay.

Table S3 Sequences of the qPCR primers used in the gene expression study.

Gene name	Sense sequence (5'-3')	Antisense sequence (5'-3')
GAPDH	TTG CCA TCA ATG ACC CCT TCA	CGC CCC ACT TGA TTT TGG A
SLFN-11	CCCGATAACCTTCACACTCA	CTGATCATGCAAGCATAGCC
hPARP-1	ATT TCG CTG ACA TGG TCT CC	ACA TGT TTC CAA GGG CAA CT

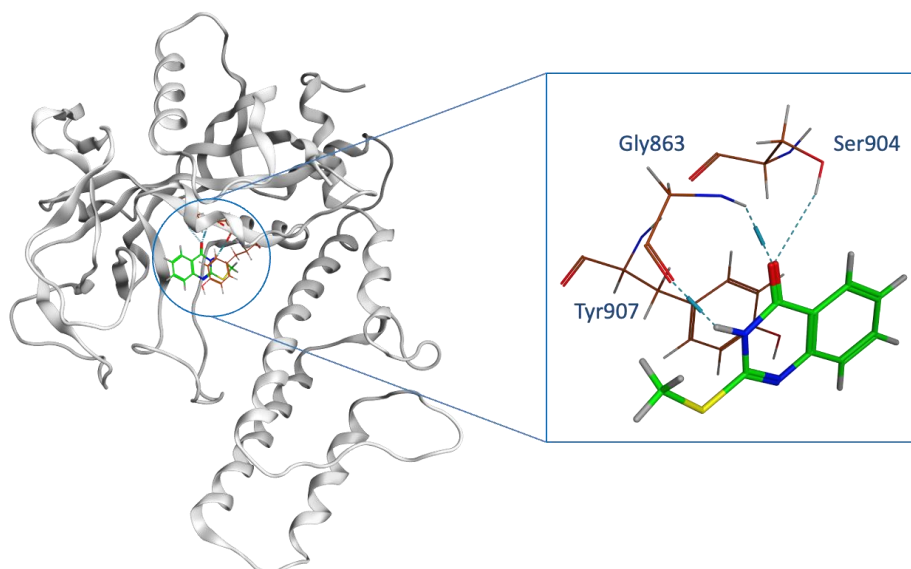


Fig.S3 The structure of the ART subdomain of hPARP-1 (PDB code: 3GJW) interacting with the newly identified hPARP-1 inhibitor (compound 57, green).

Table S4 Binding energy of the most relative compounds' interaction with the ART domain of hPARP-1 calculated by using MOE software.

Compound name	Binding energy (kcal/mol)
Compound 57	-5.90
Quinazolin-4(3 <i>H</i>)-one	-5.31
Phthalazin-1(2 <i>H</i>)-one	-5.35
Olaparib	-8.16

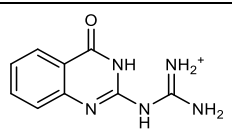
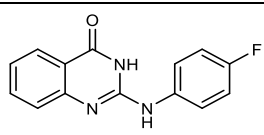
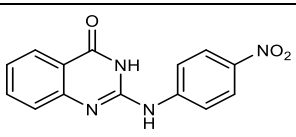
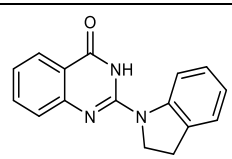
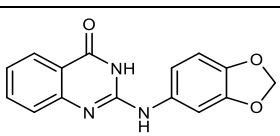
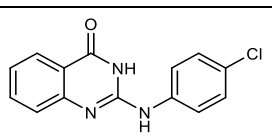
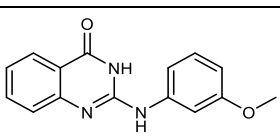
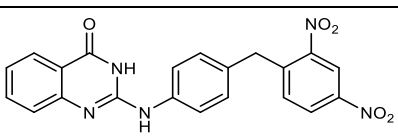
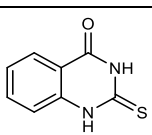
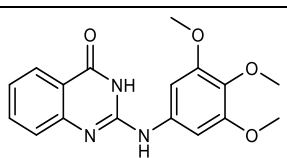
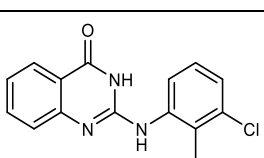
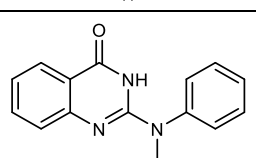
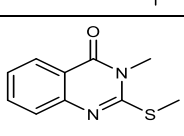
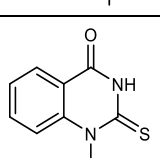
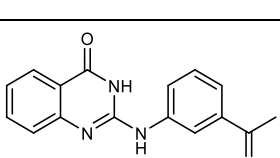
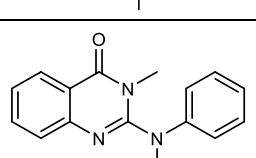
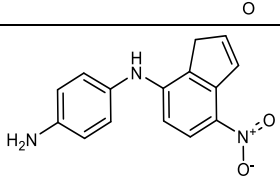
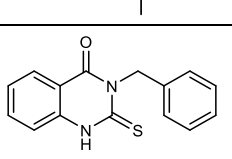
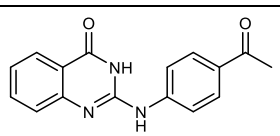
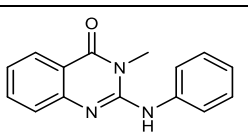
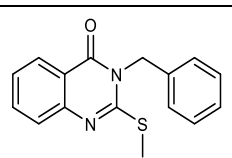
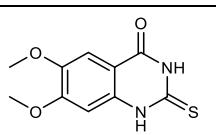
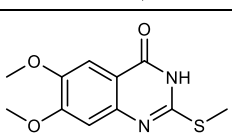
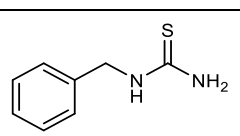
Chapter 3 : The impact of 9-azaglycophymine derivatives on the proliferation of various breast cancer cell lines *in vitro* and *in vivo*

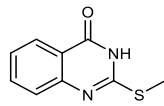
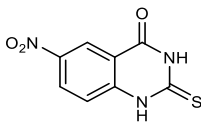
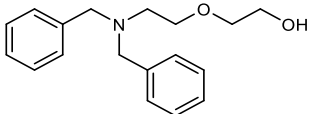
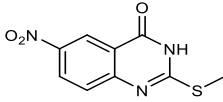
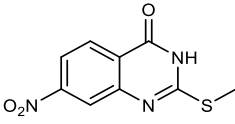
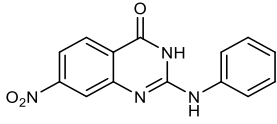
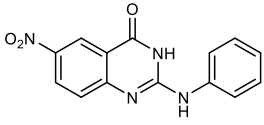
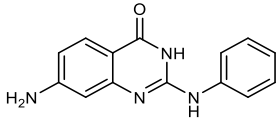
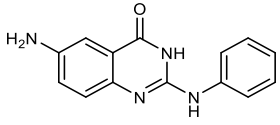
Table S5 The different expression levels of ER, PR, HER2/neu and BRCA-1 in the four investigated human breast cancer cell lines.

Genes / BC type	MCF-7	MDA-MB-468	HCC1937	BT-474
HER2/neu	-	-	-	+
PR	+	-	-	+
ER	+	-	-	+
EGFR	+	++++	+++	+
BRCA-1	allelic loss	allelic loss	mutated	allelic loss
BC type	HR+	TNBC	TNBC	HER2+

Table S6 List of tested compounds 1 – 49.

Compound	Structure	Compound	Structure
1		2	
3		4	
5		6	
7		8	
9		10	
11		12	
13		14	
15		16	

17		18	
19		20	
21		22	
23		24	
25		26	
27		28	
29		30	
31		32	
33		34	
35		36	
37		38	
39		40	

41		42	
43		44	
45		46	
47		48	
49			

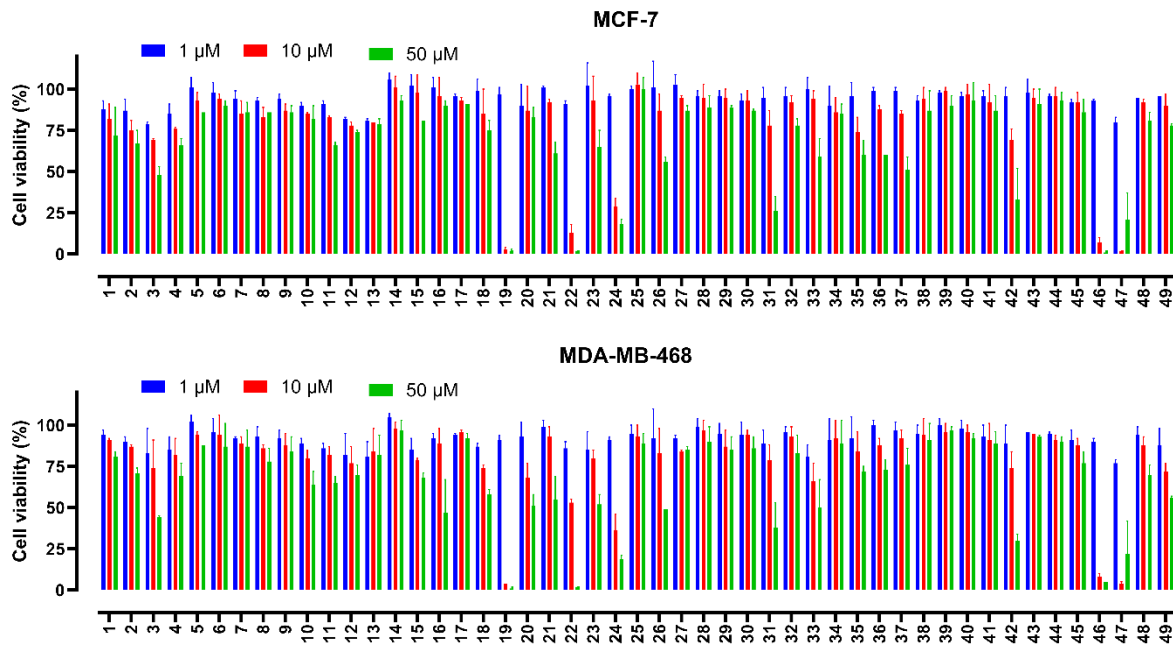


Fig.S4 MCF-7 and MDA-MB-468 cells' viability after 72 h treatment with the selected compounds and indicated concentrations. Cell viability was determined by using CV assay.

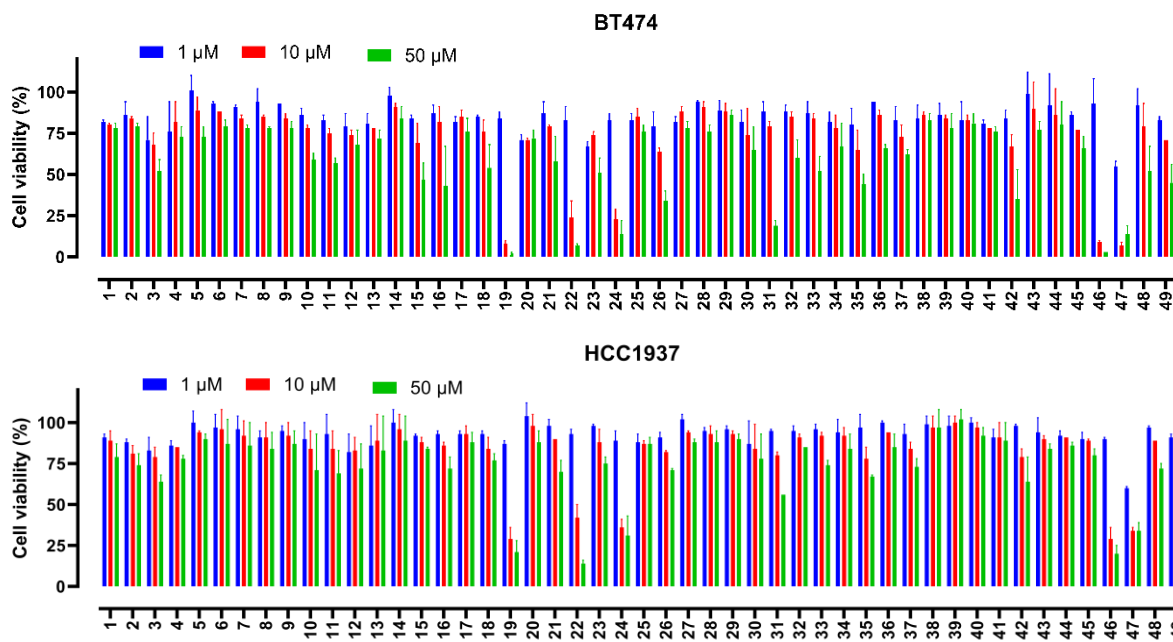


Fig.S5 BT-474 and HCC1937 cells' viability after 72 h treatment with the selected compounds and indicated concentrations. Cell viability was determined by using CV assay.

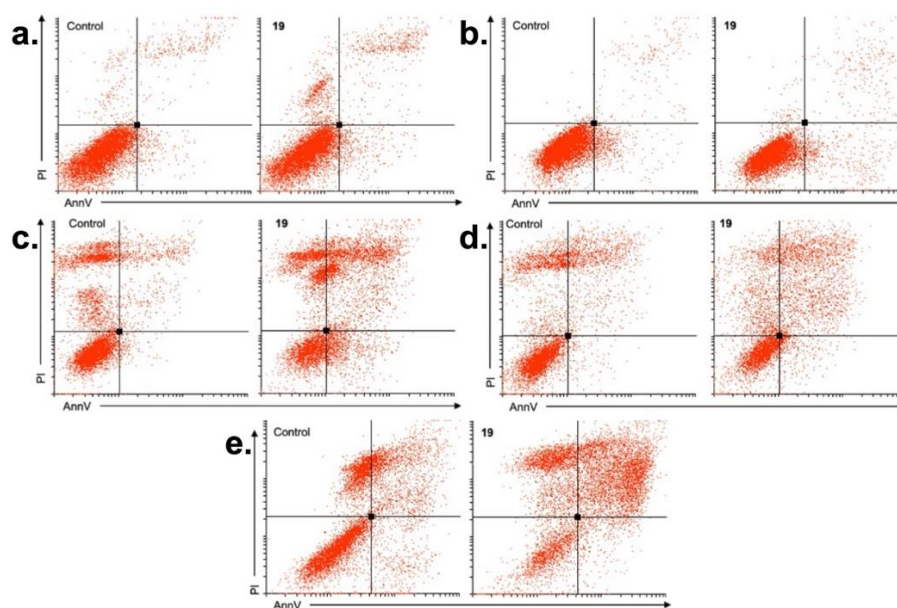


Fig.S6 Representative dot plots for the impact of compound **19** applied at IC_{50} for 72 h on the induction of apoptosis, measured by using AnnV/PI double staining against **a**, MCF-7; **b**, MDA-MB-468; **c**, BT-474; **d**, HCC1937 and **e**, 4T1 cells. For the AnnV stain, the fluorescence intensity was analyzed using excitation at 488 ± 20 nm and emission at 530 ± 30 nm (plotted at x-axis). For the PI dye, the fluorescence intensity was analyzed by using excitation and emission at 561 ± 20 and 610 ± 20 nm (plotted at y-axis), respectively. The lower left, lower right and the upper right quadrants represent live cells, early and late apoptotic cells, respectively.

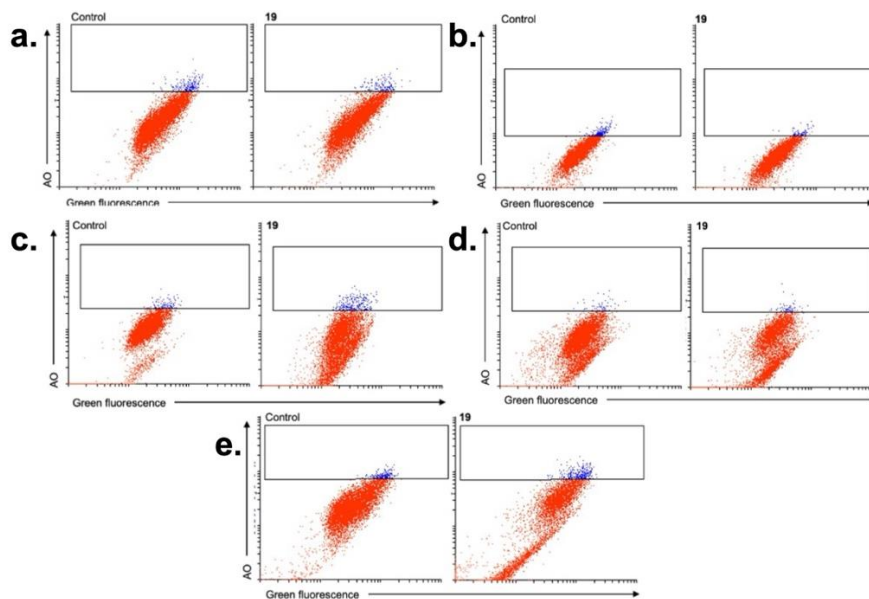


Fig.S7 Representative dot plots for the impact of compound **19** applied at IC_{50} for 72 h on the induction of autophagy, measured by performing acridine orange assay: **a**, MCF-7; **b**, MDA-MB-468; **c**, BT-474; **d**, HCC1937 and **e**, 4T1 cells. The green fluorescence intensity was analyzed by using excitation at 488 ± 20 nm and emission at 530 ± 30 nm (plotted at x-axis). For the AO dye, the fluorescence intensity was analyzed by using excitation and emission at 488 ± 20 and 695 ± 40 nm (plotted at y-axis), respectively.

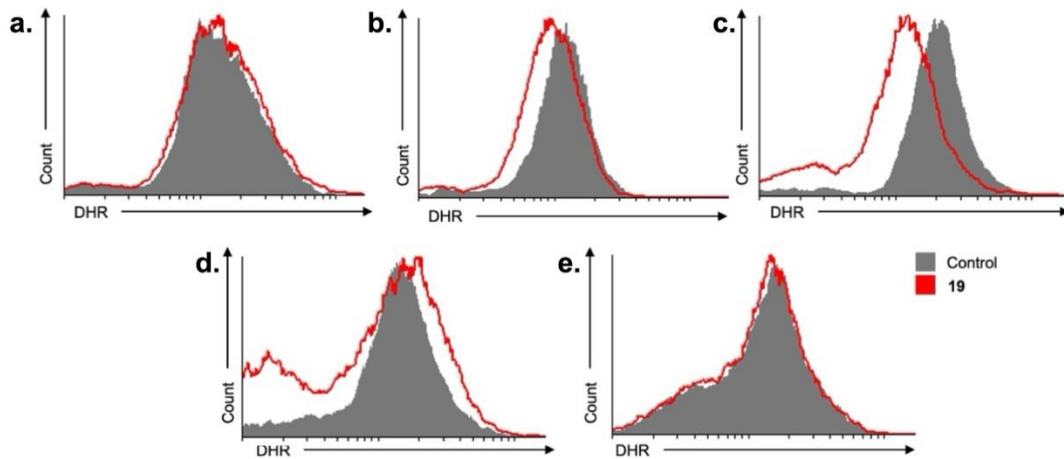


Fig.S8 Representative histograms for the impact of compound **19** applied at IC_{50} for 72 h on the induction of ROS production, determined with DHR assay by **a**, MCF-7; **b**, MDA-MB-468; **c**, BT-474; **d**, HCC1937 and **e**, 4T1 cells. For the DHR stain, the fluorescence intensity was analyzed by using excitation at 488 ± 20 nm and emission at 530 ± 30 nm (plotted at x-axis).

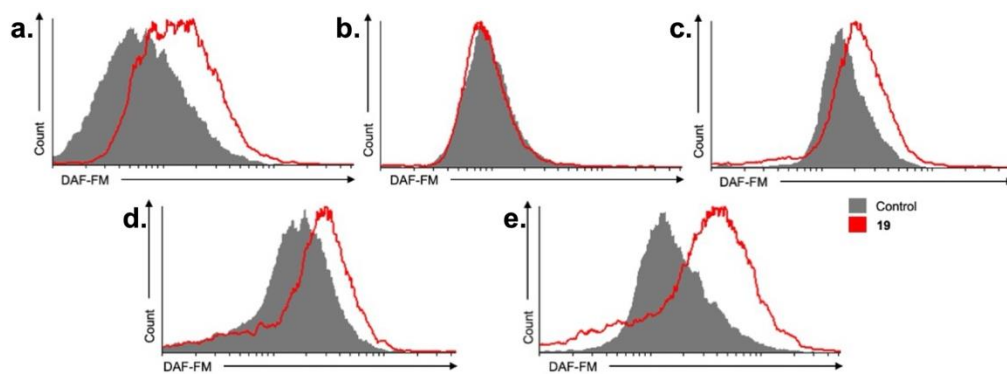


Fig.S9 Representative histograms for the impact of compound **19** applied at IC_{50} for 72 h on NO production, measured by using DAF-FM dye: **a**, MCF-7; **b**, MDA-MB-468; **c**, BT-474; **d**, HCC1937 and **e**, 4T1. For the DAF-FM stain, the fluorescence intensity was analyzed by using excitation at 488 ± 20 nm and emission at 530 ± 30 nm (plotted at x-axis).

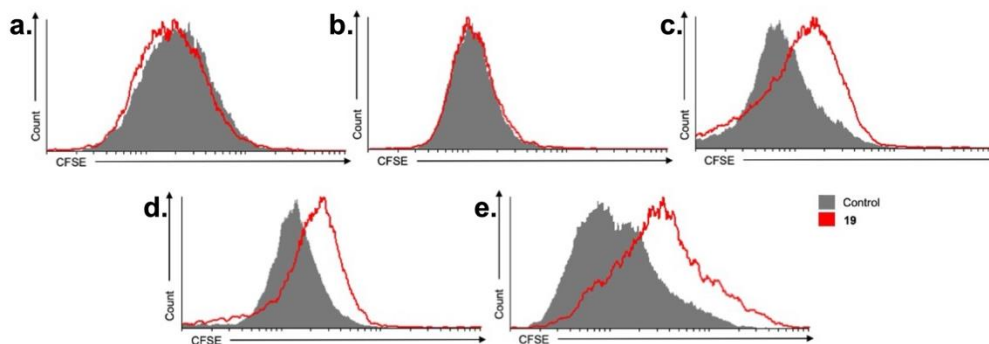


Fig.S10 Representative histograms for the impact of compound **19** applied at IC_{50} for 72 h on the inhibition of cells proliferation, in which cells were stained by using CFSE reagent, and then treated with the lead compound: **a**, MCF-7; **b**, MDA-MB-468; **c**, BT-474; **d**, HCC1937 and **e**, 4T1 cells. For CFSE stain, the fluorescence intensity was analyzed by using excitation at 488 ± 20 nm and emission at 530 ± 30 nm (plotted at x-axis).

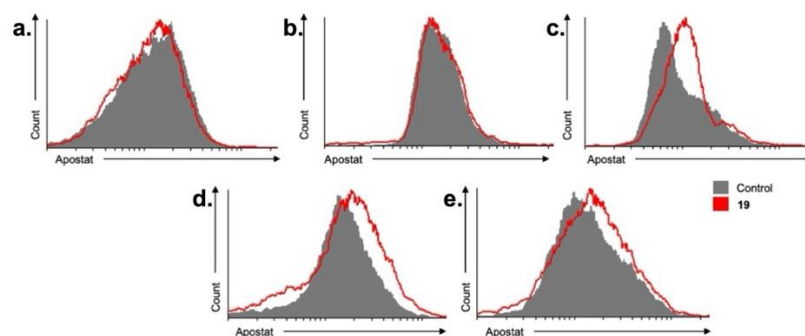


Fig.S11 Representative histograms for the impact of compound **19** applied at IC_{50} for 72 h on the induction of pan-caspases induction, measured by using the ApoStat staining kit: **a**, MCF-7; **b**, MDA-MB-468; **c**, BT-474; **d**, HCC1937 and **e**, 4T1 cells. For the ApoStat stain, the fluorescence intensity was analyzed by using excitation at 488 ± 20 nm and emission at 530 ± 30 nm (plotted at x-axis).

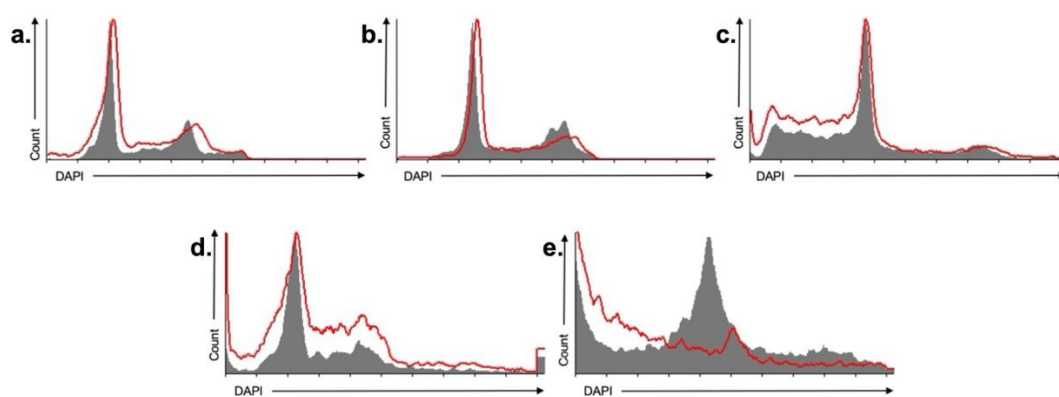


Fig.S12 Representative histograms for the impact of compound **19** applied at IC_{50} for 72 h on the cell cycle status distribution in G0/G1, S and G2/M phases, measured by using the DAPI stain: **a**, MCF-7; **b**, MDA-MB-468; **c**, BT-474; **d**, HCC1937 and **e**, 4T1 cells. For DAPI stain, the fluorescence intensity was analyzed by using excitation at 375 ± 20 nm and emission at 450 ± 20 nm (plotted at x-axis).

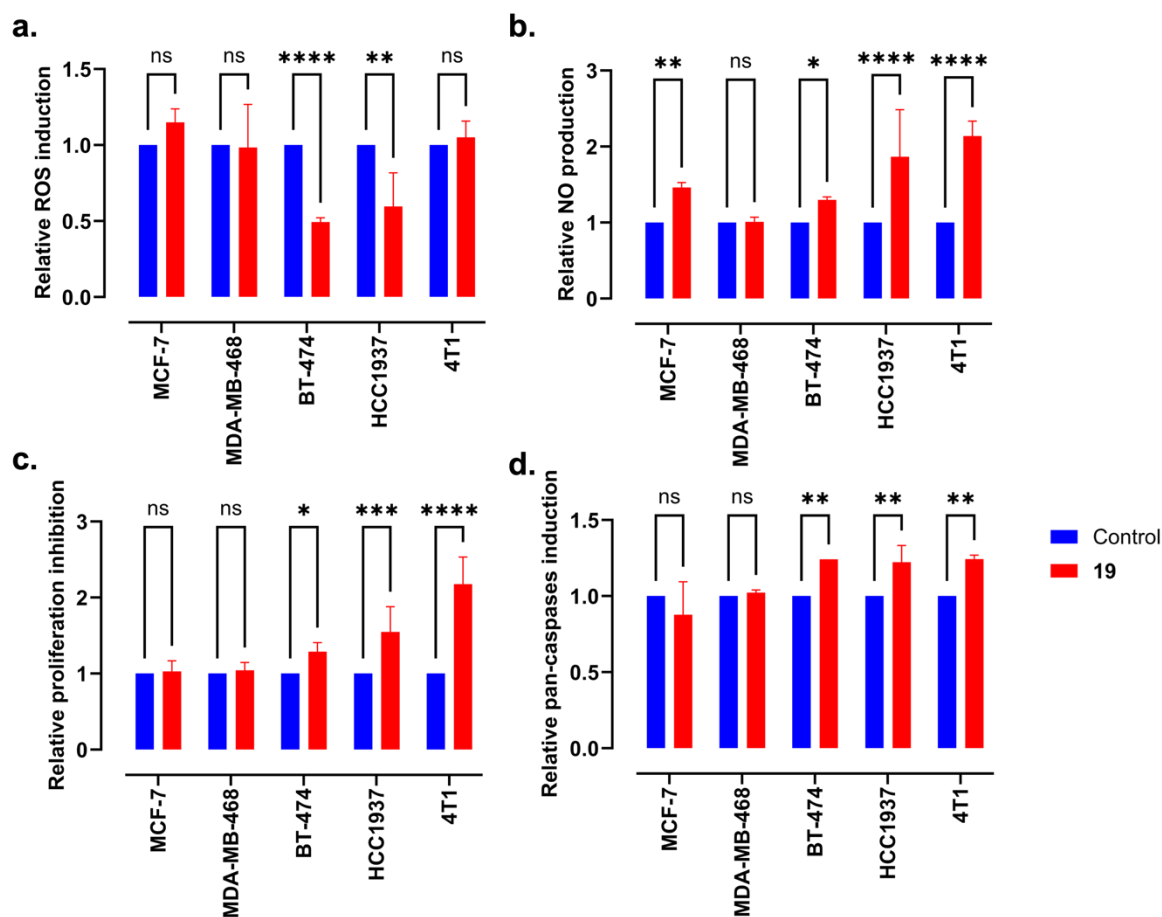


Fig.S13 Bar graphs representing the impact of compound **19** applied at IC_{50} for 72 h to breast cancer cell lines, on **a**, the induction of ROS production; **b**, the induction of NO production; **c**, the inhibition of cell proliferation; **d**, the induction of pan-caspases production. Data were normalized to the corresponding value in the untreated sample. Bars represent the mean values \pm standard deviation calculated based on three independent measurements. *, **, *** and **** $p < 0.05, 0.01, 0.001, 0.0001$ compared to the untreated control cells.

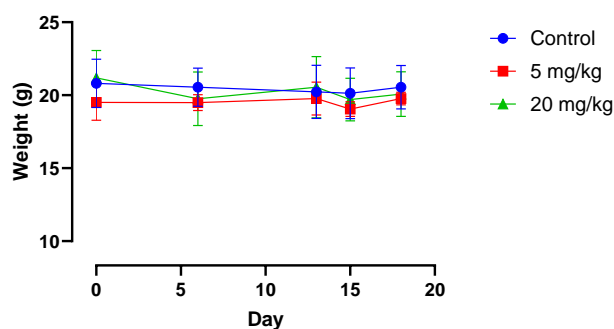


Fig.S14 Body weights of BALB/c mice upon treatment with compound **19** using doses of 5 and 20 mg/kg. The body weight was measured for all mice on day 0, 6, 13, 15 and 18 and are represented as a mean value.

Table S7 Analysis of several biochemical markers in the urine obtained from three mice treated with compound **19** representing the control, 5 mg/kg and 20 mg/kg groups. Samples were obtained on day 6 and 20, representing the first and the last day of treatment, respectively. The urine analysis was performed by using Multistix urine test stripes. “-“: marker was not detectable in the respective urine sample; “+“: marker was detected.

Biochemical markers	Control		5 mg/kg		20 mg/kg	
	Day 6	Day 20	Day 6	Day 20	Day 6	Day 20
Blood	-	-	-	-	-	-
	-	-	-	-	-	-
	-	-	-	-	-	-
Bilirubin	moderate	small	small	small	small	small
	moderate	small	small	small	small	small
	moderate	small	small	small	small	moderate
Uroglobin (mg/dL)	4	8	1	4	4	4
	8	8	4	4	4	4
	4	8	4	1	4	8
Ketones (mg/dL)	5	10	10	10	10	10
	10	5	10	10	10	5
	5	10	10	10	10	10
Proteins (mg/dL)	100	100	100	100	30	30
	100	100	100	100	30	100
	100	100	30	100	30	100
Nitriles	+	-	+	-	+	-
	+	-	-	-	+	-
	+	-	+	-	+	-
Glucose (mg/dL)	-	500	100	-	100	250
	-	-	-	-	100	-
	250	-	100	-	-	500
pH	6	6	6	6	6	5
	5	5	5	6	5	6
	6	6	5	6	5	5
Specific gravity	1.025	1.025	1.025	1.030	1.025	1.030
	1.030	1.030	1.000	1.030	1.025	1.030
	1.030	1.030	1.030	1.025	1.030	1.025
Leucocytes (cells/μL)	75	75	25	25	25	25
	75	25	25	25	25	25
	25	25	25	25	25	75

Chapter 4 : Discovery of a highly selective molecule against triple-negative breast cancer and characterization of its mode of action

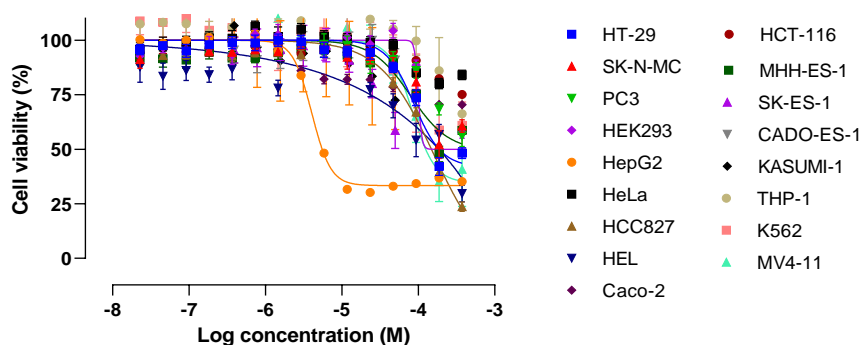


Fig.S15: Dose-response curves of the viability of various cell lines treated with selectAHRyl A for 72 h. The cell viability was determined by using resazurin assay in case of leukemia cell lines, in all other cases CV assay was used. The data are presented as the means of 2-3 independent biological replicates each with technical quadruplicates \pm SEM.

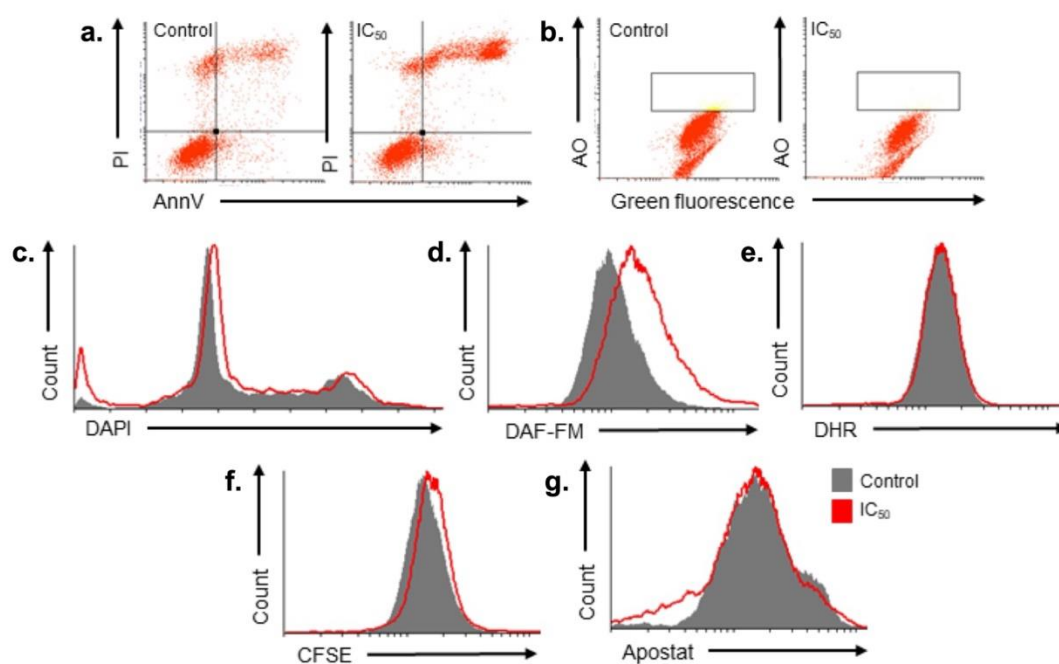


Fig.S16 Representative histograms and dot plots for the impact of selectAHRyl A at IC₅₀ for 72 h against MDA-MB-468 cell line on **a**, induction of apoptosis; **b**, activation of autophagy; **c**, cells distribution in different cell cycle phases; **d**, NO production; **e**, the induction of ROS production; **f**, cell proliferation and **g**, activation of pan-caspases. For CFSE, DHR, DAF-FM, AnnV, and ApoStat stains the fluorescence was analyzed using excitation 488 ± 20 nm and emission of 530 ± 30 nm (showed on the x-axis). For DAPI channel, the fluorescence was analyzed using excitation of 375 ± 20 nm and emission of 450 ± 20 nm (presented on x-axis). For AO and PI dyes, the fluorescence was analyzed using excitation and emission of $488 \pm 20/695 \pm 40$ or $561 \pm 20/610 \pm 20$ nm, respectively, (presented on the y-axis).

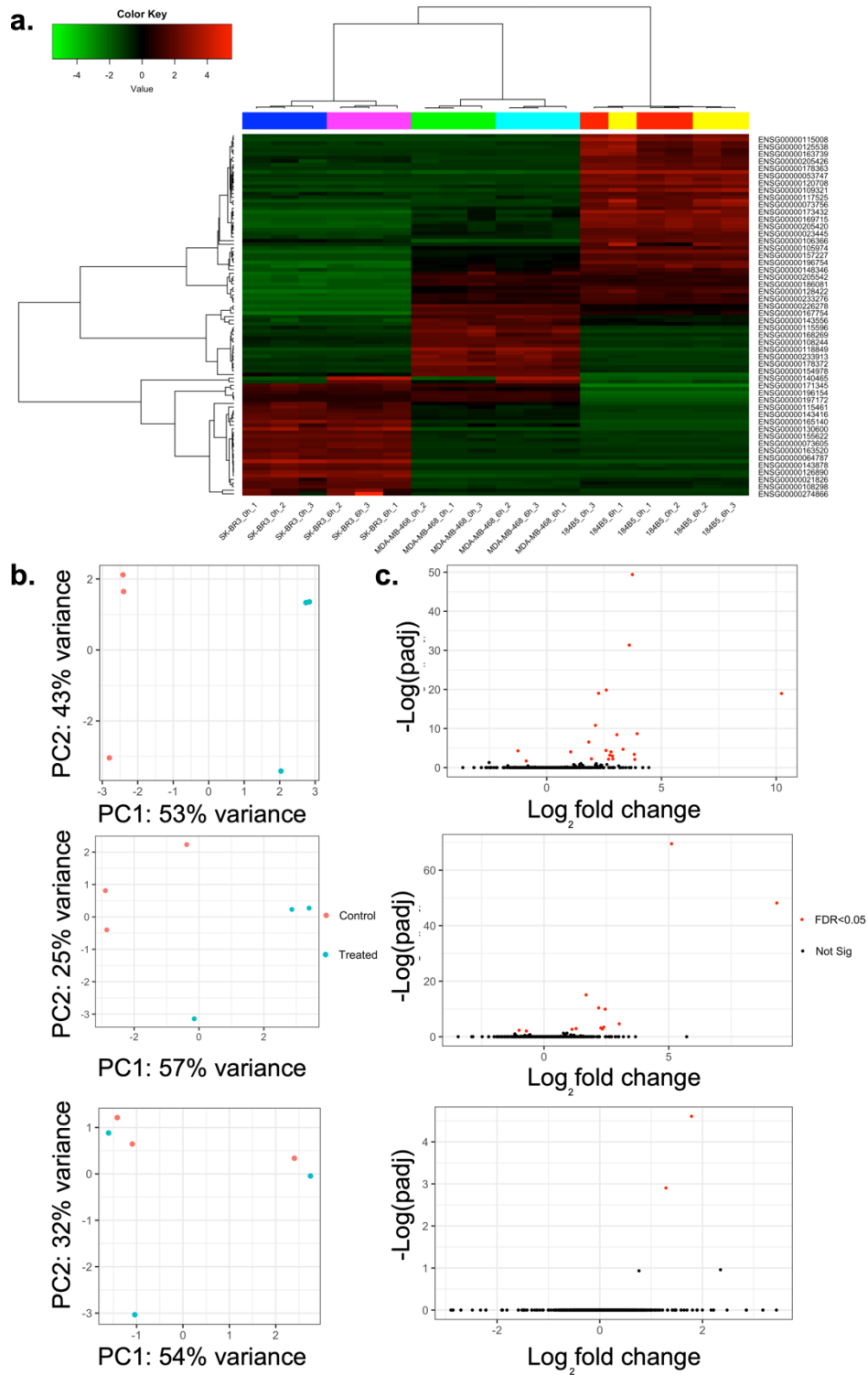


Fig.S17 a, Heat map and **b**, PCA charts comparing the gene expression profiles, i.e. mRNA expression levels, of MDA-MB-468 (top), SK-BR-3 (mid) and 184B5 (bottom) treated for 6 h at 100 μM of selectAHRyl A. Untreated samples of each cell line were included representing 0 h treatment. Data were collected from three biological replicates. **c**, Volcano plots representing the effects of selectAHRyl A against MDA-MB-468 (top), SK-BR-3 (mid) and 184B5 (bottom).

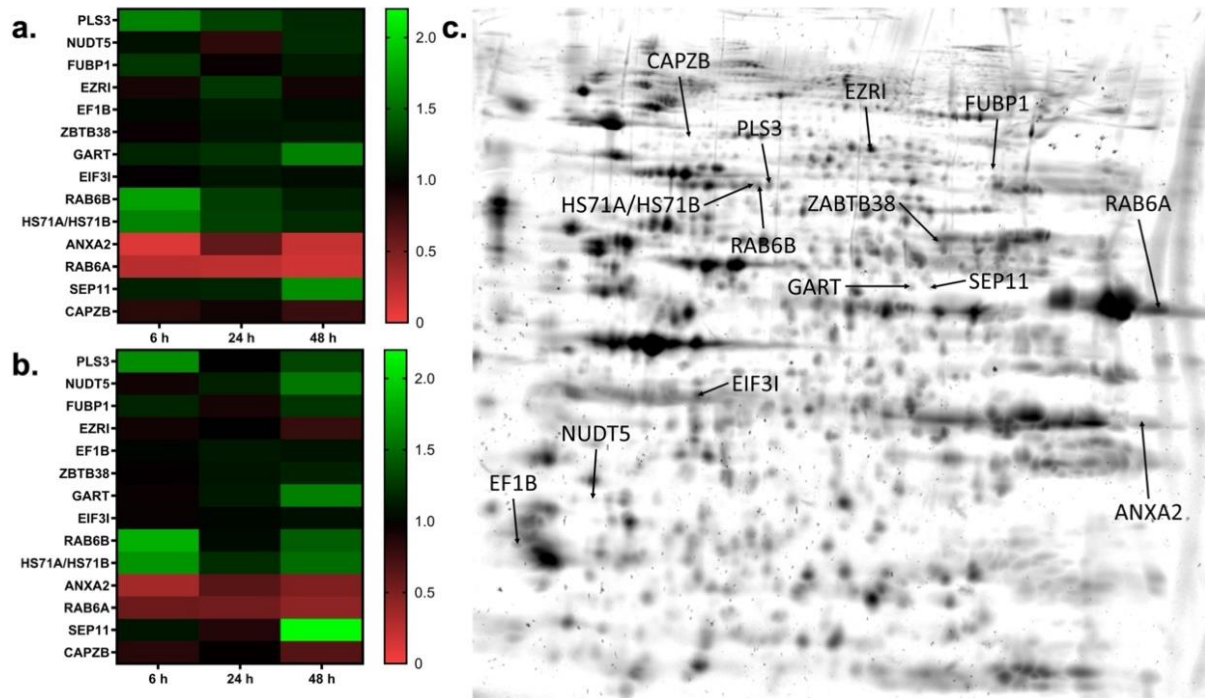


Fig.S18 Proteins that are differentially expressed in MDA-MB-468 cells upon selectAHRyl A treatment at **a**, IC₂₀ and **b**, IC₅₀. **c**, Fused gel image of MDA-MB-468 treated with both concentrations for 6, 24 and 48 h, indicated names represent the most differentially expressed proteins upon treatment.

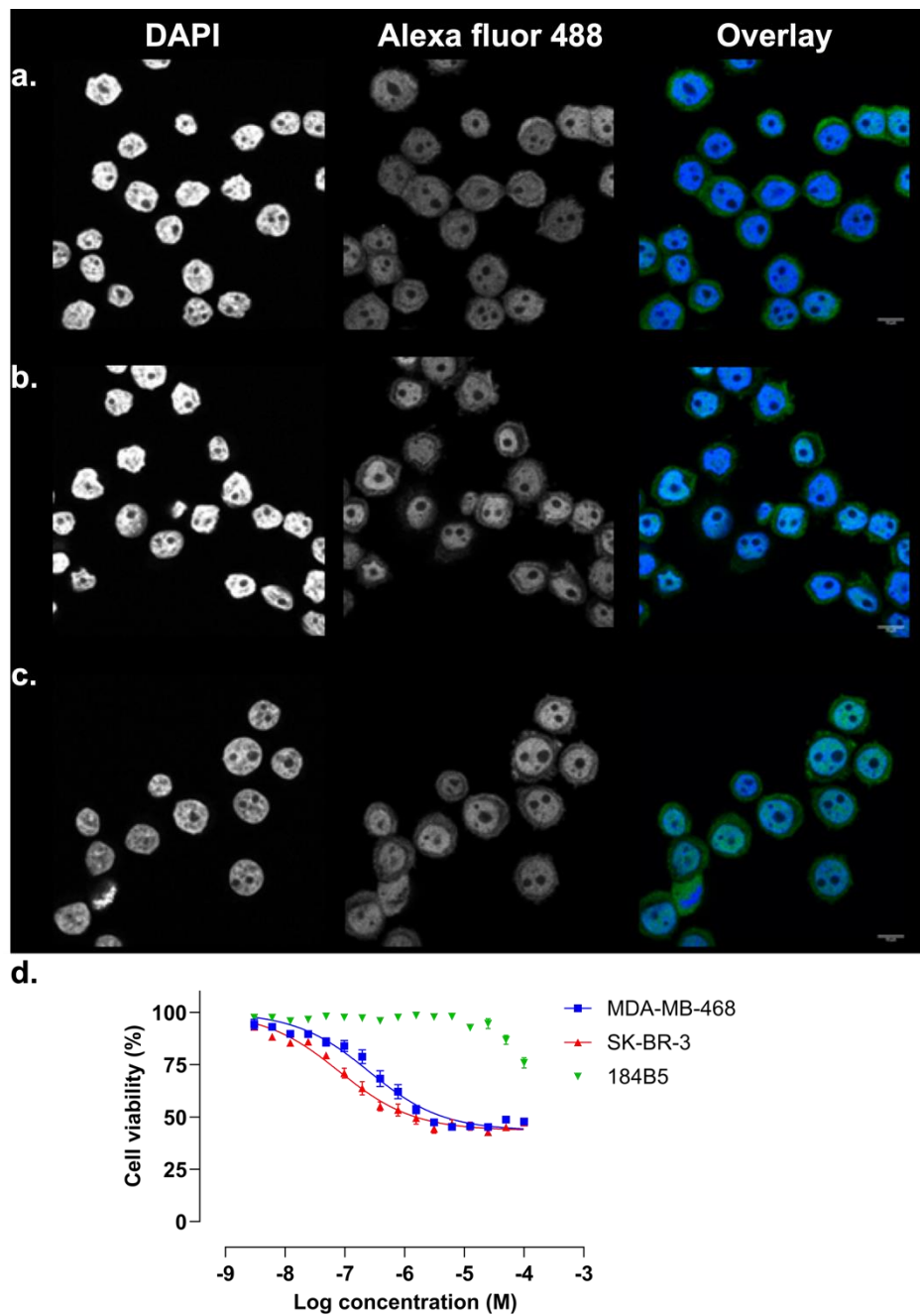


Fig.S19 Images representative for the immunofluorescence analysis of AHR in MDA-MB-468 cells treated with selectAHRyl A using IC_{50} for **a**, 0 min; **b**, 30 min and **c**, 60 min. The cells were stained with an AHR recombinant rabbit monoclonal antibody at a dilution of 1:200, and then incubated with a goat anti-rabbit IgG (H+L) Secondary Antibody, Alexa Fluor Plus 488-conjugated at a dilution of 1:1000 for 60 minutes at RT in the dark (green). Nuclei (blue) were stained with DAPI. Images were taken by a LSM900 at 63 \times magnification, scale bars = 10 μ m. **d**, Dose-response curves of the viability of breast cancer cell lines treated with FICZ for 72 h. The cell viability was determined by CV assay.

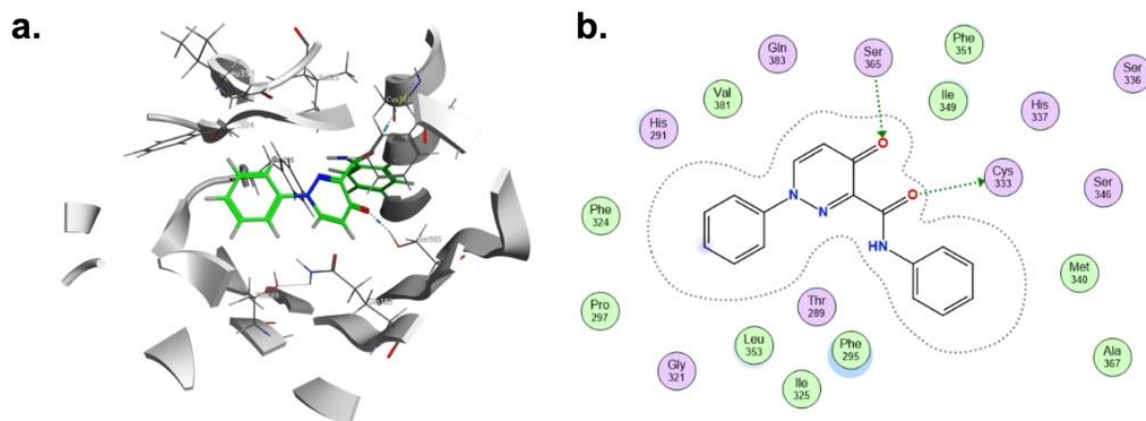


Fig.S20 a, 3D and **b**, 2D images representing the predicted interaction between selectAHRyl A and the structure of the binding pocket of AHR, the latter was predicted by using AlphaFold. The ligand-receptor docking was carried out and the images were generated by using the MOE software.

Table S8 Differentially expressed proteins in MDA-MB-468 upon treatment with selectAHRyl A at IC₂₀ and IC₅₀ for 6, 24 and 48 h.

Protein name	Gene	Uniprot ID	Mass (Da)	pI	MOWSE score	Peptide matched	Sequence coverage (%)
ADP-sugar pyrophosphatase	NUDT5	Q9UUK9	24597	4.87	60	8	37
Trifunctional purine biosynthetic protein adenosine 3	GART	P22102	108953	6.26	68	15	17
Heat shock 70 kDa protein 1A/1B	HSPA1A /1B	P0DMV8 /P0DMV9	70294	5,48	58	12	27
Ezrin	EZR	P15311	69484	5.94	183	32	45
Annexin A2	ANXA2	P07355	38808	7.57	58	11	32
Far upstream element-binding protein 1	FUBP1	Q96AE4	67690	7.18	61	12	21
Plastin-3	PLS3	P13797	71279	5.41	65	16	28
F-actin-capping protein subunit beta	CAPZB	P47756	31616	5.26	122	15	42
Septin-11	SEPT11	Q9NVA2	49652	6.36	108	18	48
Ras-related protein Rab-6A	RAB6A	P20340	23692	5.42	58	5	37
Ras-related protein Rab-6B	RAB6B	Q9NRW1	23561	5.41	62	9	48
Elongation factor 1-beta	EEF1B2	P24534	24919	4.5	77	9	52
Eukaryotic translation initiation factor 3 subunit I	EIF3I	Q13347	36878	5.38	136	18	69
Zinc finger and BTB domain-containing protein 38	ZBTB38	Q8NAP3	136567	8.34	58	14	17

Table S9 Genes showing altered expression upon treatment of MDA-MB-468 cells with selectAHRy1 A at 100 μ M for 6 h.

Ensembl	Gene	log ₂ Fold Change	pvalue	padj
ENSG00000140465	CYP1A1	10.2	0.0	0.0
ENSG00000264785	NA	4.4	0.0	1.0
ENSG00000115844	DLX2	4.2	0.0	1.0
ENSG00000253698	NA	4.2	0.0	1.0
ENSG00000163659	TIPARP	3.9	0.0	0.0
ENSG00000259341	NA	3.9	0.0	1.0
ENSG00000108602	ALDH3A1	3.8	0.0	0.0
ENSG00000260466	NA	3.8	0.0	0.0
ENSG00000138061	CYP1B1	3.7	0.0	0.0
ENSG00000103257	SLC7A5	3.6	0.0	0.0
ENSG00000278598	MIR6775	3.6	0.0	1.0
ENSG00000237232	ZNF295-AS1	3.3	0.0	0.5
ENSG00000114812	VIPR1	3.3	0.0	0.0
ENSG00000232973	CYP1B1-AS1	3.1	0.0	0.4
ENSG00000117407	ARTN	3.1	0.0	0.0
ENSG00000227292	NA	2.9	0.0	1.0
ENSG00000269926	NA	2.9	0.0	0.0
ENSG00000185022	MAFF	2.9	0.0	0.0
ENSG00000141574	SECTM1	2.8	0.0	0.0
ENSG00000229160	NA	2.8	0.0	1.0
ENSG00000128342	LIF	2.7	0.0	0.0
ENSG00000198771	RCSD1	2.7	0.0	1.0
ENSG00000272273	IER3-AS1	2.7	0.0	0.0
ENSG00000119125	GDA	2.6	0.0	0.2
ENSG00000168209	DDIT4	2.6	0.0	0.0
ENSG00000113739	STC2	2.6	0.0	0.0
ENSG00000101670	LIPG	2.4	0.0	0.3
ENSG00000175592	FOSL1	2.4	0.0	0.2
ENSG00000137331	IER3	2.3	0.0	0.0
ENSG00000137709	POU2F3	2.3	0.0	1.0
ENSG00000259583	ALDH1A3-AS1	2.2	0.0	1.0
ENSG00000172348	RCAN2	2.2	0.0	0.5
ENSG00000151715	TMEM45B	2.2	0.0	0.1
ENSG00000129194	SOX15	2.1	0.0	0.2
ENSG00000184254	ALDH1A3	2.1	0.0	0.0
ENSG00000114251	WNT5A	2.1	0.0	1.0
ENSG00000153292	ADGRF1	1.9	0.0	0.0
ENSG00000121454	LHX4	1.9	0.0	1.0
ENSG00000128965	CHAC1	1.9	0.0	1.0
ENSG00000168003	SLC3A2	1.8	0.0	0.0
ENSG00000139289	PHLDA1	1.8	0.0	1.0
ENSG00000257453	NA	1.8	0.0	1.0

ENSG00000163870	TPRA1	1.8	0.0	1.0
ENSG00000179163	FUCA1	1.6	0.0	0.3
ENSG00000179151	EDC3	1.5	0.0	0.8
ENSG00000069812	HES2	1.5	0.0	1.0
ENSG00000121895	TMEM156	1.5	0.0	0.1
ENSG00000078124	ACER3	1.5	0.0	1.0
ENSG00000125968	ID1	1.4	0.0	0.2
ENSG00000136158	SPRY2	1.4	0.0	1.0
ENSG00000185950	IRS2	1.4	0.0	1.0
ENSG00000087074	PPP1R15A	1.4	0.0	0.8
ENSG00000119669	IRF2BPL	1.3	0.0	1.0
ENSG00000129474	AJUBA	1.3	0.0	1.0
ENSG00000175197	DDIT3	1.3	0.0	1.0
ENSG00000178209	PLEC	1.2	0.0	0.4
ENSG00000110080	ST3GAL4	1.2	0.0	0.8
ENSG00000102554	KLF5	1.2	0.0	0.2
ENSG00000224516	NA	1.1	0.0	1.0
ENSG00000162337	LRP5	1.1	0.0	1.0
ENSG00000137203	TFAP2A	1.1	0.0	1.0
ENSG00000177426	TGIF1	1.0	0.0	1.0
ENSG00000075426	FOSL2	1.0	0.0	1.0
ENSG00000146648	EGFR	1.0	0.0	0.0
ENSG00000044115	CTNNA1	1.0	0.0	1.0
ENSG00000117525	F3	1.0	0.0	1.0
ENSG00000072210	ALDH3A2	1.0	0.0	1.0
ENSG00000126391	FRMD8	1.0	0.0	1.0
ENSG00000146072	TNFRSF21	1.0	0.0	1.0
ENSG00000168994	PXDC1	0.9	0.0	1.0
ENSG00000162496	DHRS3	0.9	0.0	1.0
ENSG00000163283	ALPP	0.9	0.0	1.0
ENSG00000117394	SLC2A1	0.9	0.0	0.8
ENSG00000101255	TRIB3	0.9	0.0	0.8
ENSG00000155304	HSPA13	0.9	0.0	1.0
ENSG00000183421	RIPK4	0.9	0.0	0.8
ENSG00000163993	S100P	0.8	0.0	1.0
ENSG00000168672	LRATD2	0.8	0.1	1.0
ENSG00000128422	KRT17	0.8	0.0	0.8
ENSG00000154640	BTG3	0.8	0.0	1.0
ENSG00000163083	INHBB	0.8	0.1	1.0
ENSG00000146674	IGFBP3	0.8	0.0	1.0
ENSG00000134294	SLC38A2	0.7	0.0	1.0
ENSG00000116044	NFE2L2	0.7	0.1	1.0
ENSG00000143162	CREG1	0.7	0.0	1.0
ENSG00000130066	SAT1	0.6	0.0	0.8

ENSG00000135069	PSAT1	0.6	0.0	1.0
ENSG00000198886	ND4	0.5	0.0	1.0
ENSG00000198763	ND2	0.4	0.0	1.0
ENSG00000198899	ATP6	0.4	0.0	1.0
ENSG00000198727	CYTB	0.4	0.0	1.0
ENSG00000167754	KLK5	-0.4	0.0	1.0
ENSG00000188643	S100A16	-0.4	0.0	1.0
ENSG00000184009	ACTG1	-0.4	0.1	1.0
ENSG00000169564	PCBP1	-0.5	0.0	1.0
ENSG00000171345	KRT19	-0.5	0.0	0.8
ENSG00000109971	HSPA8	-0.5	0.0	1.0
ENSG00000109062	SLC9A3R1	-0.5	0.1	1.0
ENSG00000184292	TACSTD2	-0.5	0.0	1.0
ENSG00000163220	S100A9	-0.5	0.0	0.8
ENSG00000143320	CRABP2	-0.6	0.0	1.0
ENSG00000175130	MARCKSL1	-0.6	0.0	1.0
ENSG00000175063	UBE2C	-0.6	0.0	1.0
ENSG00000011426	ANLN	-0.6	0.0	1.0
ENSG00000123975	CKS2	-0.6	0.0	0.9
ENSG00000143546	S100A8	-0.7	0.0	1.0
ENSG00000117399	CDC20	-0.7	0.0	0.8
ENSG00000134057	CCNB1	-0.7	0.0	1.0
ENSG00000137440	FGFBP1	-0.7	0.0	1.0
ENSG00000189060	H1-0	-0.7	0.0	1.0
ENSG00000277443	MARCKS	-0.7	0.0	1.0
ENSG00000182481	KPNA2	-0.7	0.0	1.0
ENSG00000189159	JPT1	-0.7	0.0	1.0
ENSG00000106211	HSPB1	-0.8	0.0	1.0
ENSG00000167755	KLK6	-0.8	0.0	1.0
ENSG00000204389	HSPA1A	-0.8	0.0	1.0
ENSG00000178372	CALML5	-0.8	0.0	0.4
ENSG00000112984	KIF20A	-0.8	0.0	1.0
ENSG00000242265	PEG10	-0.9	0.0	1.0
ENSG00000168269	FOXI1	-0.9	0.0	1.0
ENSG00000272398	CD24	-0.9	0.0	0.0
ENSG00000079215	SLC1A3	-1.0	0.0	1.0
ENSG00000179431	FJX1	-1.1	0.0	1.0
ENSG00000163347	CLDN1	-1.1	0.0	1.0
ENSG00000175793	SFN	-1.3	0.0	0.0
ENSG00000105929	ATP6V0A4	-1.3	0.0	1.0
ENSG00000128510	CPA4	-1.3	0.0	1.0
ENSG00000171617	ENC1	-1.4	0.0	0.9
ENSG00000226745	NA	-1.5	0.1	1.0
ENSG00000189120	SP6	-1.6	0.0	1.0

ENSG00000204682	MIR1915HG	-1.6	0.0	1.0
ENSG00000117318	ID3	-1.7	0.0	0.3
ENSG00000265107	GJA5	-1.7	0.0	1.0
ENSG00000107984	DKK1	-2.5	0.0	0.1
ENSG00000196196	HRCT1	-2.7	0.0	1.0

Table S10 Genes showing altered expression upon treatment of SK-BR-3 cells with selectAHRy1 A at 100 μ M for 6 h.

Ensembl	Gene	log₂Fold Change	pvalue	padj
ENSG00000140465	CYP1A1	9.33	0.00	0.00
ENSG00000232973	CYP1B1-AS1	5.72	0.00	1.00
ENSG00000138061	CYP1B1	5.11	0.00	0.00
ENSG00000063438	AHRR	3.39	0.01	1.00
ENSG00000182585	EPGN	3.02	0.00	0.00
ENSG00000140505	CYP1A2	3.00	0.03	1.00
ENSG00000169627	BOLA2	2.97	0.01	1.00
ENSG00000260466	NA	2.65	0.00	1.00
ENSG00000113369	ARRDC3	2.63	0.01	1.00
ENSG00000115844	DLX2	2.59	0.02	1.00
ENSG00000172061	LRRC15	2.46	0.03	1.00
ENSG00000141574	SECTM1	2.45	0.00	0.00
ENSG00000173641	HSPB7	2.39	0.00	0.00
ENSG00000163659	TIPARP	2.34	0.00	0.00
ENSG00000114812	VIPR1	2.28	0.00	0.00
ENSG00000184254	ALDH1A3	2.19	0.00	0.00
ENSG00000144355	DLX1	2.00	0.03	1.00
ENSG00000269926	NA	1.95	0.01	1.00
ENSG00000185022	MAFF	1.70	0.05	1.00
ENSG00000103257	SLC7A5	1.69	0.00	0.00
ENSG00000229257	NA	1.59	0.03	1.00
ENSG00000172602	RND1	1.57	0.00	0.59
ENSG00000179151	EDC3	1.47	0.00	0.46
ENSG00000275266	NA	1.44	0.02	1.00
ENSG00000111962	UST	1.29	0.05	1.00
ENSG00000115758	ODC1	1.28	0.00	0.00
ENSG00000134508	CABLES1	1.27	0.02	1.00
ENSG00000163870	TPRA1	1.25	0.03	1.00
ENSG00000173267	SNCG	1.25	0.03	1.00
ENSG00000267601	NA	1.22	0.02	1.00
ENSG00000070404	FSTL3	1.22	0.03	1.00
ENSG00000165905	LARGE2	1.20	0.00	0.26
ENSG00000274630	NA	1.16	0.05	1.00
ENSG00000210140	NA	1.14	0.04	1.00
ENSG00000172216	CEBPB	1.12	0.00	0.00
ENSG00000204389	HSPA1A	1.07	0.00	0.20

ENSG00000161091	MFSD12	1.06	0.01	1.00
ENSG00000068650	ATP11A	1.06	0.05	1.00
ENSG00000204388	HSPA1B	1.04	0.00	0.63
ENSG00000265972	TXNIP	1.01	0.02	1.00
ENSG00000130821	SLC6A8	1.00	0.01	1.00
ENSG00000121039	RDH10	0.98	0.01	0.99
ENSG00000181019	NQO1	0.92	0.00	0.05
ENSG00000163584	RPL22L1	0.85	0.04	1.00
ENSG00000137331	IER3	0.84	0.00	0.42
ENSG00000178209	PLEC	0.82	0.02	1.00
ENSG00000168209	DDIT4	0.82	0.00	0.10
ENSG00000198431	TXNRD1	0.78	0.00	0.05
ENSG00000160712	IL6R	0.74	0.03	1.00
ENSG00000141526	SLC16A3	0.69	0.02	1.00
ENSG00000134258	VTCN1	0.67	0.00	0.65
ENSG00000006327	TNFRSF12A	0.54	0.03	1.00
ENSG00000136997	MYC	0.53	0.03	1.00
ENSG00000136261	BZW2	0.48	0.03	1.00
ENSG00000153395	LPCAT1	0.47	0.05	1.00
ENSG00000044115	CTNNA1	0.47	0.02	1.00
ENSG00000087086	FTL	0.46	0.02	1.00
ENSG00000109971	HSPA8	0.36	0.03	1.00
ENSG00000100867	DHRS2	-0.41	0.01	1.00
ENSG00000166145	SPINT1	-0.44	0.05	1.00
ENSG00000106211	HSPB1	-0.45	0.03	1.00
ENSG00000115884	SDC1	-0.45	0.02	1.00
ENSG00000163220	S100A9	-0.47	0.02	1.00
ENSG00000092820	EZR	-0.49	0.01	1.00
ENSG00000189143	CLDN4	-0.50	0.05	1.00
ENSG00000170421	KRT8	-0.52	0.02	1.00
ENSG00000184009	ACTG1	-0.55	0.04	1.00
ENSG00000075624	ACTB	-0.56	0.00	0.18
ENSG00000109062	SLC9A3R1	-0.62	0.00	0.33
ENSG00000184897	H1-10	-0.63	0.04	1.00
ENSG00000177383	MAGEF1	-0.63	0.02	1.00
ENSG00000102243	VGLL1	-0.69	0.01	1.00
ENSG00000115107	STEAP3	-0.69	0.03	1.00
ENSG00000272398	CD24	-0.71	0.00	0.01
ENSG00000135821	GLUL	-0.74	0.00	0.50
ENSG00000170477	KRT4	-0.75	0.05	1.00
ENSG00000111057	KRT18	-0.77	0.00	0.33
ENSG00000188486	H2AX	-0.77	0.01	1.00
ENSG00000001617	SEMA3F	-0.78	0.05	1.00
ENSG00000135245	HILPDA	-0.79	0.03	1.00

ENSG00000218416	GPC1-AS1	-0.82	0.02	1.00
ENSG00000078804	TP53INP2	-0.83	0.01	0.87
ENSG00000124126	PREX1	-0.84	0.02	1.00
ENSG00000051108	HERPUD1	-0.86	0.01	1.00
ENSG00000255690	TRIL	-0.87	0.04	1.00
ENSG00000242265	PEG10	-0.91	0.04	1.00
ENSG00000186603	HPDL	-0.91	0.00	0.63
ENSG00000207425	NA	-0.92	0.04	1.00
ENSG00000189060	H1-0	-1.00	0.00	0.00
ENSG00000163207	IVL	-1.06	0.03	1.00
ENSG00000064195	DLX3	-1.08	0.02	1.00
ENSG00000115461	IGFBP5	-1.10	0.00	0.47
ENSG00000123080	CDKN2C	-1.15	0.05	1.00
ENSG00000188613	NANOS1	-1.16	0.03	1.00
ENSG00000265107	GJA5	-1.17	0.00	0.10
ENSG00000186834	HEXIM1	-1.17	0.01	1.00
ENSG00000171617	ENC1	-1.20	0.04	1.00
ENSG00000141750	STAC2	-1.25	0.05	1.00
ENSG00000265806	MIR4292	-1.33	0.01	1.00
ENSG00000189120	SP6	-1.47	0.04	1.00
ENSG00000226745	NA	-2.22	0.02	1.00

Table S11 Genes showing altered expression upon treatment of 184B5 cells with selectAHRyl A at 100 μ M for 6 h.

Ensembl	Gene	log₂Fold Change	pvalue	padj
ENSG00000162892	IL24	2.35	0.00	0.11
ENSG00000197632	SERPINB2	1.79	0.00	0.00
ENSG00000073756	PTGS2	1.29	0.00	0.00
ENSG00000087074	PPP1R15A	1.02	0.01	1.00
ENSG00000114422	PLAUR	0.98	0.03	1.00
ENSG00000120129	DUSP1	0.96	0.00	1.00
ENSG00000175505	CLCF1	0.91	0.02	1.00
ENSG00000148154	UGCG	0.84	0.02	1.00
ENSG00000182585	EPGN	0.83	0.04	1.00
ENSG00000109321	AREG	0.82	0.00	1.00
ENSG00000113739	STC2	0.81	0.05	1.00
ENSG00000184254	ALDH1A3	0.76	0.00	0.12
ENSG00000116285	ERRFI1	0.72	0.01	1.00
ENSG00000128422	KRT17	0.67	0.02	1.00
ENSG00000112972	HMGCS1	0.67	0.03	1.00
ENSG00000117595	IRF6	0.62	0.01	1.00
ENSG00000128272	ATF4	0.54	0.02	1.00
ENSG00000013588	GPRC5A	0.53	0.03	1.00
ENSG00000168003	SLC3A2	0.51	0.03	1.00
ENSG00000142871	CCN1	0.46	0.05	1.00

ENSG00000168209	DDIT4	0.43	0.04	1.00
------------------------	-------	------	------	------

Table S12 Primers used for the qPCR analysis. The primers were designed using Primer-Blast from NCBI.

Gene name	Sense sequence (5'-3')	Antisense sequence (5'-3')
GAPDH	TTGCCATCAATGACCCCTTCA	CGCCCCACTTGATTTTGGGA
AHRR	GCTGCTGTTGGAGTCTCTTA	GTTCTGGTGCATTACATCCG
CYP1B1	TGGATTTGGAGAACGTACCG	GACCTGATCCAATTCTGCCT
CYP1A1	GTCTTTGTAAACCAGTGGC	GAGAAACCGTTCAGGTAGGA
AHR	TTGGTTGTGATGCCAAAGGA	TCATTCGGATATGGGACTCG

Table S13 Chromatographic conditions used for UHPLC separation of the samples.

Parameter	Settings
Column	Waters Acquity UPLC BEH C18, 50 × 2.1 mm, 1.7 μm particle size
Column temperature	50°C
Eluents	
Eluent A	0.1% formic acid in water
Eluent B	0.1% formic acid in acetonitrile
Flow rate	0.3 mL/min
Injection	
Injection mode	Partial Loop
Injection volume	2 μL
Weak wash solvent	0.1% formic acid in water
Strong wash solvent	0.1% formic acid in acetonitrile
Wash volume (both)	600 μL
Sample temperature	8°C
Separation gradient	
Time (min)	% Eluent B
Initial	5
1.00	Isocratic at 5
10.00	linear gradient from 5 to 95
13.00	isocratic at 95
14.00	linear gradient from 95 to 5
19.00	isocratic at 5 (re-equilibration)

Table S14 Mass analyzer settings applied for MS/MS experiments. Psig - pound-force per square inch.

Parameter	Settings
Mass analyzer type	hybrid quadrupole-time of flight
Ionization mode	positive
Resolution	at least 30 000
Ion spray voltage	5500 V
Nebulizing gas (Gas 1)	90 psig
Drying gas (Gas 2)	70 psig
Curtain gas (CUR)	55 psig
Temperature (TEM)	450°C
Declustering potential (DP), full TOF scan	35 V
Collision potential (CE), full TOF scan	10 V
Collision potential (CE), MS/MS	15, 20, 25, 35, 45, 55 V
Mass to charge ratio (m/z) range	50-1000
Accumulation times (all experiments)	50 ms

Table S15 Key ions in positive ion ESI-MS/MS spectra of selectAHRyl A and its metabolites M1-M4. Fragments are labelled like in Fig.30b.

Analyte	Collision energy (%)	SelectAHRyl A	M1	M2	M3	M4
Retention time		5.24 min	4.90 min	4.08 min	3.79 min	3.56 min
Ion/compound						
[M+H]⁺	-	292.1088 (C ₁₇ H ₁₄ N ₃ O ₂ ⁺)	308.1038 (C ₁₇ H ₁₄ N ₃ O ₃ ⁺)	308.1037 (C ₁₇ H ₁₄ N ₃ O ₃ ⁺)	324.0989 (C ₁₇ H ₁₄ N ₃ O ₄ ⁺)	324.0982 (C ₁₇ H ₁₄ N ₃ O ₄ ⁺)
[M+H-H₂O]⁺	20	274.0987 (C ₁₇ H ₁₂ N ₃ O ⁺)	290.0932 (C ₁₇ H ₁₂ N ₃ O ₂ ⁺)	290.0933 (C ₁₇ H ₁₂ N ₃ O ₂ ⁺)	306.0894 (C ₁₇ H ₁₂ N ₃ O ₃ ⁺)	306.0864 (C ₁₇ H ₁₂ N ₃ O ₃ ⁺)
Fragment a	20/25	199.0510 (C ₁₁ H ₇ N ₂ O ₂ ⁺)	215.0458 (C ₁₁ H ₇ N ₂ O ₃ ⁺)	199.0503 (C ₁₁ H ₇ N ₂ O ₂ ⁺)	215.0463 (C ₁₁ H ₇ N ₂ O ₃ ⁺)	215.0446 (C ₁₁ H ₇ N ₂ O ₃ ⁺)
Fragment b	20/25/35	171.0558 (C ₁₀ H ₇ N ₂ O ⁺)	187.0502 (C ₁₀ H ₇ N ₂ O ₂ ⁺)	171.0552 (C ₁₀ H ₇ N ₂ O ⁺)	187.0511 (C ₁₀ H ₇ N ₂ O ₂ ⁺)	187.0481 (C ₁₀ H ₇ N ₂ O ₂ ⁺)
[b-CH₂CO]⁺	35	129.0444 (C ₈ H ₅ N ₂ ⁺)	n.d.	145.0396 (C ₈ H ₅ N ₂ O ⁺)	145.0401 (C ₈ H ₅ N ₂ O ⁺)	145.0396 (C ₈ H ₅ N ₂ O ⁺)
Fragment c	25/35	116.0493 (C ₈ H ₆ N ⁺)	132.0440 (C ₈ H ₆ NO ⁺)	116.0490 (C ₈ H ₆ N ⁺)	132.0445 (C ₈ H ₆ NO ⁺)	132.0423 (C ₈ H ₆ NO ⁺)
Fragment d	35/45/55	-	104.0490 (C ₇ H ₆ N ⁺)	-	104.0491 (C ₇ H ₆ N ⁺)	104.0483 (C ₇ H ₆ N ⁺)
[c-C₂H₂N]⁺	45/55	77.0385 (C ₆ H ₅ ⁺)	77.0386 (C ₆ H ₅ ⁺)	-	77.0379 (C ₆ H ₅ ⁺)	-
[c-C₂HN]⁺	45/55	-	-	93.0334 (C ₆ H ₅ O ⁺)	93.0336 (C ₆ H ₅ O ⁺)	93.0329 (C ₆ H ₅ O ⁺)

n.d. not detected.

IBRAHIM MORGAN

Postdoctoral researcher, Cellular and Molecular Oncology

PROFILE

Passionate scientist with extensive experience in cancer research, focusing on the discovery of small molecules targeting specific cancer types. Expert in uncovering novel mechanisms of action and selectivity using advanced and unconventional techniques. Dedicated to advancing cancer treatment through personalized therapeutic strategies and committed to continuous learning and the adoption of emerging technologies to push the boundaries of scientific discovery.

EXPERIENCE

Research Associate in Cellular and Molecular Oncology 05/2018 - Present
Leibniz Institute, Anticancer & targeting group Halle (Saale)

- **Spearheaded** the discovery of a novel breast cancer treatment compound from a library of over 30,000 candidates, leading to a patent application.
- **Trained** new lab members and external collaborators, tailoring sessions to their backgrounds and needs, making complex concepts accessible and actionable.
- **Managed** lab equipment (FACS, RT-qPCR, fluorescence microscopes) with consistent interaction with sales representatives and Field Application Scientists (FAS) from suppliers. This collaboration provided insights into both technical and business objectives, fostering successful partnerships.
- **Conducted** 300+ molecular assays, leading to the identification of 50+ compounds with anticancer potential. Communicated findings effectively to interdisciplinary teams, ensuring actionable outcomes.
- **Co-authored** 15 publications, contributing to advancements in cancer research and enhancing professional visibility.

Oncology Pharmacist 12/2014 - 05/2015
Nasser Institute Cairo

- **Delivered** personalized pharmaceutical care to over 200 cancer patients, demonstrating empathy and clarity in patient interactions.
- **Collaborated** with 50+ healthcare professionals to optimize treatment plans, showcasing an ability to work across disciplines for patient-centric outcomes.

EDUCATION

Doctor of Philosophy (PhD)-Natural sciences 2018 - 2025
Martin Luther University Halle (Saale)

Master of Science (MSc)-Natural sciences 2015 - 2018
Martin Luther University Halle (Saale)

Bachelor of Science (BSC)-Pharmacy 2007 - 2012
Cairo University Cairo

LANGUAGES

English 
Proficient (IELTS - C1)

German 
Advanced (Telc - B1)

Arabic 
Native

Skills

Analysis Software

Microsoft Office
Cyflogic
BD FacsDiva
Genevestigator
RStudio

GraphPad Prism
Flowing Software
Fiji Image Analysis
Cytoscape

Molecular Biology Techniques

RT-qPCR
Fluorescence microscopy
Electrophoresis
Western Blotting
Cell culture
preparative HPLC
FACS und flow cytometry
Automated pipetting robots

PCR
RNA-Seq
HRMS
ELISA
LC/MS

Soft Skills

Teamwork
Documentation
Time management
Adaptability
Work under pressure
Communication skills
Presentation and teaching skills

Critical thinking
Problem solving
Troubleshooting
Strategic planning
Scientific writing

Awards

Best Poster Presentation

Leibniz Research Network